DEPARTMENT OF CHEMISTRY
UNIVERSITY OF GLASGOW

A STUDY OF THE EFFECTS OF POTASSIUM VAPOUR ON CARBONISED MATERIALS

by

LORRAINE S. GARRICK

Thesis submitted for the degree of
DOCTOR OF PHILOSOPHY

SEPTEMBER 1992

To the memory of ANNA MARIA KODUR

CONTENTS

CHAPTER THREE: EXPERIMENTAL

CHAPTER FOUR: RESULTS FOR THE FEED AND EXTUYERE COKE AND THE CARBONISED SUCROSE AND PVA

CHAPTER NINE: DISCUSSION OF THE RESULTS FOR THE SAMPLES PREPARED VIA AN OPEN CARBONISATION SYSTEM

ACKNOWLEDGEMENTS

I would like to express my thanks to my supervisors Dr. Thomas Baird and Dr. John R. Fryer for all the help, advice and encouragement they have given me throughout the course of my research at Glasgow University.

I would also like to thank my fellow workers in the Electron Microscopy Group for their useful discussions and in particular Davi Thom, Margaret Mullen and Eoin Robertson for their technical assistance.

I am particularly indebted to Mr Ray Hutchins and the technical staff of the Electrical Engineering Department at Glasgow University for providing access to equipment.

Many other people contributed to this work and it would be difficult to thank everyone individually, thus, I take this opportunity to express my thanks.

I wish to thank my family and friends for their support throughout the course of my research at Glasgow University and during the writing of this thesis and Des who proof read and assisted with the production of this manuscript.

This study was made possible by the financial support given to me by British Coal for which I am very grateful. I would also like to express my thanks to British Coal for providing samples for analysis and for the preparation of samples as requested.

DECLARATION

This thesis is a record of the work carried out by the author in the Department of Chemistry at the University of Glasgow, under the supervision of Dr T. Baird and Dr. J.R. Fryer.

No part of this work has been previously submitted in any previous application for a degree.

Some of the work described in this thesis has appeared in the following papers:-

1. Garrick, L.S, Fryer, J.R. and Baird, T. HREM study of graphitisable and non-graphitisable carbon. EUREM 88, Proc. 9th Europ. Congr. Electron Microsc., (Goodhew, P.J. & Dickinson, H.G., Eds.), London: Inst. Phys., Conf. Ser. No. 93, pp 281-282 (1988).

2. Garrick, L.S., Baird, T. and Fryer, J.R. A high resolution study of carbonised materials. CARBON 88, Int. Conf. on Carbon (McEnaney, B. & Mays, T.J., Eds.), London : Soc. of Chem. Ind., Inst. Phys. Publ. pp 125-127 (1988).

3. Garrick, L.S., Fryer, J.R. and Baird, T. Microstructural study of the effects of potassium vapour on carbonised materials. Proc. 12th International Congress on Electron Microsc., San Francisco: San Francisco Press. pp 1082-1083 (1990).

SUMMARY

Metallurgical coke in the blast furnace provides a permeable matrix through which reducing gases may ascend and molten materials descend. The coke bed matrix permeability is thus an important property of the coke for blast furnace operations. A lack of permeability will inevitably lead to a poor gas distribution and result in a reduction of the furnace output and efficiency.

A decrease in the permeability of the carbonaceous coke matrix arises when changes, induced by the blast furnace environment, occur in the properties of the material and affect the matrix voidage by causing a reduction of coke strength.

A major influence of change within the blast furnace is the presence of recirculating alkali, particularly potassium, which is known to induce considerable microstructural change (enhanced localised ordering), within the metallurgical coke. These microstructural changes, lead to structural weakening and the subsequent degradation of the coke structure as a consequence of a variety of factors:-

1. The formation of an intercalated material that results in expansion of the carbon lattices. This structure would thus be more accessible and susceptible to degradation by chemical and mechanical attack.

2. Structural ordering by single or repeated intercalation orders the structure by the removal of crystallographic defects. This would create interfaces

between ordered and disordered carbon and thus weaken the material.

3. The occurrence of different microstructural forms within the carbon would affect degradation through differential volume expansion and give rise to localised stresses.

The resulting degradation and structural weakening of the coke has a detrimental affect on the coke bed matrix by reducing the coke mean size and voidage of the material and ultimately coke strength.

The present research has been orientated towards investigating the affect and susceptibility of different carbon structures to alkali attack. The structural changes occurring within these carbons being studied as a model for the more heterogeneous coke system. Knowledge of the induced structural changes and affects of the parameters involved would allow conclusions to be drawn as to the most suitable methods or treatments for reducing or eliminating the destruction of metallurgical coke, in the blast furnace, by alkali vapours.

The majority of this work has involved analysis of the microstructural aspects of the different carbons and the changes induced therein.

The work can be divided into two parts:-

1. The carbonisation of the parent materials, under various conditions, up to 800 and 1100°C, and the subsequent study of the calcined products by thermogravimetry and x-ray diffraction with complimentary morphological and structural investigations made by

scanning and transmission electron microscopy.

2. Exposure of the carbonised materials to potassium vapour and an investigation of the resultant microstructure by high resolution electron microscopy (HREM) in correlation with x-ray diffraction, scanning electron microscopy and flame photometry measurements of potassium concentrations.

Prior to exposure with potassium vapour, the carbonised materials, arising from both the non-graphitising and graphitising carbons, exhibited an abundance of short-range (L_a=1-10nm) ordered structure with interplanar spacings that encompassed a wide range of values (0.33-0.72nm). Areas of long-range ordered structure (L_a>10nm) were also evident, but to a lesser extent than the non-graphitised carbon structure, and displayed interplanar spacing within a much smaller range (0.31-0.41nm). Also visible in some of the carbonised samples, though to a much lesser extent than either of the long or short-range ordered structures, were regions of convoluted structural order that generally exhibited interplanar spacings, L_a and L_c values that were indistinguishable from any associated long-range ordered structure.

Initally, this convoluted structure was only detected after exposure of the PVA(800) and SUC(800) to potassium vapour. However, the low temperature 'carbonisation' study of sucrose also revealed areas displaying convoluted structure. Thus, the convoluted structure, originally thought to evolve as a result of exposure to potassium vapour develops within the carbon matrix during

carbonisation, although the structure was not detected at all the carbonisation treatments for the same carbonised materials.

The presence of potassium, promoted structural development, in the carbonised samples arising from both the graphitising and non-graphitising carbons. This was manifested as an increase in the regions of long-range ordered structure, the extent of the ordered domains was still not as abundant as the short-range ordered structure, development of convoluted structural order and both a decrease and an increase in the interplanar spacings. A decrease in interplanar spacings arising as a result of potassium penetration into the carbonised microstructure and the subsequent collapse of these expanded lattice planes to a more ordered structure. The corresponding increase, developing as a consequence of an intercalated or residue compound causing an expanded carbon structure.

CHAPTER ONE

INTRODUCTION

1.1- INTRODUCTION

Conditions in modern blast furnaces are such, that the coke is subjected to severe chemical, thermal and mechanical stresses (Goleczka et al., 1982(b)). An important property of coke for blast furnace operations is the formation of a permeable matrix, so that heat and reducing gases can be generated and distributed in a proper manner (Lu, 1980; Goleczka et al., 1982(a)).

Previous studies (Davies et al., 1978; Hatano et al., 1980; Lu, 1980; Lu and Holditch, 1982; Shevlin et al., 1986) have shown that potassium found within the blast furnace has a detrimental effect on the coke bed matrix. The alkali penetrates the unreacted feed cokes structure setting up local stresses due to the volume expansion experienced by the carbon matrix. These stresses enable cracks to propagate and thus contribute to the cokes degradation and structural weakness. This in turn leads to a decrease in the permeability of the coke bed matrix and, as a consequence, reduces the output and fuel efficiency of the furnace.

1.2- THE BLAST FURNACE

Coke is charged into the top of the blast furnace with crushed limestone and iron ore (iron oxides) (figure 1.1). The purpose of the limestone is to act as a fluxing agent by collecting the mineral impurities in the furnace. The function of the coke is to act as a support to the burden by providing a supporting skeleton. Air, heated by the hot

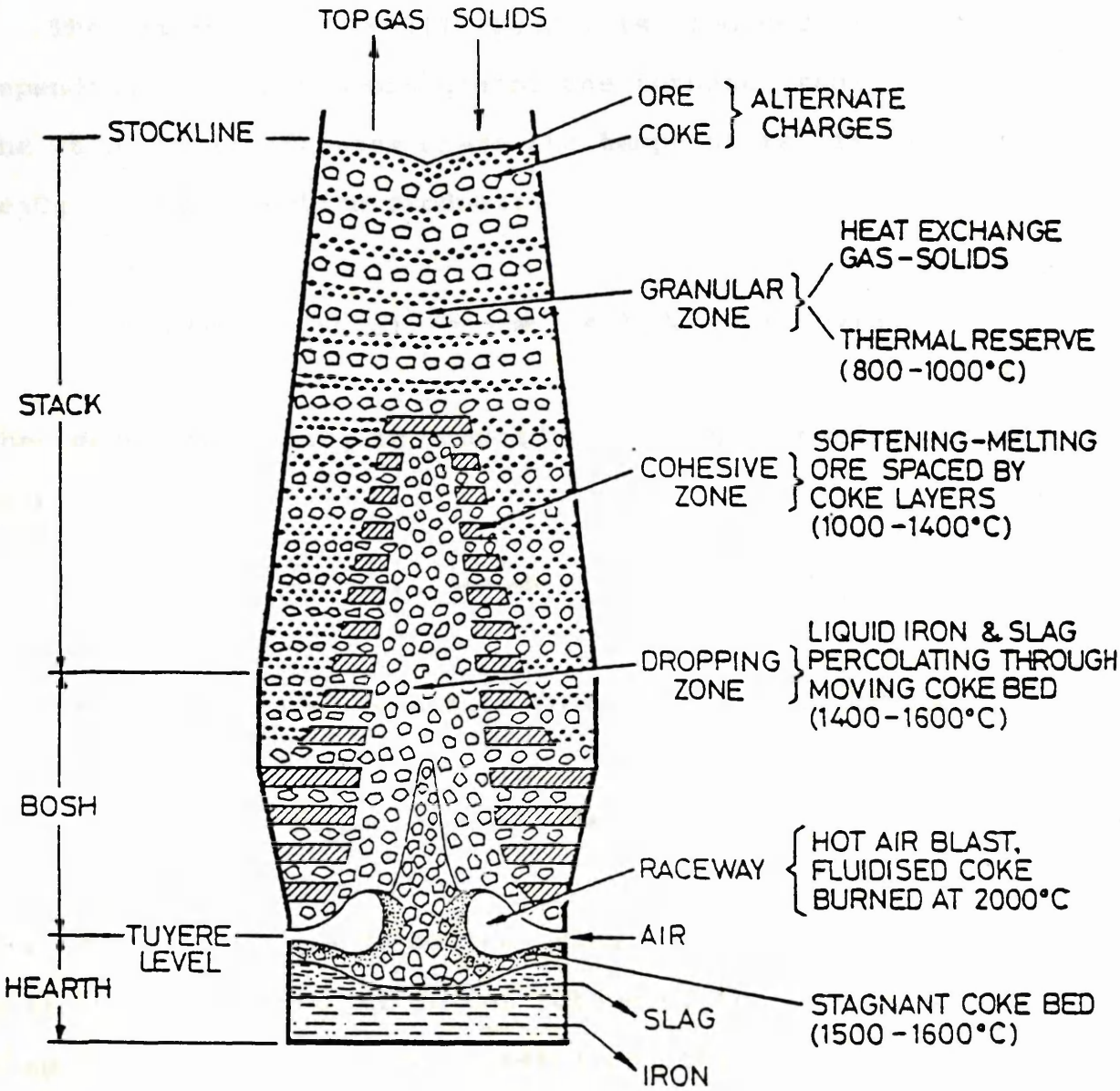

Figure 1.1: Schematic diagram of a blast furnace.

exhaust gases, is blown in near the base of the furnace and produces a reaction zone in which the incoming air reacts with the carbon to form carbon monoxide, liberating considerable amounts of heat (temperature of the furnace at this point is around 2000°C.

The iron ore, usually Fe_2O_3, is reduced in stages depending on the temperature of the furnace region. Near the top of the furnace where the temperature is lowest, Fe_3O_4 is the reduction product:-

$$3Fe_2O_{3(s)} + CO_{(g)} \longrightarrow 2Fe_3O_{4(s)} + CO_{2(g)}$$

The descending Fe_3O_4 is reduced to FeO in a lower, hotter zone:-

$$Fe_3O_{4(s)} + CO_{(g)} \longrightarrow 3FeO_{(s)} + CO_{2(g)}$$

In the hottest zone, reduction to metallic iron occurs:-

$$FeO_{(s)} + CO_{(g)} \longrightarrow Fe_{(l)} + CO_{2(g)}$$

The molten iron and molten slag, principally calcium silicate, then collect in the bottom of the furnace. The slag floats on top of the molten iron, thus protecting the metal from oxidation by the incoming air. The slag and iron are then periodically drawn off.

1.3- ALKALIS IN THE BLAST FURNACE

Alkalis in the blast furnace contribute to a wide range

of operational problems ranging from changes in coke permeability to a reduction in the life of a blast furnace (Armatorio et al., 1971; George and Peart, 1973; Hawkins et al., 1974; Davies et al., 1978; Hatano et al., 1980; Narita et al., 1981).

The behaviour of alkalis and their detrimental effect on the blast furnace has been studied and discussed by many authors (Abraham and Staffanson, 1975; Davies et al., 1978; Kondoh et al, 1981; Goleczka et al., 1983; Goleczka and Tucker, 1985; Lu and Holditch, 1982).

Alkalis enter the blast furnace, mainly in the form of complex silicate compounds, via both the mineral matter inherent in the coke and the iron ore material. The alkalis are eventually removed from the blast furnace as the constituents in slag and dust material (Hawkins et al., 1974; Kondoh et al., 1981). The remainder is carried up with the gases and is deposited on the burden, the refractories or is removed in the flue top gases. Not all the alkali is removed in this manner and a certain amount accumulates and recirculates in the furnace.

Davies et al. (1978) proposed a simplified model for this recirculation behaviour (figure 1.2). The model concentrates primarily on the potassium species within the blast furnace, as it not only has a greater influence on coke property (Kondoh et al., 1981) but its concentration in the burden is usually higher than that of sodium. Alkali is generated from the silicate compounds within the burden:

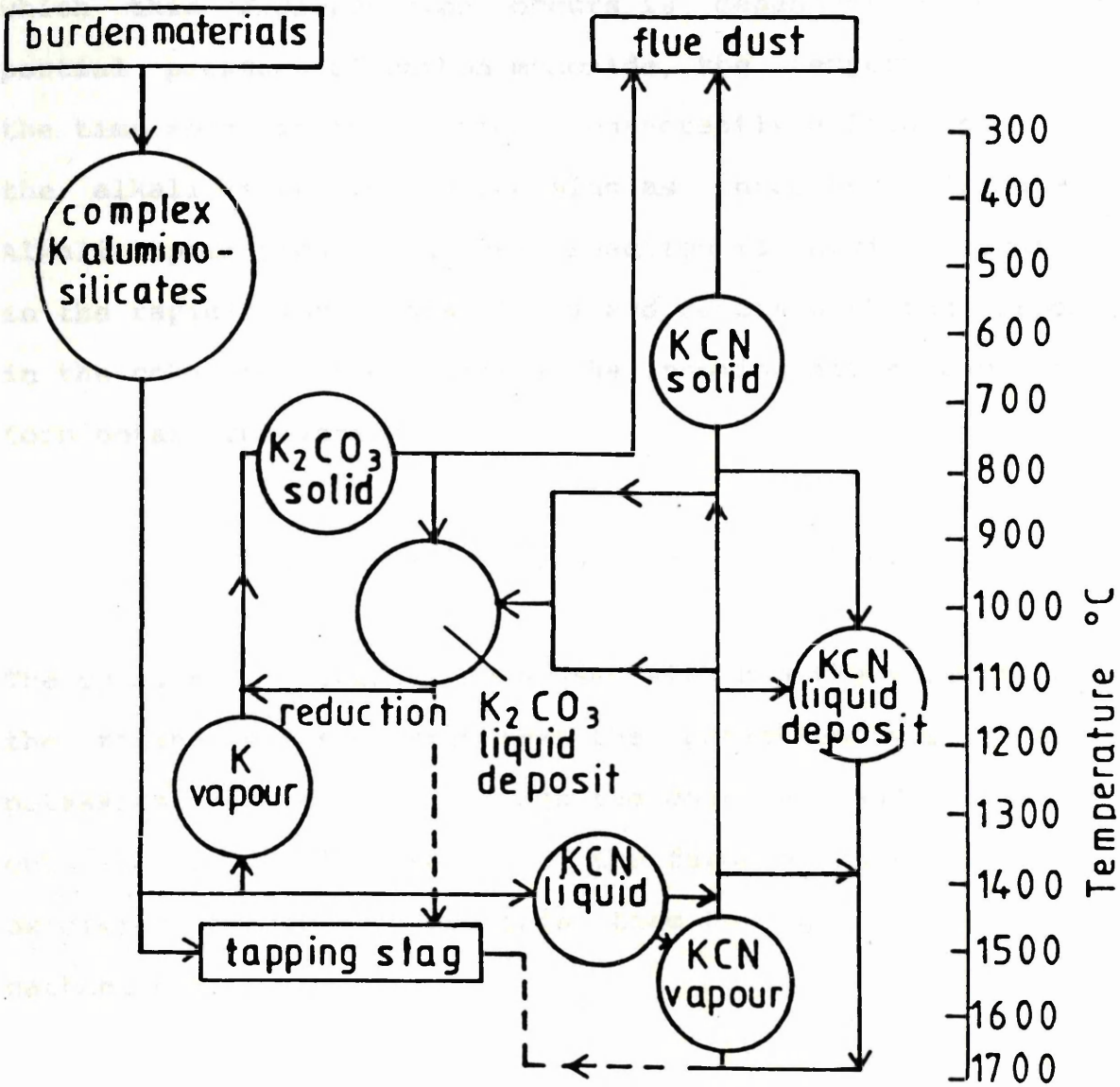

Figure 1.2: Potassium recirculation within the blast furnace.

$$2K_2SiO_3 + 6C \longrightarrow 2K_{(g)} + 2Si + 6CO_{(g)}$$

These compounds do not decompose until they reach the high temperature regions (1500°C) of the furnace, the extent to which this decomposition occurs is dependent upon the partial pressure of carbon monoxide, the temperature and the time spent in this region. Consequently a large part of the alkali is removed in the slag as unreacted silicate. Alkali vapour produced by this reaction is carried upwards in the rapidly moving gas stream and reacts with the carbon in the coke and nitrogen, from the incoming air stream, to form potassium cyanide:

$$2K_{(g)} + 2C_{(l)} + N_{2(g)} \longrightarrow 2KCN_{(g)}$$

The cyanides are readily condensed although the velocity of the rising gases ensures that the potassium vapour and potassium cyanide rise through the coke bed and condense out in the cooler regions of the furnace where a more oxidising atmosphere converts them to the more stable carbonate species:

$$2K_{(g)} + 2CO_{2(g)} \longrightarrow K_2CO_{3(l)} + CO_{(g)}$$

Both the carbonates and unreacted cyanides may be deposited on the descending burden materials, coating them in a dust or a liquid depending on the temperature. As the coated burden descends to the high temperature regions of the

furnace, conditions are suitable to allow reduction of the carbonate back to metallic vapour:

$$K_2CO_{3(l)} + CO_{(g)} \longrightarrow 2K_{(g)} + 2CO_{2(g)}$$

This returns to the higher zones in the furnace to be re-oxidised to the carbonate and so completes the cycle.

Recirculating alkali within the blast furnace cannot be avoided but can be controlled, although the conditions which control and minimise the effects is very much dependent on the operational parameters of each individual furnace.

The optimum removal of alkalis by slag are unfortunately the opposite to those needed for a low sulphur content in the metal. Lowering the slag basicity increases the levels of sulphur found in the metal, thus requiring a costly desulphurisation process. This difficulty can be overcome by raising the slag volume. This gives an increased alkali removal without increasing the sulphur to metal ratio, however, this will decrease the cost efficiency of the furnace.

1.4- COKE TYPES

Coke properties differ depending on the application and requirements of the coke. Coal selection, pretreatment, blending and the coking process all combine to determine the characteristics and quality of the coke produced. The most important cokes produced from coal are the

metallurgical cokes, although coke may be produced from several organic precursors e.g. petroleum feedstocks, coal tar.

There are two main consequences of coke production by the pyrolysis of coal. First, the creation of a strong porous material suitable for use in the iron and steel industry (the main users of metallurgical coke) and second the production of vast amounts of volatile organic matter which have a variety of uses (figure 1.3).

1.5- FORMATION OF METALLURGICAL COKE

Only a limited range of coal rank i.e. bituminous coals, produce acceptable metallurgical cokes. In general, coals of lower rank decompose when heated and coals of higher rank do not soften (Gray, 1989).

Once suitable coals have been selected, they are cleaned (this is orientated towards reducing the ash and sulphur content) and pulverised to a size suitable to achieve the maximum bulk density of the coal without creating excess fines, which are detrimental to the carbonisation process. When powdered or finely ground coal is heated in bulk, it forms a porous mass which on cooling contracts and cracks. This results in structural weakening and the subsequent degradation of the coke structure (Grainger and Gibson, 1981).

The crushed coals are then blended in predetermined proportions, depending on the coke specification, before being charged to the coking ovens where a temperature of

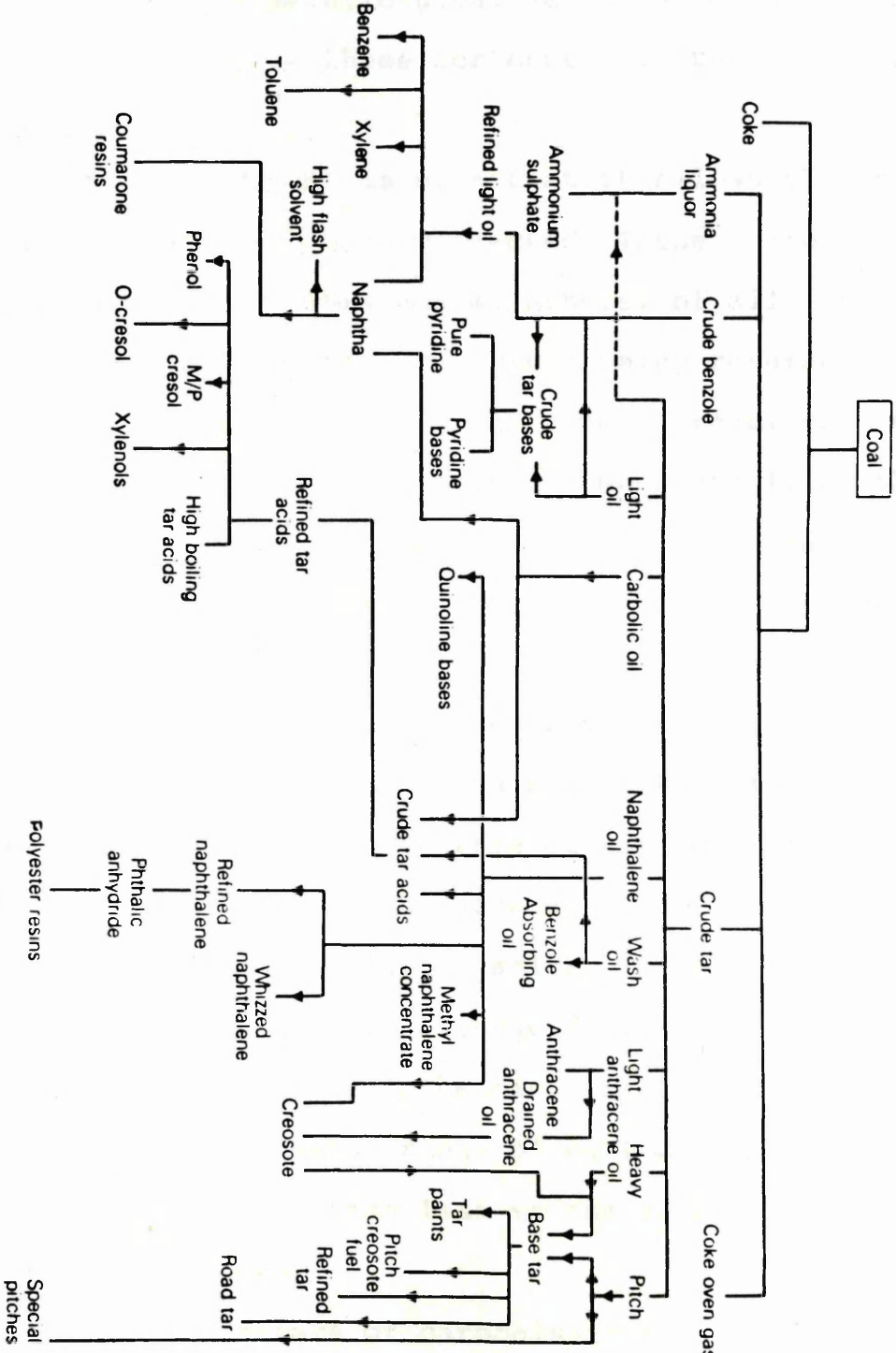

Figure 1.3: The by-products of coal carbonisation and some of the products that can be recovered.

around 1000°C is maintained. The coking process continues until almost all the volatile matter has been removed from the coke. The maximum metallurgical value is gained when the coke retains up to three per cent of the original volatile matter

The coking oven design is such that it allows the by-product gases produced to be collected. These gases are then stripped, by condensers and scrubbers, of all useful components e.g. ammonia and tar, before being returned to the oven and burned to supply the heat required for the carbonisation process. The useful components from the by-product gases are then processed to give products such as ammonium sulphate fertiliser, tar pitch and sulphuric acid.

Two factors important in the production of blast furnace coke are the rate of carbonisation and the final carbonisation temperature. The rate of carbonisation is important as it determines the size and strength of the coke produced. High stresses arise from a rapid carbonisation and give rise to a large degree of fissuring in the coke structure. A lower heating rate, particularly in the very important plastic range of carbonisation, will reduce these stresses and thus lead to the production of a larger and stronger coke.

The final temperature of carbonisation (the maximum temperature attained) is also important as it determines, along with the time spent at this temperature, the residual amount of volatile matter retained in the coke structure.

This is an important factor as the volatile matter content affects the thermo-mechanical stability of the coke (Goleczka et al., 1982(a)).

Carbonisation times vary, depending on the nature of the coal and the quality of the coke required, but are normally around eighteen to thirty hours. The centre of the charge reaches around 1000°C within a period of about twelve to fourteen hours and remains at this temperature for the remainder of the carbonisation period.

The formed coke mass is removed from the oven, cooled and size screened before being ready for use in the blast furnace.

1.6- COKE DEGRADATION

Coke in the blast furnace fulfils three roles:-

1. It provides a source of reducing gas by the production of carbon monoxide (carbon dioxide being regenerated at each stage of iron oxide reduction)

$$CO_{2(g)} + C_{(s)} \longrightarrow 2CO_{(g)}$$

The rate at which this Boudouard (solution loss) reaction (Boudouard, 1899, 1901(a) and (b)), occurs determines the reactivity of the coke.

2. It is the main source of heat in the furnace.

3. It provides a permeable matrix through which gases may ascend and molten materials descend.

Thus the performance of the coke is important in

determining the output and fuel efficiency of the furnace. A lack of permeability leads to a poor gas distribution which is vital for iron oxide reduction. A decrease in the coke matrix permeability arising when changes, induced by the blast furnace environment, occur to the properties of the coke.

The interaction of carbon with alkalis is extremely complex and results in a wide variety of chemical reactions including carbon gasification and the formation of lamellar intercalates.

1.6.1- GASIFICATION

Carbon gasification, reviewed by several authors (Kroger and Angew, 1939; Walker et al., 1959; Walker et al., 1968; Lewis, 1970), can generally be described as the combustion of carbonaceous materials, many of which have extremely complex and variable structures.

The carbon gasification reaction is itself extremely complex and further complicated by the gaseous environment of the reaction as well as the constantly changing heterogeneous surfaces, the complex chemical structures and the presence of inorganic impurities in the carbonaceous materials. These factors contribute to altering the reactivity of the carbon and can thus have a catalytic effect on the gasification process.

The diverse catalytic effects and mechanisms of the gasification reactions on carbon have been studied and reviewed by many authors (Walker et al., 1968; Lewis,

1970). Although it is not yet possible to explain all the observed catalytic effects within one mechanistic framework, two general mechanisms have been successful in interpreting the effect in various types of carbon gasification reaction.

These can be broadly classified into:-

1. The electron transfer mechanism (Long and Sykes, 1950): many of the catalytically active additives have unfilled energy bands that are capable of accepting electrons from the carbon matrix or posses labile electrons that can be donated to the carbon. This electron transfer is assumed to result in a redistribution of pi electrons, a weakening of the carbon-carbon bonds at edge sites of the graphite sheets and an increase in the carbon-oxygen bond strength during the catalysed oxidation reaction.

Several authors (Hedden et al., 1959; Harker, 1960) have modified the electron transfer mechanism to interprete the catalytic gasification reactions of carbon.

Using a variation of the mechanism, to account for the catalytic effects of alkali metal carbonates, Franke and Meraikib (1970) suggested the formation of intercalation compounds between the alkali metal and the carbon matrix.

2. The oxygen transfer mechanism (Neumann et al., 1931):- the active catalysts for carbon gasification are regarded as oxygen carriers that undergo oxidation-reduction cycles on the surface of the carbon. Thus intermediate compounds, such as a metal oxide, are formed in the presence of the oxidising gaseous environment. The oxide is then reduced on contact with the carbon substrate

and the cycle is repeated as the mobile particle migrates to the carbon surface.

The catalytic action of alkali metal oxides and carbonates on the catalytic gasification of carbon by this mechanism has been extensively studied by McKee and Chatterji (1975).

This idea of alkali metal lamellar compounds (Franke and Meraikib, 1970: electron transfer mechanism) and the cycles postulated by McKee and Chatterji (1975: oxygen transfer mechanism) have subsequently been used by Wen (1980) to try and elucidate the alkali metal carbonate catalytic gasification of carbon. An important stage in this catalytic gasification method is the formation of free alkali metal:

$$M_2CO_{3(l)} + 2C_{(s)} \longrightarrow 2M_{(g)} + 3CO_{(g)}$$

attained by heating the alkali metal carbonates in an inert atmosphere. In the absence of carbon very little K_2CO_3 would thermally decompose, even when heated to 1000°C. However, when carbon is introduced to the system, the K_2CO_3 reacts at temperatures as low as 800°C.

Coke in the blast furnace undergoes unavoidable degradation as a result of combustion i.e. carbon gasification by the solution loss (Boudouard) reaction (Walker et al., 1968; Lewis, 1970). The presence of alkali further enhances this degradation by acting as a catalyst for the solution loss reaction (McKee and Chatterji, 1975).

Many authors describe the uncatalysed solution loss

reaction as the most important factor in coke breakdown (Kojima et al., 1977; Tate et al., 1979; Benedict and Thompson, 1980; Hatano et al., 1982), while others argue the importance of different influencing factors e.g. the catalytic effect of the alkalies, causing the solution loss reaction to occur at lower temperatures, (Botham et al., 1974; British Steel Corp., 1983; Goleczka et al., 1982(b)).

There are a wide variety of:-

1. influencing factors: the presence of any inorganic impurities, their concentration over the carbon surface (active sites) and the diffusion of gases to these sites (McKee, 1981), and

2. catalysts: alkali metal oxides and salts (Patrick and Shaw, 1972), iron and its oxides (King and Jones, 1931, Walker et al., 1968), many of which are present in metallurgical coke and significantly influence the rate of carbon gasification (Adair et al., 1971; Marsh and Rand, 1971).

This excessive gasification of carbon results in a weakened coke structure and leads to breaking and the generation of fines.

1.6.2- INTERCALATION

Coke degradation can arise as a result of the formation of intercalation compounds and their associated volume expansion.

Intercalation compounds are formed by the penetration of guest chemical species between the layers in a host

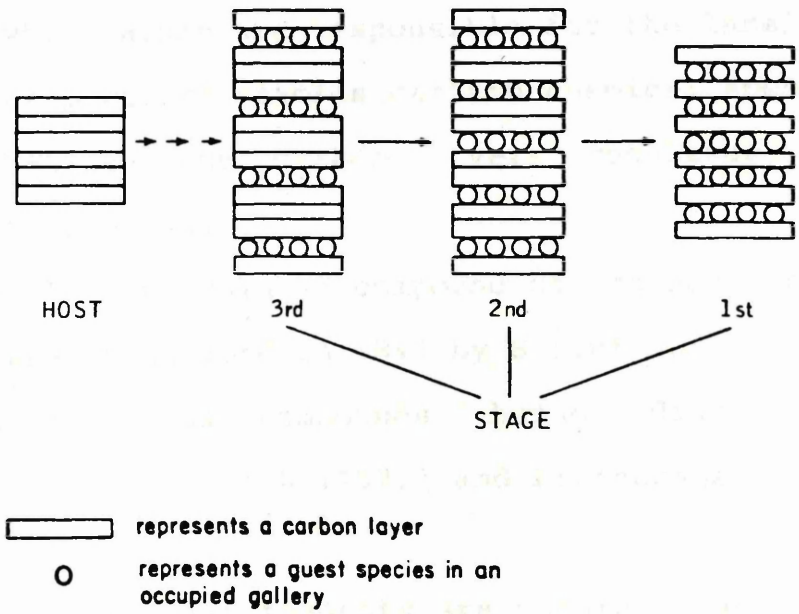

Figure 1.4: Staging in graphite intercalation compounds.

material. The intercalate assumes an ordered arrangement within the lattice, occupying, in the most concentrated case every interplanar spacing (C_8K). In less concentrated compounds the intercalate will occupy every second ($C_{24}K$), third or more interplanar space, thus giving rise to the various stages or degree of intercalation causing expansion of the layers in the c-axis direction (figure 1.4).

The highly anisotropic nature of graphite, with strong bonding within each layer (sigma electrons) and relatively weak van der Waals bonding between the layers (pi electrons, which alone are responsible for the lamellar and electronic properties) enables certain chemical species to penetrate between the carbon layers resulting in an intercalated compound.

The first intercalated compound of carbon, graphite sulphate, was described in 1841 by Schauffautl with the first alkali metal compounds being discovered by Fredenhagen and Cadenbach (1926) and Fredenhagen and Suck (1929).

Known intercalating reagents are numerous, and the work carried out on the formation and characterisation of intercalates has been the subject of many reviews (Ubbelohde and Lewis, 1960; Ebert, 1976; Armaud and Touzain, 1977; Herold, 1977 and 1979; Selig and Ebert, 1980) and can be distinguished into three main classes.

1. <u>Non-conducting Compounds</u>

Due to the formation of a covalent bond with the intercalate, the graphite planes become puckered and lose their aromatic character and conducting ability.

2. Lamellar Compounds

Lamellar compounds arise when the intercalate assumes an ordered arrangement within the graphite lattice.

To understand the electronic properties of graphite intercalation compounds it is useful to use the band structure of graphite, as in most circumstances intercalation of graphite does not lead to gross changes in the carbon layers. In view of the weak interlayer bonding in graphite it is sufficient to treat the band structure of the material as an isolated layer i.e. a simplified two dimensional model.

The energy levels of the pi electrons form a continuous series that constitutes a valence band for the fundamental state of graphite and a conduction band for excited states. For pure graphite the valence band is completely filled and the conduction band is completely empty. This results in the fermi level (highest energy level occupied) coinciding with the point at which the conduction and valence bands meet.

Inserted reagents are partly ionised (Rudorff and Hoffman, 1938; McDonnell et al., 1951; Hennig and McClelland, 1955; Hennig, 1956 and 1960; Ubbelohde, 1961), implying that the carbon layer is able to donate or receive electrons altering the electrical and magnetic properties of graphite. Thus two types of lamellar compound can be distinguished (Robert et al., 1973), dependent on whether the carbon layers, in the intercalation compound formed, are:-

(a) positively charged compounds (p-type) in which the

carbon layers have donated electrons from the valence band to the guest reagent e.g. halogens. The observed high electrical conductivity of these compounds is a result of the appearance of new charge carriers, the vacancies created in the valence band by the removal of electrons, and are therefore positive or

(b) negatively charged compounds (n-type) where the carbon layers have become negatively charged through acceptance of electrons, to the conduction band, from the intercalated material e.g. alkali metals. Consequently this partial filling of the conduction band results in a marked increase in the conducting properties of graphite after intercalation has taken place.

Although conductivity in both types of compound markedly increases after intercalation, the removal of electrons from the valence band (pi orbitals) or addition of electrons to the conduction band (antibonding pi orbitals) decreases the strength of the bonding in the layers.

3. <u>Residue Compounds</u>

Residue compounds readily form as a result of the decomposition of a lamellar type intercalation compound. As the lamellar type compound decomposes it loses most of the intercalated material. A definite proportion of intercalate remains within the carbon however, dependent on the nature of the parent lamellar compound and the original carbon, and it is this which constitutes the residue compound. The structure and composition of residue compounds has been studied by many workers (Hennig, 1952; Ubbelohde, 1957;

Maire and Mering, 1959; Heerschap and Delavignette, 1967; Daumas and Herold, 1971).

1.7- AIM OF THIS STUDY

The aim of the present study has been to examine the effect of potassium, at simulated blast furnace temperatures, on different carbon structures produced under differing carbonisation conditions. This required a comparison of the microstructure of the carbonised samples both before and after exposure to potassium vapour. The ultimate aim is to produce a coke resistant to alkali attack and thus reduce or eliminate blast furnace coke degradation by alkali vapours.

1.8- CARBONISATION

Organic materials are the main and almost exclusive raw material for the production of carbons and graphites. When heat treated, under an inert atmosphere, to temperatures below 1000°C, these carbonaceous materials are converted to carbon as the main product and to different volatile compounds as by-products. This process is known as carbonisation (Fitzer et al., 1971).

The thermal conversion of organic material to carbon and graphite is dependent on reaction parameters, such as the pyrolysis temperature, heating rate and residence time at the pyrolysis temperature. The structure of the resulting carbon is also directly dependent on the nature and composition of the organic precursor (Edstrom and

Lewis, 1969).

During pyrolytic decomposition a number of parallel and sequential reactions occur, thus, the pyrolysis reaction mechanism is extremely complex and yields products, predominantly aromatic compounds, which are difficult to separate and characterise. Some of the chemical and physical changes occurring during the conversion of organic materials to carbon include an increase in the carbon to hydrogen ratio (Hüttinger, 1971), increased molecular weight (Lewis and Petro, 1976), decrease in solubility (Honda et al., 1970), increase in free radical concentration (Singer and Lewis, 1978) and an increase in aromatic layer size (Ruland, 1965(b)).

Many workers have studied the complex chemistry associated with carbonisation using a variety of characterisation techniques, nuclear magnetic resonance (Bartle and Jones, 1969; VanderHart and Retcofsky, 1976; Maciel et al., 1979; Dickinson, 1980), mass spectroscopy (Sharkey et al., 1966; Evans and Marsh, 1971; Lewis, 1980), x-ray diffraction (Ruland, 1965(b); Simon et al., 1977), neutron inelastic scattering (Leung and Safford, 1970) and electron spin resonance (Singer and Lewis, 1964; Lewis and singer, 1967; Lewis and Singer, 1981) and established that carbonisation is consistent with a thermal polymerisation process (Lewis, 1973, 1982).

Despite the complexity of the carbonisation process considerable progress towards understanding the reaction mechanisms of carbonisation has come from studies with model compounds (Kinney et al., 1957; Lewis and Edstrom,

1961; Ruland, 1965(b); Lewis and Singer, 1969; Evans and Marsh, 1971; Fitzer et al., 1971; Lewis, 1980; Lewis, 1982; Oberlin, 1984) and the development of improved methods for separation (Edstrom and Petro, 1968; Bartle et al., 1979; Schultz et al., 1979; Blumer et al., 1980) and characterisation.

This enhanced ability to characterise carbonaceous materials has shown the importance of molecular rearrangement and dehydrogenative polymerisation on the overall carbonisation process and has also demonstrated the difficulty in relating the relationships of the starting structure to final graphitisability due to the thermal rearrangement in the early stages of the carbonisation process.

The general reaction scheme of Lewis (1982) (figure 1.5) shows carbonisation to be an aromatic growth and polymerisation process in which any non-aromatic structures are first aromatised. The small aromatic structure is then polymerised to an aromatic polymer, which ultimately achieves a graphite network, the degree of three dimensional order depending on the ability of the aromatic building blocks to polymerise.

The overall process of carbonisation is exceedingly complex and is believed to involve bond cleavage, formation of a free radical intermediate, molecular rearrangement, thermal polymerisation and aromatic condensation reactions, many occurring simultaneously during the carbonisation process.

From a mechanistic point of view they can be considered

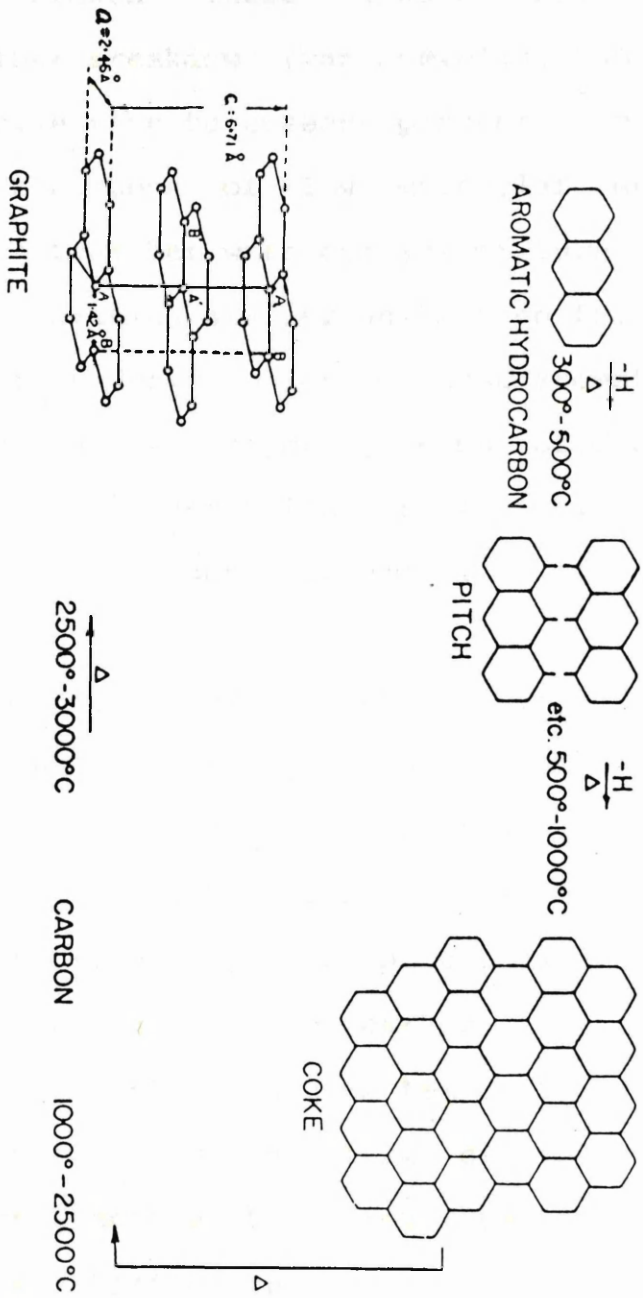

Figure 1.5: General reaction scheme for carbonisation.

separately, indeed Grainger and Gibson (1981) described the free radical condensation mechanism resulting as the organic material is heated and cross-linkages in the component are broken. These linkages between aromatic groups can further breakdown (van Krevelan, 1961; Fitzer et al., 1971) to give rise to gaseous products such as methane and other hydrocarbons of low molecular weight (the volatile matter) together with complex mixtures of organic materials. The remaining heavier units then form semi-coke on resolidification during which adjacent aromatic clusters link. Hydrogen is the major gaseous product in the condensation of the larger units; its formation and removal resulting in the subsequent condensation of neighbouring aromatic units.

Thus carbonisation involves the heating of the parent material in the absence of air, resulting in the removal of volatile matter. These volatiles have a higher hydrogen content than the parent material from which they are composed and consequently the parent materials carbon content is increased. Pure carbon is obtained at temperatures around 1600°C. Higher temperatures however, do not increase purity but result in crystal ordering to graphite or near graphite structures (Oberlin, 1975(a)) by the process of graphitisation.

On heating to temperatures between 1000 and 3000°C carbons tend to evolve towards the ordered structure of graphite by the process of graphitisation. The process can be considered as a disorder-order transformation involving the annealing of structural defects. The graphitisation

behaviour of a carbon is thus dependent on both its structure and the conditions of formation from the original organic precursor.

1.9- GRAPHITISATION

The ease and extent of graphitisation varies widely among different types of carbon. Franklin (1951(a) and (b)) described the transformation of "soft" or graphitisable carbons to the structure of graphite by heat treatment, substantial or complete graphitisation occurring as a function of thermal treatment alone. The class of "hard" or non-graphitisable carbons retain an imperfect structure (Franklin, 1951(b)) even after prolonged heat treatment at high temperatures (e.g. 2hr at 3200°C).

The definition of graphitisation as the development of the stable Bernal structure (1924) (figure 1.5) may be considered as a process that involves the development of an initially disordered structure to that of a crystallographic ordered structure. This can be referred to in terms of the development of three dimensional order from an initially two dimensionally ordered carbon.

The graphitisation behaviour of a carbon is determined by the organic precursor and the conditions under which the pyrolysis and carbonisation processes are carried out (Kipling and Shooter, 1965; Blayden, 1969). This determines the nature, concentration and distribution of defects in the structure. The non-graphitising carbons form a cross-linked structure not easily rearranged to an orderly

stacking pattern, consequently graphitisation becomes difficult as geometric factors prevent crystal growth. In the case of carbons that can be graphitised readily, the crystallites retain mobility in the plastic stage and align themselves in a roughly parallel fashion (figure 1.6).

The graphitisation process has been the subject of many reviews (Maire and Mering, 1970; Fischbach, 1971; Pacault, 1971; Robert et al., 1973; Oberlin, 1984) and can be described as occurring in various stages.

As a result of the increased heat treatment temperature of graphitisation, the planar aromatic ring structures (basic structural units) formed during the carbonisation process pile up in parallel by two's and three's. Molecular orientation then occurs to improve their stacking order by the removal of interstitial defects. These misorientated basic structural units then coalesce into stacks of distorted layers (L_c increases). With increasing temperature (above 2000°C) the wrinkling of the layers decrease and the basic structural units coalesce into stiff and perfect layers. The diameter of the layers, L_a, increases and an increasing number of layers reach the graphitic stacking order. This process is summarised in figure 1.7.

1.10- GRAPHITE STRUCTURE

Carbon is a naturally occurring element which exists, in its pure form, in one of two main allotropic forms: diamond and graphite. These are crystallographically ordered forms, but carbon can also exist in a wide range of

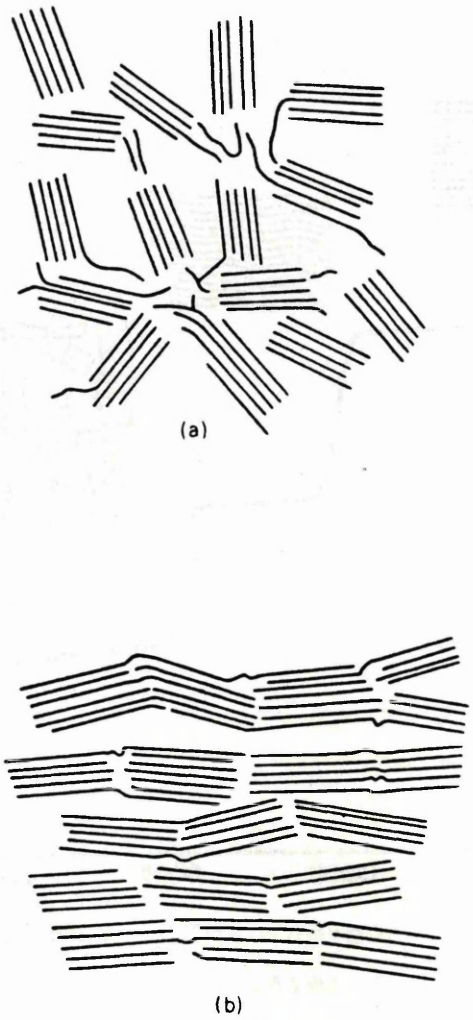

Figure 1.6: Arrangement of crystals in (a) a non-graphitising carbon; randomly orientated crystallites and (b) a graphitising carbon; near parallel arrangement of crystallites.

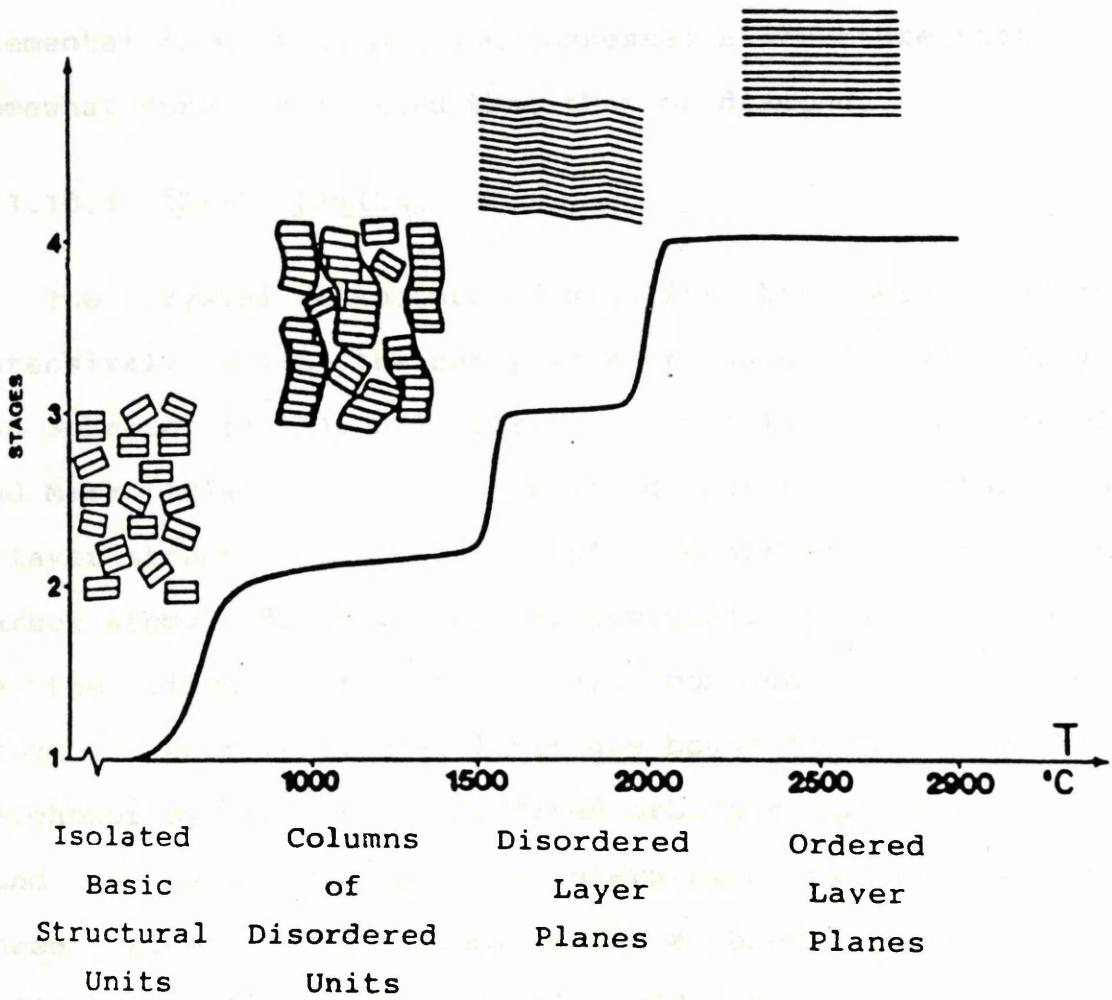

Figure 1.7: Various stages of graphitisation.

disordered or imperfectly ordered structures.

In diamond the carbon atoms are bound by sp^3 hybridised bonds of length 0.154nm, which results in a tetrahedral structure (figure 1.8) and the characteristic strength associated with diamond.

All carbons, other than diamond possess "graphite" units, thus graphite is by far the most commonly occurring elemental form of carbon and possesses a structure that is somewhat more complicated than that of diamond.

1.10.1- IDEAL LATTICE

The crystal structure of graphite has been studied extensively since the early work of Ewald (1914), Debye and Scherrer (1917), Hull (1917), Bernal (1924) and Hassel and Mark (1924). It was established that the structure is a layer structure composed of infinite planes, formed from carbon atoms ordered in regular hexagons, similar to those in the rings of aromatic organic compounds. The carbon atoms in each individual layer are bound to their nearest neighbour by three sp^2 hybridised orbitals and separated by bond angles of 120°, with an interatomic distance between these atoms of 0.1421nm, such a bond length being indicative of one third double bond character (Pauling, 1945). The fourth valence electron of each carbon atom is delocalised over the whole plane, giving the layer planes their aromatic character. The layer planes are in a parallel array, bound together by van der Waals forces with the interlayer spacing for well oriented graphite being 0.33538nm (Franklin, 1951(a)). In less well orientated

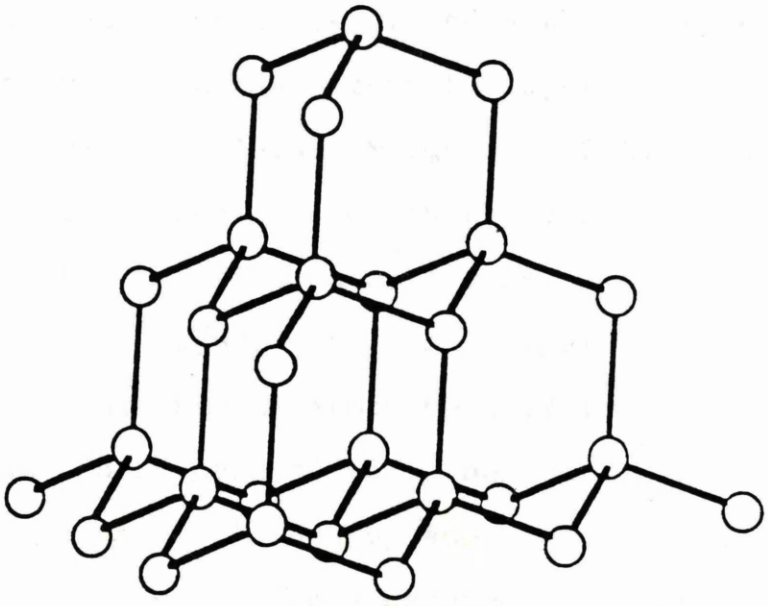

Figure 1.8: Tetrahedral structure of diamond.

graphite, Franklin (1951(a)) stated that the experimentally determined interplanar distance is an average value, which is dependent on the proportion of both oriented layers with a spacing of 0.33538nm and disorientated layers of 0.344nm spacing.

Two types of stacking sequence occur for the carbon planes: hexagonal (Bernal, 1924) and rhombohedral (Laidler and Taylor, 1940; Lipson and Stokes, 1942(a) and (b)).

The stacking sequence between the carbon layers in graphite has been shown to be of the ABAB.... type i.e. the hexagonal form, where the alternate layers are in perfect coincidence (Bernal, 1924; Maughin, 1926). Figure 1.9 illustrates the hexagonal graphite structure and the equivalence of the alternate layers. The relationship between adjacent layers is also apparent as being a translation of one carbon-carbon bond (figure 1.10).

The plane unit cell of this hexagonal structure is defined by two atoms A_o and B_o and two crystallographic vectors $\underset{\sim}{a}_1$ and $\underset{\sim}{a}_2$ which are separated by an angle of 120° (figure 1.11). The unit length of these vectors was evaluated by Trzebistowski (1937) to be 0.2456nm. In order to define the three dimensional hexagonal structure of graphite, a further vector $\underset{\sim}{a}_3$ is necessary. This vector is perpendicular to the plane of the layers and its unit length is twice the distance between adjacent layer planes i.e. 0.6708nm (Charlier and Charlier, 1987).

In addition to the hexagonal form, graphite has also been shown to exist as a rhombohedral structure (Taylor and Laidler, 1940 ; Lipson and Stokes, 1942(a) and (b)). This

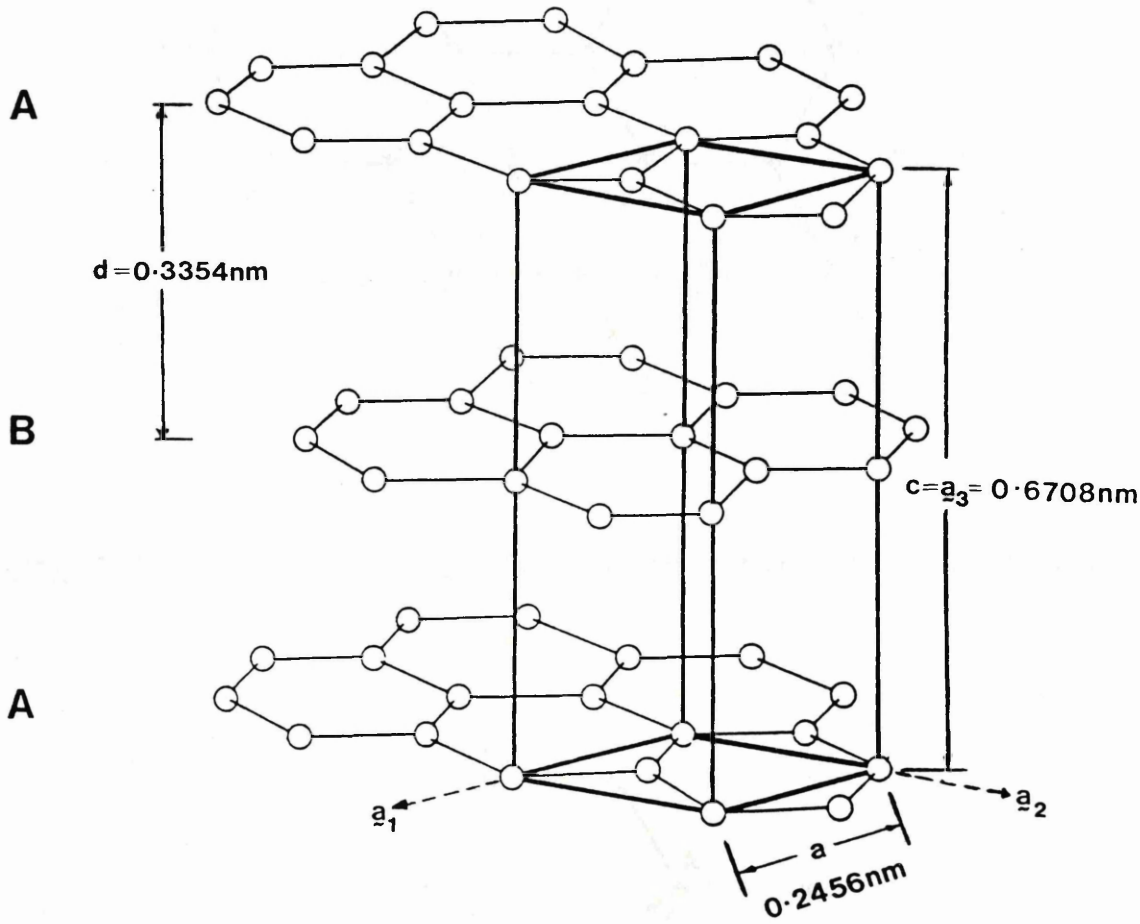

Figure 1.9: Hexagonal graphite structure showing the layer arrangement and unit cell.

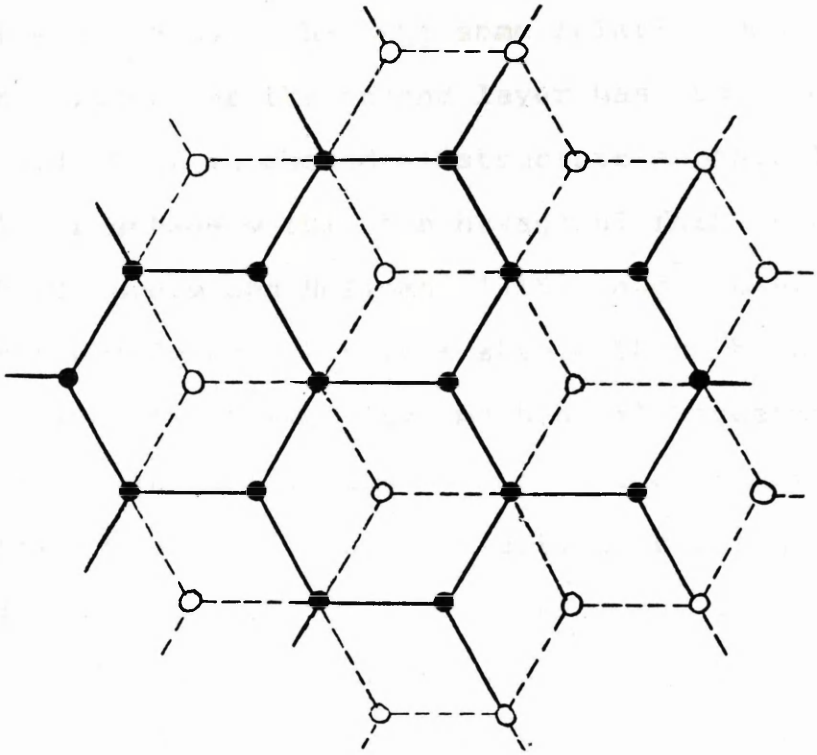

Figure 1.10: Basal plane projection of hexagonal structure.

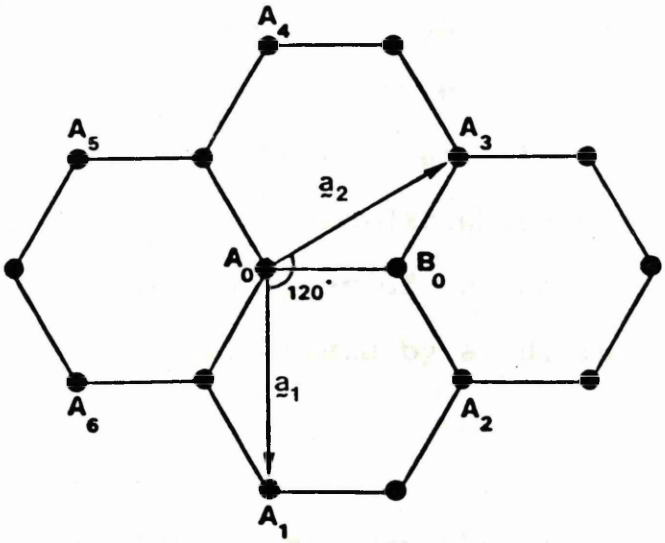

Figure 1.11: Graphite layer plane.

type of graphite possesses an ABCABC.... stacking sequence, in which the third layer has the same relative position to the second layer as the second layer has to the first (figure 1.12). This rhombohedral structure appears to exist as a small percentage within the hexagonal form (Finch and Wilman, 1936; Boehm and Hoffman, 1955) and never on its own. It is thermodynamically less stable than the hexagonal structure and is formed by mechanical treatment or grinding. Its formation occurs as a result of a deformation of the hexagonal lattice by a selective sliding of the layer planes (Bacon, 1952(a); Baker et al., 1961), reverting to the hexagonal form on heat treatment (Boehm and Coughlin, 1964) and chemical treatment (Taylor and Laidler, 1940; Lukesh, 1951).

1.10.2- NON-IDEAL CRYSTAL STRUCTURE

Even the purest of graphites do not conform to the idealised lattice structure and good three dimensional crystals of appreciable size are rare.

Two common types of defect are found in graphite crystals. One is a stacking disorder which may arise from a shift in the relative positions of the carbon layers. The second type of defect is caused by a disruption of the carbon plane.

1. Stacking Disorder

A stacking disorder occurs when the carbon layer planes no longer conform to an ABAB.... or ABCABC.... type stacking sequence. The weak nature of the interlayer

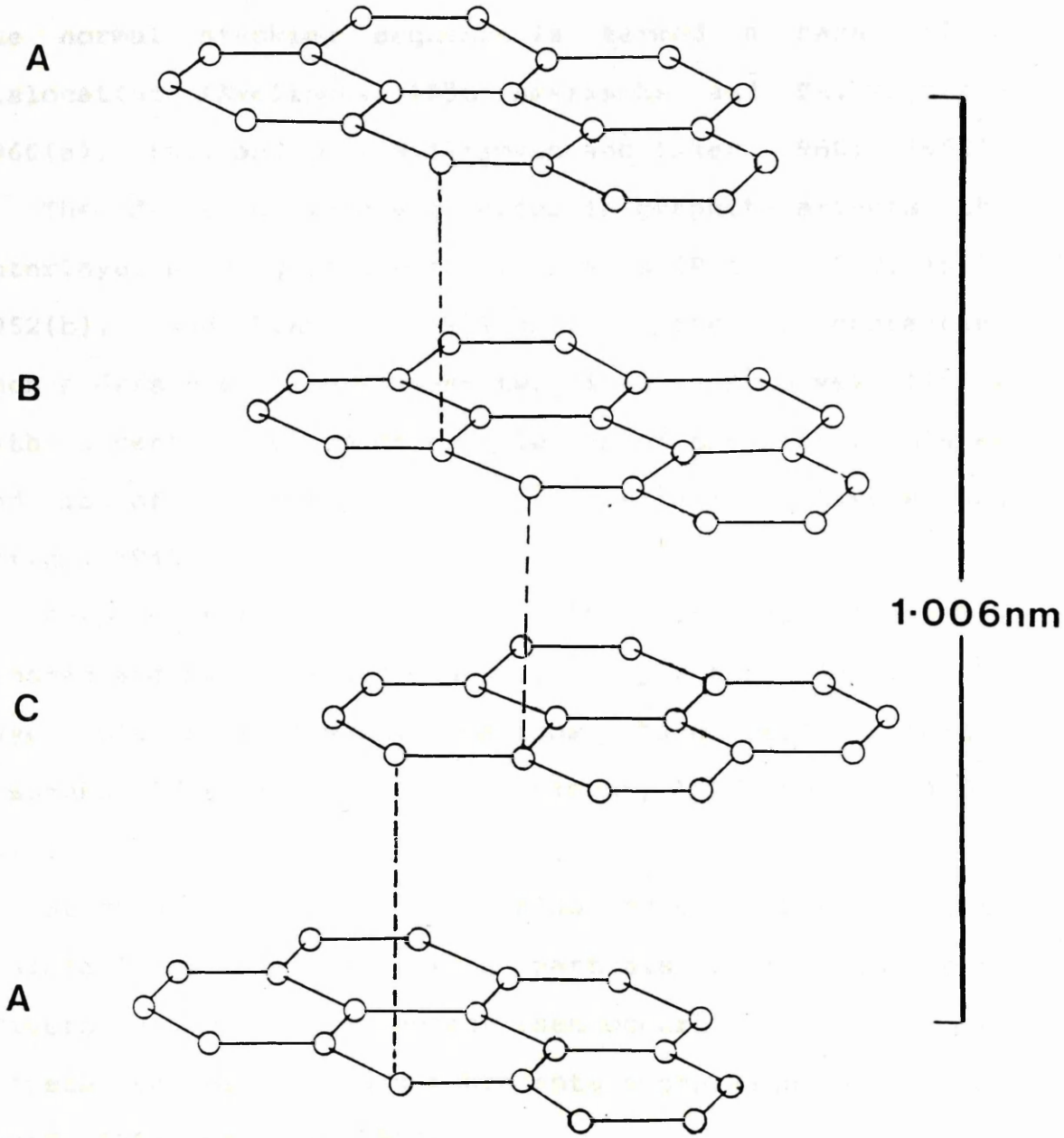

Figure 1.12: Rhombohedral graphite structure.

bonding forces in the graphite crystals suggest that slip, parallel to the basal plane will be very likely to occur. This ease of relative movement of the layers can lead to misalignment of successive layer atoms. This deviation from the normal stacking sequence is termed a basal plane dislocation (Amelinckx, 1956; Amelinckx and Delavignette 1960(a), (b), and (c); Williamson and Baker, 1960, 1962).

The degree of such a disorder in graphite affects the interlayer spacing of the carbon planes (Bacon, 1950, 1951, 1952(b), 1958; Franklin, 1951(a)). A material containing such a defect still possesses two dimensional crystallinity with a certain degree of parallelism of the layer planes and is often referred to as "turbostratic" (Biscoe and Warren, 1942).

Despite the intrinsic difficulties in their formation (Thomas and Evans, 1967) dislocations perpendicular to the layer planes (screw dislocations) have been reported (Tsuzuku, 1959; Fitzer and Schlesinger, 1965; Hennig, 1965, 1966).

Stacking disorders can also arise when perfect dislocations dissociate into partials with fractional Burgers vectors. The defect then occurs in the region between the partials and represents a stacking fault zone (Read, 1953; Friedel, 1964).

2. <u>Layer Defects</u>

The second type of defect in the graphite structure is known as a layer defect and arises from the disruption of the carbon layer planes from their planar aromatic state. The disruption can be caused by the formation of a hole

defect (Ubbelohde, 1957; Ubbelohde and Lewis, 1960) as a result of irradiation of the sample. This causes a displacement or removal of carbon atoms to form interstitials (Bollman, 1960, 1961(a), (b) and 1963). As these vacancies possess inherent unsaturation of atom vacancies, they would be expected to be sites of enhanced reactivity due to the extra bonding availability of edge carbon atoms within them (Long and Sykes, 1948). Layer defects also arise by the occurrence of twin planes, produced by tilting of the carbon layers (Lukesh, 1950; Baker et al., 1965). These defects can also be produced by forming bonds with impurity atoms and by the presence of intercalated atoms (Heerschap et al., 1964).

1.10.3- ELECTRONIC STRUCTURE OF GRAPHITE

In graphite, each carbon atom is bound to its three nearest neighbours by equivalent bonds (sigma), which as previously mentioned, are localised corresponding to an sp^2 hybridisation of the atomic orbitals. Of the four valence electrons possessed by each carbon atom, three are involved in this type of covalent bonding. The remaining electron is delocalised over the carbon plane in the pi orbital system.

Due to the distance between layer planes (interlayer spacing), in relation to the interatomic distance within a carbon plane, the interactions between the layers are normally disregarded and the electronic structure of graphite treated as a two dimensional problem.

It was initially thought (Coulson, 1947; Wallace, 1947)

that the pi bond could be regarded as a filled valence band and an empty conduction band. However, work by Coulson and Taylor (1952) and McClure (1959) later described the conduction and valence bands as touching or narrowly overlapping at the corners of the Brillouin zone.

Graphite is now regarded as a semi-metal, consisting of small isolated pockets of holes in the valence band and an equal number of pockets of electrons in the conduction band. This model of graphite resulted from work by Slonczewski and Weiss (1958) who, in deducing this structure, included in their calculations the perturbation of the interlayer interactions. The semi-metal characteristics of graphite, unlike a semi-conductor, has a small but infinite overlap of the valence and conduction bands resulting in its high electrical conductivity. The electronic structure and Fermi surface of graphite have been studied extensively and reviewed by Haering and Mrozowski (1960) and Cracknel (1969) with a more recent mathematical treatment by Charlier and Charlier (1987).

1.10.4- DISORDERED CARBONS

The structure of all disordered carbons e.g. cokes, chars, carbon blacks etc. is based to a greater or lesser extent on the graphite structure, although the arrangement of the layers with respect to each other is much more disorganised than in graphite.

The x-ray diffraction spectra of all disordered carbons have two characteristic features in common. They contain

(001) peaks which arise from stacks of parallel layer planes and peaks of the type (hk) which result from the regular structure within the individual layer plane segments and denotes a two dimensional structure (Fischbach, 1971). The absence of (hkl) peaks, as found in graphite, indicate that there is little or no stacking order of the parallel layer planes.

From these characteristics, Warren (1941) formulated the turbostratic model. In this model, disordered carbons are considered to exist as parallel stacks of graphitic layer planes. The layers however, are displaced from the typical ABAB.... stacking sequence either by small translations in a direction parallel to the plane or by a rotation about the c-axis (normal to the plane). This displacement from the equilibrium stacking relationship (ABAB....) results in an increased mean interlayer spacing due to a reduction of the van der Waals bonding forces between layers.

This turbostratic model was extensively studied and revised (Biscoe and Warren, 1942; Bacon, 1950, 1951, 1952(b), 1954, 1958; Franklin, 1950, 1951(a) and (b); Houska and Warren, 1954; Warren, 1956; Warren and Bodenstein, 1965, 1966) and lead to the conclusion that in order to understand the structures of disordered carbons, layer plane defects as well as stacking disorders must be considered. The importance of layer plane defects and distortion effects was endorsed by work carried out by Ergun (1968(a) and (b)), Ergun and Gifford (1968, 1969), Ruland (1965(a), 1967(a) and (b), 1968), and Perret and

Ruland (1968, 1969). Studies by Franklin (1951(b)) also introduced disorganised carbon and single layers, disorganised carbon being single or small clusters of carbon atoms which do not exist as part of a graphite layer.

Some of the failings of the turbostratic model were pointed out by Mering and Maire (1960) who went on to propose a model based on the properties of imperfect layer planes rather than perfect layers in a disordered arrangement (Maire and Mering, 1970). They proposed the presence of "interstitial" carbon atoms firmly attached to each side of the layer planes. These atoms are assumed to be the cause of lattice distortion and thus of the increase in the interlayer spacing. Differences in the graphitisation behaviour of carbons, with a similar proportion of structural disorder, could then be explained as a result of the varying concentrations of interstitial atoms present (Schiller et al., 1967).

During graphitisation the structure undergoes a transition of these interstitials from a disordered to an ordered arrangement relative to the hexagonal layers to which they are attached (Schiller and Mering, 1967). This is followed by removal of the defects first from one side of the layer plane and then the other. This loss of the interstitial imperfections allowing the formation of the ordered ABAB.... stacking sequence. Although Mering and co-workers have provided physical, structural and chemical evidence in support of this model, it would seem unlikely that this model could sufficiently describe the complex

nature of highly disordered carbons and their graphitisation.

There are two problems associated with this model. It assumes the presence of only one specific type of imperfection in the structure and the model is based on work carried out on polyvinyl chloride samples and conventional pitch cokes, its applicability to a wider range of carbons was not investigated. Mering also noted that the assumed interstitial defect differs from the mobile interstitial carbon atoms formed by radiation damage (Wallace, 1966), although, it would seem unlikely that even if it were related to the "bound" interstitial, that it would persist to significantly high temperatures to participate extensively in the graphitisation process. Even with its limitations, this model successfully describes many features relevant to the structure of real carbons.

It is generally accepted that the bonding, associated with each carbon atom, within a layer plane is composed of three identical single bonds and one resonating bond. This is the bonding state in turbostratic carbon based on a model, for the disordered structure, proposed by Pauling (1966). For graphite however, he proposed a quinoid structure, possessing two single bonds and one double bond per atom, producing a large out of plane buldge associated with the double bond. Coincidence of these bulges with the open hexagon centres in the adjacent layers would stabilise the ABAB.... type stacking sequence and enhance the van der Waals bonding resulting in a reduction of the interlayer spacing. The graphitisation process in this model could

then be considered as the transformation of the resonating bond to the quinoid structure.

Pauling noted that x-ray diffraction, magnetic susceptibility and layer plane compressibility are consistent with this model. However, problems associated with the model do arise. The quinoid structure would result in an orthorhombic crystal structure with two distinct interplanar distances within the layer planes instead of one, and the relative displacement of the layers would also differ from that of a hexagonal structure. Ergun (1968(a)) argued several points against Pauling's model but concluded that the evidence was inconclusive on the existence of a quinoid structure in graphite.

The probability and importance of the occurrence of interstitial carbon atoms (both individual and clusters), as well as "cross-linked" or distorted carbon-carbon bonds and holes in layer planes have been documented by a number of authors (Ruland, 1964, 1965(a) and (b), 1967(a) and (b), 1968; Perret and Ruland, 1968, 1969; Strong, 1969) as has the importance of layer curvature (Woodruff, 1969).

The work of Ruland has shown not only that a good linear relationship exists, with relatively little scatter, between the mean interlayer spacing and the relative mean square (r.m.s.) displacement of adjacent layers parallel to the layers. But also, that the r.m.s. displacement of adjacent layers normal to the layers decreases as the mean interlayer spacing decreases, although the scatter band is broad and r.m.s. displacement values of adjacent layers normal to the layers are, in general, significantly larger

than the differences between the mean and minimum interlayer spacings. A further point noted was that the incidence of rhombohedral stacking drops sharply as the mean interlayer spacing falls below 0.338nm, but is still significant in moderately well graphitised material.

Some important points emerge from these statements. The first shows that there is no fundamental basis for the mean interlayer spacing of 0.344nm (Franklin, 1951(a)) that is traditionally associated with random parallel stacking. There is, however, evidence for differences in the defect structure of different carbons with the same mean interlayer spacings, and the increased mean interlayer distances of disordered carbons must largely result from defects rather than stacking disorders as shown by Rulands second point. Ruland does acknowledge the importance of a variety of defect types both within and between the layers and suggests that graphitisation occurs by the annealing out of defects as with the Maire/Mering model (Maire and Mering, 1970).

From the traditional parameters used in the description of turbostratic carbon only the mean interlayer spacing seems to have survived in the many new models that have been developed. It now however seems likely that a significant proportion of the interlayer spacing increase in disordered carbons arises as a result of defects within and between the layers (Maire et al., 1968).

During these many reviews and proposals of newer models, parameters such as L_a (layer diameter) and L_c (stacking height) have been questioned and or replaced by

other parameters. The interpretation of the apparent layer diameter L_a has been shown to have numerous correlations with other structural or physical properties and for this reason its interpretation is of particular importance. The accuracy of the measured L_a value with the actual dimensions of the layer structure has been questioned, but it is now generally accepted that the measured value of L_a is appreciably smaller than the average diameter of the layer planes.

Effectively, L_a is a measure of the average size of planar, defect-free regions. Thus, although the extent of the imperfect layer structure may be large, layers that are bent or contain holes will give smaller values of L_a. To determine the true layer size, a variety of x-ray diffraction techniques have been developed (Short and Walker, 1963; Bouraoui and Mering, 1964; Eeles and Wilson, 1965) however, they are extremely complex to employ.

L_a values are probably best interpreted as an indication of the relative flatness and perfection of the layers, rather than as real crystallite layer diameters. The actual extent of the defective layer structure is however, very important and may be the fundamental basis for distinguishing between graphitising and non-graphitising carbons. In the case of non-graphitising carbons, the layer segments are small (Schiller et al., 1968; Perret and Ruland, 1968) as opposed to graphitising carbons in which the layer structure appears to be extensively developed (Ergun, 1968(a)).

CHAPTER TWO

ELECTRON MICROSCOPY

2.1- TRANSMISSION ELECTRON MICROSCOPY

2.1.1- HISTORICAL INTRODUCTION

Microscopy's foundations lie in the early part of the seventeenth century, with the development of the art, in that period, being dominated by Anton van Leeuwenhoek (1632-1723), who became successful both in the construction and use of the instrument.

The work of Abbe (1873) later demonstrated that improvements in microscope resolution would eventually be limited by the wavelength of light employed, the smallest resolvable distance being observed at close to one-half of this wavelength.

Essentially the resolution of a microscope is defined as the smallest distance (g) between two points in the object which may be distinctly reproduced in the image. Detailed calculations (Abbe, 1873) show that the smallest structure of which an image can be produced is of the order:-

$$k \lambda / n_o \sin \alpha \qquad (2.1)$$

where: k is a constant

λ is the wavelength of the illumination

$n_o \sin \alpha$ is the numerical aperture of the objective lens.

The value of k is dependent on the coherence of illumination, with a figure of 0.61 being applicable

in microscopy. Thus:-

$$g = 0.61\lambda / n_o \sin\alpha \qquad (2.2)$$

From this equation the best resolution will be attained using a combination of shortest wavelength with largest numerical aperture. For a light microscope this results in an optimum resolving power of the order 200nm (0.2 μm).

The discovery of x-rays (Röntgen, 1895), i.e. electro-magnetic radiation with wavelengths much shorter than those of light (λ=0.1-0.2nm), aroused hopes that a microscope might be constructed that would overcome the limitations imposed by the use of visible light. X-rays, however, are not directly suitable for microscopy as effective refracting lenses cannot be made; the refractive index of all substances for X-rays being close to unity, thus making it difficult to find materials that will act as lenses. The development of magnetic and electrostatic lenses (Busch, 1926, 1927) showed X-rays still to be unsuitable for microscopy, as unlike electrons, they are uncharged and cannot be focussed.

Discoveries in the 1920's offered a solution to the wavelength limitation and led eventually to the construction of an electron microscope. The development of the wave-particle duality theory (de Broglie, 1924) and of wave mechanics (Schrödinger, 1926) suggested that the wavelength of an electron would be less than that associated with light and thus the construction of an electron microscope should provide an instrument of higher

resolving power than that of a light microscope. An added benefit of using electrons to image a sample is that the wavelength associated with the electron depends on the potential through which it is accelerated, thus allowing a varied range of wavelengths to be obtained. The wavelength associated with an electron accelerated through a potential of 100KeV is 0.0037nm whereas if a potential of 1000KeV is utilised, a wavelength of 0.000087nm is obtained.

The idea of using electron beams for microscopy is often assumed to have been a logical consequence of the hypothesis of the wave nature associated with an electron due to de Broglie (1924) and its experimental confirmation (Davisson & Germer, 1927; Thomson & Reid, 1927). In fact, the initial investigations of imaging by Knoll & Ruska (1932) were based on studies by Busch (1926, 1927) who treated electrons as classical charged particles and demonstrated that axially symmetric electrostatic and magnetic fields could act as lenses for an electron beam, i.e. would focus electrons in analogy to a glass lens for a light beam. As Ruska (1980) makes clear, it was only later that the wave formulation was pointed out to them, opening up the prospect of attaining a very high resolution.

Further development of the electron microscope, throughout the 1930's and 40's, was made possible through the work of numerous scientists (Ruska, 1934; von Borries & Ruska, 1939; Burton et al., 1939; Hillier & Vance, 1941; von Ardenne, 1944; Hillier & Ramberg, 1947), with

"perfected" electron microscopes becoming commercially available at the beginning of the 1950's. Since then, their development has steadily progressed, mainly in the direction of increasingly better resolving power and increasingly higher accelerating voltages, reaching far beyond the vision of its originators, Knoll and Ruska, in its physical and engineering aspects, as well as its applications, which now extend into almost all scientific disciplines.

The first electron microscope (Ruska, 1934) was capable of attaining a resolution of 50nm (0.05 μm). Commercial instruments now available are achieving a resolution of 0.3nm routinely, with higher accelerating voltage instruments, such as the Cambridge 600keV microscope (Nixon et al., 1977; Cosslett et al., 1979; Cosslett, 1980; Smith et al., 1983(a)) approaching atomic resolution for suitable specimens, and have achieved a lattice resolution of less than 0.1nm (Hall & Hines, 1970; Murata et al., 1976; Iijima, 1977; Fryer, 1983; Marks & Smith, 1983; Smith et al., 1983(b), 1985) thus allowing a better understanding of material structure in many diverse fields (Hirsch et al., 1965; Murata et al., 1976; Fryer & Smith, 1986; Buseck, 1985).

The history of electron microscopy and diffraction has been well documented (Mulvey, 1967; Ruska, 1980; Cosslett, 1981, 1987; Goodman, 1981; Hawkes, 1985) and the electron optical theories and development of the instrument have been extensively reviewed (Zworykin et al., 1945; Cosslett, 1951, 1970, 1981; Hirsch et al., 1965;

Hall, 1966; Grivet, 1972; Hawkes, 1972; Cowley, 1979; Geiss, 1979; Spence, 1981; Wischnitzer, 1981; Watt, 1985). The increasing application of electron microscopy to a wide variety of materials has also led to particularly rapid developments in specimen preparation techniques (Kay, 1965; Glauert, 1972; Keown, 1974; Reid, 1974; Watt, 1985;).

2.2- PRINCIPLES OF THE ELECTRON MICROSCOPE

Most electron microscopes are constructed along similar principles to light microscopes. That is, they consist of an illumination source, a series of condenser lenses, which focus the illuminating radiation at the specimen, and a series of enlarging lenses. In the electron microscope these enlarging lenses are magnetic and focus not light, but an accelerated electron beam. The basic structural features of a transmission electron microscope (TEM) are shown schematically in figure 2.1.

2.2.1- THE ELECTRON SOURCE

The illumination source is a fine beam of electrons generated from a hot cathode emitter at a selected negative potential from within the electron gun. Ideally, this source would produce a coherent beam of monochromatic electrons, however, in practice this is not possible. The polycrystalline filament exposes different crystal planes, thus the emission flux is not constant. In addition electrons are emitted from the shoulders of the filament and so a point source situation is not obtained.

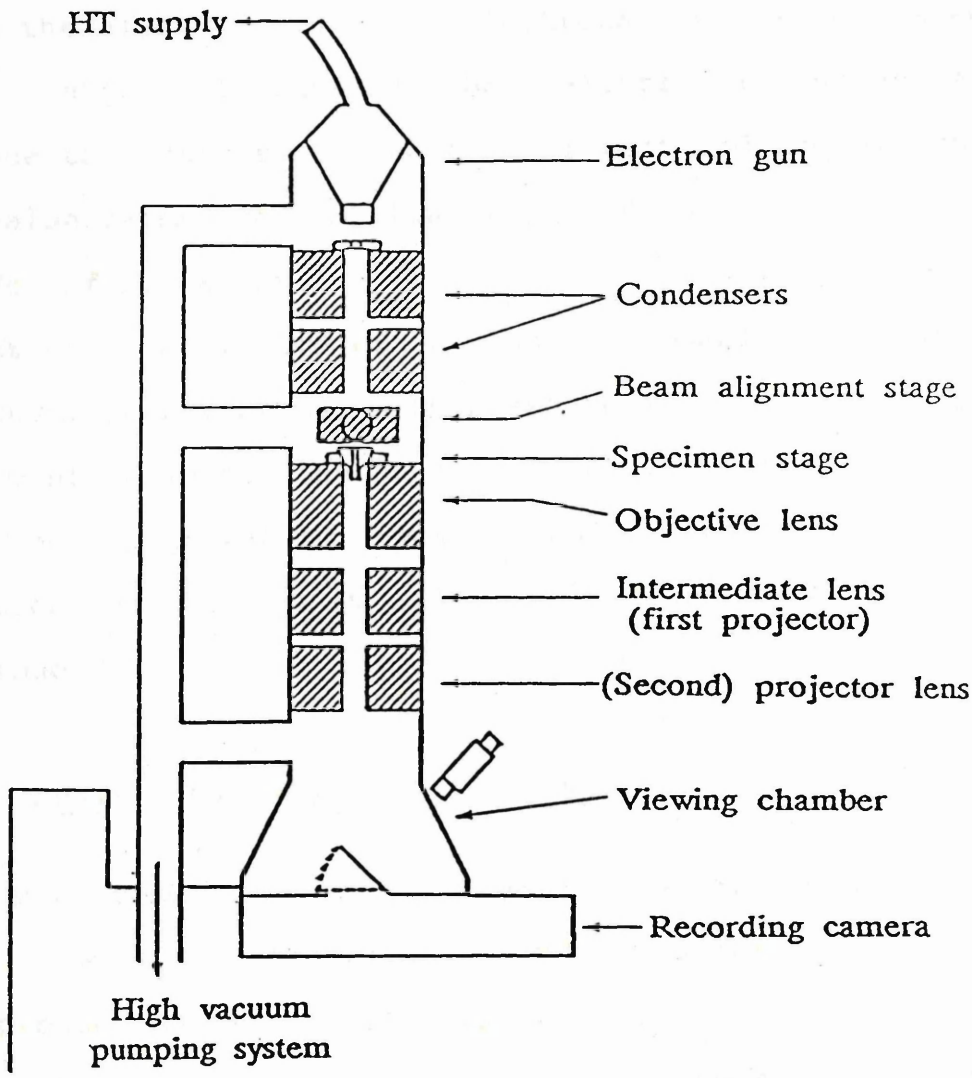

Figure 2.1: Schematic diagram of a high resolution transmission electron microscope.

In general, the electron source takes the form of an electrically heated tungsten hairpin filament (Haine & Einstein, 1952; Haine & Cosslett, 1961; Hall, 1966), mechanically stable at temperatures where the workfunction of the electrons is exceeded, thus, emitting electrons from its surface.

From the electron gun the electrons are accelerated to a high velocity by the electrical potential difference that exists between the filament and anode, the exact value depending on the type of microscope and its mode of operation.

Electrons only travel for any reasonable distance in a vacuum. Accordingly, the pressure in the microscope column must be maintained at 10^{-3} Pa or less. And, having almost no penetration power the specimen under examination must be thin or all the electrons would fail to pass through it.

2.2.2- SPATIAL AND TEMPORAL COHERENCE

Coherent conditions are necessary to obtain contrast in the final image formation. These conditions are approached by the production of a minimum spot size.

Improved electron beam coherence and intensity can also be achieved by using special pointed tungsten filaments (Wolf & Joy, 1971) or lanthanum hexaboride (LaB_6) cathodes (Lafferty, 1951; Broers, 1969; Ahmed, 1971; Batson et al., 1976; Yonezawa et al., 1977). The use a field emission cathode (Crewe et al., 1968), as an alternative to

electrical heating, also derives similar benefits. However, although these filaments give a higher coherence and greater beam intensity than hairpin filaments they require a more careful alignment procedure and are less convenient to use.

An improved or partial coherence can be achieved with a tungsten hairpin filament by diverging the electron beam from a focussed spot and filling the condenser aperture. This results in a corresponding loss of brightness and thus, a balance must be made between a minimum spot size to gain intensity and an improved coherence (spatial coherence).

Mechanical, thermal and external influences on the microscope (temporal coherence) must also be taken into account as these modify the focus of the scope and the precision to which the microscope can be adjusted.

2.2.3- THE LENS SYSTEM

To achieve the magnification and resolution required from electron microscopy an imaging system must be employed. The more lenses available the wider the magnification range, the greater the flexibility in balancing aberrations and the more convenient the operation.

2.2.4- THE CONDENSER SYSTEM

The condenser lens system is used to control the intensity of illumination as well as the relative aperture

of illumination at the object.

An electromagnetic condenser lens system with a field limiting aperture, employed to eliminate any contribution from electron beams widely deflected away from the optic axis, focuses the divergent electron beam onto the specimen. After leaving the gun filament the electrons form a crossover, a demagnified image of which is then projected onto the specimen by the condenser lens system.

For high resolution studies a double condenser system is normally employed. The first condenser lens producing the demagnified image of the electron source which is subsequently projected onto the specimen surface by the second condenser lens. The incorporation of a second condenser lens adds flexibility and control to the illumination system and the area illuminated at the object. This results in a very small minimum spot size, with the advantage of enhanced brightness concentrated over a small area. Thus, even at the highest magnifications, the final image is not too dim.

In addition to the lenses, the condenser system also possesses a fixed and a variable aperture which restrict the diameter of the beam.

2.2.5- THE MAGNIFICATION SYSTEM

The magnification system comprises objective, intermediate and projector lenses which magnify and focus the electrons that are scattered by the specimen.

When the electron beam strikes the specimen, which must

be thin, a number of complex scattering processes can occur (section 2.3.1). Many of the scattered electrons that have passed through the specimen now enter the objective lens.

This lens is the most critical component in the microscope as it determines the resolution and contrast in the image. The reason for this is that it is the only lens in the microscope that significantly contributes to the spherical and chromatic aberration of the optical system; since it is the only lens in which the electrons are reasonably steeply inclined to the axis. An objective aperture inserted near the back focal plane of the lens is employed for the purpose of increasing contrast and reducing spherical aberration. The objective lens detects, transmits, magnifies and focuses the modified electron beam and thus its design and aberrations are critical to the overall performance of the microscope.

In light microscopy, individual lens defects may be corrected by using a series of convergent and divergent lenses. However, unlike optical glass lenses, electromagnetic lenses are always convergent and thus lens defects in the electron microscope cannot be compensated for in an analogous manner. Thus electron microscopes require an objective lens of extremely high quality.

Subsequent lenses, the intermediate and projector lenses, although less critical to overall microscope performance, have two functions. Their most important is to magnify the intermediate image produced by the objective lens. The final image is generally produced on a fluorescent screen, the final magnification being

controlled by altering the excitation of the intermediate and projector lenses simultaneously. The other function of these lenses is to alter the mode of operation of the microscope. By altering the strength of the intermediate and projector lenses, the final screen can be arranged to be conjugate, not with the intermediate image, but, to any other plane of interest. For instance diffraction patterns, formed at the back focal plane of the objective lens, can be viewed in the diffraction mode in which the intermediate and projector lenses form a highly magnified image of the diffraction pattern, the area for diffraction being selected by a selected area diffraction aperture.

The intermediate and projector lenses contribute virtually no spherical aberration due to the slope at which electrons pass through them. They may introduce distortion and chromatic aberration, however careful design of a system allows both of these defects to be kept acceptably small.

The final image, viewed on a fluorescent screen, is focussed by varying the focal length of the objective lens and can be recorded photographically for a more permanent and detailed record.

The instrument used in the present study was a JEOL JEM 1200EX electron microscope with either a pointed tungsten filament or a lanthanum hexaboride cathode as the electron source. The image forming lenses number six; namely, an objective lens, an objective mini-lens, three stage intermediate lenses and a projection

lens. Using this combination, a magnification of 1,000,000 may be obtained. The whole optical column is maintained at a vacuum of 10^{-5} Pa. An accelerating voltage of 120keV with this instrument gives an electron beam wavelength of 0.003nm. Considering the λ factor only, this should allow the direct imaging of atomic details. However, as will be seen later, spherical and chromatic lens aberrations (sections 2.4.3 and 2.4.4) and other limitations on information retrieval (section 2.4) set a practical limit on the performance of the electron microscope.

2.3- IMAGE FORMATION AND CONTRAST

Under ideal conditions, two factors determine the transfer of information from the specimen:-

1. The mode of image formation i.e. interaction of the beam with the specimen.
2. The contrast that any one piece of information has in the final image.

Image formation and contrast arise as a result of the interaction of an electron wave with a specimen, to form at the exit surface, a transmitted wave which may be interpreted as being the recombination of scattered and undeviated waves. This transmitted wave then travels along the optic axis of the microscope to a point where the electron image of the specimen can be viewed and recorded. Under ideal circumstances there is a linear relationship between the structure of the object and the contrast

observed in the image.

2.3.1- BEAM-SPECIMEN INTERACTION

The electron microscope is based on the principles of interaction between fast electrons and the electrostatic potential of the specimen (Coulomb interactions). Almost all the incident electrons pass through (assuming that the specimen thickness is not too great), with only those passing close to the atoms being deflected.

The interaction of a high energy electron beam with a thin solid specimen generates a variety of signals all of which yield information on the nature of the solid (figure 2.2). In electron microscopy, it is the transmitted electrons that are of importance and these can be classified into three types:-

1. There are the directly transmitted electrons which pass through the sample with little change to their wavelength or direction,
2. the elastically scattered electrons which undergo a directional change but retain their energy and
3. the inelastically scattered electrons which undergo both a directional change and a partial loss of energy.

The energy lost while passing through the specimen can cause heating, ionisation and lead to radiation damage of the specimen, involving either an excitation of the core atoms and atomic nuclei in the specimen, or a transfer of energy from the incident electrons to the electrons in the specimen resulting in bond breakage and consequently alteration of the specimen structure (Hobbs, 1987).

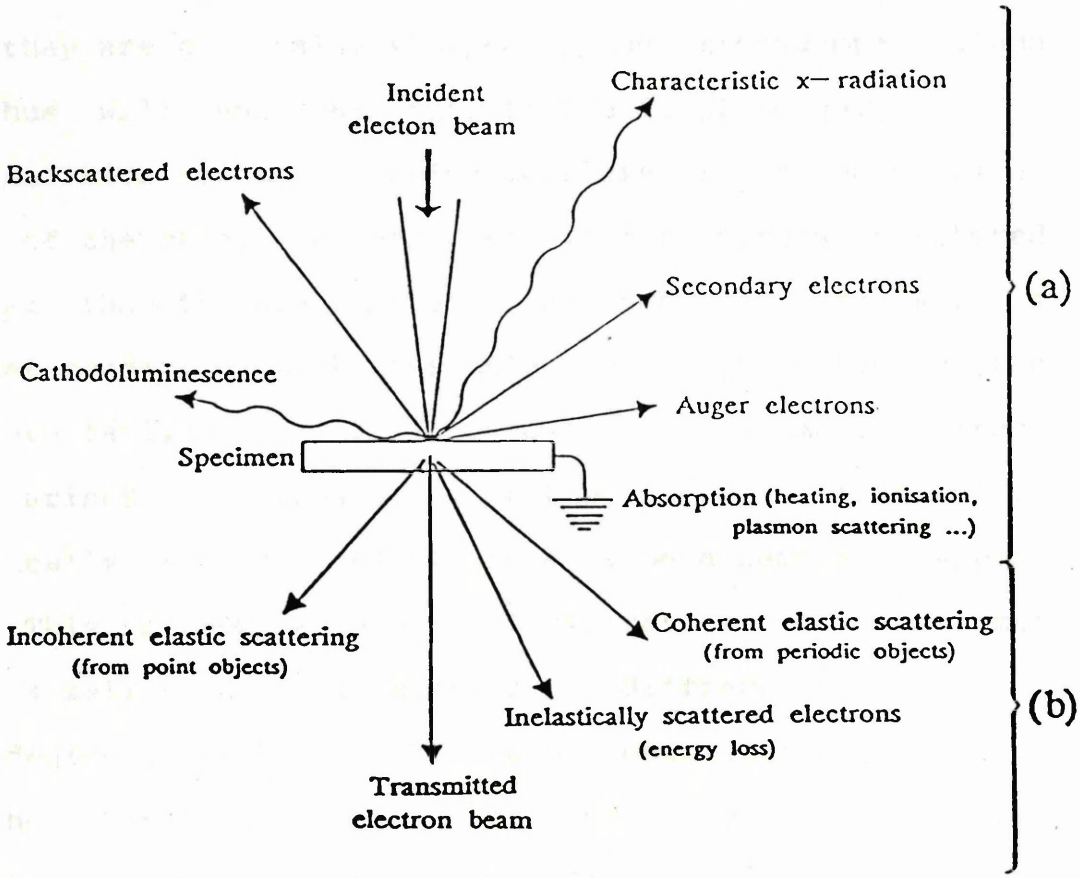

Figure 2.2: Schematic representation of information resulting from the interaction between the electron beam and the specimen in (a) scanning and analytical electron microscopy and (b) conventional and scanning transmission electron microscopy.

2.3.2- ELASTIC SCATTERING

Elastic scattering occurs when the incident electrons interact with the atomic nuclei of the specimen and are deflected without any loss of energy. Increasing atomic number or thickness of the specimen increases the elastic scattering of the electrons. This results in electrons being deflected away from the optic axis such that they are physically stopped by the microscope column and thus will not contribute to the final image.

Insertion of an objective aperture, in the back focal plane of the objective lens, such that electrons scattered greater than the aperture angle are removed, results in a similar condition, with those electrons interrupted by the aperture failing to contribute to the image. Image contrast then arises, as those areas of the specimen from which elastically scattered electrons have been removed, appear dark. This is known as amplitude contrast or for a specimen with a defined periodic structure, diffraction contrast. The degree of such contrast can be controlled by the size of the objective aperture used and in general is only important at low to medium resolution.

Contrast obtained by deliberately including the direct transmitted beam and some of the diffracted beams forms what is termed a bright field image (figure 2.3(a)). Alternatively, a dark field image can be obtained, a high contrast image of reduced intensity, by excluding all beams except the particular diffracted beams of interest (figure 2.3(b)).

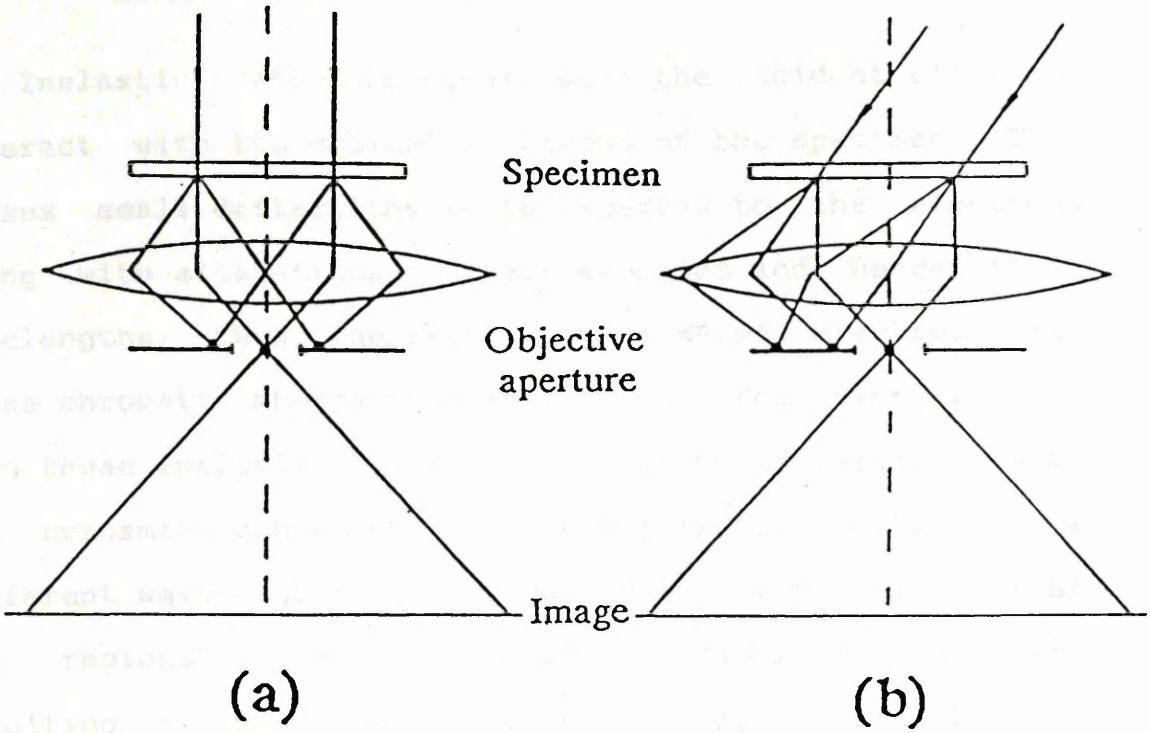

Figure 2.3: Imaging modes in the TEM: (a) bright field and (b) dark field.

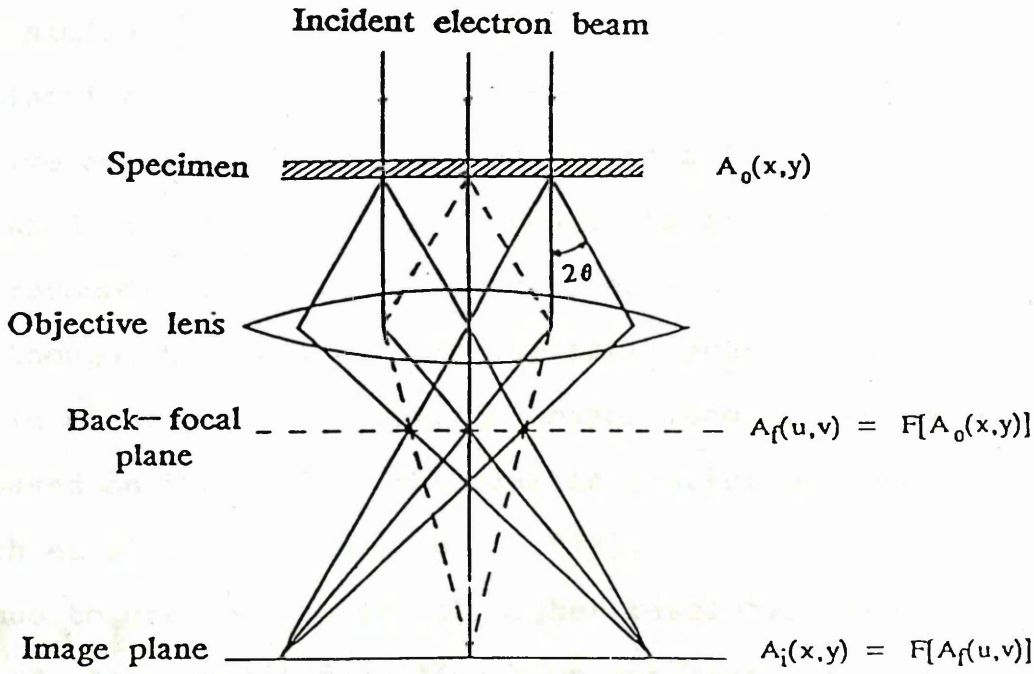

Figure 2.4: Schematic diagram of the formation of an image by the lens in a TEM. The mathematical formulations of the wave amplitude in various planes along the optic axis are indicated.

2.3.3- INELASTIC SCATTERING

Inelastic scattering occurs when the incident electrons interact with the orbital electrons of the specimen. This causes small deflections to be imparted to the electrons along with alterations to their energies and hence their wavelengths; thus, inelastically scattered electrons may cause chromatic aberrations in the image formation process. When these inelastically scattered electrons recombine with the transmitted beam there is an interaction between the different wavelengths. This produces a resultant wave that has regions of reinforced and diminished intensity resulting in either increased or diminished regions of contrast in the final image. This phenomenon only becomes visible at slightly out of focus conditions and is known as inelastic phase contrast.

A similar process, elastic phase contrast, arises for the elastically scattered electrons passing through the objective aperture. Image contrast again being increased or diminished if suitable focus conditions are selected to allow recombination with the undeviated electron beam.

Although, both elastic and inelastic scattering events occur in electron microscopy, the major imaging techniques are based on the predominant elastic scattering processes (Hirsch et al., 1965; Humphreys, 1979).

Thus to obtain contrast at higher resolution than that obtained from amplitude/diffraction contrast, elastically scattered electron beams are recombined and the phase difference between them enhanced by defocussing the

objective lens (elastic phase contrast). Inelastically scattered electrons will also undergo some phase recombination, however the defocus value for which this is significant is far removed from that required for the elastically scattered electrons (Misell, 1971).

If the elastically scattered electrons arise from a periodic structure in the specimen - a crystalline structure with a set of lattice planes - then a related periodicity in the image may be obtained. This information may only be obtained for periodicities orientated parallel to the electron beam and is the basis of "lattice imaging" in high resolution electron microscopy. Small periodicities, normal to the electron beam, will produce elastically scattered electrons at large angles. Provided a sufficiently large objective aperture is used, these electrons will be transmitted. However, they will be focussed at a point distant from the optical axis of the objective lens and will thus be subject to lens aberrations which severely affect phase contrast image retrieval and interpretation.

The interpretation of elastic phase contrast effects can only be carried out with relative ease for thin specimens (less than 10nm) where electrons are considered to undergo only single scattering events and thus conform to kinematic (weak phase object) approximations (Whelan, 1959; Hirsch et al., 1965). Kinematical theory however can only be considered an approximation, as in reality, multiple scattering events do occur and the more complex dynamical scattering theory is necessary to account for the

scattered amplitudes and phases resulting from this situation (Cowley and Moodie, 1957).

2.3.4- PHASE CONTRAST MECHANISM

The electrons, scattered elastically through a variety of Bragg angles by the specimen, form a diffraction pattern in the back focal plane of the objective lens. This Fraunhofer diffraction pattern corresponds mathematically to the intensities of a Fourier transform of the object, expressed in terms of spatial frequency, areas of which may be removed by insertion of the objective apertures. In order to obtain the final image, the diffraction pattern undergoes a further Fourier transform to the image plane and is then further magnified by the remaining lens systems of the microscope. The photographic plate records the intensity distribution, thus, if multiple scattering has occurred in the object it will be visible in the images as changes in contrast. This contrast reflects phase differences caused by multiple scattering in the object rather than structural features of the object. Thus, for this reason, only thin specimens should be examined, as the image of a thick specimen will reflect not only the structure of the specimen but multiple scattering events also.

Figure 2.4 schematises the formation of an image by the objective lens. The principle is the same as that of the Abbe theory for gratings in light optics (Abbe, 1873); If the scattered and the undeviated beams can be made to

recombine, so preserving their amplitudes and phases, then a lattice image of the planes which are diffracting may be resolved directly (phase contrast).

The Abbe theory of imaging may be translated into mathematical form for thin specimens (less than 10nm), where only single scattering events are considered to occur (kinematical conditions: Cowley, 1975(a)), thus the relative intensities of the scattered and transmitted beams can be calculated (Hirsch et al., 1965; Gevers, 1978).

The image contrast, represented by the intensity transmitted to the image plane, can be quantitatively explained by considering the amplitude of the elastically scattered electrons as they pass through the specimen to form a diffraction pattern in the back focal plane of the objective lens. These beams are then recombined, taking account of phase modulations induced by the specimen and objective lens defects to form an amplitude distribution in the image plane. The amplitude distribution is then represented on the screen as an intensity distribution, and corresponds to the contrast observed in the micrograph.

As indicated in figure 2.4, the distribution of the wave amplitude $A_f(u,v)$ in the back-focal plane (the diffraction pattern) is related to the amplitude $A_o(x,y)$ of the transmitted wave, at the exit surface of the specimen (object plane), by a Fourier transform:-

$$A_f(u,v) = F\left[A_o(x,y)\right] \qquad (2.3)$$

where x,y and u,v are co-ordinates perpendicular to the

optic axis in the object and back-focal plane respectively.

The waves will then propagate from the back-focal plane to the image plane, where they interfere to give the amplitude distribution $A_i(x,y)$. This interference may be represented by a second Fourier transform:-

$$A_i(x,y) = F\left[A_f(u,v)\right] = F\left\{F\left[A_o(x,y)\right]\right\} \qquad (2.4)$$

This formulation shows that the imaging process, i.e. the operation of obtaining the amplitude and phase distribution in the image given that in the object, can be regarded as two successive Fourier transforms:-

$$\text{SPECIMEN} \xrightarrow[\text{Transform}]{\text{Fourier}} \text{DIFFRACTION PATTERN} \xrightarrow[\text{F.T.}]{\text{inverse}} \text{IMAGE}$$

A more detailed mathematical form is expressed by Erickson (1973) and Cowley (1975(b)).

For a crystal at the exact Bragg orientation, the appearance of a sharp spot in the diffraction pattern reflects the periodic oscillation of the transmitted wave amplitude with a frequency proportional to 1/d. The oscillation reproduces the regular spacing of the set of diffracting planes. If both the unscattered wave and the diffracted wave are allowed to pass through the objective aperture, their interference in the image plane will bring about a periodic variation of the intensity in the form of fringes which may be interpreted as a magnified image of the lattice planes. This is the phase contrast effect, which governs the appearance of the image in the high

resolution electron microscope (HREM).

The effect of insertion of an objective aperture in the back focal plane of the objective lens is to remove some of these spatial frequencies. As a result, the amplitude distribution in the image is no longer an exact reproduction of the transmitted wave. If the specimen is limited to a point, its image will not be a perfect point but a small disk (the Airy disk), of diameter D_A with:-

$$D_A = 0.61(\lambda / \alpha_o) \qquad (2.5)$$

where α_o is the maximum scattering angle that is admitted through the objective aperture. D_A is the resolution limit of any wave optical instrument in the absence of lens aberration.

As the electron wavelength is much less than interatomic distances, atomic details should be, in principle, clearly revealed. Unfortunately, electron lenses are far from perfect. The main defect is spherical aberration C_s. Its geometric effect is that the scattered waves are focussed in slightly different image planes for different values of the scattering angle 2θ. This phenomenon can be accounted for by the introduction of (χ) an instrumental phase adjustment factor (Heidenreich, 1964), first derived by Scherzer (1949):-

$$\chi = -\pi C_s (2\theta)^4 / 2\lambda \qquad (2.6)$$

to the waves scattered by an angle 2θ.

Another alteration to the phase of each wave must be considered. If the focus of the objective lens is varied so that the image plane is shifted along the z axis by an amount ΔF (the defect of focus or defocus) from its former position, the distribution of the wave amplitude in the former image plane may be obtained by introducing a phase delay (Heidenreich, 1964):-

$$\chi_F = \pi \Delta F (2\theta)^2 / \lambda \qquad (2.7)$$

As $2\theta = \lambda / d$ (Bragg law), the total phase delay, which is a rearrangement of Scherzer's expression (Scherzer, 1949), becomes:-

$$\chi = \pi \lambda / d^2 (\Delta F - C_s \lambda^2 / 2d^2) \qquad (2.8)$$

The objective aperture subtends the maximum angle (α_o) of scattered electrons that can be used for image formation. If this aperture is decreased in size, then the effect of spherical aberration is reduced, however the information carried to the image plane will also be diminished.

Under single scattering conditions (thin specimens) the resultant amplitude distribution in the back focal plane of the objective lens is the sum of the transmitted unscattered beam and the elastically scattered beam. If the undeviated and the scattered waves are out of phase, their interference in the image plane will not give a faithful image of the wave transmitted by the specimen. If this

transmitted wave contains only one spatial frequency 1/d, it is possible, using equation (2.8), to adjust ΔF to compensate for the phase delay introduced by C_s. The spacing of the fringes which are then obtained in the image plane corresponds to the spacing of the lattice plane. The problem of imaging several different spatial frequencies together is more complex. For a perfect lens ($\sin \chi = 1$) all these frequencies would be faithfully reproduced in the image; the term $\sin \chi$ is called the phase contrast transfer function (PCTF) (Hanszen, 1971; Erickson, 1973) and determines the transfer of object information to the image plane. However, due to defects present in magnetic lenses this is not the case. The final image contrast is thus dependent on the term $\sin \chi$ (PCTF) which has different values at different spatial frequencies, depending on the scattering angle for the particular frequency, the defocus value (ΔF) and the spherical aberration (C_s) of the objective lens.

Some examples of the variation of $\sin \chi$ as a function of the spatial frequency 1/d nm^{-1} ($= \lambda / \alpha_o$), assuming coherent illumination over a range of defocus values, are shown in figure 2.5(a). The diagram relates to a JEOl JEM 100C microscope operated at 100KeV with a spherical aberration coefficient (C_s) of 0.67mm and an objective aperture of 50 μm.

It is desirable to operate a microscope at a defocus value (ΔF) with the maximum possible continuous range of spatial frequencies of the same contrast. Figure 2.5(a) shows that there exists an optimum value of ΔF for which

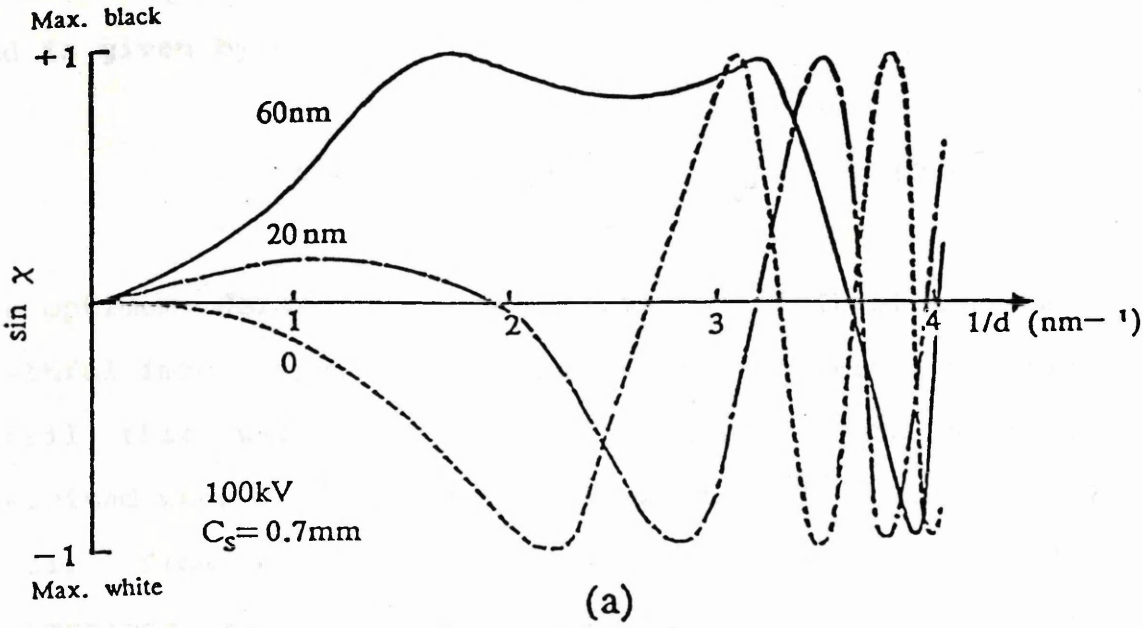

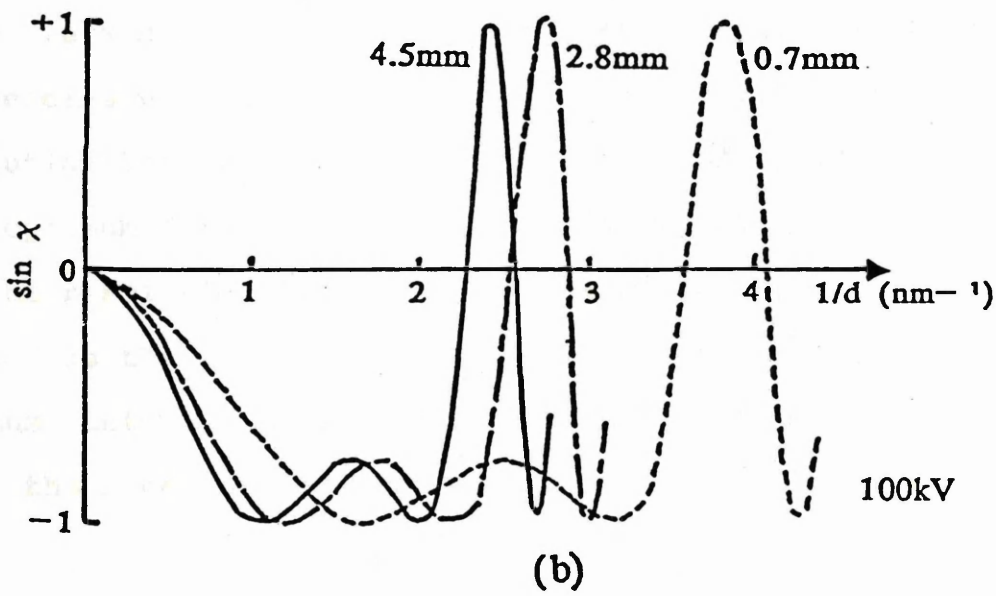

Figure 2.5: A comparison of PCTF curves: (a) for a range of values of defocus ΔF=0, 20 and 60nm underfocus, and (b) for various spherical aberration coefficients, C_s=4.5, 2.8 and 0.7, under optimum defocus conditions.

sin $\chi \simeq 1$ lies within a fairly broad range of 1/d frequencies at 60nm defocus. This is known as the "optimum defocus" value or "Scherzer" focus (ΔF) (Scherzer, 1949) and is given by:-

$$\Delta F = 1.19(\lambda C_s)^{1/2} \qquad (2.9)$$

The optimum defocus (ΔF) defines the limit of the most faithful image reproduction down to the smallest structural detail that will be obtained. However, care must be exercised when interpreting such images, as the absence of detail from other periodicities can lead to false assumptions and thus erroreous observations about the structure under examination.

The objective lens may thus be considered as a "filter" which retains, for imaging, only the range of spatial frequencies within which sin $\simeq 1$. Figure 2.5(b) shows the resolution loss that occurs as the value of C_s is increased from optimum defocus (ΔF) value at 100KeV.

The resolution limit D_{min} of the microscope is usually defined as the largest value of d for which $\sin\chi = 0$ at the optimum defocus. Eisenhandler & Siegel (1966) calculated D_{min}, the Scherzer cut-off, to be:-

$$D_{min} = 0.65 C_s^{1/4} \lambda^{3/4} \qquad (2.10)$$

From this it follows that an improvement of resolving power requires a reduction of C_s (i.e. a more perfect lens) and of λ (i.e. a higher operating voltage). However, the

performance of the microscope is also affected by other factors, such as the instabilities of the high-voltage supply and lens current (chromatic aberration) and the electron source.

The electron source, so far, has been considered to be of perfect spatial and temporal coherence. However, in reality, the electron microscope has a finite illumination source size (partial spatial coherence) and the electrons emitted are not completely monochromatic. This partial spatial coherence imposes an "envelope" function (Hanszen, 1971; Hanszen & Trepte, 1971; Frank, 1973; Misell, 1973; Boerchia & Bonhomme, 1974) on the calculated transfer function, and ultimately sets a limit on the information transfer attainable. Consequently, the PCTF has to be modified to allow for the effects of chromatic aberration and partial coherence as shown below:-

$$\sin \chi' = \sin \chi . E_{\alpha} . E_{\epsilon} \qquad (2.11)$$

where E_{α} is the envelope function representing damping of the PCTF, due to partial coherence and E_{ϵ} represents the PCTF modification due to chromatic aberration (Frank, 1973; Fejes, 1977). This equation however, is only an approximation as partial coherence is defocus dependent. Frank (1973) showed that the coherence and chromatic envelopes would give a more accurate description by integration over an appropriate focal range.

Coherence is also dependent on the illuminating angle α. Figure 2.6 shows the same PCTF as in figure 2.5, this

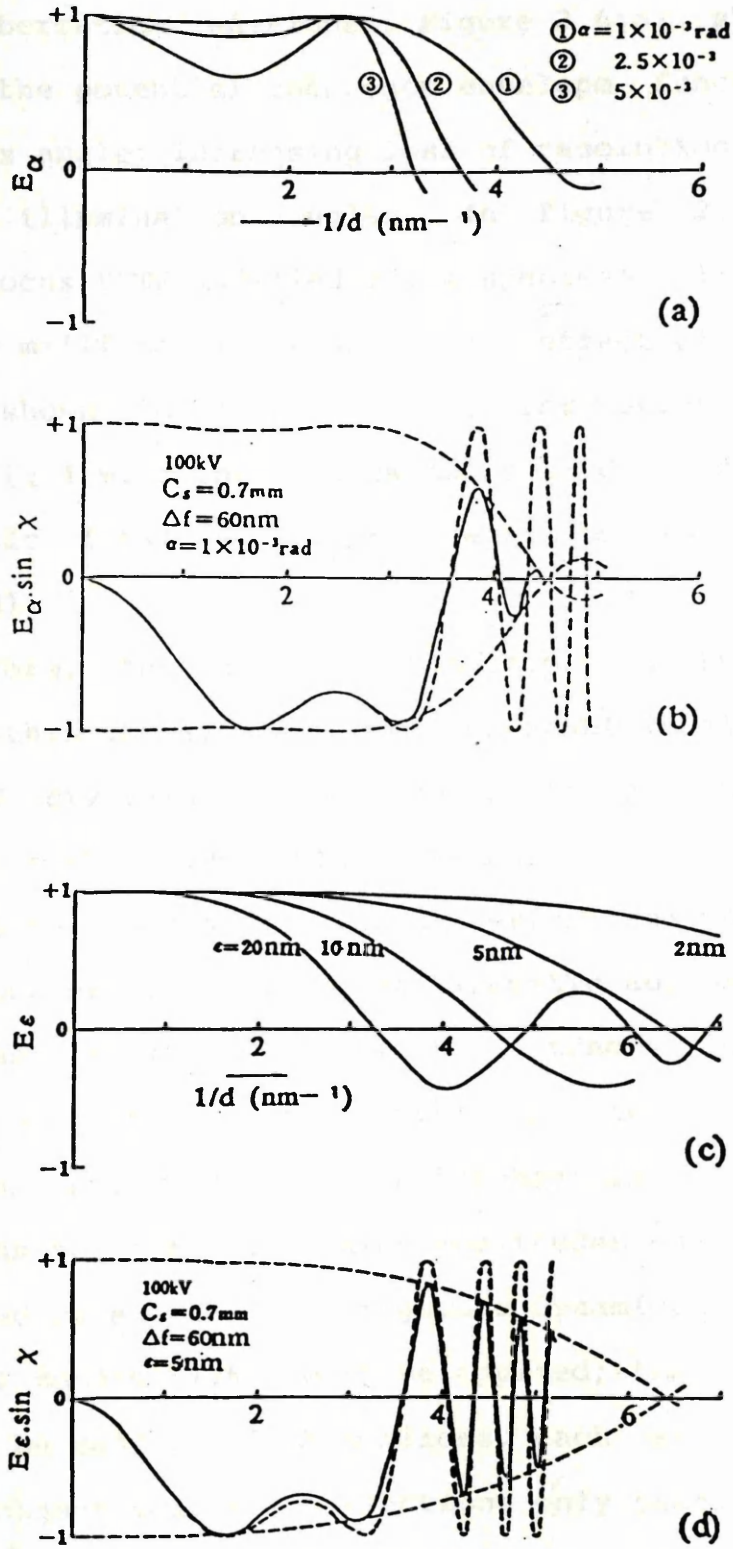

Figure 2.6: (a) Envelope function E_α, for various specimen illumination angles, (b) PCTF $E_\alpha \sin \chi$ modified for $\alpha = 10^{-3}$ rad. (c) Envelope function E_ϵ, (d) PCTF $E_\epsilon \sin \chi$ modified for $\epsilon = 5$nm.

time incorporating the effects of partial coherence and chromatic aberration envelopes. Figure 2.6(a) shows the effect on the potential coherence envelope functions of varying this angle; increasing loss of resolution results for larger illumination angles. In figure 2.6(b) the optimum defocus PCTF modified for a specimen illumination angle of one milli-radian is shown. The effect of chromatic spread is shown in figure 2.6(c) for several focal variations (ϵ) with the optimum defocus PCTF modified for the chromatic focal variation ϵ equal to 5nm shown in figure 2.6(d).

Furthermore, the effects of multiple scattering of electrons within the sample become important in all but the thinnest of crystals. Within the limits of the stated approximations the phase contrast transfer theory provides a good guide to the high resolution performance that can be expected. However, in reality the kinematic approximations, used in the derivation of the PCTF theory lose their validity, the effects of multiple scattering becoming important as real specimens do not behave as ideal phase objects. Thus to obtain the exact amplitudes and phases of the scattered waves, the more rigorous dynamical treatment of Cowley & Moodie (1957) must be applied; the object is assumed to be made up of thin slices, each an individual weak phase object scattering electrons only once. Summation of the successive phase and amplitude changes induced in the incident wave are then used to describe the resultant object wave. The solutions obtained depending on the varying degrees of approximation applied. Detailed

mathematical treatment of the dynamical theory has been outlined by various authors (Cowley & Moodie, 1957; Allpress et al., 1972; Lynch & O'Keefe, 1972; Goodman & Moodie, 1974; Cowley, 1975(b); Whelan, 1978).

In the type of 100keV microscope used in early studies, the point resolution was of the order of 1nm (Hillier, 1946; Menter, 1956). Nowadays lenses and goniometer stages can be so constructed (Hawkes, 1980; Kuzuya et al., 1984) as to permit, firstly, a point resolution of 0.2nm (Harada & Warble, 1978; Hutchison, 1982) and, secondly, the facility of orienting the specimen so as to allow the imaging of essentially any particular projection of its structure. With such resolution, details of the projected surface atomic structures of certain materials can be assessed (Hutchison, 1978; Bovin et al., 1985; Bursill et al., 1985; Buseck, 1985; Hutchison & Briscoe, 1985; Smith, 1985, 1986; Iijima, 1986; Kang et al., 1987; White et al., 1987).

When microscopes are operated at their highest level of resolution, the specimen under investigation experiences intense electron irradiation, to such an extent in some cases, that alterations affect the integrity of the information sought from the specimen. Problems do, therefore, arise due to specimen damage and sometimes it is not possible to fully utilise the resolution capabilities due to the beam sensitivity of the material.

2.4- LIMITATIONS ON INFORMATION RETRIEVAL

The information which can be recorded from electron microscopy is contained in the electrons scattered during passage through the specimen. The information desired is represented by perturbations in the electron waves. Electron optical defects can cause similar perturbations, however, if these are suppressed to a lower level than specimen perturbations then meaningful resolution may result, although interpretation can be complicated by other factors, important in the control of image quality.

2.4.1- CALIBRATION OF THE MICROSCOPE

Accuracy in calibration of the instrument for high resolution imaging or diffraction patterns is critically important for quantitative microscopy (Haine & Cosslett, 1961; Agar, 1965; Edington, 1974; Hines, 1984). There are two types of calibration procedure. One, termed a permanent calibration procedure, is performed when the instrument is installed and is periodically checked during its life or if the instrument is modified. The other, termed a routine calibration, is performed each time the instrument is used and results in the alignment of the microscope imaging system.

2.4.2- ALIGNMENT OF THE OBJECTIVE LENS AXIS

Misalignment of this lens seriously reduces the resolving power of the microscope due to increased

spherical aberration and sensitivity to chromatic aberration. The scattered electrons within the microscope travel close to the optic axis, therefore aberrations such as coma and distortion are not of great importance.

2.4.3- SPHERICAL LENS ABERRATION

As a magnetic lens field is not spherically symmetric, spherical aberration is an important lens defect. The focal length of the lens is not constant across the diameter of the lens with the result that the imaged rays are not brought to a point of focus. This effect can be minimised by reducing the aperture of the lens, but generally spherical aberration determines the attainable resolution.

2.4.4- CHROMATIC LENS ABERRATION

Chromatic aberration arises due to variations in both the electrical stability (lens currents) of the microscope and the energy of the electrons. To minimise the effects, the lens currents must be stabilised to avoid a lens with a continually alternating focal length. The high voltage power supply must also be stabilised, thus allowing sufficiently monoenergetic electrons to be obtained. As the electrons pass through the specimen however, they lose energy causing both a loss of coherence at the specimen and chromatic effects in all subsequent lenses.

2.4.5- ADJUSTMENT OF OBJECTIVE ASTIGMATISM

Astigmatism arises from rotational variation in the

focal length of the lens due to an asymmetric magnetic field. It can be caused by a number of factors such as inaccurate lens manufacture, inhomogeneous pole pieces and contamination within the microscope causing distortion fields due to charging. The effect of astigmatism is most critical in the objective lens and thus contains a system of electromagnetic stigmator lenses which may be used to apply a compensating field and thus correct the effects of astigmatism allowing the electrons to be brought to a common focus; correction being established when a symmetrical Fresnel fringe is obtained around a hole in a holey carbon support film or when the grains of a carbon support film appear symmetrical (Haine & Mulvey, 1954).

2.4.6- SPECIMEN CONTAMINATION

The build up of amorphous, usually carbonaceous material on the specimen can give rise to charging effects which obscure the detail of the specimen. The residual atmosphere within the microscope column contains, in addition to normal atmospheric gases, non-deposited species and quantities of hydrocarbons which may have arisen from sources such as vacuum pumping fluids, sealing gaskets, photographic plates or any parts which have been directly handled by the operator. The non-deposited species present react with the specimen or adsorb on it (Hartman et al., 1974; Moodie and Warble, 1974), with the hydrocarbons being deposited on all internal surfaces of the microscope including the specimen (Hillier, 1948; Ennos, 1953; Fryer, 1979). This surface film becoming fixed in place by

polymerisation:ion induced by electron bombardment. This process occurs constantly as the specimen is viewed, the hydrocarbon layer being replenished continuously. Thus a permanent deposit builds up on a sample during specimen examination and is referred to as "contamination".

Modern electron microscopes reduce this contamination problem by the use of an anti-contamination device, generally a liquid nitrogen cooled jacket surrounding the specimen, thus removing the contaminants by preferential condensation. Another method employed is the production of an extremely high and clean vacuum by the use of dry pumps.

2.4.7- RADIATION DAMAGE

Most materials undergo some form of radiation damage during examination in the electron microscope, these alterations affecting the specimen to such an extent in some cases, that, they lead to a total loss of specimen structure (Holland et al., 1983). Radiation damage occurs in many materials and has been extensively studied (Burton et al., 1947; Hobbs, 1979, 1984, 1987; Csencsits & Gronsky, 1987; Dahmen et al., 1987; Sharma et al., 1987; Smith et al., 1987). The mechanisms and consequences of radiation damage and how they may best be avoided or minimised during examination have also been extensively addressed (Burton et al., 1947; Glaeser, 1975; Jones, 1975; Makin, 1978; Fryer, 1979; Hobbs, 1979, 1984; Urban, 1979; Holland et al., 1983; Brown, 1987).

Encapsulation of organic crystals by carbon films

proved to be an extremely successful way to minimise irradiation damage (Fryer & Holland, 1984; Holland, 1984). Image intensifiers have also been used to aid focus adjustment at low beam doses (English & Venables, 1971, 1972). A system that permits photography of beam sensitive specimens with minimal exposure has also been developed (Williams & Fisher, 1970) so that the specimen is subjected to exposure of the electron beam only for the duration of the photographic exposure.

The carbonised products, for electron microscopy examination in this study, were relatively beam stable and thus did not require any special attempts to minimise radiation damage.

2.4.8- MECHANICAL STABILITY

Mechanical stability, mainly drifting of the specimen stage as well as thermal or mechanical vibrations can cause a reduction in image quality, especially during high resolution imaging. Modern microscopes generally employ secure mounts, with a hydraulic damping system supporting the column to minimise the effects of mechanical vibrations with time allowed for re-equilibration each time a new area of specimen is examined. Mechanical stability can also be compensated for by using film (x-ray) requiring a reduced exposure time.

Thermal instability develops as the beam intensity increases, causing the thermal expansion between the specimen and support grid contributing to specimen drift. This effect may be minimised be spreading the electron

beam, thus making it more coherent.

However, as a result of this, the intensity will be reduced and the increased beam current necessary to retain the intensity, reduces the coherence of illumination and thus the resolution of the image. Consequently the choice of illumination conditions must be a compromise, the beam must be bright enough to keep exposure times low to minimise loss in resolution from specimen drift.

2.5- OPTICAL DIFFRACTION ANALYSIS

To aid interpretation of high resolution micrographs, it is common practice to record a "focal series" of micrographs by successive stepwise variation of the objective lens defocus value. Such a series reflect the difference in high resolution image content due to the variation in contrast transfer properties with defocus, as discussed previously (Section 2.3.4). These differences can be quantitatively detected by producing optical diffraction patterns (optical transforms) from the micrographs using laser optics, on an "optical bench".

The optical transform provides an intensity map of spatial frequencies pertaining to the optical density distribution on the micrograph and thus reflects the microscope transfer function at the time the micrograph was recorded. Spatial frequencies for which no information is contained in the micrograph ($\sin \chi = 0$) appear dark in the optical transform and bright areas in the transform correspond to spatial frequencies for which contrast information was transferred to the original micrograph.

Millward & Jefferson (1978) applied linear transfer theory, to the optical diffraction technique, to demonstrate the information content of the optical transform. However, since the optical transform reflects an intensity distribution, the information content is related to the square of the transfer function, so the absolute value of the function, positive or negative, is not revealed.

Optical diffraction analysis is an extension of the Abbe-Porter treatment (Abbe, 1873; Porter, 1906). Following the appearance of the laser in 1960, optical diffraction became a practical vehicle for data-processing. Details of the method, with applications to microscopy, have been described by many authors (Thon & Siegel, 1970; Horne & Markham, 1973; Power & Pincus, 1974; Pincus, 1978;).

The source of illumination is a laser which radiates a coherent monochromatic illumination. The input is a micrograph and the resulting optical diffraction pattern (ODP) is a two-dimensional Fourier transform of the input image. This transform is a graph of the distribution of orientations and spacings of the elements in the input.

The optical bench equipment used in this study is shown in figure 2.7. The illumination source is a helium-neon laser (Spectra Physics, Model 132) in a Polaron optical diffractometer. The system can be used to identify the separate periodicities in a micrograph containing overlapping periodic objects. Instrumental defects, such as astigmatism, specimen drift and instability, can also be diagnosed. Astigmatism leads to an elliptically shaped Fourier transform for the amorphous carbon support film as

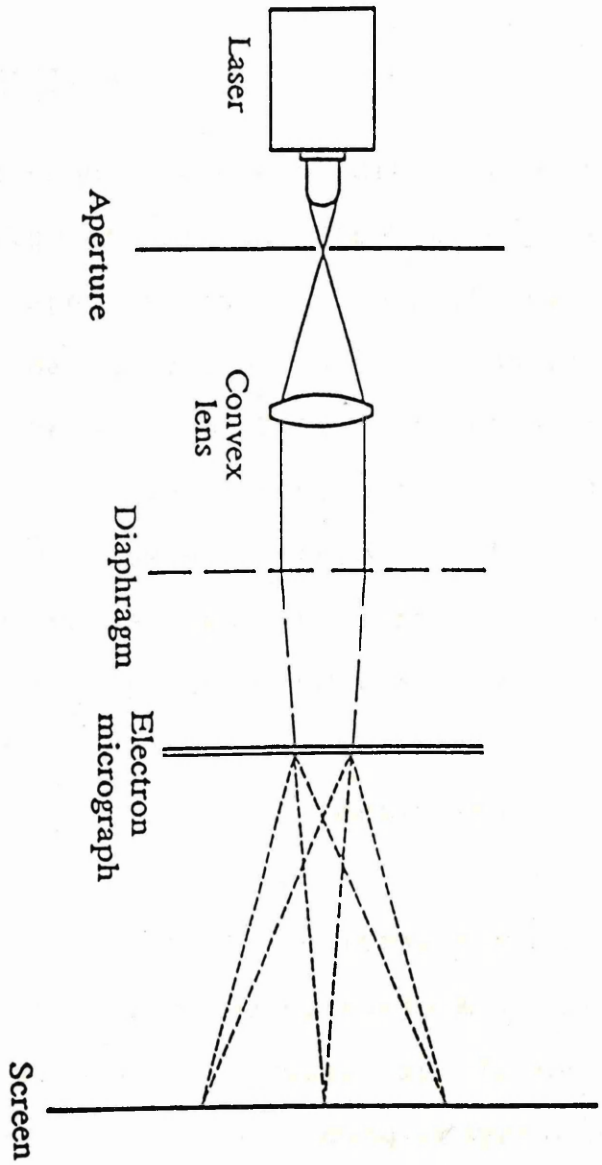

Figure 2.7: Schematic diagram of a bench mounted optical diffractometer for the analysis of electron micrographs.

opposed to the circular pattern for well corrected micrographs (Thon & Siegel, 1970) with specimen drift leading to a loss of Fourier components in the direction of the drift. Image filtering and reconstruction can be carried out although care must be taken to avoid artifacts (Fryer, 1979).

2.6- ELECTRON DIFFRACTION

Specimen examination by electron diffraction provides a rapid visual assessment of the degree of structural ordering within a specimen and the effect of radiation damage before an image is recorded. Specimens with crystal planes parallel to the electron beam diffract electrons in accordance with the Bragg law. Undeviated incident electron beams and diffracted beams are focused at the back-focal plane of the objective lens and there form a diffraction pattern. The diffraction pattern and the intermediate image (figure 2.8) are always present in the microscope, with the intermediate lens setting determining which is projected onto the image plane . In the electron diffraction mode, the intermediate lens, instead of being focused on the intermediate image, (figure 2.8(a)) as is the case in the transmission mode, is focused on the diffraction pattern and corresponding adjustment of the projector system magnifies this pattern onto the final image screen (figure 2.8(b)). The displayed diffraction pattern is formed from electrons incident on any part of the specimen. Often, however, the diffraction pattern of a

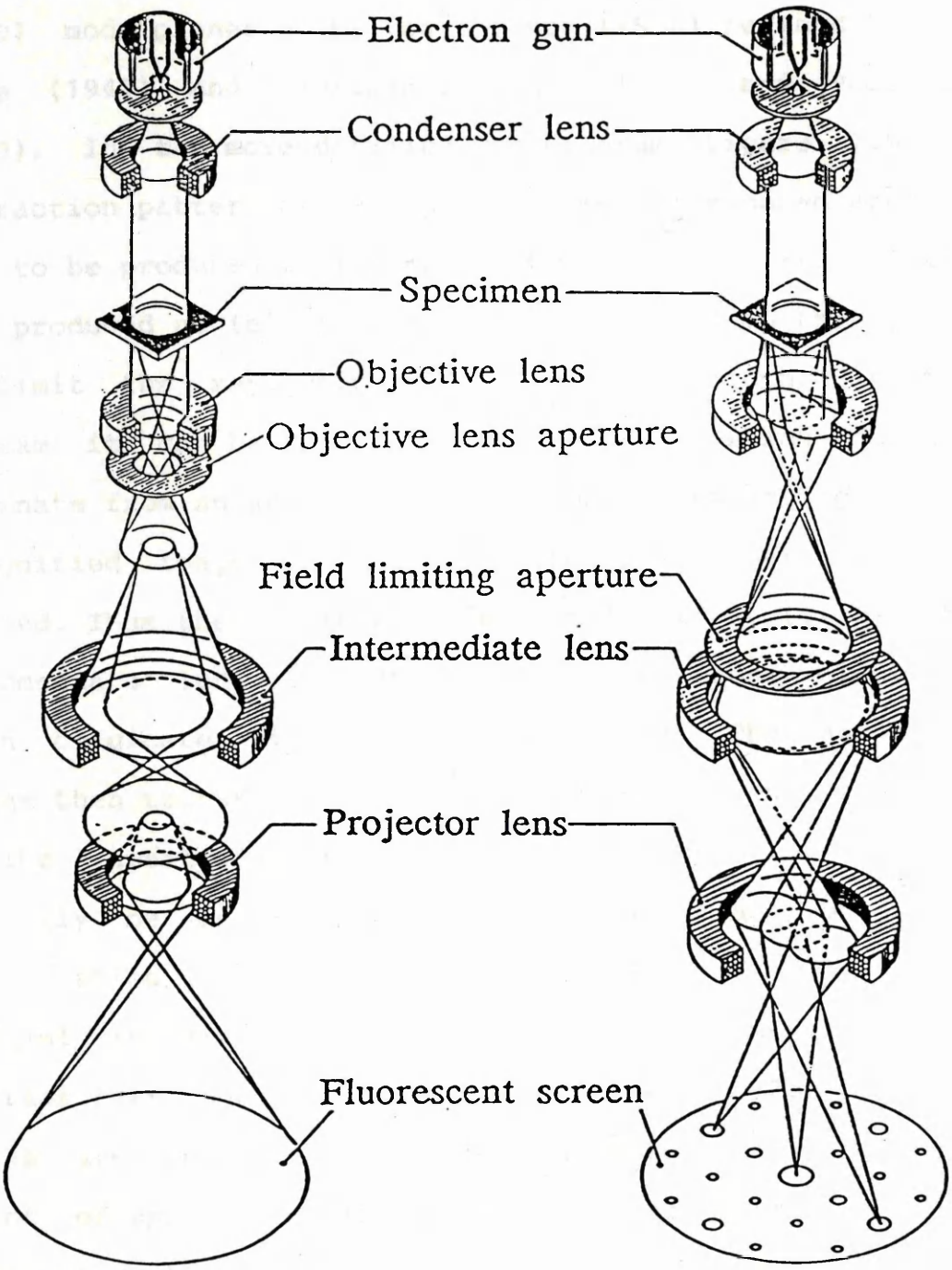

ELECTRON MICROSCOPE IMAGE
(a)

ELECTRON DIFFRACTION PATTERN
(b)

Figure 2.8: Comparison between (a) image and (b) electron diffraction pattern formation in the transmission electron microscope.

small area or crystallite is required, and this can be achieved using the selected area electron diffraction (SAED) mode pioneered by von Boersch (1936) refined by Le Poole (1947) and described by Agar (1960) and Phillips (1960). In the more detailed ray diagram (figure 2.9) a diffraction pattern of the whole of the illuminated area is seen to be produced in the plane at (c) and an image of the area produced at (d). An aperture is inserted in this plane to limit the rays which pass down the column. In the diagram it can be seen that any electrons which do not originate from an area on the specimen corresponding to the demagnified image of the selected area aperture are stopped. Thus the diffraction pattern formed at (e) by the intermediate lens is composed only from those electrons which originate within the selected area. The projector system then transfers this pattern to the viewing screen.

The apertures inserted in the plane at (d) can typically be as small as 20 μm. With an objective magnification of 50 times, a selected area of only 400nm (0.4 μm) in diameter can be analysed. However, these diagrams correspond to perfect thin lenses, whilst magnetic lenses are known to have large aberrations. Due to the effect of spherical aberrations, electrons scattered from areas other than the selected area can contribute to the diffraction pattern formed at (f). The significance of the contribution from these electrons depends on the angle at which the electrons pass through the objective lens (Agar, 1960). Thus the area of specimen contributing to the diffraction pattern varies for each spot and increases with

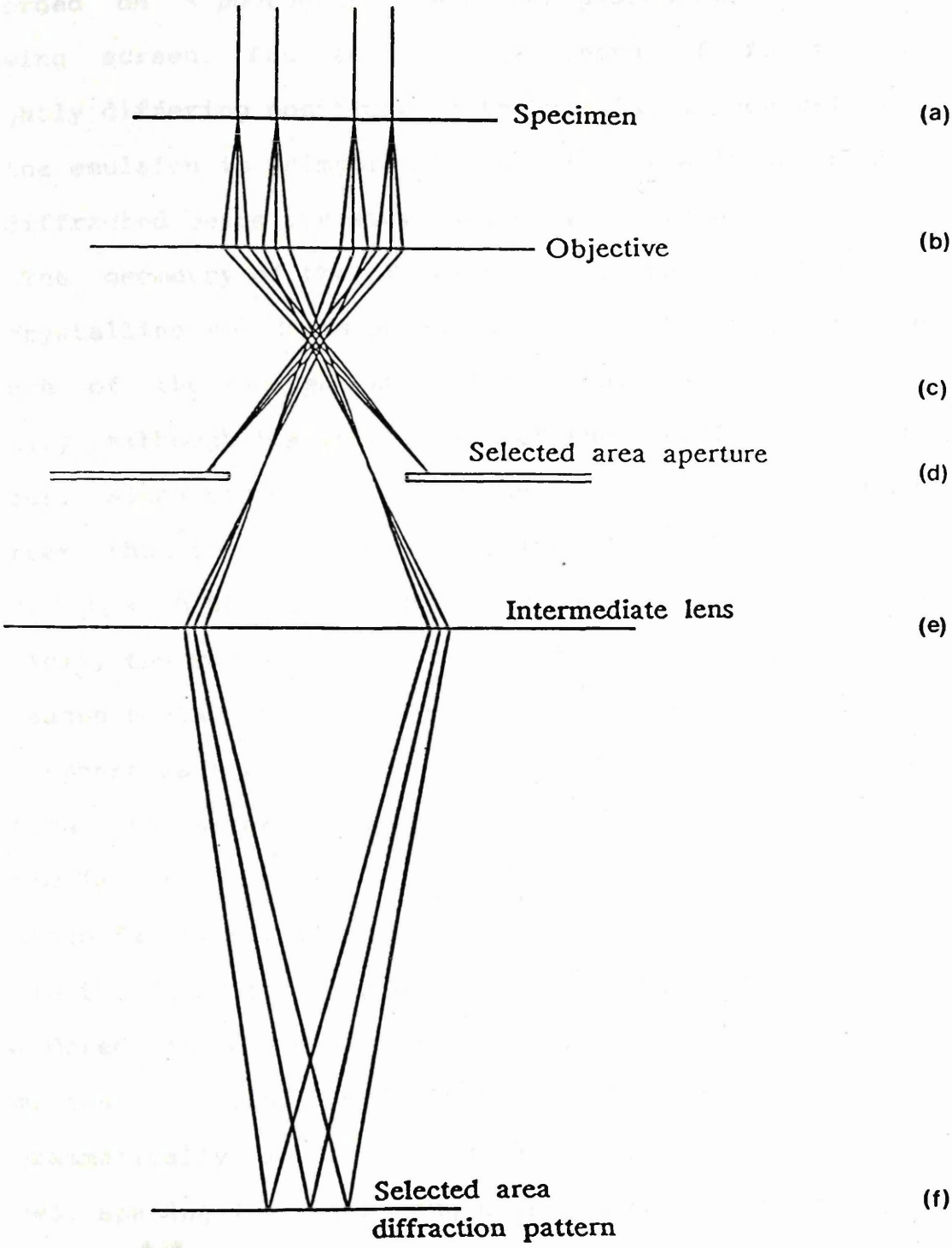

Figure 2.9: The selected-area aperture ensures that only electrons coming from a chosen region in the specimen contribute to the electron diffraction pattern.

increasing scattering angle.

The diffraction pattern produced by this technique is recorded on a photographic emulsion placed close to the viewing screen. Due to the large depth of focus, the slightly differing positions of the viewing screen relative to the emulsion is unimportant. In this way a large number of diffracted beams are simultaneously recorded.

The geometry of the diffraction (coherent scattering) by crystalline solids is essentially the same whatever the nature of the incident wave (electron, x-ray, neutron, etc...) although the intensities of the reflections will differ. Since the wavelength of an electron is very much shorter than that of x-ray radiation (for 100keV electron beam, λ = 0.0037nm whilst for x-ray of Cu, K_α line = 0.154nm), the radius of the Ewald reflection sphere ($1/\lambda$) increases to the extent that it can be assumed that part of the sphere is a plane. Accordingly, by using a reciprocal lattice (an array of points, each corresponding to a particular (hkl) plane) a diffraction pattern can be analysed fairly simply.

In the diffraction mode the electron microscope may be considered as a simple electron diffraction camera. The formation of an electron diffraction pattern (EDP) is shown diagrammatically in figure 2.10 for a set of lattice planes, spacing (d), at an angle θ to the incident beam. If R is the distance between the incident and the diffracted beam at the plane of the photographic plate and L the camera length, which is dependent upon the lens excitation:-

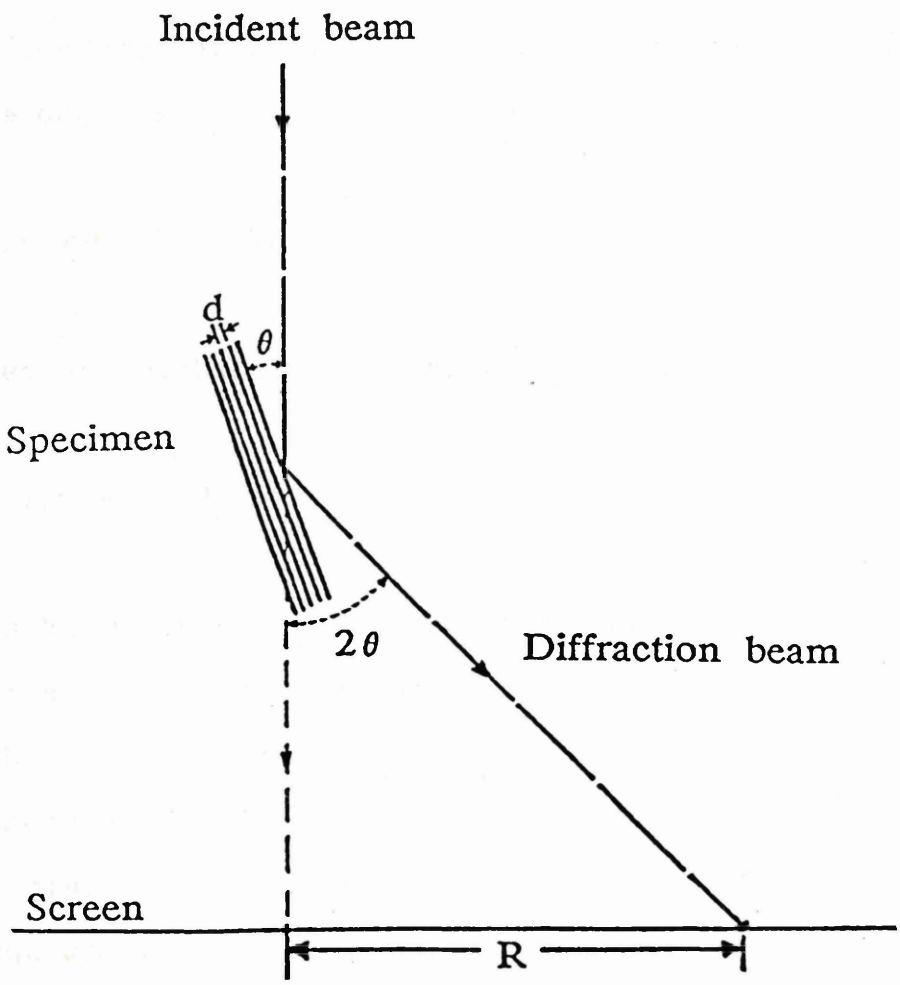

Figure 2.10: The transmission electron microscope as a simple diffraction camera.

$$R/L = \tan 2\theta \qquad (2.12)$$

the Bragg law for first order diffraction (n=1) can be applied:-

$$n\lambda = 2d \sin\theta \qquad (2.13)$$

Since θ , exaggerated in the diagram, is normally less than three degrees, the approximation:-

$$\tan 2\theta \simeq 2\sin\theta \simeq 2\theta \qquad (2.14)$$

can be used and combines 2.12 and 2.13 to give:-

$$R/L = \lambda/d \quad \text{or} \quad Rd = \lambda L = K \qquad (2.15)$$

where K is known as the camera constant and is fixed for a particular set of operating conditions. λ is the electron wavelength (λ = 0.0037nm $\ll$ d for 100KeV electrons) and L is the effective camera length, which is equivalent to the physical distance between the diffraction plane and the final image screen, given by:-

$$L = f_0 M_1 M_2 M_3 \qquad (2.16)$$

where f_0 is the focal length of the objective lens and M_1, M_2 and M_3 are the magnification factors of the intermediate and projector lenses.

In practice, the camera constant (K) is determined using a standard specimen with known diffraction spacings (e.g. graphite) studied under the same microscope conditions as the unknown. Thus:-

$$d_{unknown} = K/R_{measured} \qquad (2.17)$$

The identification of the unknown substance from an electron diffraction pattern is then accomplished by comparing electron diffraction data with the available tabulated x-ray diffraction data published by the Joint Committee on Powder Diffraction Standards (Philadelphia, USA). If many fine particles are within the area selected, the EDP obtained will be in form of Debye-Scherrer rings, somewhat similar to those observed by x-ray powder diffraction; an individual small particle will give a spot single crystal pattern. However, unlike x-ray diffraction where the crystal is rotated, the electron microscope specimen is stationary and therefore only lattice planes approximately parallel to the electron beam give reflections that can be recorded. Thus the relative intensities of the diffracted beam are often different, and in some cases forbidden reflections occur, caused by multiple scattering within the specimen. This restriction, however, can be used to determine the orientation of the specimen.

To obtain accurate electron diffraction results, the diffraction mode must be precisely set up, in particular, the specimen height and lens current should be standardised

for correlation of measurements. Within these limitations, lattice spacings can be obtained to an optimum of 1% accuracy.

Andrews et al., (1971) noted a linear variation in the camera constant with diffraction ring diameter, due to the decreasing validity of expression (2.14) for greater theta values.

The EDP contains the structural data, periodicities and orientations for the plane projected normal to the electron beam. The restriction that only lattice planes near parallel to the electron beam will contribute to the diffraction pattern allows determination of specimen orientation, since the specimen lies normal to the plane giving rise to the recorded reflections. Formulae are available which allow calculation of interplanar spacings, angles between planes, zone axes (the direction normal to the diffraction planes) and angles between zone axes for common crystal systems (Andrews et al., 1971; Beeston, 1973; Edington, 1975). Displacements and changes in intensities of specific reflections can provide information about changes within a specimen (Hirsch et al., 1965) and fading of a diffraction pattern under electron beam irradiation gives a correlation between the dimensions of fine structure in a specimen and its radiation stability (Fryer, 1979).

2.7- SCANNING ELECTRON MICROSCOPY

2.7.1- INTRODUCTION

Development of the scanning electron microscope (SEM) has been almost entirely due to the work started in Cambridge (1948) and continued there under the direction of Oatley (Oatley et al., 1965; Cosslett, 1967; Oatley, 1972). Several authors have published reviews of SEM including Cosslett (1970), Fisher et al. (1970) and Kammlott (1971).

Originally, the popularity of the instrument was due to its ability to image solid specimens in a strikingly three-dimensional manner. Now however, in addition to imaging, many other modes of operation are possible (Everhart, 1960; Wells, 1974; Heinrich, 1975; Reimer, 1976). These are illustrated diagrammatically in figure 2.2 and used in conjunction with an appropriate detection system, can provide a particular information about the properties of a specimen.

When an accelerated beam of electrons impinges on the surface of a solid, a reflection process occurs and electrons are emitted from the target. Rudberg (1936) demonstrated that emitted electrons have a range of energies from zero to that of the incident beam, this energy distribution being the basis for classifying such electrons. Electrons having emission energies from zero to fifty electron volts are termed true secondary electrons, while those above this energy are referred to as backscattered or inelastically scattered primaries.

Reflected electrons have high emission velocities and as such their path to the detector is essentially a straight line, while those of the secondary electrons can be affected by applied magnetic fields and are generally sharply curved. Consequently reflected electrons will only yield information on parts of the specimen for which there is a straight line path between them and the detector. Secondary electrons are not subject to this limitation and will provide far more detail about a rough surface. Normally the detector is set up for detection of secondary electrons and the reflected ones are ignored as far as possible.

Thus, scanning electron microscopy functions upon the electron emission ability of solids, particularly that of the secondary electrons which Everhart et al. (1959) demonstrated to be superior in comparison to reflected electrons for revealing specimen detail.

The mode of operation used in this study was the emissive mode which produces micrographs showing the topography or surface shape of the specimen.

2.7.2- PRINCIPLES OF SCANNING ELECTRON MICROSCOPY

The principle of SEM, used for examining a solid specimen in the emissive mode, is closely comparable to that of a closed-circuit TV system (figure 2.11).

In the TV camera, light from the object forms an image on a special screen; the signal from the screen depending on the image intensity at the point being scanned. This

Reflected electrons have high emission velocities and as such their path to the detector is essentially a straight line, while those of the secondary electrons can be affected by applied magnetic fields and are generally sharply curved. Consequently reflected electrons will only yield information on parts of the specimen for which there is a straight line path between them and the detector. Secondary electrons are not subject to this limitation and will provide far more detail about a rough surface. Normally the detector is set up for detection of secondary electrons and the reflected ones are ignored as far as possible.

Thus, scanning electron microscopy functions upon the electron emission ability of solids, particularly that of the secondary electrons which Everhart et al. (1959) demonstrated to be superior in comparison to reflected electrons for revealing specimen detail.

The mode of operation used in this study was the emissive mode which produces micrographs showing the topography or surface shape of the specimen.

2.7.2- PRINCIPLES OF SCANNING ELECTRON MICROSCOPY

The principle of SEM, used for examining a solid specimen in the emissive mode, is closely comparable to that of a closed-circuit TV system (figure 2.11).

In the TV camera, light from the object forms an image on a special screen; the signal from the screen depending on the image intensity at the point being scanned. This

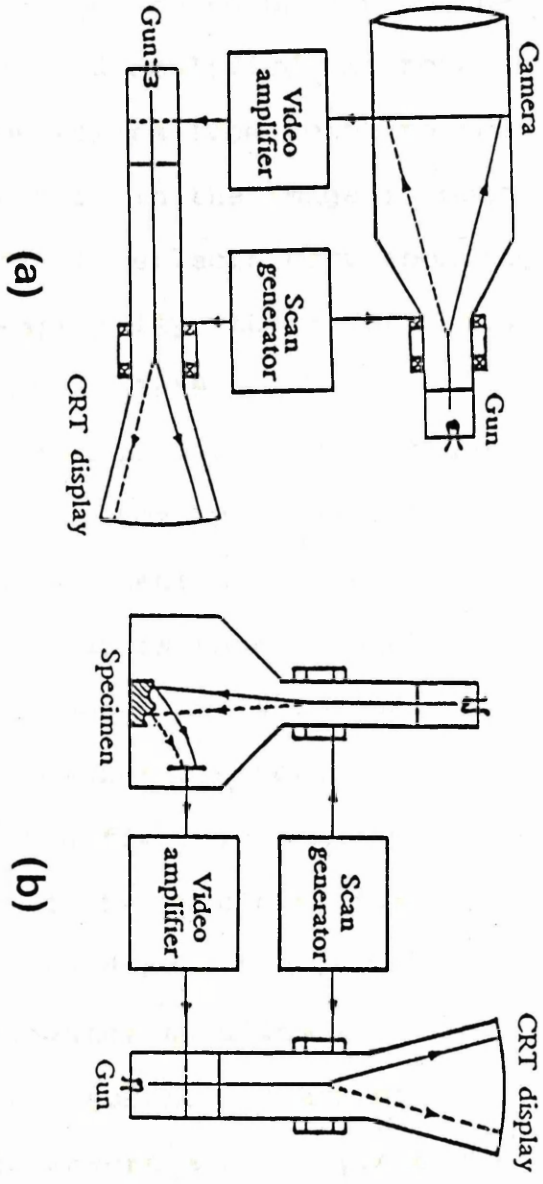

Figure 2.11: Comparison between (a) a TV closed-circuit system and (b) a scanning electron microscope.

signal is then used to modulate the brightness of a cathode-ray tube (CRT) display (van Essen, 1979).

In SEM, object "illumination" is from a very narrow incident beam, typically a few hundreds of angstrom units in diameter and is referred to as a probe. The specimen under examination is scanned with this fine beam of electrons. The electrons scattered back from the specimen surface are collected and amplified to form the video signal. As the emission varies from point to point on the specimen surface so contrast in the image is obtained; this variation in image contrast reflects corresponding features about the object, especially those of its surface topography (Everhart et al., 1959).

The principle of SEM is outlined in figure 2.12. A beam of electrons, accelerated by potentials up to 50KeV, is generated from a triode electron gun (usually a tungsten filament). The electron beam is then brought to a focus on the surface of the specimen i.e. is focused into a minute probe, by a series of magnetic electron lenses. Scanning coils situated before the final lens allow the beam to be moved over the surface of the specimen, just as the spot on a television tube is scanned over the screen. The coils are also fitted with a stigmator to allow the correction of astigmatism. The specimen surface is arranged at an angle to the beam axis, to ensure a high yield of scattered electrons are collected by the detector. The detector consists of a scintillator, to which a bias voltage may be applied, connected by a light pipe to a photomultiplier and a video amplifier. The output from the latter is used to

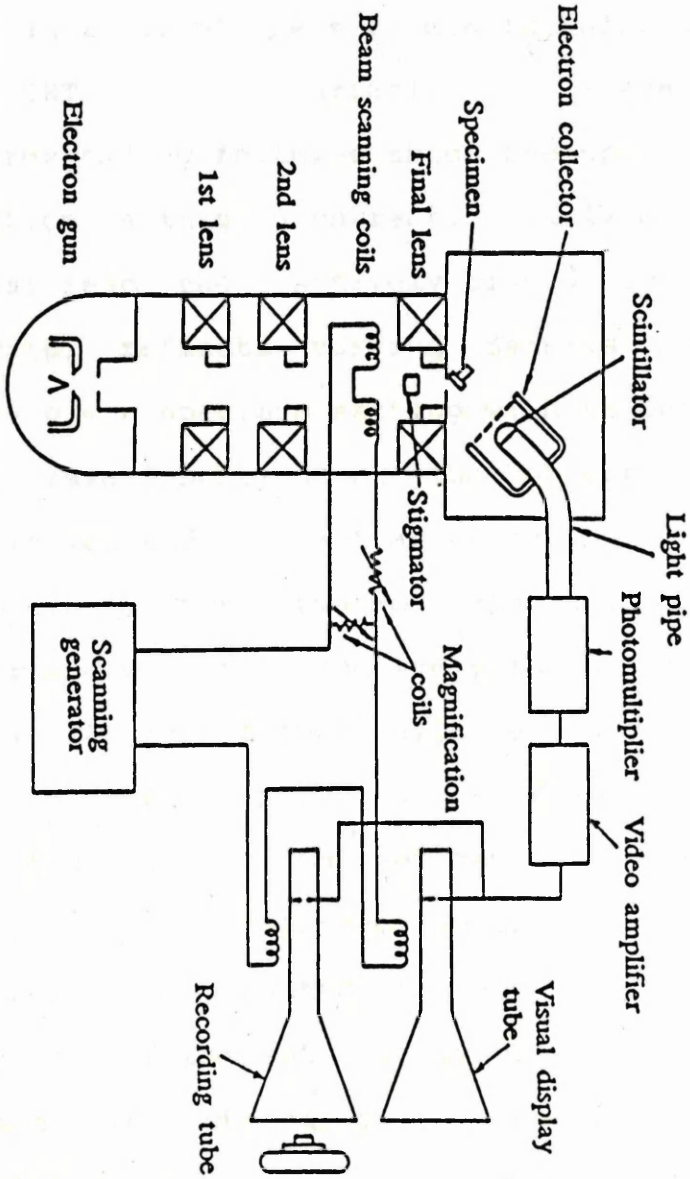

Figure 2.12: Schematic diagram of the scanning electron microscope.

control the modulating electrode of a CRT and thus the brightness of the spot on the face of the tube. The CRT is scanned synchronously with the scan of the probe on the specimen, the brightness of the CRT spot varying in sympathy with the electron output from the specimen surface, thus an image of the specimen is built up on the face of the CRT with the variation in image contrast reflecting corresponding features about the specimen.

This variation in imaging current, usually of secondary electrons, that reach the positively biased scintillation detection device, reflects varying details about the object. For any given specimen setting with respect to the primary beam, raised portions of the object experience greater irradiation and will act as an enhanced source of secondary electrons. Thus elevations and depressions will appear brighter and darker respectively in the final image.

For visual display a tube with a long-persistence screen must be used, operating at frame repetition frequency of the order of one per second owing to the weakness of the signal. The electron optical column and specimen chamber are evacuated to a high vacuum of less than 10^{-4}mbar by independent systems of rotary and oil diffusion pumps. For photographic recording, a short-persistence high-definition tube is used, the exposure being made in the form of a single frame scan over a time of 1 to 10 minutes. The magnification obtained is given by the ratio of the width of scan on the tube to the width of scan on the specimen, and is conveniently controlled by varying the latter, as indicated in figure 2.12. The

resolving power of the instrument (Simon, 1970) is governed by a number of factors: the shot noise in the electron image, the current density which can be focussed into the probe, the properties of the electron gun, the aberrations of the electron lenses and the properties of the collector system. Pease and Nixon (1965) reported a best resolution of 15nm +/- 3nm and an average resolution value of 20-30nm. Modern day instruments however, have an average resolution of around 5nm with 2nm attainable.

2.7.3- IMAGE FORMATION AND CONTRAST

The mechanism of contrast formation in the image is complicated depending on the physical and electrical conditions over the specimen surface. It also depends on whether the detector receives only the true secondary electrons (of low energy) or the reflected primary electrons (of high energy), or both (Pease, 1971; Everhart & Hayes, 1972). Normally the secondary electrons are much more numerous and convey more information, however, the reflected electrons give greater contrast.

Three factors chiefly determine the image contrast, their relative influence depending on the nature of the specimen under examination:-

1. Surface topography: Variation in the angle presented by the specimen surface to the incident beam profoundly affects the fraction of the electrons, primary and secondary, that are collected.

2. Chemical constitution: The yield of secondary electrons depends on the secondary emission coefficient, which, for most materials, differs very little from unity and thus only rarely contributes appreciably to contrast. On the other hand, the yield of reflected electrons depends on the atomic number of the element encountered. Thus contrast differences will be observable whenever the specimen surface contains elements of widely differing atomic number.

3. Potential variations: Since the secondary electrons leave the specimen with very low energies, their trajectories are strongly influenced by the potential on the surface, thus, the proportion reaching the detector will vary.

In the SEM used in this study, a Philips SEM 500, two magnetic lenses, condenser and scanning, were used which can produce an electron probe with a minimum diameter of about 1nm. This microscope was operated at an accelerating voltage of 3-6keV and a specimen tilt angle of 10°.

CHAPTER THREE

EXPERIMENTAL

3.1- MATERIALS

3.1.1- AROMATIC HYDROCARBONS

Most of the aromatic hydrocarbons were obtained from commercial sources in the form of powders and used without further purification. Table 3.1 and table 3.2 shows the aromatic hydrocarbons used.

3.1.2- GASES

Industrial, high purity, Argon and Nitrogen gases, supplied by B.O.C. Ltd, were used as the carrier gases. The purity of both gases was >99.998%.

3.1.3- REAGENTS

Potassium carbonate is the alkali usually deposited in blast furnace cokes (Goleczka et al., 1982(b)), thus BDH anhydrous potassium carbonate (analar grade) was used as the source of potassium when reacted in the furnace. This source has previously been shown (Shevlin, 1986, 1987) to produce successful replication of the extuyere microstructural forms when reacted with feed cokes in laboratory experiments.

3.2- SAMPLE PREPARATION

The aromatic hydrocarbons were carbonised, in an inert atmosphere, at selected temperatures under varying conditions. Two carbonisation systems were employed:-

COMPOUND	STRUCTURE	REFERENCES
Anthracene (b)	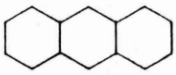	(i) (ii) (iii) (vii) (viii) (x) (xi)
Chrysene (a)	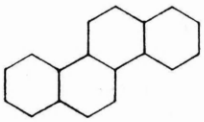	(ii) (iii)
Fluoranthene (b)	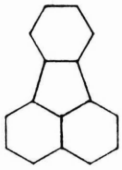	(ii) (iv) (v) (vi) (viii)
Phenanthrene (b)	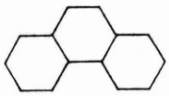	(ii) (iii) (vii) (viii) (ix)
Pyrene (a)	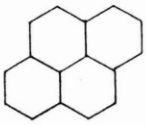	(ii) (iii)
p-Terphenyl (a)		(iv) (v) (vi) (viii)

(a) non-graphitising carbon
(b) graphitising carbon

(i) Oberlin, 1984
(ii) Lewis & Edstrom 1961
(iii) Sharkey et al. 1966
(iv) Edstrom and Lewis, 1969
(v) Lewis, 1982
(vi) Buseck et al., 1987
(vii) Kinney et al., 1957
(viii) Fitzer et al., 1971
(ix) Evans and Marsh, 1971
(x) Oberlin et al., 1975(b)
(xi) Lewis, 1980

Table 3.1 Structural formula of the aromatic hydrocarbons carbonised via a closed carbonisation system and exposed to potassium vapour.

COMPOUND	STRUCTURE	REFERENCES
Acenaphthylene (b)	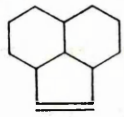	(iii) (iv) (ix) (viii) (v) (x)
Decacylene (b)		(i) (ii) (iii) (v)
Dibenzanthrone (b)	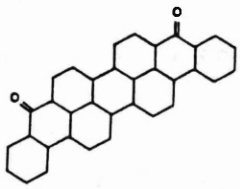	(i) (ii) (iii)
Polyvinyl acetate (b) (PVA)	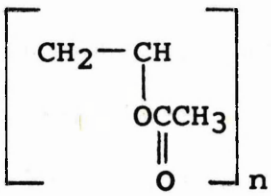	(vi) (vii)
Sucrose (a)	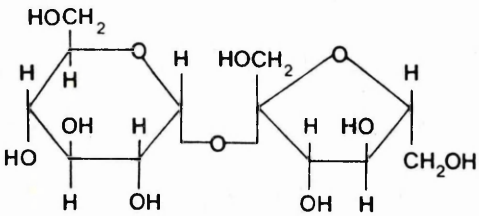	

(a) non-graphitising carbon
(b) graphitising carbon

(i) Marsh and Wynne-Jones, 1964
(ii) Kipling et al., 1964
(iii) Edstrom and Lewis, 1969
(iv) Lewis & Edstrom, 1961
(v) Fitzer et al., 1971
(vi) Gilbert et al., 1962
(vii) Grassie, 1952
(viii) Buseck et al., 1987
(ix) Ruland, 1965(b)
(x) Lewis, 1982

Table 3.2 Structural formula of the aromatic hydrocarbons carbonised via an open carbonisation system and exposed to potassium vapour.

1. An open system where the samples to be carbonised were prepared under atmospheric pressure (section 3.2.1).

2. A closed system where the samples to be carbonised were charred under their own vapour pressure (section 3.2.2).

The carbonised samples were then characterised before being exposed to potassium and further analysis.

3.2.1- CARBONISATION OF THE AROMATIC HYDROCARBONS (OPEN SYSTEM)

A tubular furnace with a silica glass reaction vessel was used in the carbonisation of the aromatic hydrocarbons. Although two makes of tubular furnace were employed, a Baird and Tatlock (London, U.K.) M193 and a Carbolite (Sheffield, U.K.) CTF 12/65, the same handling procedure was used in both furnace operations.

The experimental set-up was as shown in figure 3.1. A straight silica glass tube (720mm x 25mm and 1085mm x 85mm for the two furnaces above respectively) open at both ends was used as an outer sleeve reaction vessel. A second silica glass tube (220mm x 20mm and 850mm x 75mm for the two furnaces above respectively) acted as an inner sleeve. Into this inner sleeve, were placed silica boats (50mm x 10mm and 100mm x 15mm for the two furnaces above respectively), containing the aromatic hydrocarbon to be carbonised. Each end of the silica glass outer tube was then sealed so as to allow the introduction of an inert carrier gas at one end and the exit from the system of any by-products, picked up by the stream of inert gas, at the

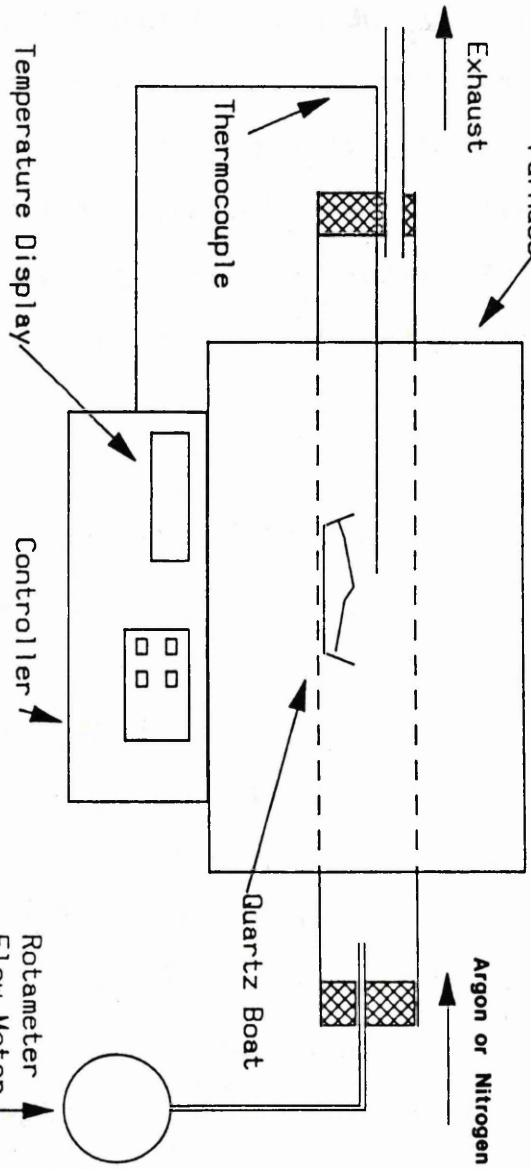

Figure 3.1: Carbolite Tube furnace.

other. The inert carrier gases were introduced and removed from the furnace by rubber tubing.

The furnace temperature was raised by the desired increment (1°C, 3°C or 10°C/min) until the carbonisation temperature (800°C or 1100°C) was attained. This temperature was maintained for the duration of the soak period (2hrs or 15hrs) before cooling. The temperature was registered by the furnace thermocouple (Chromel/Alumel and Platinum/Platinum 13% Rhodium for the two furnaces above respectively) corresponding to the centre of the furnace hot zone, the point at which the boat containing the aromatic hydrocarbon had been placed.

3.2.2- CARBONISATION OF THE AROMATIC HYDROCARBONS (CLOSED SYSTEM)

These unreactive polynuclear aromatic hydrocarbons could only be prepared by first charring the organic materials under their own vapour pressure (Lewis and Edstrom, 1961) as such materials simply melt and distill away leaving no carbonaceous residue in an open system.

The samples first had to be charred in a steel bomb or similar equipment prior to attaining the carbonisation temperature. A sample of the material to be charred was sealed inside a steel bomb previously flushed with either argon or nitrogen to displace the air. The steel bomb was then placed in a furnace and the sample calcined at 3°C/min until a temperature of 550°C was reached. A two hour soak period at this temperature then followed, before allowing the sample to cool. The charred sample was removed from the

steel bomb and heated in a stream of nitrogen at a heating rate of 3°C and 20°C/min to a carbonisation temperature of 800°C with a two hour soak period prior to cooling.

This method of preparation was exceedingly time consuming and required the use of specialised equipment. For this reason these samples were prepared by British Coal.

3.2.3- EXPOSURE OF THE CARBONISED AROMATIC HYDROCARBON TO POTASSIUM VAPOUR

The experimental set-up for the exposure of carbonised samples to potassium vapour was the same as that in the open carbonisation system (figure 3.1). However, two silica boats were inserted into the silica tube for each potassium exposure reaction. The first boat (boat 1) contained the carbonised aromatic hydrocarbon which was to be exposed to potassium vapour. The second boat (boat 2) contained a quantity of the same carbonised hydrocarbon as was in boat 1, intimately mixed with anhydrous potassium carbonate. The stream of inert gas introduced into the tube, carried the potassium vapour generated from the carbonised hydrocarbon/potassium carbonate mixture (boat 2) over boat 1. The reaction between the potassium vapour and the carbonised hydrocarbon contained in boat 1, was continued until all the potassium vapour generated had passed over boat 1. This was assumed when no further purple vapour was observed. This purple vapour, observed at the exit end of the outer silica tube, has been shown previously (Shevlin, 1987), using Energy Dispersive X-ray Analysis (EDXRA), to

be potassium, and has thus passed over boat 1 during the reaction period. The amount of potassium carbonate and carbonised hydrocarbon used, usually maintained a flow of potassium vapour for a period of around two hours, this being deemed sufficient time for any reaction between the potassium vapour and the carbonised hydrocarbon (boat 1) to have occurred.

The temperature of boat 2, containing the carbonised aromatic hydrocarbon/potassium carbonate mixture, was slowly raised (1°C/min) until a temperature of around 1000°C was attained. Again, this temperature was registered by the furnace thermocouple corresponding to the centre of the furnace hot zone. The temperature of boat 1 was monitored by means of an external thermocouple, introduced to the furnace at a position corresponding to that of boat 1. The temperature of boat 1, containing only carbonised hydrocarbon, was normally found to be around 750-850°C. In all cases the furnace temperature was maintained at the soak temperature until no further generation of potassium vapour was observed. This ensured that any reaction occurring between the potassium vapour and the carbonised hydrocarbon had occurred at the maximum temperature attained by boat 1 and not during the furnace cooling period. This system has previously been found to successfully replicate microstructural changes induced by a blast furnace environment (Shevlin, 1987). The materials resulting from this experiment were thus considered to be representative of the structural effects that would be observed during passage through a blast furnace.

3.3- STRUCTURAL CHANGES EFFECTED BY HEATING

3.3.1- HIGH TEMPERATURE TREATMENT

In order to separate the effects of alkali attack from thermal effects, carbonised samples were heated in the absence of alkali. This was carried out in the same experimental set-up as for the open system carbonisation of aromatic hydrocarbons (section 3.2.1) in which the sample was heated in an inert atmosphere. The heating rates were the same as those used during carbonisation (1°C, 3°C and 10°C/min). Once the desired temperature (1100°C) was attained this temperature was maintained for various soak periods (2hrs and 15hrs). The samples were subsequently allowed to cool while maintaining the inert atmosphere of argon.

3.3.2- REACTION OF SAMPLES AT BELOW CARBONISATION TEMPERATURE

Again, in order to separate thermal effects from chemical effects carbonised samples were reacted with potassium vapour at below their carbonisation temperatures. This ensured that any observed structural changes would be due only to chemical effects, as the samples had previously been exposed to higher temperatures during the carbonisation soak periods and thus would not be affected by reheating to a lower temperature.

The method employed for these experiments was identical to that used to expose the carbonised samples to potassium vapour (Section 3.2.3). However, in this set of experiments

the carbonised material/potassium carbonate mixtures (boat 2) were reacted at around 850°C, for a longer period (around four hours). The reaction was continued until all the potassium vapour generated had passed over the carbonised material in boat 1. Thus any reaction occurring between the carbonised sample and potassium vapour had occurred at the observed temperature and not during the furnace cooling period. The temperature of boat 1, which contained only carbonised sample was found to be around 600-650°C in all cases. The samples were then allowed to cool, while maintaining the flow of inert gas.

3.4- EFFECT OF INERT CARRIER GASES

Preparation of carbonised samples and their reaction with potassium vapour were repeated many times in order to obtain relevant data and reproducible results, as it has been found that the nature of potassium reactions with carbons can be quite varied (Marsh et al., 1987). During the repetition of these experiments the reaction design was maintained although in some cases the inert carrier gas used was altered. This was in order to examine any possible effects due to the carrier gas, although in all cases the gases used were inert and it was thought unlikely that the gases would affect the results obtained.

3.5- ELECTRON MICROSCOPY SPECIMEN PREPARATION

Most materials are initially in an unsuitable form for TEM examination and a number of standard procedures have

been developed by which specimens may be prepared for electron microscopy examination (Keown, 1974).

3.5.1- SPECIMEN PREPARATION FOR TEM

In the course of this study, two techniques were used, namely, ultrasonic dispersion and dry dusting. This section is concerned with the description of these two techniques.

1. Ultrasonic Dispersion

An agate mortar and pestle were used to crush the solid powder before being transferred to a micro test tube containing water and placed in an ultrasonic bath. A slurry of the solid/water mixture was then withdrawn from the test tube using a finely drawn Pasteur pipette and a drop placed on a standard 3mm copper grid which had previously been coated with a film of carbon. The grids were then allowed to dry at around 30°C, in a laboratory oven, before transfer to the microscope.

The carbonised samples reacted with potassium could not be prepared in the above manner due to the possibility of formation of intercalated material and the reactive nature of these species which readily degrade when in contact with air or water. These samples were prepared for TEM analysis by dry dusting.

2. Dry Dusting

The carbonised powder was finely crushed using an agate mortar and pestle prior to the reaction with potassium. After the reaction, the powdered sample could simply be dusted onto standard 3mm copper grids. Care had to be taken

however, due to the reactive nature of potassium intercalated species, to avoid contact with air or water. Thus once exposed to potassium, the samples were kept in an inert atmosphere of argon in a glove box, prior to examination in the microscope.

The samples were examined on a JEOL 1200EX microscope operated at an accelerating voltage of 120KeV. This microscope was also fitted with an image intensifier system and frame storage facility to aid in viewing specimens. The final images were recorded on photographic film (Ilford EM film).

3.5.2- PREPARATION OF THIN CARBON FILMS

The thin carbon support film for the TEM copper grids was prepared by the Bradley process (Bradley, 1954) which is schematised in figure 3.2(a). Spectroscopically purified graphite was evaporated on to a cleaved mica substrate using the high vacuum evaporating system schematised in figure 3.2(b). The films were subsequently floated off the mica onto distilled water and hence onto the copper specimen grids. This was achieved by draining off the distilled water and letting the thin carbon film settle onto the grids which had been placed in the bottom of a flotation tank.

3.5.3- SPECIMEN PREPARATION FOR SEM

The morphological features of the parent sample and the sample obtained from its exposure to potassium vapour were

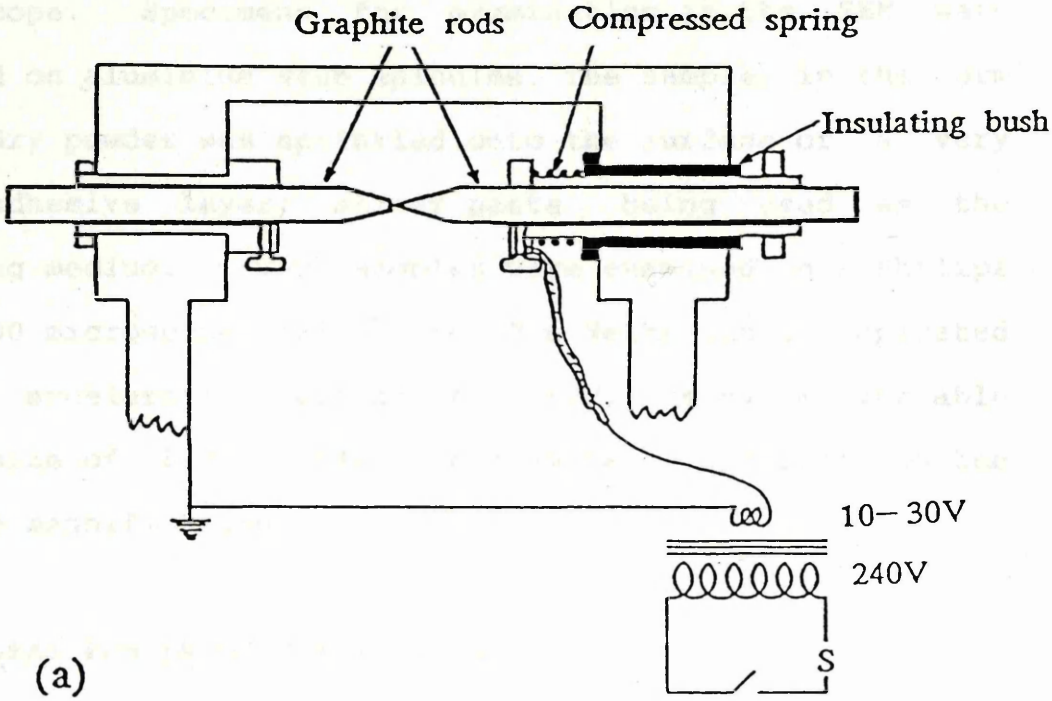

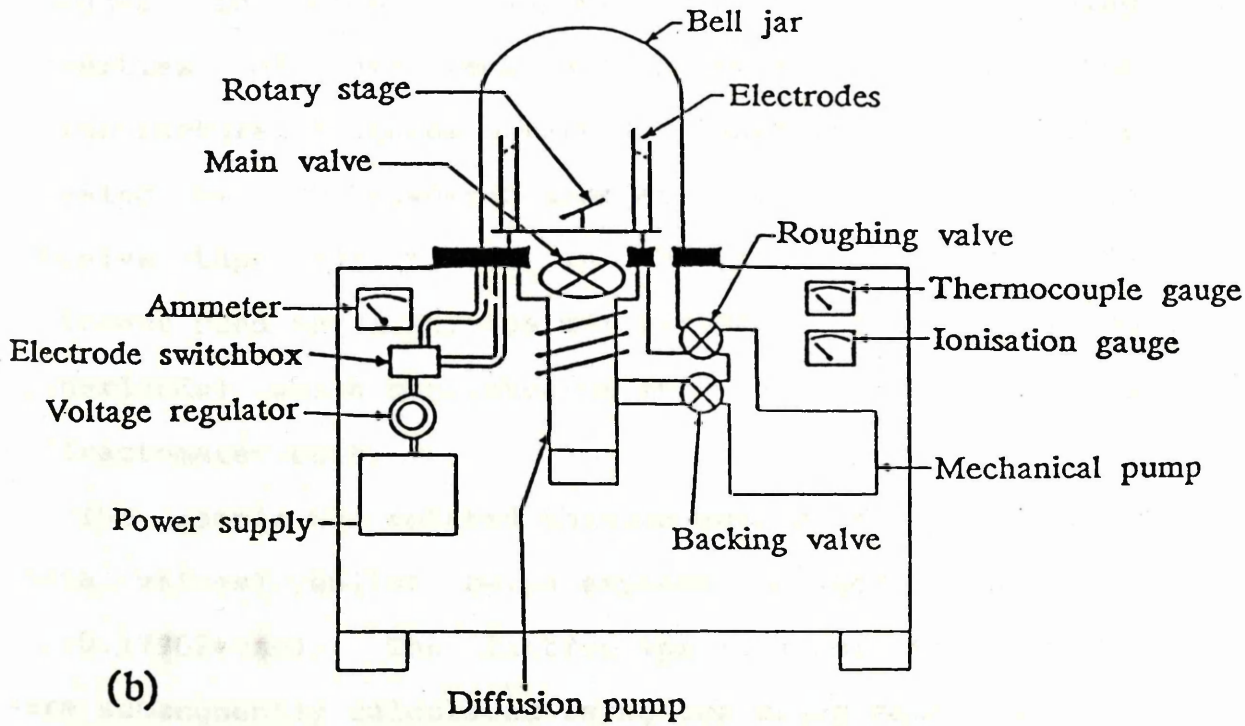

Figure 3.2: (a) Practical source of evaporation of carbon by the Bradley process and (b) a standard vacuum evaporator.

investigated by the examination in the scanning electron microscope. Specimens for examination in the SEM were mounted on aluminium stub spindles. The sample, in the form of a dry powder was sprinkled onto the surface of a very thin adhesive layer; silver paste being used as the mounting medium. The samples were examined on a Philips SEM 500 microscope (Eindhoven, The Netherlands) operated at an accelerating voltage of 3-6keV, using a variable spot size of 0.25 μm-64nm in diameter, depending on the working magnification.

3.6- X-RAY POWDER DIFFRACTION (XRD)

XRD studies were employed to complement the HREM analysis of the carbonised materials, both before and after exposure to potassium vapour. Due to the averaging properties of this technique however, many of the microstructural features observed by HREM were not directly revealed by XRD. Powdered samples were mounted flat on adhesive tape and placed in the XRD equipment. The equipment used was a Philips diffractometer (Eindhoven, The Netherlands) which consisted of an x-ray generator and a diffractometer unit.

The sample was rotated through angles of 4-60° (two theta values) whilst being exposed to CoK_{α} radiation (λ=0.1790260nm). The lattice spacings for the samples were subsequently calculated using the Bragg equation:-

$$\lambda = 2d \sin\theta$$

3.7- THERMOGRAVIMETRIC ANALYSIS (TGA)

Thermogravimetric analysis measures quantitative weight loss as a function of temperature. Powdered samples of the carbonised hydrocarbons, were analysed by thermogravimetric methods, both before and after exposure to potassium vapour, to observe the effects chemical treatment afforded some of the samples.

The instrument employed for these studies was a Du Pont (Wilmington, USA) 990 analyser combined with a Du Pont 951 thermogravimetric unit. The powdered samples were suspended in platinum boats and heated in a stream of air (flow rate 50ml/min). The samples were analysed in the temperature range 0-1200°C, using a heating rate of 20°C/min. The temperature was measured using a Chromel/Alumel thermocouple suspended about three millimetres above the sample, in order to obtain an accurate temperature measurement. The resulting weight loss was measured by the thermobalance and plotted as a percentage weight loss against temperature.

As far as possible, the samples for analysis were prepared by the same procedure. This was important in order to minimise problems arising from differences in sample weight, particle size and packing, which all combine to change the nature of the thermogravimetric curve.

3.8- FLAME PHOTOMETRY AND POTASSIUM UPTAKE MEASUREMENTS

An accurately weighed amount of each carbon that had been exposed to potassium vapour was placed in a glass

test-tube with 5ml 18.3M H_2SO_4 and 5ml 15.6M HNO_3. The open end of the tube was sealed prior to heating in a sand tray. The sand tray was heated to a temperature of around 180°C for a period of three hours. After a period of cooling the contents of the tube were centrifuged for 20 minutes at 2940 r.p.m. (Relative Centrifugal Field, RCF, 1280xg). The supernatant was then removed, filtered and retained for analysis. The sedimentation at the bottom of the tube was resuspended in 5ml 18.3M H_2SO_4 and 5ml 15.6M HNO_3, and the heating and spinning process repeated several times. In each case the supernatant was retained for analysis. The potassium present in these supernatant samples was then taken to indicate the amount of potassium 'taken up' by the carbons. Blank samples were prepared, as a standard background count for potassium concentration, by repeating the whole procedure, identical in all respects, except one had no sample present, as an acid blank, and the rest with the carbonised samples before exposure to potassium vapour. Thus any potassium that was being picked up from any other source would be included in the standard background count.

All the collected samples were analysed for potassium content using a standard (Evans Electroselenium Ltd.) flame photometer. Standard curves for potassium concentration were plotted using atomic absorption standard potassium nitrate solutions.

Potassium uptake measurements were also performed, although only on the PVA(800) and SUC(800) samples, (table 4.1), and three different feed coke samples. Each sample was exposed to potassium according to the following method.

In the silica reaction flask separate tantalum weighing pans, containing approximately 100 - 200mg of potassium metal and 100mg of the sample under examination, were heated in a slow flow of nitrogen ($50cm^3/min$). A heating rate of $10^oC/min$ was used to reach the desired temperature of 400^oC. This temperature was then maintained until the increase in weight recorded by the sample was constant.

This reaction method was then discontinued due to operational problems.

CHAPTER FOUR

RESULTS FOR THE FEED AND EXTUYERE COKE AND THE CARBONISED SUCROSE AND PVA

4.1- INTRODUCTION

The overall aim of this study was to characterize any microstructural changes occurring in different carbonised materials as a result of exposure to potassium vapour. An examination of the relative uptake of potassium in each of the carbonised materials would determine which, if any of the carbonised materials could be added to the blast furnace coke to preferentially absorb or be attacked by the potassium, with the purpose of reducing or eliminating the detrimental changes that occur in blast furnace metallurgical coke structure due to recirculating alkali.

Preliminary studies were performed on a selection of feed and extuyere cokes to determine the reproducibility of the microstructures previously observed for metallurgical coke samples (Shevlin et al., 1986) and to assess the extent of microstructural change. This change was then used as a reference to which the carbonised materials could be compared.

Graphitisation of polyvinyl acetate and sucrose at 3000° is known to result in the formation of a graphitisable and non-graphitisable carbon respectively. These materials were used to represent the two extremes of graphitisability and to determine the type of carbonised matrix microstructure, prepared at a carbonisation temperature of 800°C, with the greater susceptibility to potassium attack. Subsequently, a selection of known graphitisable and non-graphitisable carbons were carbonised at different heating rates and carbonisation temperatures,

with varying soak periods at the carbonisation temperature.

All these carbonised materials were examined both before and after exposure to potassium vapour to determine the nature of the material prior to exposure and any differences that occurred as a result of exposure.

This chapter reports on the results obtained for three feed and extuyere cokes and the 800°C carbonised sucrose and polyvinyl acetate, both before and after exposure to potassium vapour. Each sample was studied using the techniques of TEM, SEM, XRD and TGA, and the results are tabulated (table 4.5) at the end of the chapter.

4.2- ANALYSIS OF METALLURGICAL COKE SAMPLES (FEED AND EXTUYERE COKES)

The unreacted cokes (feed coke) and cokes that have encountered the blast furnace environment (extuyere coke) were prepared and supplied by British Coal (table 4.2).

4.2.1- TRANSMISSION ELECTRON MICROSCOPY (TEM)

The feed coke samples examined exhibited a typical non-graphitised carbon structure (L_a=1-5.5nm) with lattice spacings in the range 0.34-0.37nm (L_c=0.68-3nm) (figure 4.1). A small proportion of the non-graphitised carbon structure also exhibited lattice spacings with values in the range 0.42-0.48nm (L_c=0.42-3nm). Also present in the samples were areas of highly ordered crystalline material (L_a=10-130nm) with lattice spacings ranging from 0.33-0.70nm (L_c=5-56nm) (figure 4.2). This material which

Figure 4.1: HREM of the feed coke sample revealing the non-graphitised carbon structure (0.34-0.37nm).

Figure 4.2: HREM of the feed coke sample displaying the highly ordered mineral matter and the non-graphitised carbon structure.

appeared to be randomly distributed throughout the feed (and extuyere) coke samples was assumed to be mineral matter (Shevlin et al., 1986), inherent in metallurgical cokes, arising from the parent coal.

The extuyere samples showed three additional distinct types of microstructure; the non-graphitised carbon structure (L_a=1-5nm) with lattice spacings in the range 0.34-0.37nm (L_c=0.68-3.5) was still apparent; a greater majority of the lattice spacings had become enlarged to between 0.42-0.48nm (L_c=0.84-3.5nm) (figure 4.3); the samples also contained areas of extensively ordered long-range structure (L_a=15-95nm) exhibiting lattice spacings of 0.35nm (L_c=2.8-35nm) (figure 4.4).

4.2.2- POWDER X-RAY DIFFRACTION ANALYSIS (XRD)

The feed coke trace (figure 4.5) exhibited a double peak within an overall interplanar spacings range (36.0-14.8^{o}) 0.289-0.695nm. The most intense peak was centered at (30.2^{o}) 0.344nm with the second broader region peaking at (21.6^{o}) 0.478nm. The height of the peaks relative to each other gave some indication of the relative proportions of the lattice spacings present.

The extuyere trace revealed that a double peak still remained (figure 4.6) and that the interplanar spacing range remained constant at (36.0-14.8^{o}) 0.289-0.695nm. However, a sharpening of the peak centered on (30.4^{o}) 0.341nm and a reduction of the broad (21.4^{o}) 0.482nm peak height had occurred.

Figure 4.3: HREM of the extuyere coke sample exhibiting the expanded carbon structure (0.42-0.48nm).

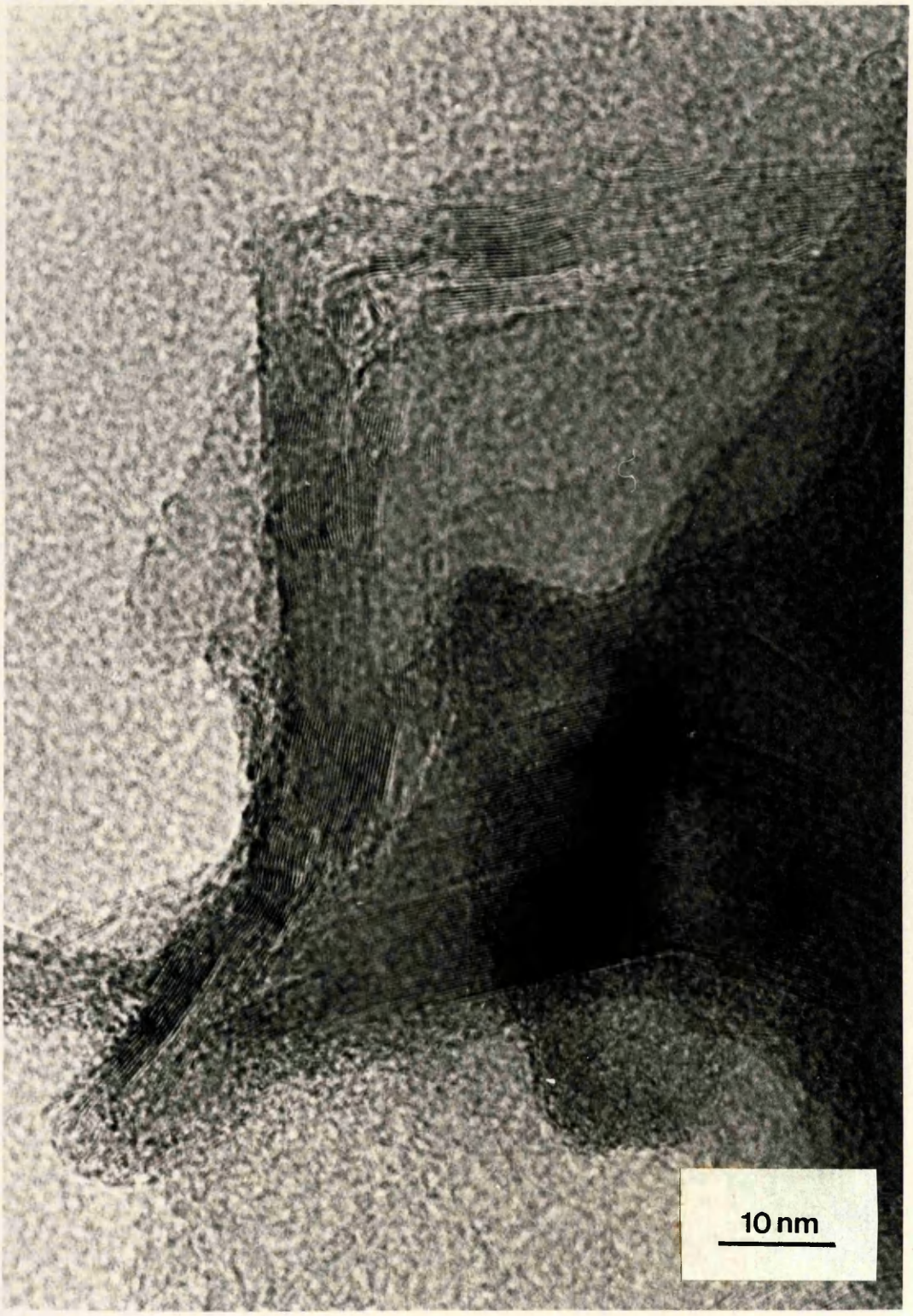

Figure 4.4: HREM of the extuyere coke sample showing the extensively ordered carbon structure (0.35nm).

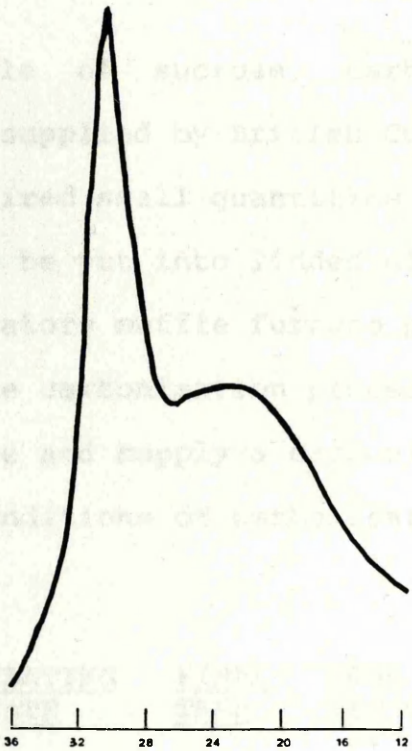

Figure 4.5: XRD trace of the feed coke sample.

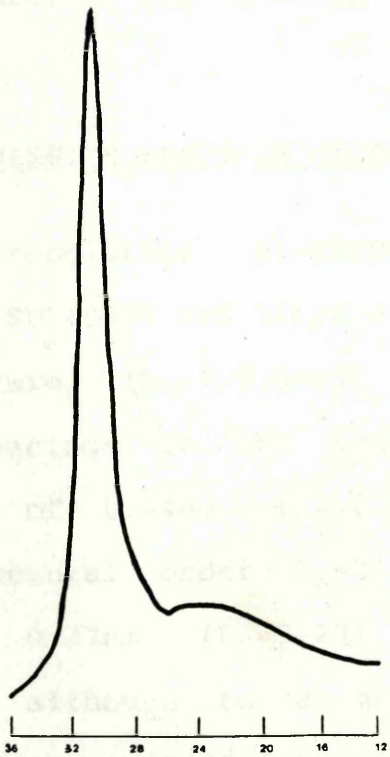

Figure 4.6: XRD trace of the extuyere coke sample.

4.3- ANALYSIS OF CARBONISED SUCROSE- SUC(800)

This sample of sucrose, carbonised at 800°C was prepared and supplied by British Coal. The carbonisation procedure required small quantities of the material, in its raw state, to be put into lidded nickel dishes and packed into a laboratory muffle furnace programmed to heat to 800°C. The same carbonisation procedure was used by British Coal to prepare and supply a carbonised PVA sample (section 4.5). The conditions of carbonisation are detailed in (table 4.1).

COMPOUND	HEATING RATE	FINAL TEMP	SOAK PERIOD	ATM	CODE
Sucrose	3°C/min	800°C	2hr	N_2	SUC(800)
PVA	3°C/min	800°C	2hr	N_2	PVA(800)

Table 4.1 Conditions of sucrose and polyvinyl acetate carbonisation.

4.3.1- TRANSMISSION ELECTRON MICROSCOPY (TEM)

A high resolution electron microscopy (HREM) examination of SUC(800) exhibited a typical non-graphitised carbon structure (L_a=1-8.5nm), (figure 4.7), with interplanar spacings in the range 0.41-0.54nm and a typical value of 0.44nm (L_c=0.82-1.8nm). Areas with extensive structural order (L_a=20-90nm) and interplanar spacings of 0.37nm (L_c=3-27) were also observed (figure 4.8), although to a much lesser extent. The presence of these areas of extensive structural order was surprising, in view of the non-graphitising nature of

Figure 4.7: HREM of the SUC(800) sample revealing the non-graphitised carbon structure (0.44nm).

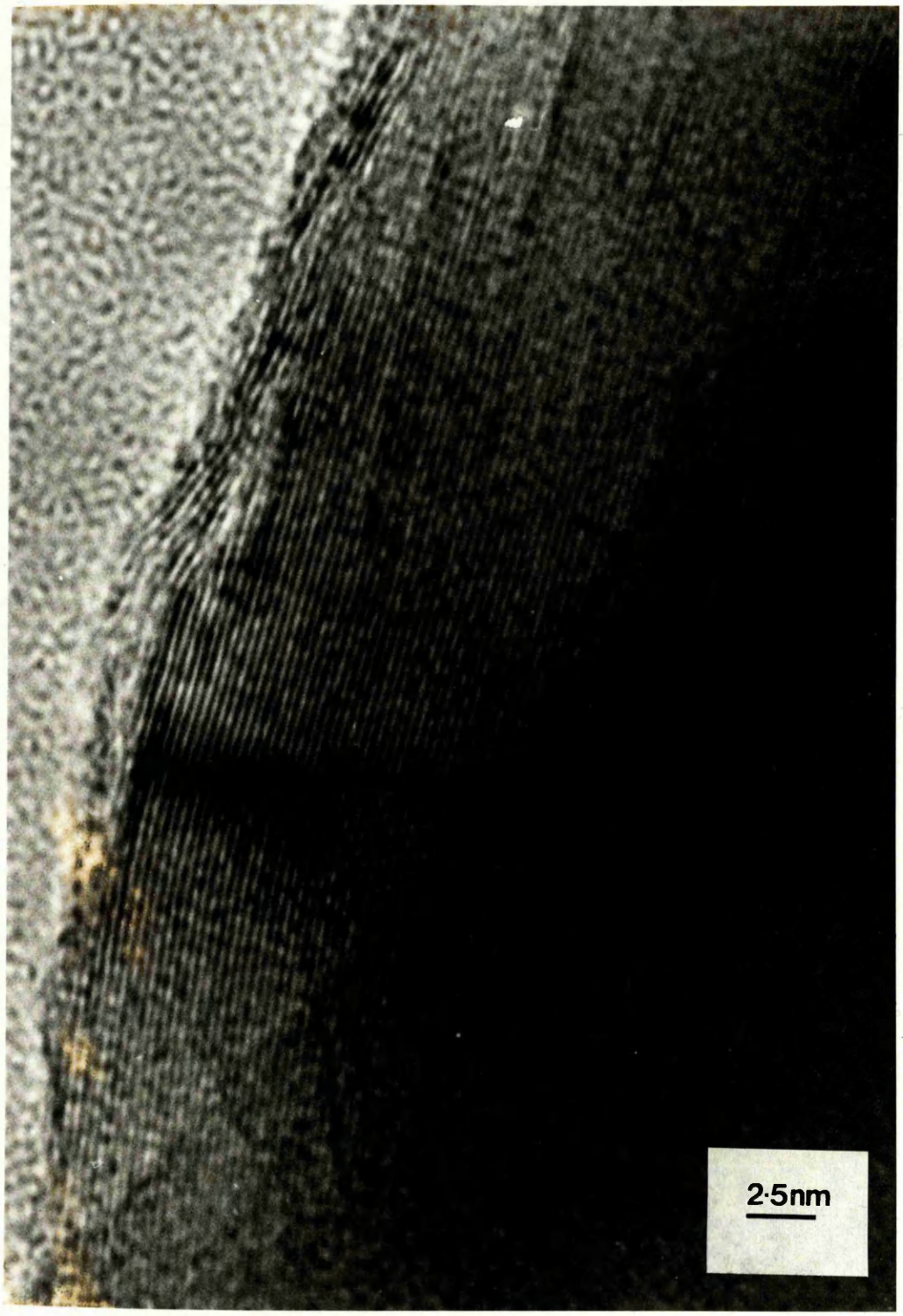

Figure 4.8: HREM of the SUC(800) sample showing areas of extensive structural order (0.37nm).

sucrose, and a low temperature 'carbonisation' study of the sucrose was performed (section 4.9).

4.3.2- SCANNING ELECTRON MICROSCOPY (SEM)

Examination of the SUC(800) sample by SEM revealed a smooth external surface with no detectable surface cracks or pores (figure 4.9).

4.3.3- POWDER X-RAY DIFFRACTION ANALYSIS (XRD)

Examination of the x-ray diffraction trace for the SUC(800) sample revealed two peak areas within the interplanar spacings range (38.8-14.8^{o}) 0.269-0.695nm (figure 4.10). The sharpest, most intense peak of the trace centered on (21.2^{o}) 0.486nm, with the broader, less intense peak centered at (23.2^{o}) 0.445nm.

4.3.4- THERMOGRAVIMETRIC ANALYSIS (TGA)

The thermogravimetric curve for SUC(800) (figure 4.11, trace (a)) showed an overall weight loss of 98.5% at around 675°C. Ocurring in two stages, the commencement of weight loss was observed almost immediately, at around 50°C. The first stage, occurring between 50 and 500°C, involved a weight loss of around 5%. During the second stage, a weight loss of 93.5% was noted, between 500 and 675°C.

Trace (b) revealed one peak for the rate of sample weight loss, the onset of which started and increased rapidly at 500°C to peak at 650°C and then decreased until

Figure 4.9: SEM of the SUC(800) sample showing the very smooth outer surface.

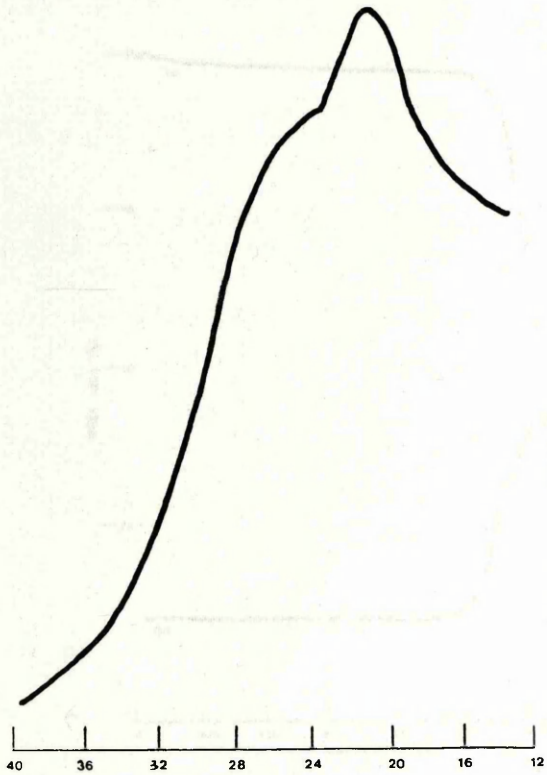

Figure 4.10: XRD trace of the SUC(800) sample.

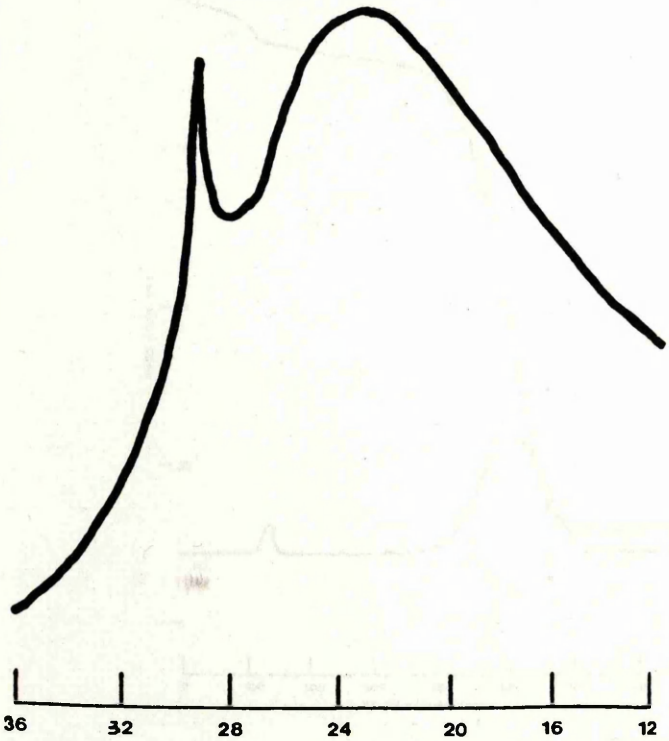

Figure 4.14: XRD trace of the SUC(800)K sample.

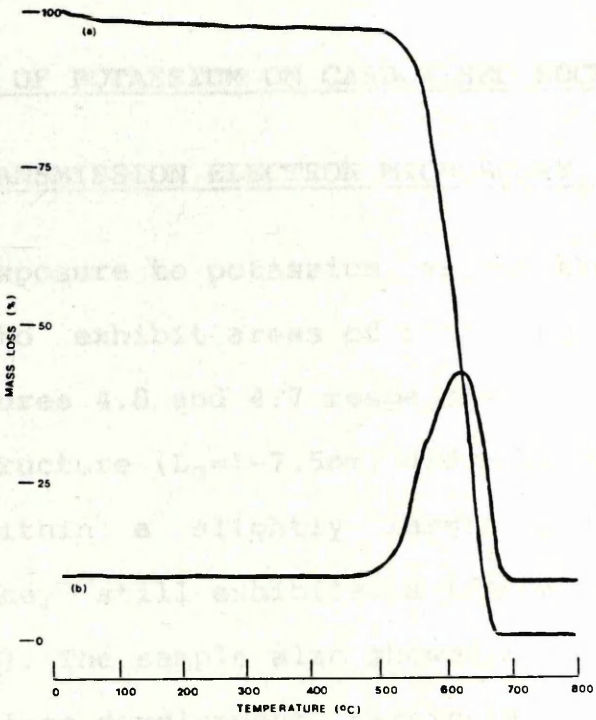

Figure 4.11: TGA trace of the SUC(800) sample: (a) % weight loss with temperature and (b) rate of weight loss.

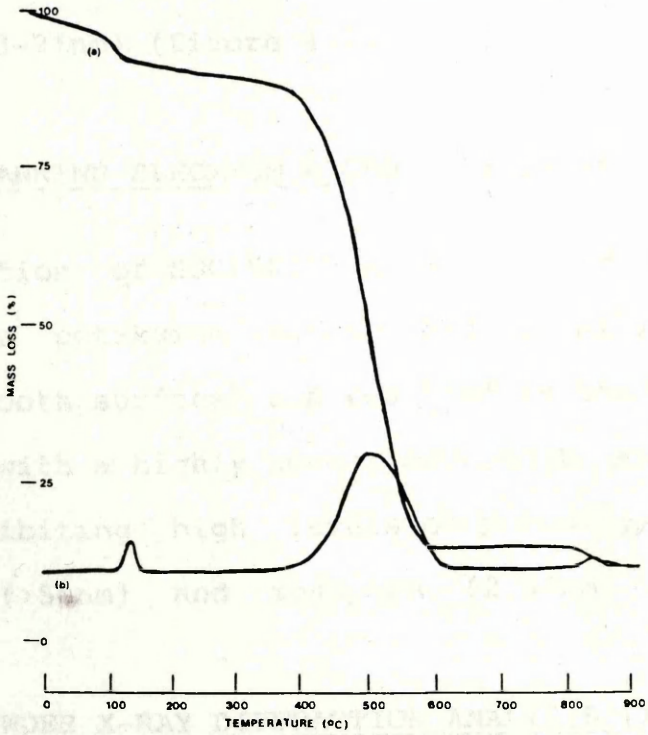

Figure 4.15: TGA trace of the SUC(800)K sample: (a) % weight loss with temperature and (b) rate of weight loss.

weight loss completion at 700°C.

4.4- EFFECT OF POTASSIUM ON CARBONISED SUCROSE- SUC(800)K

4.4.1- TRANSMISSION ELECTRON MICROSCOPY (TEM)

After exposure to potassium vapour the SUC(800) sample continued to exhibit areas of both long and short-range order, figures 4.8 and 4.7 respectively. The short-range ordered structure (L_a=1-7.5nm) did however reveal lattice spacings within a slightly larger range 0.35-0.76nm although they still exhibited a typical value of 0.44nm (L_c=0.7-7nm). The sample also showed a significant increase in layer plane development, particularly in terms of the appearance of convoluted structures (L_a=5-135nm). These new areas of ribbon-like structural ordering developed with interplanar spacings of 0.32-0.38nm and a typical value of 0.36nm (L_c=3-21nm) (figure 4.12).

4.4.2- SCANNING ELECTRON MICROSCOPY (SEM)

Examination of SUC(800)K sample by SEM revealed that exposure to potassium vapour had totally altered the original smooth surface and resulted in the formation of a structure with a highly porous honeycomb surface (figure 4.13), exhibiting high levels of porosity in both the macropore (>50nm) and mesopore (2-50nm) size ranges.

4.4.3- POWDER X-RAY DIFFRACTION ANALYSIS (XRD)

Examination of the x-ray diffraction trace for the

Figure 4.12: HREM of the SUC(800)K sample revealing the appearance of convoluted structural order.

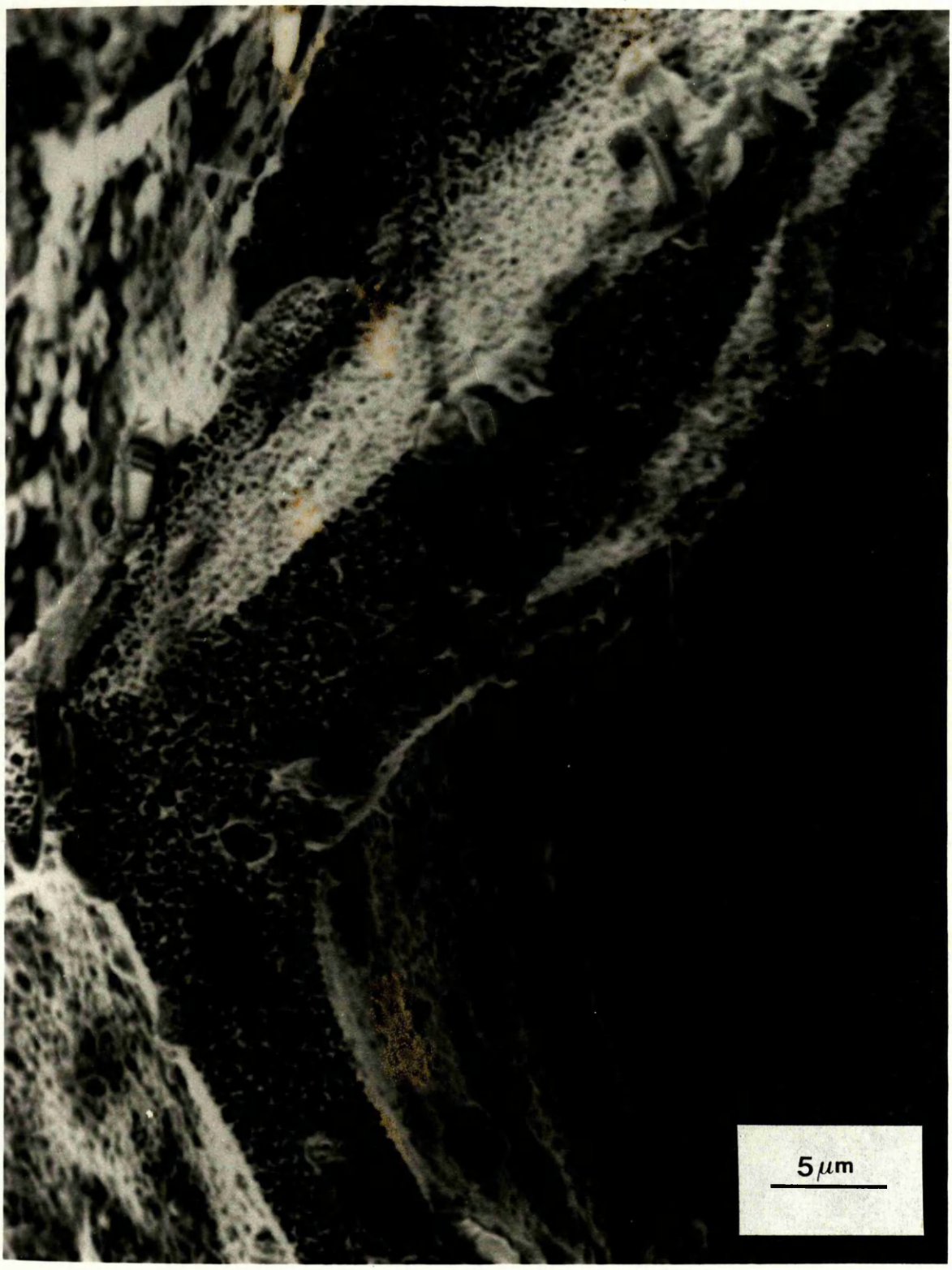

Figure 4.13: SEM of the SUC(800)K sample revealing the honeycomb surface and high levels of porosity.

SUC(800)K sample revealed two peak areas within the interplanar spacings range (35.8-13.6°) 0.291-0.756nm (figure 4.14). The sharpest peak of the trace, displayed within the interplanar spacings range (30.4-27.6°) 0.341-0.375nm, is centered at (28.8°) 0.359nm. The remaining peak, exhibiting a slightly greater peak height, occurs within the interplanar spacings range (27-13.6°) 0.383-0.756nm and is centered around (23.4°) 0.441nm.

4.4.4- THERMOGRAVIMETRIC ANALYSIS (TGA)

The thermogravimetric curve for SUC(800)K (figure 4.15, trace (a)) showed an overall weight loss of 90% at around 900°C. Occurring in three stages (trace (b)), the maximum rate of sample weight loss for each stage occurred at 140, 515 and 840°C. Commencement of weight loss was immediate, with a 5% reduction occurring between 0 and 140°C. The second stage, occurred between 140 and 585°C and involved a 79% weight loss. The third and final stage, occurring between 585 and 900°C, represented a weight loss of 6%.

4.5- ANALYSIS OF CARBONISED POLYVINYL ACETATE- PVA(800)

This sample of polyvinyl acetate (PVA), carbonised at 800°C (table 4.1) was prepared and supplied by British Coal. The carbonisation procedure was the same as that described for SUC(800) (section 4.3).

4.5.1- TRANSMISSION ELECTRON MICROSCOPY (TEM)

Analysis of the graphitisable carbon sample (PVA(800)) revealed, as expected, areas of extensively well-ordered long-range structure (L_a=13-85nm) with interplanar spacings in the range 0.33-0.35nm (L_c=2-36nm) (figure 4.16). The short-range ordered structure (L_a=1-7nm) exhibited lattice spacings within the range 0.35-0.48nm with a typical value of 0.42nm (L_c=0.7-2nm) and was similar to the non-graphitised structure shown in figure 4.7.

4.5.2- SCANNING ELECTRON MICROSCOPY (SEM)

SEM examination of the PVA(800) sample revealed areas with a smooth external surface displaying cracks and pitting (figure 4.17). The sample also revealed a smooth, folded, flow-like lamellar structure where the smooth exterior surface had been removed (figure 4.18).

4.5.3- POWDER X-RAY DIFFRACTION ANALYSIS (XRD)

Examination of the x-ray diffraction trace for the PVA(800) sample revealed a broad double peak with interplanar spacings in the range (40.0-14.4^{o}) 0.261-0.714nm (figure 4.19). The most intense peak of the trace occurred in the interplanar spacings range (40.0-25.6^{o}) 0.261-0.404nm and was centered around (30.0^{o}) 0.345nm. The second, less intense peak, occurring between (25.6-14.4^{o}) 0.404-0.714nm was centered around (22.0^{o}) 0.469nm.

Figure 4.16: HREM of the PVA(800) sample showing areas of extensive structural order (0.33-0.35nm).

Figure 4.17: SEM of the PVA(800) sample showing an area of smooth external surface displaying cracks.

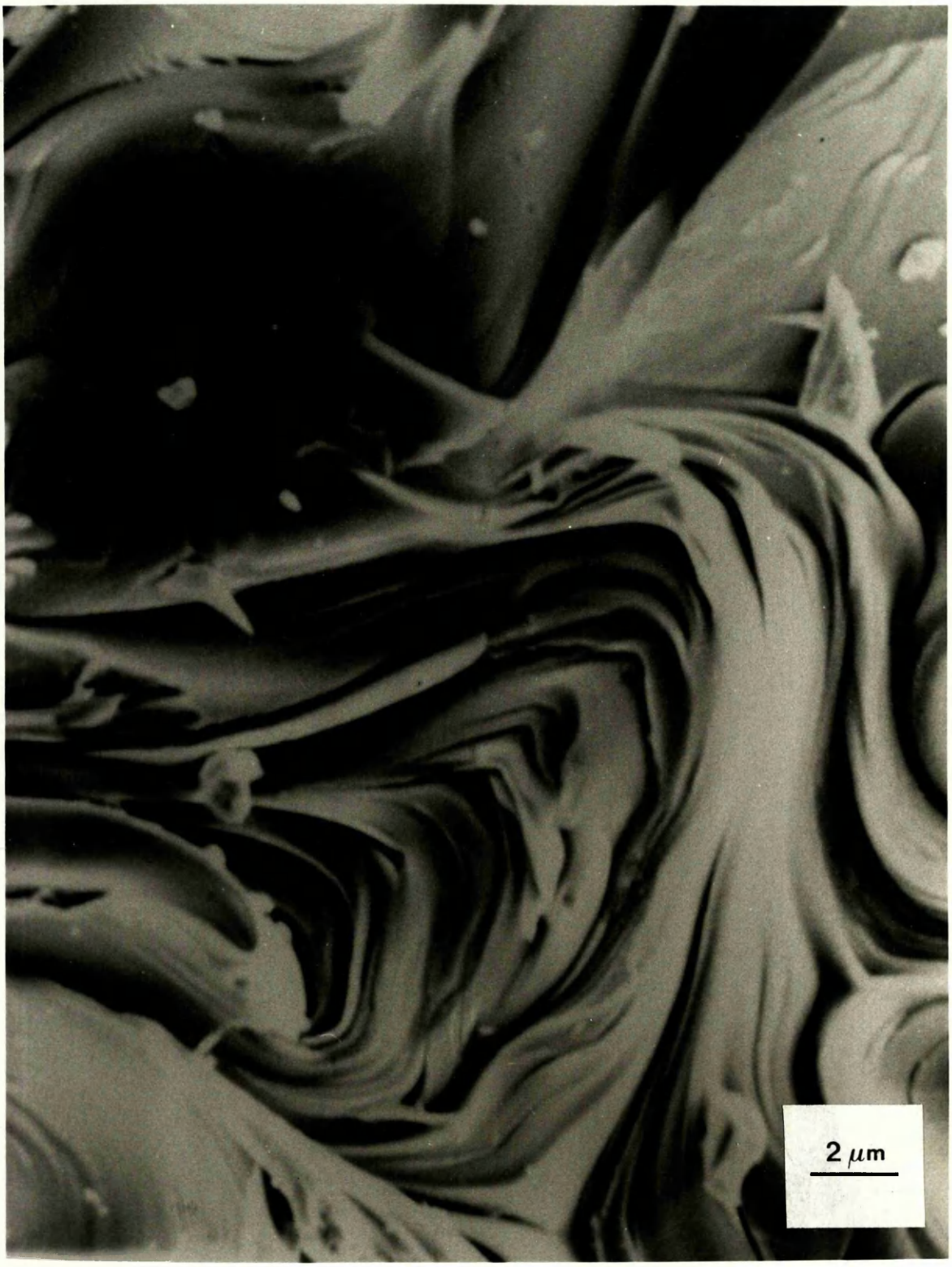

Figure 4.18: SEM of the PVA(800) sample showing the smooth, folded, flow-like lamellar structure.

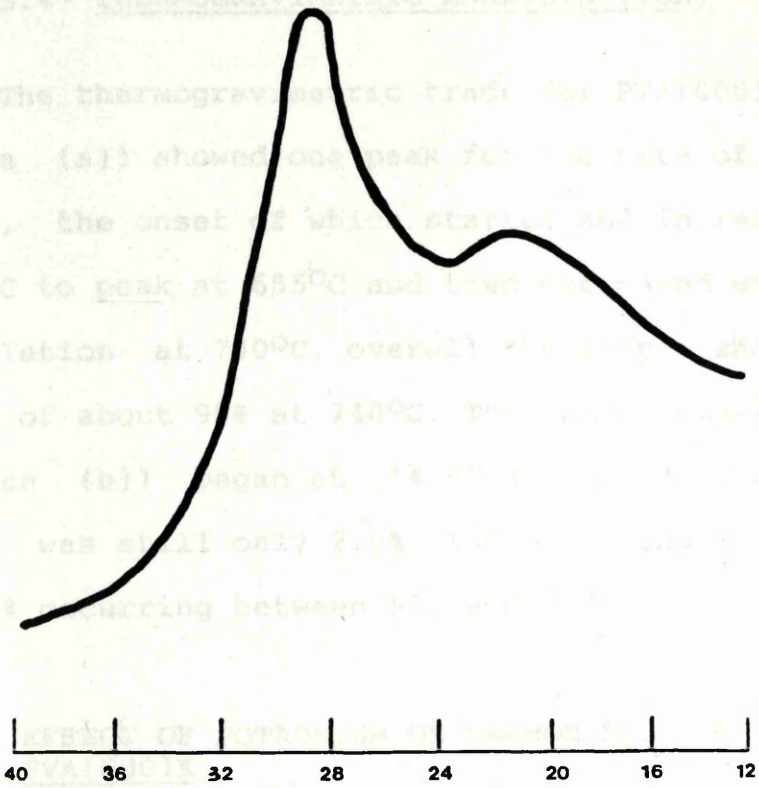

Figure 4.19: XRD trace of the PVA(800) sample.

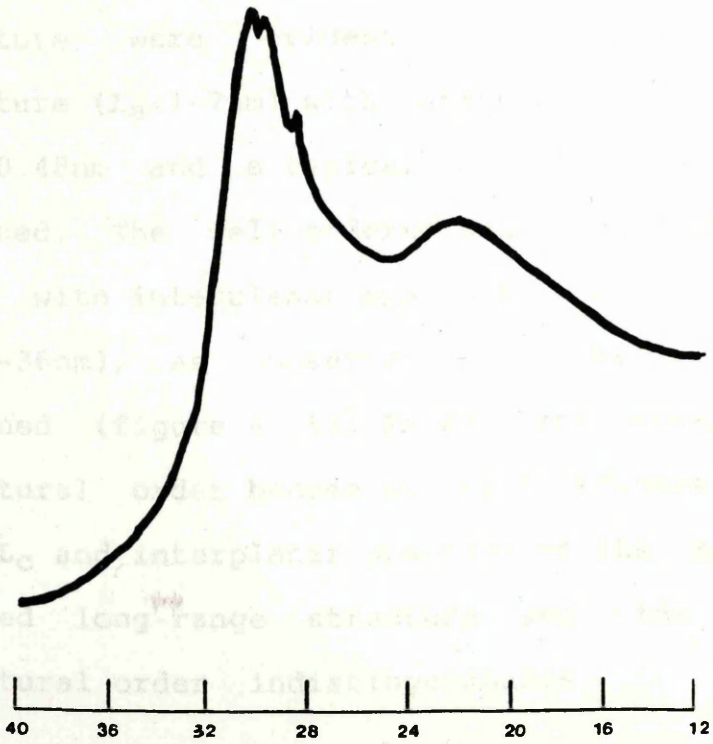

Figure 4.23: XRD trace of the PVA(800)K sample.

4.5.4- THERMOGRAVIMETRIC ANALYSIS (TGA)

The thermogravimetric trace for PVA(800) (figure 4.20, trace (a)) showed one peak for the rate of sample weight loss, the onset of which started and increased rapidly at 550°C to peak at 655°C and then decreased until weight loss completion at 740°C, overall the sample showing a weight loss of about 98% at 740°C. The commencement of weight loss (trace (b)) began at 140°C and by 530°C the total mass loss was still only 2.5%. The remaining weight loss of 95.5% occurring between 530 and 740°C.

4.6- EFFECT OF POTASSIUM ON CARBONISED POLYVINYL ACETATE-PVA(800)K

4.6.1- TRANSMISSION ELECTRON MICROSCOPY (TEM)

After exposure to potassium vapour, three types of structure were evident. The non-graphitised carbon structure (L_a=1-7nm) with interplanar spacings in the range 0.35-0.48nm and a typical value of 0.42nm (L_c=0.7-2nm) remained. The well-ordered long-range structure (L_a=13-85nm) with interplanar spacings in the range 0.33-0.35nm (L_c=2-36nm), as observed in the PVA(800) sample, also remained (figure 4.16). In addition, areas of convoluted structural order became apparent (figure 4.21) with the L_a, L_c and interplanar spacings of the extensively well-ordered long-range structure and the new ribbon-like structural order indistinguishable.

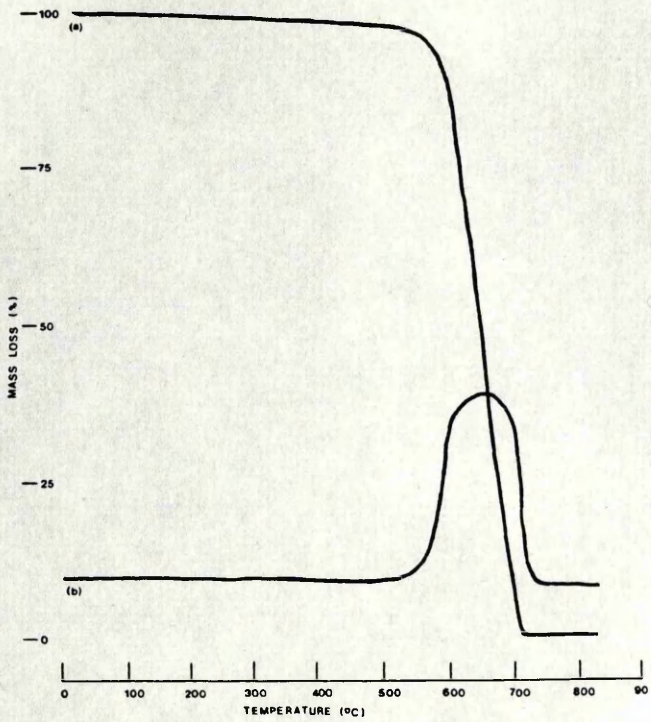

Figure 4.20: TGA trace of the PVA(800) sample: (a) % weight loss with temperature and (b) rate of weight loss.

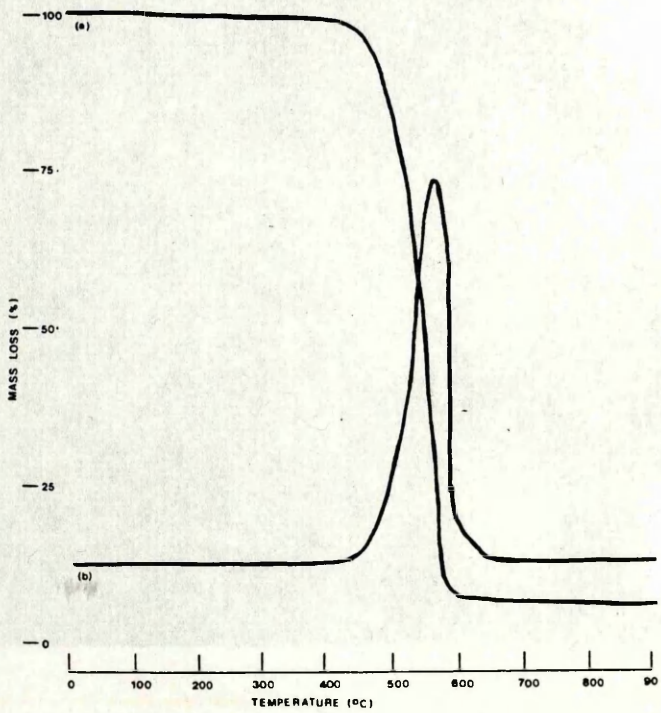

Figure 4.24: TGA trace of the PVA(800)K sample: (a) % weight loss with temperature and (b) rate of weight loss.

Figure 4.21: HREM of the PVA(800) sample after exposure to potassium vapour revealing areas exhibiting the new convoluted structure.

4.6.2- SCANNING ELECTRON MICROSCOPY (SEM)

Examination of the PVA(800) sample after exposure to potassium revealed a smooth, folded, flow-like lamellar surface exhibiting cracks, fractures, large holes leading to the interior and evidence of porosity (figure 4.22).

4.6.3- POWDER X-RAY DIFFRACTION ANALYSIS (XRD)

Examination of the x-ray diffraction trace for the PVA(800)K sample revealed one broad peak and three sharp peaks within the interplanar spacings range (40.0-14.4^{o}) 0.261-0.714nm (figure 4.23). The three sharp, most intense peaks of the trace occurred in the range (40.0-25.6^{o}) 0.261-0.404nm and were centered, in order of decreasing intensity, around (30.4^{o}) 0.341nm, (30.0^{o}) 0.345nm and (28.4^{o}) 0.365nm respectively. The broader, less intense peak, occurring between (25.6-14.4^{o}) 0.404-0.714nm was centered at (22.0^{o}) 0.469nm.

4.6.4- THERMOGRAVIMETRIC ANALYSIS (TGA)

The thermogravimetric trace for PVA(800)K (figure 4.24, trace (b)) exhibited one peak for the rate of sample weight loss. The rate of weight loss started and increased rapidly at 430°C to peak at 575°C and then decreased until weight loss completion at 660°C. Overall the sample showed (trace (a)) a weight loss of about 93% at 625°C. The commencement of weight loss began at 135°C and by 430°C the total mass loss was only 2.5%. The remaining weight

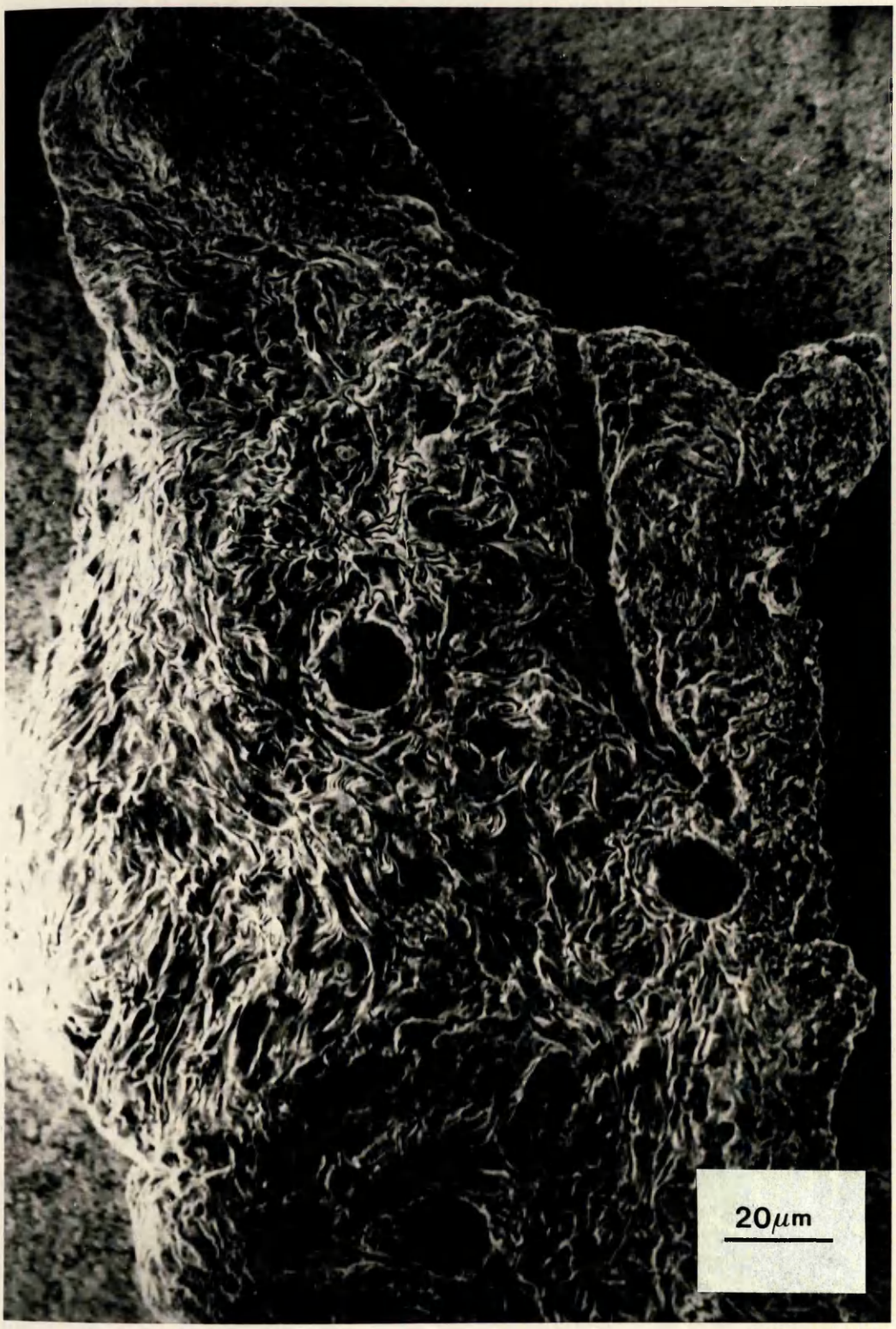

Figure 4.22: SEM of the PVA(800)K sample showing fractures, porosity and large holes leading to the interior.

loss of 90.5% occurred between 430 and 625°C.

4.7- FLAME PHOTOMETRY AND POTASSIUM UPTAKE MEASUREMENTS

Flame photometry and potassium uptake measurements were undertaken to determine which, if any, of the two carbonised carbons and three feed cokes were more susceptible to alkali attack. The potassium uptake measurements were recorded for each sample, heated to and maintained at a temperature of 400°C, until the weight increase, due to potassium vapour, was constant. The flame photometry results were obtained after exposure of the samples to potassium vapour at a temperature of 800°C.

SAMPLE	WEIGHT INCREASE (mg) per 100mg of sample	K CONC. (mg) per 100mg of sample
PVA(800)	28.580	4.464
SUC(800)	33.300	4.576
Feed Coke (Scunthorpe)	5.345	---
Feed Coke ($Redcar_1$)	4.710	---
Feed Coke ($Redcar_2$)	12.750	---

Table 4.2 The weight increase from the potassium uptake measurements and the corresponding potassium concentration from flame photometry.

4.8- EFFECT OF INERT CARRIER GASES

The carbonised sucrose and PVA samples were exposed to potassium vapour using different inert carrier gases, argon and nitrogen. Examination of each sample, by HREM and XRD,

did not reveal any salient microstructural differences when an alternative carrier gas was used, indeed examination of the samples revealed no obvious structural carrier gas dependence.

4.9- ANALYSIS OF LOW TEMPERATURE SUCROSE 'CARBONISATION'

The extent of observed ordering in some areas of the 800°C carbonised sucrose was surprising and required further study via a low temperature sucrose 'carbonisation' investigation.

The uncarbonised sucrose sample was supplied by British Coal. The method of 'carbonisation' was identical to that used for the open system carbonisation of aromatic hydrocarbons (section 3.2.1). The conditions of carbonisation are detailed in table 4.3.

Each sample was studied using the techniques of TEM, XRD and TGA. The results are tabulated in table 4.6.

COMPOUND	HEATING RATE	FINAL TEMP	SOAK PERIOD	ATM	CODE
Sucrose	---	---	---	---	SUC
Sucrose	3°C/min	150°C	2hr	N_2	SUC(150)
Sucrose	3°C/min	250°C	2hr	N_2	SUC(250)
Sucrose	3°C/min	300°C	2hr	N_2	SUC(300)
Sucrose	3°C/min	500°C	2hr	N_2	SUC(500)
Sucrose	3°C/min	700°C	2hr	N_2	SUC(700)
Sucrose	3°C/min	1000°C	2hr	N_2	SUC(1000)

Table 4.3 Conditions for low temperature 'carbonisation' of sucrose.

4.9.1- TRANSMISSION ELECTRON MICROSCOPY (TEM)

Examination of the sucrose sample prior to heating revealed areas of both long and short-range order. The short-range ordered structure (L_a=1-2.5nm) exhibited interplanar spacings of around 0.56nm (L_c=1.12-2.5nm) (figure 4.25). The long-range ordered structure (L_a=20-75nm) exhibited interplanar spacings in the range 0.33-0.34nm (L_c=1.65-40nm) (figure 4.26).

Heating the sucrose sample to 150°C, SUC(150), revealed a non-graphitised carbon structure (L_a=1-10nm), similar to the structure exhibited in figure 4.25 with interplanar spacings in the range 0.34-1.02nm and a typical value of 0.71nm (L_c=0.68-3nm). The sample also exhibited areas of long-range ordered structure (L_a=40-118nm) with interplanar spacings in the range 1.12-1.15nm (L_c=10-55nm) (figure 4.27).

At 250°C, the calcined sucrose sample, exhibited a short-range ordered structure (L_a=1-2.5nm) with interplanar spacings of between 0.66-0.68nm (L_c=1.32- 2.8nm), similar to the non-graphitised structure revealed in figure 4.25. Also present were areas of long-range ordered structure (L_a=10-125nm) with interplanar spacings within the range 0.43-0.46nm (L_c=4-80nm) (figure 4.28). Some areas also exhibited a long-range ordered structure with interplanar spacings of between 0.97-1.02nm (L_a=13-30nm, L_c=3-20nm). In addition areas exhibiting the development of convoluted structure (L_a=8-28nm) became apparent (figure 4.29) with interplanar spacings of between 0.33-0.34nm (L_c=3.5-16nm).

Figure 4.25: HREM of the showing the non-graphitised carbon structure exhibited by the SUC sample (0.56nm).

Figure 4.26: HREM of the sucrose sample showing areas with a long-range ordered structure (0.33-0.34nm).

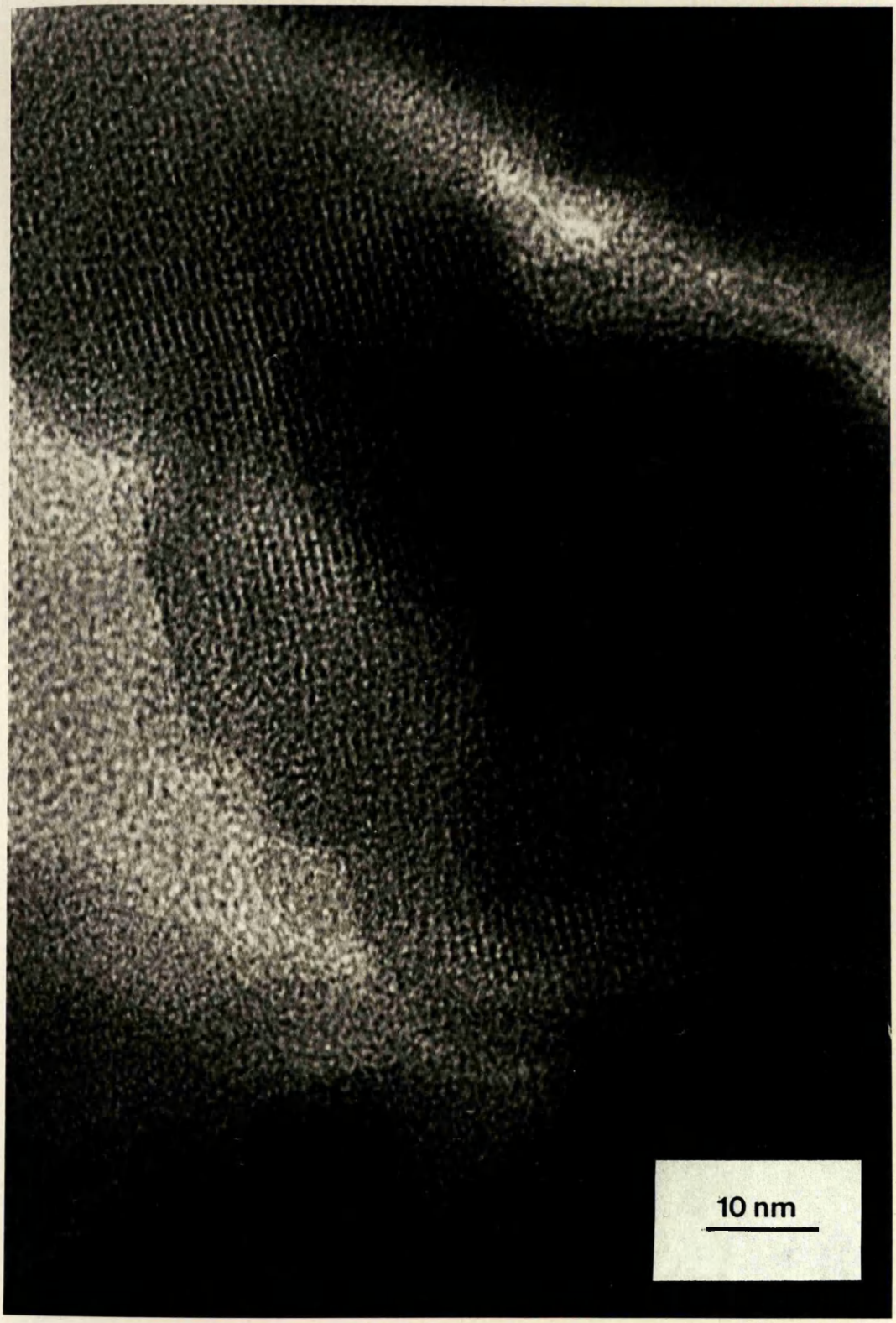

Figure 4.27: HREM of the SUC(150) sample showing the long-range ordered structure (1.12-1.15nm).

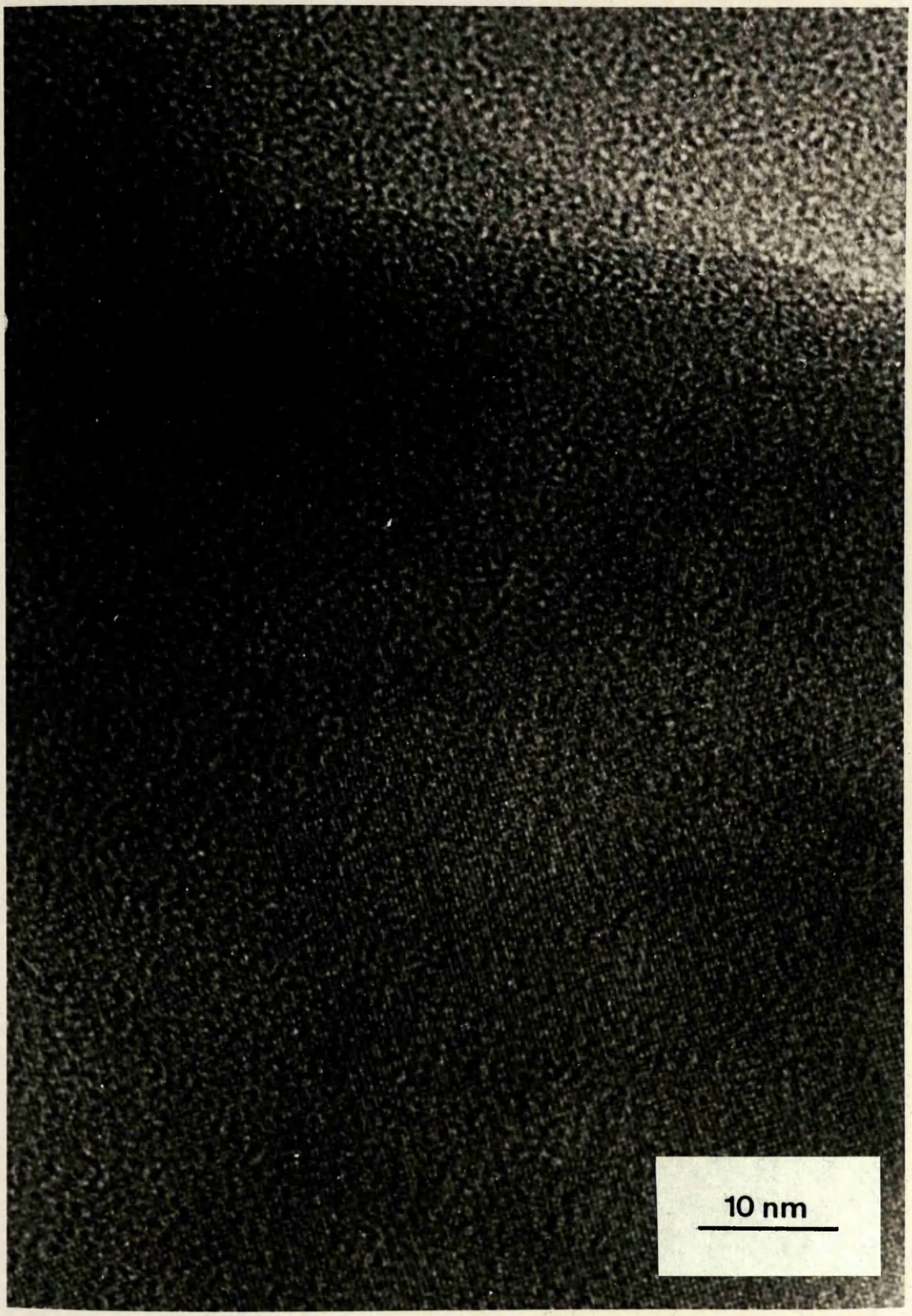

Figure 4.28: HREM of the SUC(250) sample showing the long-range ordered structure (0.43-0.45nm).

Figure 4.29: HREM of the SUC(250) sample revealing both a convoluted and long-range ordered structure (0.33-0.34nm).

The interplanar spacings, L_a and L_c values, of these new convoluted structures and the long-range ordered structure associated with it, were indistinguishable.

At 300°C the calcined sucrose material SUC(300) exhibited areas of short-range order (L_a=1-3nm) with lattice spacings in the range 0.43-0.54nm and a typical value of 0.47nm (L_c=0.86-2.5nm) (figure 4.30). Also present were areas of extensively ordered long-range structure (L_a=11-50nm) with lattice spacings around 0.34nm (L_c=1.7-35nm) (figure 4.31).

After heating to 500°C, the SUC(500) sample revealed a non-graphitised carbon structure (L_a=1-5nm) with lattice spacings in the range 0.42-0.56nm and a typical value of 0.48nm (L_c=0.84-2.5nm), similar to the short-range ordered structure displayed in figure 4.30. The sample also exhibited areas of extensively ordered long-range structure (L_a=15-68nm) with interplanar spacings of around 0.34nm (L_c=2-25nm). In addition areas of convoluted structure (L_a=10-55nm, L_c=2-10nm) became apparent (figure 4.32) with the interplanar spacings of the extensively ordered long-range structure and the new convoluted structural order indistinguishable.

Heating the sucrose material to 700°C, SUC(700), exhibited both short (L_a=1-8.5nm) and long (L_a=20-90nm) range ordered structure with interplanar spacings of (0.41-0.54nm and 0.37nm) and L_c values of (0.82-1.8nm and 3-27nm) respectively, very similar to those obtained for the SUC(800) sample (figure 4.7 and figure 4.8).

Examination of the SUC(1000) sample revealed both long

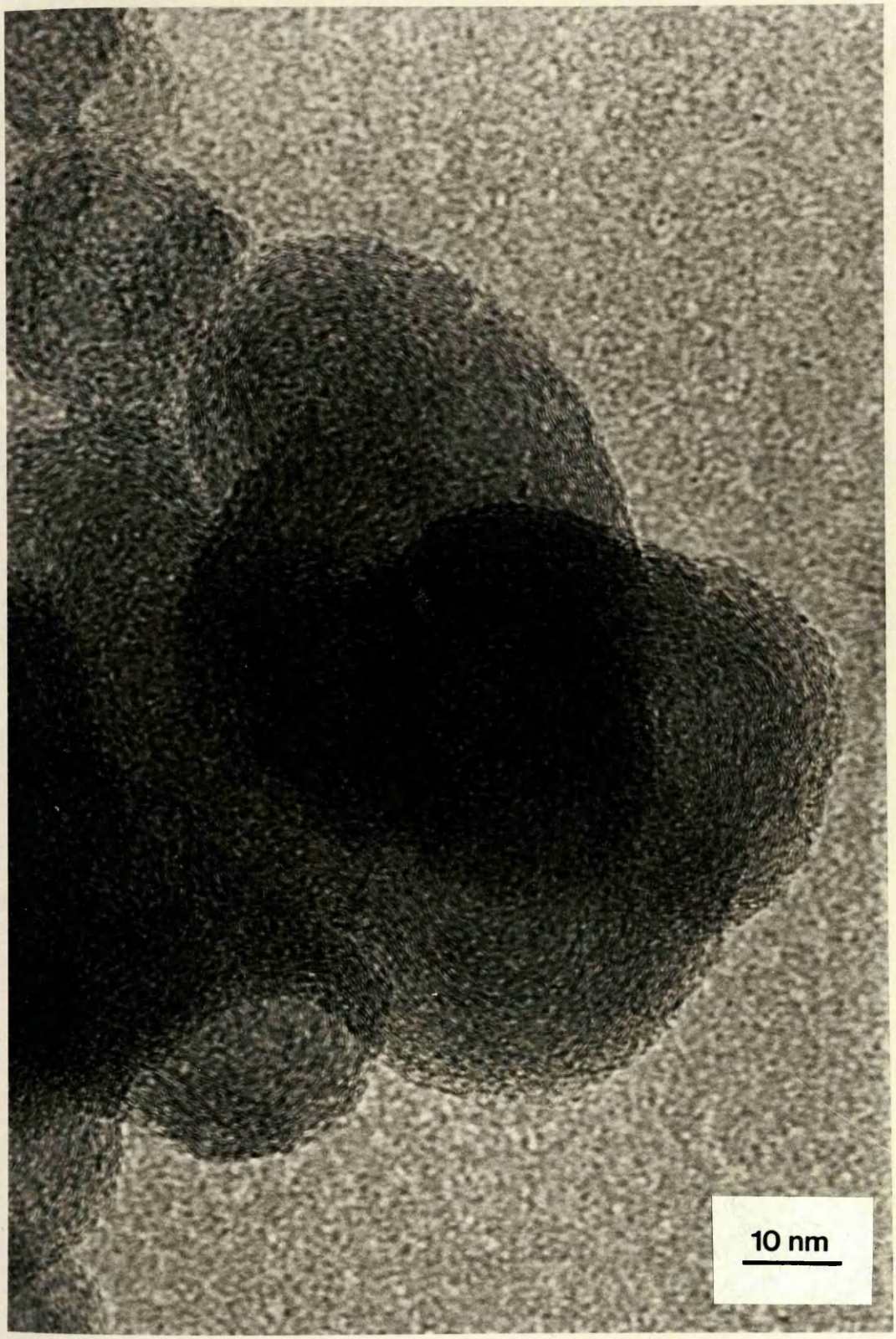

Figure 4.30: HREM of the SUC(300) sample showing the short-range ordered structure (0.42-0.56nm).

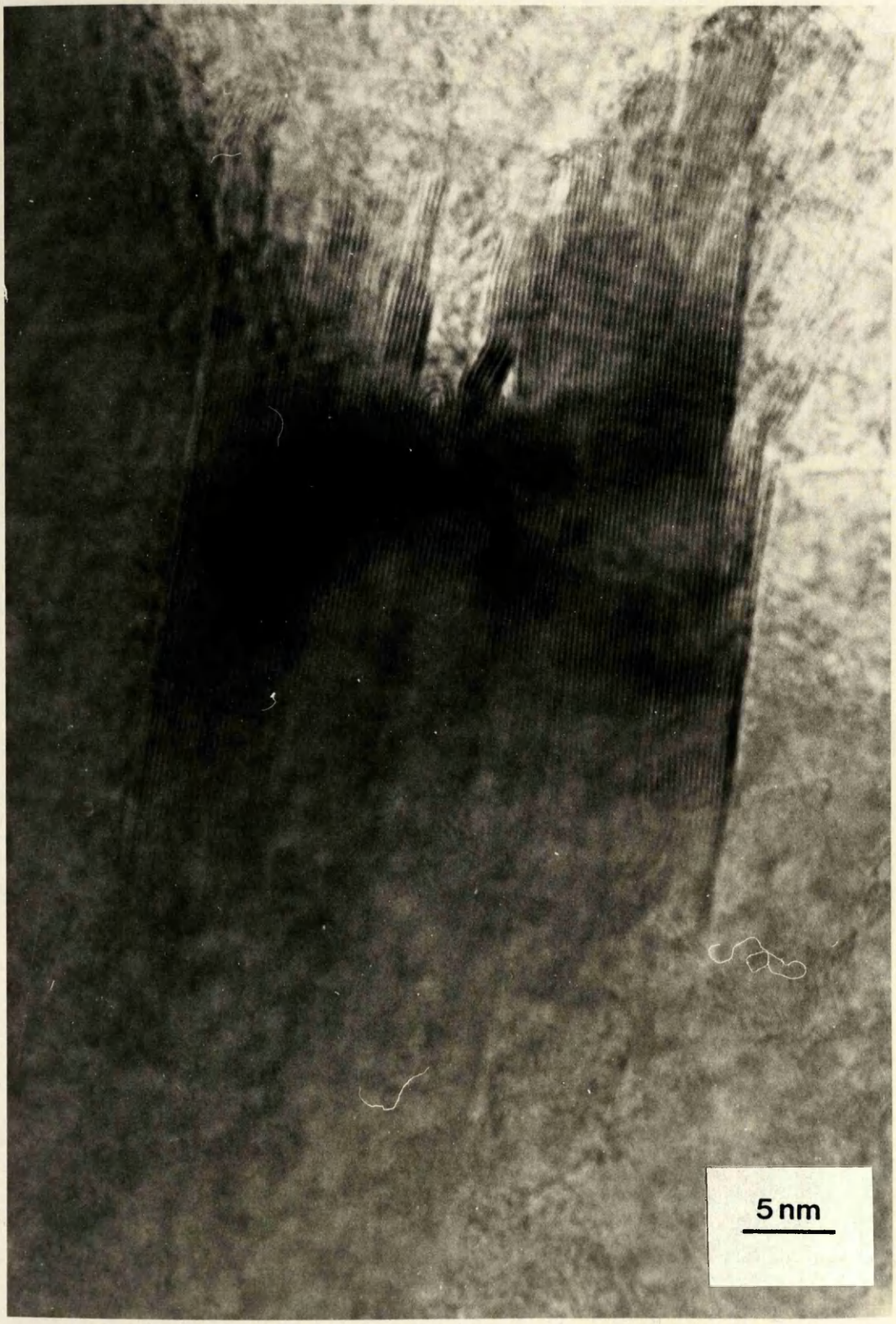

Figure 4.31: HREM of the SUC(300) sample displaying areas of long-range ordered structure (0.34nm).

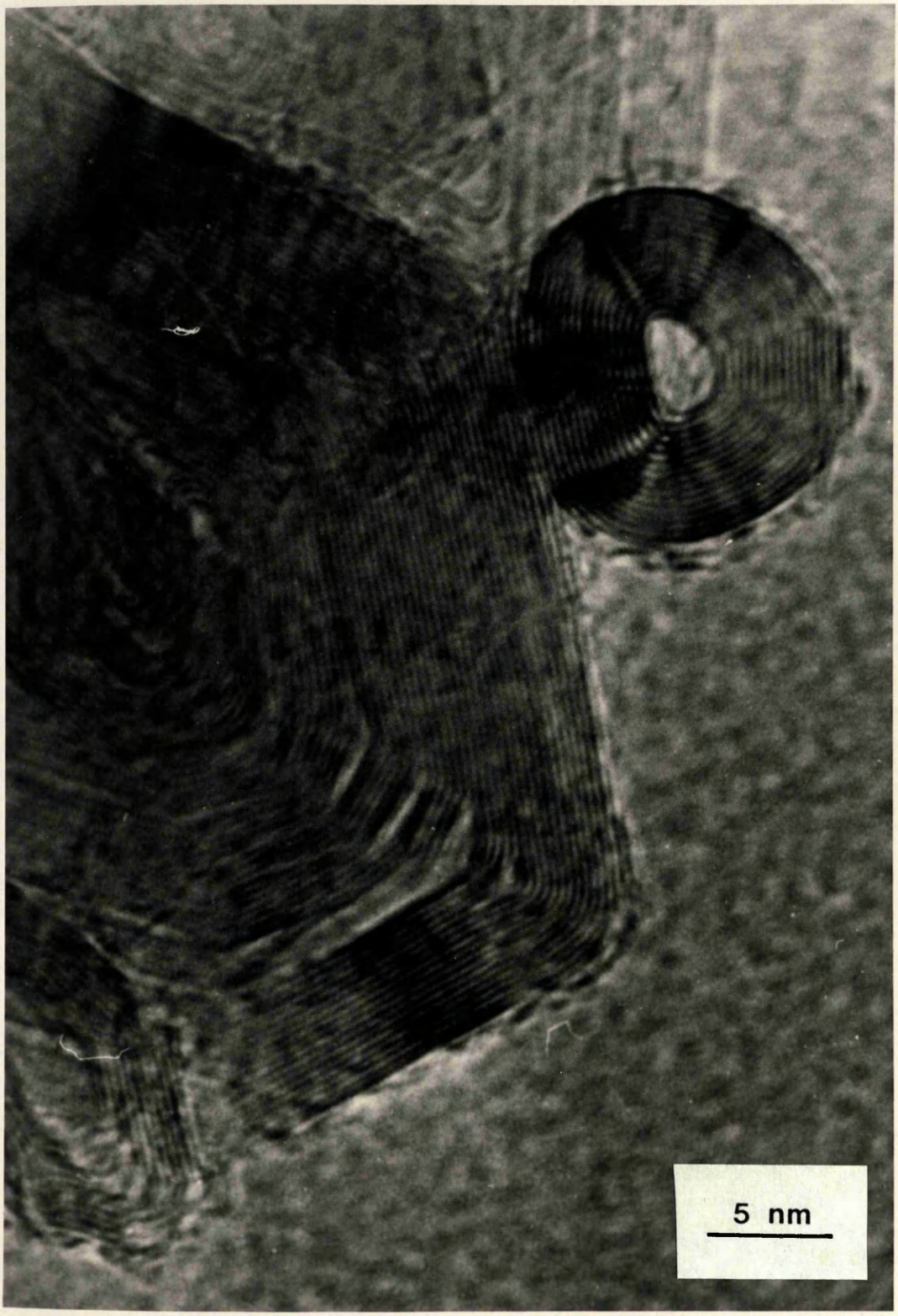

Figure 4.32: HREM of the SUC(500) sample exhibiting both the convoluted and long-range ordered structure (0.34nm).

and short-range ordered structures. The non-graphitised carbon structure (L_a=1-7nm) exhibited interplanar spacings in the range 0.36-0.48nm with a typical value of 0.39nm (L_c=0.72-2.5nm) (figure 4.33). The long-range ordered structure (L_a=23-72nm) exhibited lattice spacings within the range 0.32-0.36nm (L_c=2.5-26nm).

Also evident (figure 4.34) were areas displaying a tangled mesh of ribbon-like appearance (L_a=7-25nm, L_c=0.64-5nm) and interplanar spacings indistinguishable from the long-range ordered structure.

4.9.2- POWDER X-RAY DIFFRACTION ANALYSIS (XRD)

Examination of the x-ray diffraction trace for the SUC(250) sample revealed one broad peak and three smaller, sharper peaks within the interplanar spacings range (38.0-8.0^{o}) 0.275-1.283nm (figure 4.35). The broad peak centered around (21.0^{o}) 0.491nm with the three sharp peaks, centered in order of decreasing intensity, at (15.25^{o}) 0.675nm, (13.0^{o}) 0.791nm and (10.3^{o}) 0.997nm.

Both the SUC(300) and the SUC(500) x-ray diffraction traces (figure 4.36) exhibited one broad peak. The peak for the SUC(300) sample was centered at (20.6^{o}) 0.501nm and within the interplanar spacings range (36.3-9.3^{o}) 0.287-1.104nm. The peak exhibited by the SUC(500) sample was centered at (20.8^{o}) 0.496nm, within the interplanar spacings range (40.0-17.6^{o}) 0.262-0.585nm).

Examination of the SUC(700) sample by x-ray diffraction revealed a trace exhibiting three peaks, two displaying

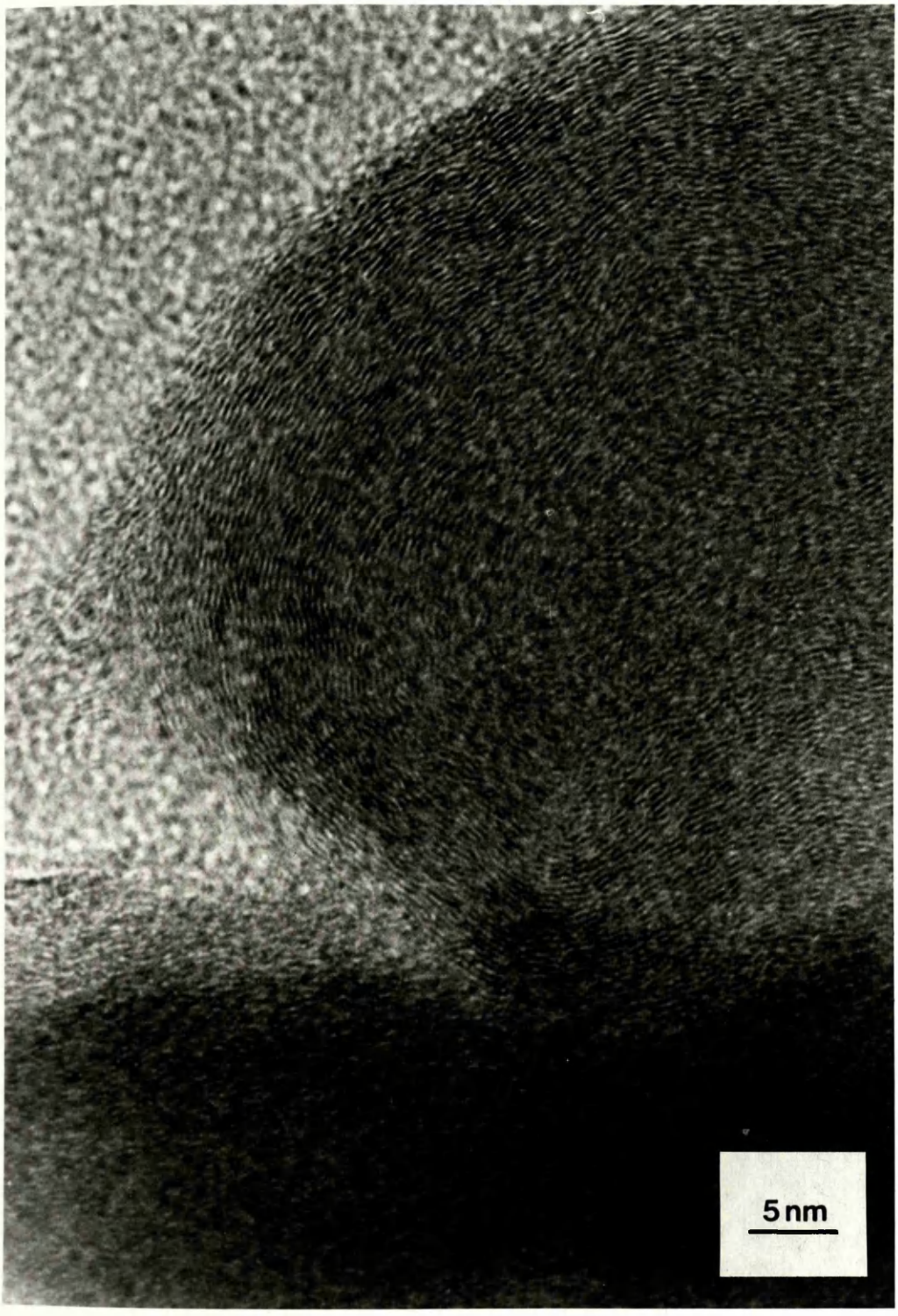

Figure 4.33: HREM of the SUC(1000) sample displaying the non-graphitised carbon structure (0.36-0.48nm).

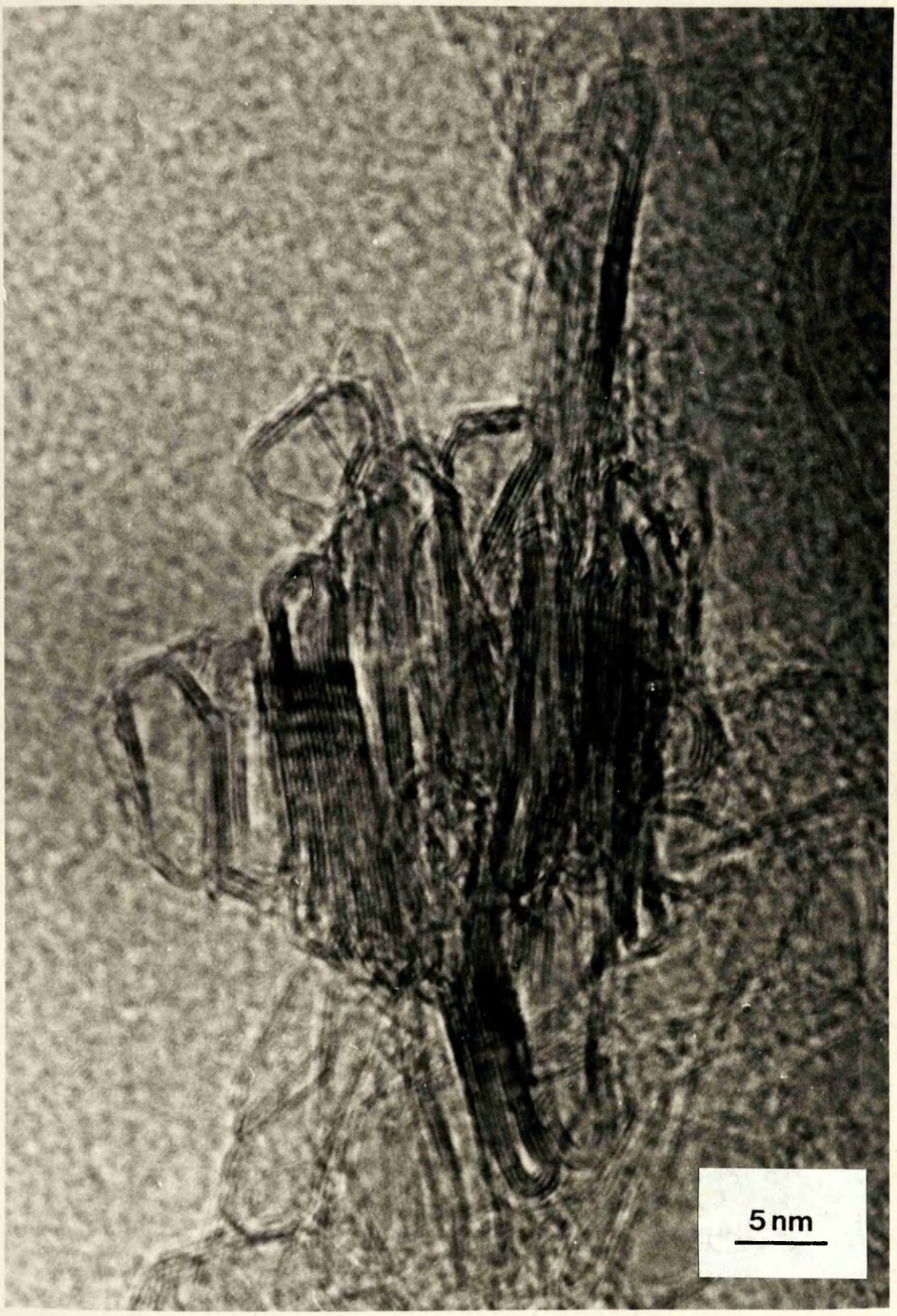

Figure 4.34: HREM of the SUC(1000) sample displaying a tangled mesh of ribbon-like appearance (0.32-0.36nm).

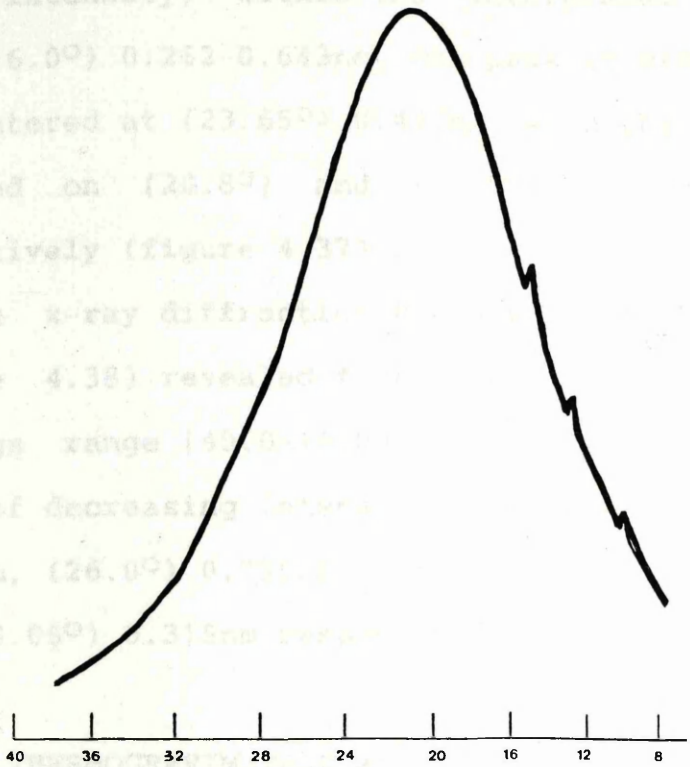

Figure 4.35: XRD trace of the SUC(250) sample.

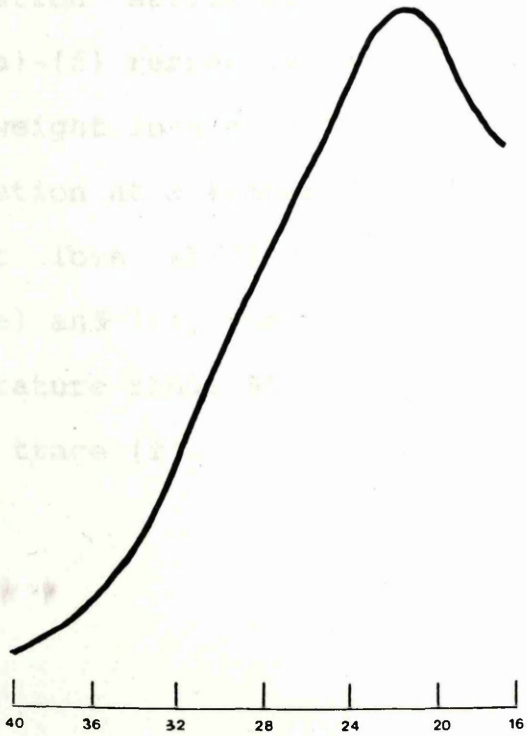

Figure 4.36: XRD trace of the SUC(500) sample.

equal intensity, within the interplanar spacings range (40.0-16.0°) 0.262-0.643nm. The peak of greatest intensity was centered at (23.65°) 0.437nm, with the remaining peaks centered on (20.8°) and (26.0°), 0.496nm and 0.398nm respectively (figure 4.37).

The x-ray diffraction trace for the SUC(1000) sample (figure 4.38) revealed five peaks within the interplanar spacings range (40.0-16.0°) 0.262-0.643nm. The peaks, in order of decreasing intensity, were centered around (24.0°) 0.430nm, (26.0°) 0.398nm, (21.5°) 0.490nm, (30.5°) 0.345nm and (33.05°) 0.315nm respectively.

4.9.3- THERMOGRAVIMETRIC ANALYSIS

The thermogravimetric curves for the SUC, SUC(150), SUC(250), SUC(300), SUC(500) and SUC(1000) low temperature 'carbonisation' series of samples are shown in figure 4.39, traces (a)-(f) respectively. Traces (a)-(d) revealed the onset of weight loss at 250°C, with weight loss continuing to completion at a temperature of 625°C. The commencement of weight loss shifted to 500°C for the remaining two traces, (e) and (f), the total weight loss occurring within the temperature range 500°C to 700°C and within one peak at 650°C for trace (f).

Figure 4.37: XRD trace of the SUC(700) sample.

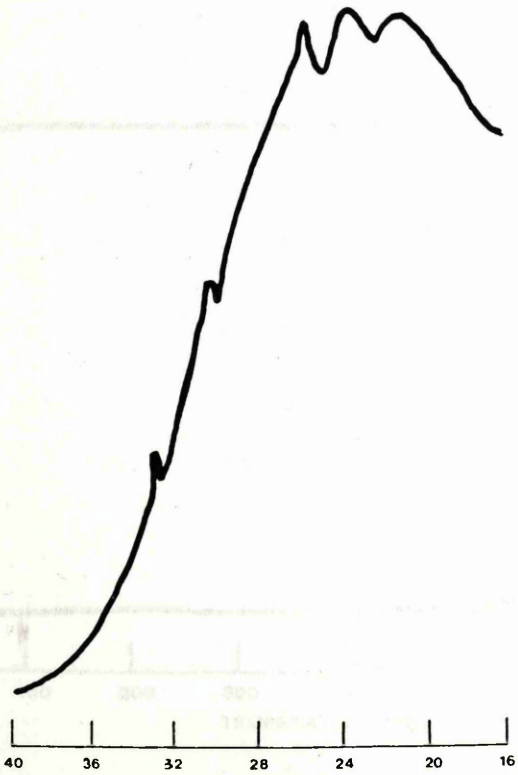

Figure 4.38: XRD trace of the SUC(1000) sample.

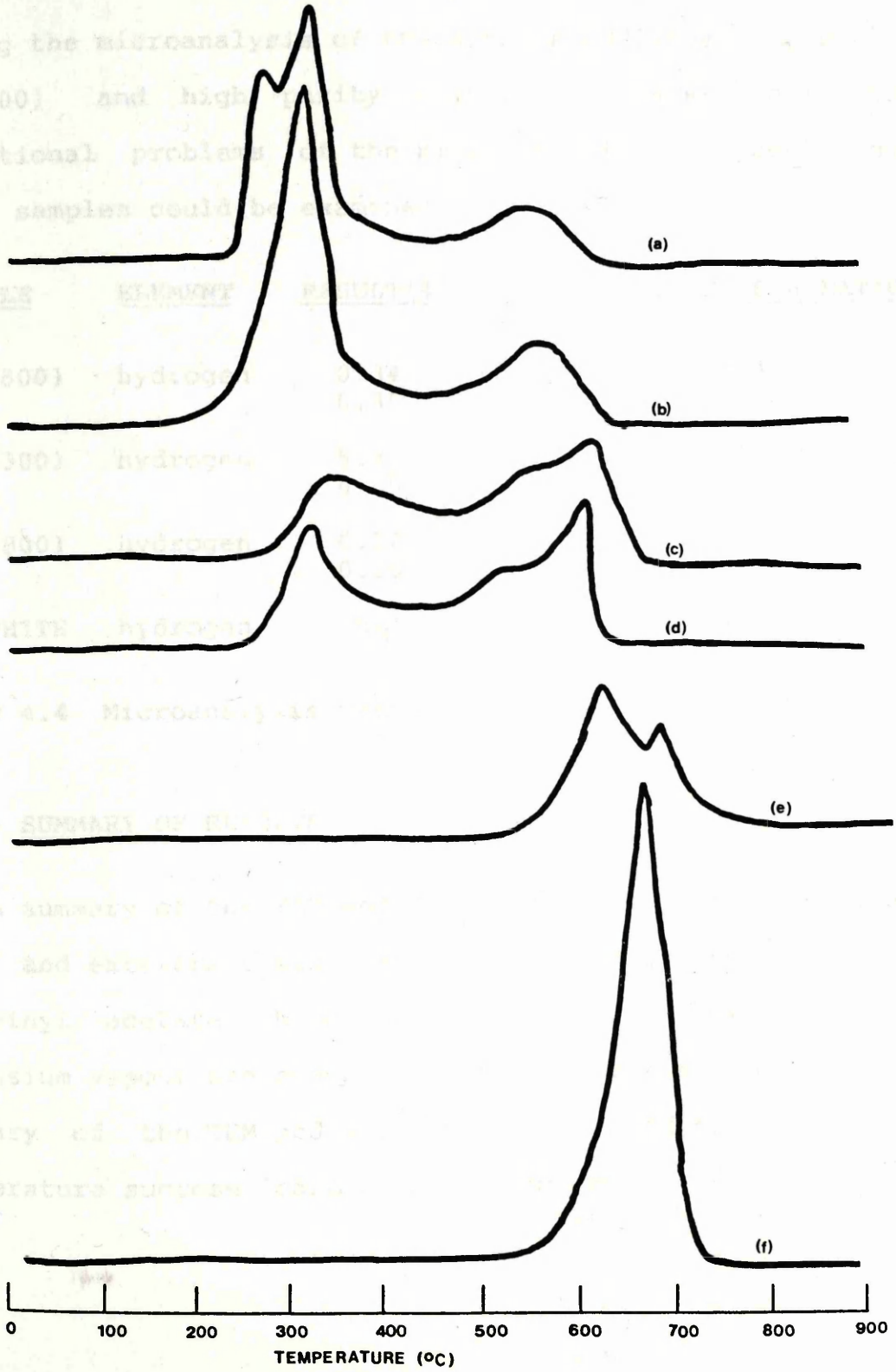

Figure 4.39: TGA traces (rate of weight loss) for the low temperature 'carbonisation' sucrose series.

4.9.4- MICROANALYSIS

The elements, carbon and hydrogen, were tested for during the microanalysis of the samples SUC(300), SUC(800), PVA(800) and high purity graphite. However, due to operational problems of the microanalysis equipment, no other samples could be examined.

SAMPLE	ELEMENT	RESULT(%)	APPROXIMATE C:H RATIO
PVA(800)	hydrogen	0.34 0.35	24:1
SUC(300)	hydrogen	5.27 4.09	2:1
SUC(800)	hydrogen	0.32 0.38	24:1
GRAPHITE	hydrogen	nil	---

Table 4.4 Microanalysis results.

4.10- SUMMARY OF RESULTS

A summary of the TEM and XRD results obtained from the feed and extuyere cokes, the 800°C carbonised sucrose and polyvinyl acetate, both before and after exposure to potassium vapour are shown in table 4.5. Table 4.6 shows a summary of the TEM and XRD results obtained for the low temperature sucrose 'carbonisation' study.

SAMPLE	MICROSTRUCTURE	L_a(nm)	L_c(nm)	d(nm)	XRD(nm)
Feed coke	S.R.O	1-5.5	0.68-3	0.34-0.37	0.344
	S.R.O	1-5.5	0.42-3	0.42-0.48	0.478
	mineral mattter	10-130	5-56	0.33-0.70	
Extuyere coke	S.R.O	1-5	0.68-3.5	0.34-0.37	0.341
	S.R.O	1-5	0.84-3.5	0.42-0.48	0.482
	L.R.O	15-95	2.8-35	0.35	
SUC(800)	S.R.O	1-8.5	0.82-1.8	0.44	0.486
				(0.41-0.54)	0.445
	L.R.O	20-90	3-27	0.37	
SUC(800)K	S.R.O	1-7.5	0.7-7	0.44	0.359
				(0.35-0.76)	0.441
	L.R.O	20-90	3-21	0.36	
	ribbon	5-135	3-21	0.36	
				(0.32-0.38)	
PVA(800)	S.R.O	1-7	0.7-2	0.42	0.345
				(0.35-0.48)	0.469
	L.R.O	13-85	2-36	0.33-0.35	
PVA(800)K	S.R.O	1-7	0.7-2	0.42	0.341
				(0.35-0.48)	0.345
	L.R.O	13-85	2-36	0.33-0.35	0.365
	& ribbon				0.469

S.R.O - short-range order
L.R.O - long-range order

Table 4.5 Summary of the TEM and XRD results for the feed and extuyere coke, and SUC(800) and PVA(800), both before and after exposure to potassium vapour.

SAMPLE	MICROSTRUCTURE	L_a(nm)	L_c(nm)	d(nm)	XRD(nm)
SUC	S.R.O	1-2.5	1.12-2.5	0.56	---
	L.R.O	20-75	1.65-40	0.33-0.34	---
SUC(150)	S.R.O	1-10	0.68-3	0.71	---
				(0.34-1.02)	---
	L.R.O	40-118	10-55	1.12-1.15	---
SUC(250)	S.R.O	1-2.5	1.32-2.8	0.66-0.68	0.491
	L.R.O	10-125	4-80	0.43-0.46	0.675
	L.R.O	13-30	3-20	0.97-1.02	0.791
	L.R.O & ribbon	8-28	3.5-16	0.33-0.34	0.997
SUC(300)	S.R.O	1-3	0.86-2.5	0.47	0.501
				(0.43-0.54)	
	L.R.O	11-50	1.7-35	0.34	
SUC(500)	S.R.O	1-5	0.84-2.5	0.48	0.496
				(0.42-0.56)	
	L.R.O	15-68	2-25	0.34	
	ribbon	10-55	2-10	0.34	
SUC(700)	S.R.O	1-8.5	0.82-1.8	0.44	0.437
				(0.41-0.54)	0.496
	L.R.O	20-90	3-27	0.37	0.398
SUC(1000)	S.R.O	1-7	0.72-2.5	0.39	0.430
				(0.36-0.48)	0.398
	L.R.O	23-72	2.5-26	0.32-0.36	0.490
	ribbon	7-25	0.64-5	0.32-0.36	0.345
					0.315

S.R.O - short-range order
L.R.O - long-range order

Table 4.6 Summary of TEM and XRD results for the low temperature 'carbonisation' study.

CHAPTER FIVE

DISCUSSION OF THE RESULTS FOR THE FEED AND EXTUYERE COKE AND THE CARBONISED SUCROSE AND PVA

5.1- INTRODUCTION

Since their is no standard definition of short-range and long-range order, for this study S.R.O. encompasses structures exhibiting an L_a value of 1-10nm and the L.R.O. structures are regarded as those exhibiting an L_a value of >10nm. L_a values of less than 1nm where recorded for the non-graphitised carbon structures by HREM. These values could be attributed to the non-graphitised structure, however, it was not possible to distinguish between actual L_a values and background noise.

Analysis of the results presented for the feed and extuyere coke samples and the carbonised sucrose and PVA samples will be discussed individually with a comparison of any overall group relevance.

5.2- FEED AND EXTUYERE COKES

The feed coke x-ray diffraction trace revealed a wide range of carbon lattice spacings, represented by two overlapping peaks. The interplanar spacings centered around one of the peaks, 0.344nm, were consistent with the non-graphitised carbon structure observed with HREM (0.34-0.37nm). The second peak, centered on 0.478nm, would be accounted for by the presence of both mineral matter, 0.30-0.70nm from HREM, present in the original parent material and the very small proportion of non-graphitised carbon material that exhibited lattice spacings with values in the range 0.42-0.48nm.

Examination of the extuyere samples by XRD, revealed a

much sharper, more intense peak for the carbon-carbon interplanar distance relative to that from the feed coke samples. The carbon peak corresponding to 0.341nm of the extuyere x-ray diffraction trace had been sharpened and heightened as compared to the feed coke trace, the increased peak height corresponding to a greater number of lattices falling within this 2θ range, arising from both the non-graphitised carbon and the long-range ordered structures. This would cause a change in the relative proportions of the peak heights, although in the case of the extuyere trace the peak centered on 0.482nm represents not only the inherent mineral matter but also the increased proportion of the larger lattice spacings 0.43-0.47nm observed by HREM.

Overall the XRD traces from the feed and extuyere cokes were consistent with the HREM observations and indicated that the extuyere coke structure was more ordered than that of the feed coke.

Previous high resolution electron microscopy studies (Shevlin et al., 1984, 1985, 1986) have shown that alkali penetration of metallurgical coke structure results in the production of two distinct types of microstructure, a non-graphitised carbon structure and areas with an extensively ordered carbon structure. The observations of the present study by HREM and XRD, revealed that the feed coke's microstructure markedly differed from that of the extuyere coke, indicating a correlation between this study and the previous work.

5.3- CARBONISED SUCROSE- SUC(800) AND SUC(800)K

The short-range ordered structure exhibited by the SUC(800) sample is as would be expected for a non-graphitising carbon. However, due to the presence of areas with extensive structural order and in view of the non-graphitising nature of sucrose a study was made of various samples from the carbonisation thermal decomposition course (section 4.9 and 5.7).

The subsequent XRD analysis of the SUC(800) sample was consistent with the non-graphitised carbon structure observed by HREM. The two overlapping peaks centered at 0.445nm and 0.486nm corresponding with the 0.44nm typical value and 0.41-0.54nm interplanar spacings range measured from HREM. There was no individual peak definition for the areas of extensive long-range structural order observed by HREM, it must therefore be concluded that the signals from these regions were not sufficiently intense, due to their small relative proportion, and are encompassed within the interplanar spacings range of the trace.

After exposure to potassium vapour, the XRD analysis of the SUC(800) sample confirmed the structural ordering observed by HREM. A wide range of lattice spacings were evident both before and after exposure to potassium vapour, however, not only did the peaks in the latter (0.359nm) become prominent and evident, in the region corresponding to the observed long-range structural order, but the trace exhibited the peaks in a smaller range of 2θ values, indicative of a more ordered particle size.

No evidence of intercalation compounds were detected by XRD analysis, this does not necessarily mean that no intercalation compounds were formed however. Intercalation compounds are unstable and degrade when exposed to the atmosphere. In the present work such degradation could result on exposure of the samples to the atmosphere during the period of removal from the furnace to analysis by XRD or insertion into the microscope. Examination of the SUC(800)K sample by HREM did reveal the formation of a non-graphitised carbon structure exhibiting an expanded structure (0.35-0.76nm), it must be concluded therefore that the signals from these regions are not sufficiently intense or stable enough to be detected by the XRD equipment.

Microstructural analysis of the SUC(800) and SUC(800)K samples revealed a variety of different microstructures. On exposure to potassium vapour areas of the carbon structure experienced changes which resulted in the ordering of carbon layer planes and in the formation of extensively ordered long-range and convoluted, ribbon-like structures. As with the structural ordering exhibited by the extuyere coke samples, the resultant structural changes observed in the SUC(800) sample are probably a consequence of potassium penetration into the carbonised sucrose microstructure and the subsequent collapse of these expanded lattice planes to a more ordered structure (Hennig, 1952; Ubbelohde, 1957; Carr, 1970; Crespin et al., 1977; Goleczka and Tucker, 1985).

The SEM investigation of the SUC(800) and SUC(800)K

samples revealed a remarkable difference in their macrostructure. The SUC(800) sample exhibited a very smooth external surface with the SUC(800)K sample revealing a macrostructure that consisted of a highly porous honeycomb network, exhibiting high levels of porosity in both the macropore (>50nm) and mesopore (2-50nm) size ranges with the pores varying not only in size but shape.

Prior to exposure with potassium vapour the SUC(800) sample displayed a smooth external surface which at the fractured edges revealed a continuous smooth structure throughout, thus the extent of macrostructural change as a result of exposure to potassium is surprising. From the microanalysis study, the SUC(800) sample revealed a variable composition at a temperature of 800°C, thus, exposure of the sample to potassium vapour, resulting in the formation of a sample with a highly porous nature, may arise as a result of the intermediate compounds present being readily attacked by the potassium vapour.

Thermogravimetric analysis of the SUC(800) sample exhibited a single, broad peak, for the rate of sample weight loss. Commencing at 500°C, peaking at 628°C and ending at 675°C this peak accounted for a weight reduction of 93.5%. Overall a weight reduction of 98.5% was recorded, including a 5% reduction occurring within the temperature range 50-500°C. The SUC(800)K TGA trace exhibited three peaks and an overall weight reduction of 90%. The first peak accounted for a 5% weight loss (maximum weight loss occurring at 140°C) and exhibited a lower rate of weight loss compared with the second, most dominant peak. This

peak accounted for 79% of the weight loss (maximum weight loss occurring at 515°C) with the third peak accounting for the remaining 6% (maximum weight loss occurring at 840°C). The presence of potassium therefore not only causes the commencement of weight loss to occur at a lower temperature, implying that the presence of the potassium is having a catalytic effect on the weight loss reaction but also, in this case, is causing the decomposition reaction to occur as a three stage process, probably arising as a result of the potassium exposed carbonised material forming various intermediate compounds that require different temperatures to bring about thermal decomposition. The total weight reduction also varies between the SUC(800) and SUC(800)K samples the difference resulting from the inability of all the potassium intermediate compounds to decompose within the temperature range of this TGA study.

5.4- CARBONISED POLYVINYL ACETATE- PVA(800) AND PVA(800)K

Analysis of the graphitisable carbon, PVA(800), revealed an extensively well-ordered long-range structure both prior to and after exposure to potassium vapour. It was expected that the PVA carbonised sample would exhibit a structure representative of a graphitisable carbon, but the degree of structural ordering obtained from carbonisation at 800°C proved quite surprising. Due to the advanced structural order observed in the unexposed carbonised material it was not possible to obtain meaningful data from HREM as to whether the potassium vapour had any influence on the microstructure of the PVA(800) sample.

The interplanar spacings observed for the long and short-range order, both before and after exposure to potassium vapour were indistinguishable, although after exposure to potassium vapour, areas of new convoluted, ribbon-like structural order became apparent, to a much greater extent, than was found in the corresponding sucrose experiment. These initial studies with the carbonised sucrose (SUC(800)) and PVA (PVA(800)) revealed a convoluted structural order, but only after exposure of the carbonised materials to potassium vapour. This convoluted structure was thus thought to evolve as a result of exposure to potassium vapour and be indicative of alkali attack.

The x-ray diffraction study of the exposed and unexposed PVA(800) sample revealed a very similar trace for both samples. The resultant XRD trace after exposure of the PVA(800) sample to potassium vapour revealed an increased peak definition, than that obtained for the unexposed PVA(800) sample, the difference being that the 0.345nm peak displayed by the unexposed PVA(800) had become split into three peaks, of decreasing intensity, centered at 0.341, 0.346 and 0.365nm respectively. The two, dominant, overlapping peaks were still those which gave lattice spacings of 0.345nm and 0.469nm, confirming the indistinguishability of the two samples, consistent with the HREM observations.

Investigation of the PVA(800) macrostructure by SEM, revealed a smooth external surface exhibiting cracks and some pitting. Lamellar layers were evident where the smooth

external surface had been removed. Examination of the PVA(800)K sample revealed cracks; composed of a folded lamellar structure, fractures, porosity and large holes leading to the interior. Although morphological differences exist between the carbonised and the potassium exposed PVA sample, they are not as profound as the differences revealed for the SUC(800) and SUC(800)K samples. Thus, from the SEM investigation the SUC(800) sample would be expected to be more susceptible to alkali attack.

A weight reduction of 98% was recorded for the thermogravimetric analysis of the PVA(800) sample. Commencing at 550°C and ending at 740°C, one broad peak was exhibited for the rate of weight loss accounting for 95.5% of weight reduction, the remainder, 2.5%, occurred within the temperature range 140-530°C. Examination of the PVA(800)K TGA trace also revealed one peak, for the rate of sample weight loss. Accounting for a 90.5% weight loss, the peak commenced at 430°C and ended at 660°C. Overall a weight reduction of 93% was recorded, including a 2.5% reduction between 135 and 430°C. Thus, as was found from the corresponding TGA study of the SUC(800) and SUC(800)K samples, the presence of potassium results in a reduced total weight loss and the catalytic effect of the potassium on the PVA sample results in a lowering of the starting temperature of decomposition by approximately 120°C.

5.5- FLAME PHOTOMETRY AND POTASSIUM UPTAKE MEASUREMENTS

From the HREM, XRD and SEM studies, both the

graphitisable and non-graphitisable carbonised materials appear susceptible to alkali attack, with the potassium vapour influencing their structural development by creating areas of localised ordering within the carbon matrix and altering the macrostructure of the non-graphitisable sample quite significantly. Initial quantitative potassium uptake and flame photometry measurements undertaken to determine which, if any, of the two carbonised samples was more susceptible to alkali attack, inferred the non-graphitisable sample, SUC(800), to be the more susceptible.

The mass differences observed between the two techniques of potassium uptake measurement and flame photometry, appear to be considerable (28.580mg and 33.300mg of potassium/100mg of sample compared to 4.484mg and 4.576mg of potassium/100mg of sample for the PVA(800) and SUC(800) samples respectively). Potassium uptake measurements are made directly as the sample is being heated and exposed to potassium vapour, the examination continuing until the weight increase recorded by the sample is constant. Preparation of the exposed carbonised samples for analysis by the technique of flame photometry requires the need for continuous handling of the sample to allow the collection of several supernatant volumes. The two techniques are thus not directly comparable but generally the flame photometry results reveal a trend as to the carbonised materials susceptibility to potassium vapour.

Measurements (potassium uptake), carried out on three different samples of feed coke, revealed a lower susceptibility to potassium uptake (4.7-12.8mg of

potassium/100mg of sample) than both the 800°C carbonised sucrose and PVA. Influence from the annealing process that such feed cokes receive during their preparation has previously been found to improve their resistance to alkali attack (Goleczka and Tucker, 1985) and improve their thermo-mechanical stability. Thus although the feed cokes do not exhibit a carbon matrix with extensive structural order, they are less susceptible to alkali attack than the unannealed carbons.

The experimental evidence, from this study, would appear to indicate that the structural order of the carbonised PVA increases the material's resistance to alkali attack and that the affinity of the potassium reaction overcomes the mechanical stresses which are opposed to interlayer cross-linking separation in the carbonised sucrose. This result is in accord with the findings of Hawkins et al. (1974) who showed that carbons with high degrees of graphitisation, as in the carbonised PVA material, exhibited better resistance to alkali attack.

5.6- EFFECT OF INERT CARRIER GASES

In order to determine if the type of inert carrier gas used, altered or had any significant effect on the microstructure of the potassium exposed carbonised materials, various inert carrier gases were used when exposing the carbonised materials to potassium vapour.

Examination, by HREM and XRD, of the effects of the different inert carrier gases on the carbonised sucrose and

PVA samples when exposed to potassium vapour revealed no significant differences in any of the microstructural forms and appeared to be independent of the inert carrier gas used. It has been reported (Shevlin, 1987) that the effects of the non-reacting carrier gases on coke properties can be profound but this is thought to be more significant in the macrostructural properties of the material.

5.7- LOW TEMPERATURE 'CARBONISATION' OF SUCROSE- SUC, SUC(150), SUC(250), SUC(300), SUC(500), SUC(700) AND SUC(1000)

The low temperature 'carbonised ' samples were subject to beam radiation damage in the electron microscope, although some areas remained sufficiently unaffected and unaltered to allow lattice images to be successfully obtained.

The long-range ordered structure evident at 150°C and 250°C was assumed to be an intermediate organic decomposition product of sucrose rather than an indication of graphitic structural order. It would appear that the organic crystalline structure of the sucrose starting material is gradually destroyed as the temperature is increased. Evidence to support this incomplete decomposition proposal was obtained from the microanalysis of the calcined sucrose products which revealed a high hydrogen content (C:H=2:1) for the SUC(300) sample, whereas a much higher ratio was found for carbonisation at 800°C (C:H=24:1) as would be expected. Ordering of the structure has been shown to occur as the percentage carbon content

rises from C:H=2:1 to C:H=24:1, between 300 and 800°C respectively, via the alignment, of layer planes to form localised graphitic regions that are unable to join together to form larger graphitic areas, carbonisation of the sucrose material to 1000°C revealing no significant structural differences, by HREM, compared with carbonisation to 800°C.

Initially, from the SUC(800) and PVA(800) study, the observed convoluted, ribbon-like structures were thought to evolve as a result of exposure to potassium vapour and to be the result of a residue compound rather than intercalation to a more ordered structure. HREM examination of the SUC(250) and SUC(500) samples revealed similar convoluted structures, prior to exposure with potassium vapour, although to a much lesser extent. Thus the potassium vapour in the SUC(800) and PVA(800) samples would appear to have enhanced the formation of these convoluted, ribbon-like areas rather than caused their development.

Examination of the low temperature 'carbonisation' sucrose samples by XRD revealed a broad, single peak, exhibiting a wide range of carbon lattice spacings for the SUC(300) and SUC(500) samples. The interplanar spacings centered around the 0.501nm and 0.496nm peaks respectively, were consistent with the non-graphitised carbon structure observed by HREM, the long-range ordered structure, in both samples, being encompassed by the broad single peak but showing no individual peak definition. XRD analysis of the SUC(1000) sample confirmed not only that the peaks in the region 0.345nm and 0.315nm became prominent and evident, in

the region corresponding to the observed long-range structural order, but the trace exhibited the peaks in a smaller range of 2θ values, indicative of a more ordered particle size consistent with the HREM observations.

Thermogravimetric analysis of the SUC, SUC(150), SUC(250) and SUC(300) samples exhibited more than one peak for the rate of sample weight loss. The onset of combustion for each of the samples starting at approximately 250°C with the commencement of weight loss for the SUC(500) and SUC(1000) shifting to 500°C, the total weight loss occurring within the temperature range 500°C to 700°C and as a one stage process at SUC(1000).

For the low temperature 'carbonised' samples, the decomposition reaction occurs in numerous stages. This is as a result of the 'carbonised' material forming various intermediate compounds that require different temperatures to bring about thermal decomposition. As the temperature at which the samples are carbonised and prepared is increased so these intermediate compounds disappear from the trace, having already reached their thermal decomposition temperature during preparation.

5.8- CONCLUSIONS

Reaction of the feed cokes and carbonised sucrose and PVA materials with potassium vapour appears to cause enhanced localised ordering. This ordering of the carbon structure can be extensive, with the greatest degree of structural ordering being observed when the carbonised

sucrose was exposed to potassium vapour. The most severe morphological changes in macrostructure were observed by SEM when the SUC(800) sample was exposed to potassium vapour and the smooth external surface was totally altered to reveal a honeycomb porous structure. Potassium uptake and flame photometry measurements undertaken to determine, which, if any, of the carbonised materials was more susceptible to alkali attack implyed that the non-graphitising carbonised material 'picked up' more potassium. It is thus inferred from this investigation that the non-graphitising carbonised materials are more susceptible to alkali attack.

The degree and extent of structural ordering observed in the carbonised PVA sample was far greater than that expected. It was thought that the carbonised PVA sample would exhibit a structure representative of a graphitisable carbon, but the degree of structural ordering obtained from carbonisation at 800°C proved quite surprising.

Examination of the SUC(800) and PVA(800) carbonised samples revealed convoluted, ribbon-like structures that were initially thought to evolve as a result of exposure to potassium vapour and to be the result of a residue compound rather than intercalation to a more ordered structure. HREM examination of the SUC(250) and SUC(500) samples revealed similar convoluted structures, prior to exposure with potassium vapour. Thus the potassium vapour in the SUC(800) and PVA(800) carbonised samples would appear to have enhanced the formation of these convoluted, ribbon-like areas rather than caused their development.

The observed changes in microstructure, after exposure of the carbonised samples to potassium vapour, were concluded to be independent of the inert carrier gas used.

CHAPTER SIX

RESULTS FOR THE SAMPLES PREPARED VIA A CLOSED CARBONISATION SYSTEM

6.1- INTRODUCTION

This chapter reports on the results obtained for the group of compounds carbonised via a closed carbonisation system (table 6.1) and their subsequent exposure to potassium vapour. Each sample was studied by TEM, SEM, XRD and TGA to allow analysis of the microstructural aspects of the different carbonised materials and the subsequent changes induced therein. The chapter then concludes with a tabulated summary of the TEM and XRD results (table 6.3).

COMPOUND	HEATING RATE	FINAL TEMP	SOAK PERIOD	ATM	CODE
Anthracene	3°C/min	800°C	2hr	N_2	Anthra 800_3
Anthracene	20°C/min	800°C	2hr	N_2	Anthra 800_{20}
Anthracene	1°C/min	800°C	2hr	Ar	$Anthra_1$
Chrysene	3°C/min	800°C	2hr	N_2	Chrysene 800_3
Chrysene	20°C/min	800°C	2hr	N_2	Chrysene 800_{20}
Fluoranthene	3°C/min	800°C	2hr	N_2	Fluor 800_3
Fluoranthene	20°C/min	800°C	2hr	N_2	Fluor 800_{20}
Phenanthrene	20°C/min	800°C	2hr	N_2	Phen 800_{20}
Pyrene	3°C/min	800°C	2hr	N_2	Pyrene 800_3
Pyrene	20°C/min	800°C	2hr	N_2	Pyrene 800_{20}
p-Terphenyl	3°C/min	800°C	2hr	N_2	Terphen 800_3
p-Terphenyl	20°C/min	800°C	2hr	N_2	Terphen 800_{20}

Table 6.1 The conditions of preparation for the aromatic hydrocarbons carbonised via a closed carbonisation system.

6.2- ANALYSIS OF CARBONISED ANTHRACENE

Graphitisation of anthracene at 3000°C is known to result in the formation of a graphitising carbon (Kinney et al., 1957). In this study three carbonised samples were prepared and examined.

6.2.1- TRANSMISSION ELECTRON MICROSCOPY (TEM)

The Anthra 800_3 and Anthra 800_{20} samples both exhibited a non-graphitised carbon structure (L_a=1-7nm) with lattice spacings in the range 0.33-0.39nm and a typical value of 0.35nm (L_c=0.7-2.5nm) (figure 6.1).

The $Anthra_1$ sample revealed a non-graphitised carbon structure (L_a=1-4.5nm) with lattice spacings in the range 0.34-0.41nm and a typical value of 0.36nm (L_c=0.7-3nm). The sample also exhibited a long-range ordered structure (L_a=5-17nm) with interplanar spacings in the range 0.33-0.37nm and a typical value of 0.34nm (L_c=2-13nm) (figure 6.2).

6.2.2- SCANNING ELECTRON MICROSCOPY (SEM)

Both the Anthra 800_3 and Anthra 800_{20} samples exhibited a smooth external surface with no detectable cracks or pores. The samples also revealed sheet-like lamellar layers where the smooth external surface had been removed (figure 6.3).

Examination of the $Anthra_1$ sample by SEM revealed a smooth external surface displaying large cracks with no visible evidence of pores (figure 6.4).

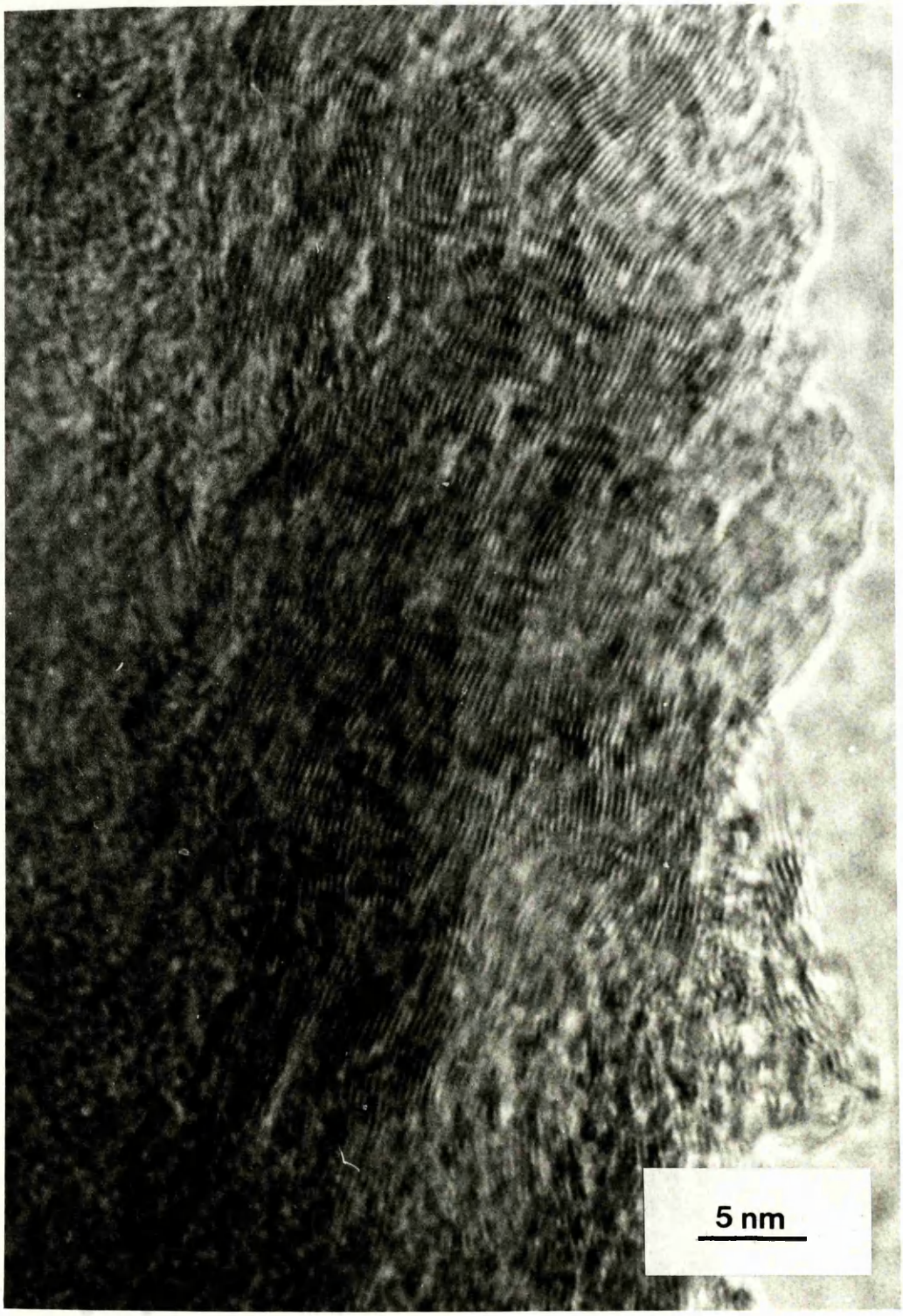

Figure 6.1: HREM representative of the Anthra 800_3 and Anthra 800_{20} samples showing the non-graphitised carbon structure (0.33-0.39nm).

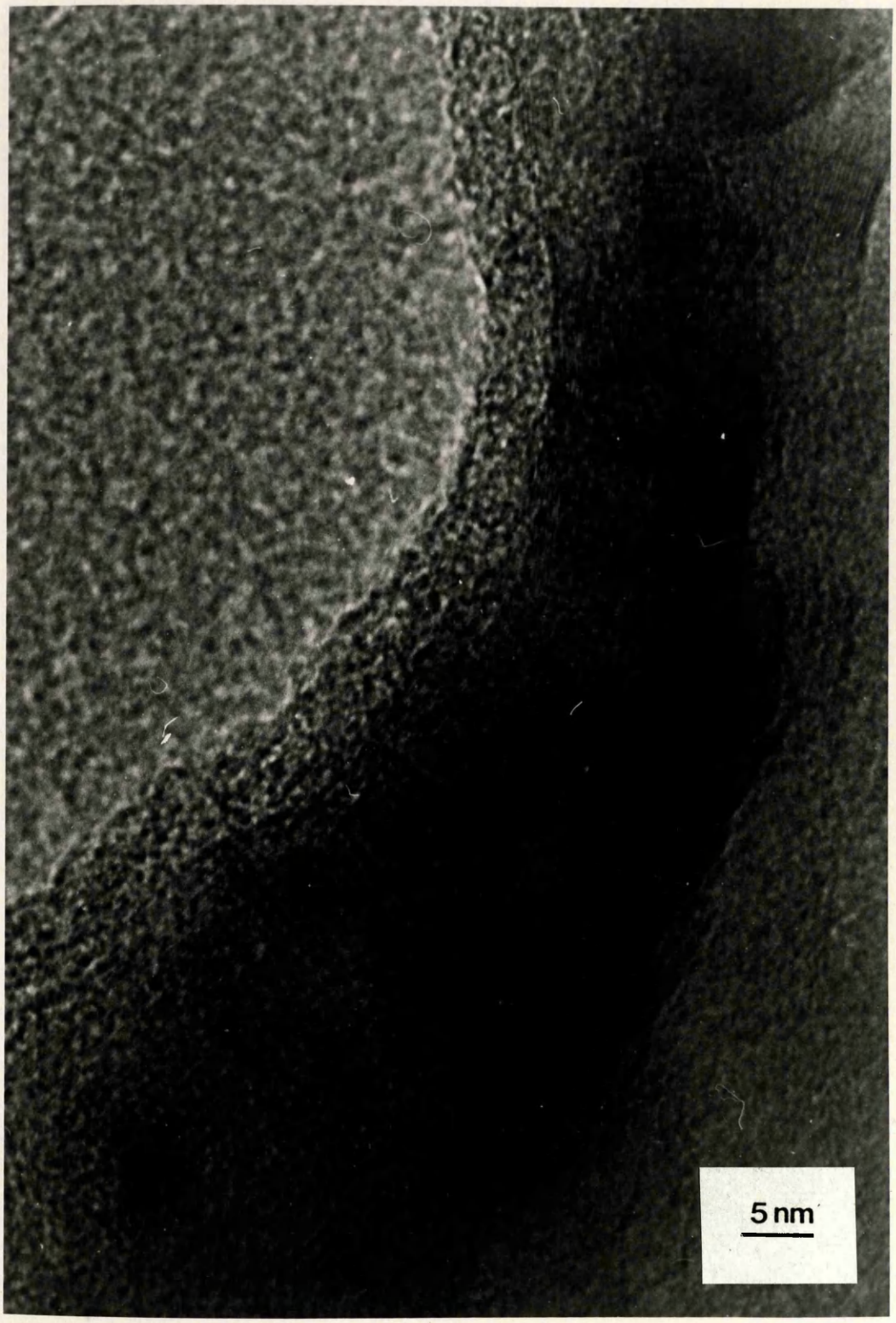

Figure 6.2: HREM revealing the long-range structural order (0.34nm) exhibited by the $Anthra_1$.

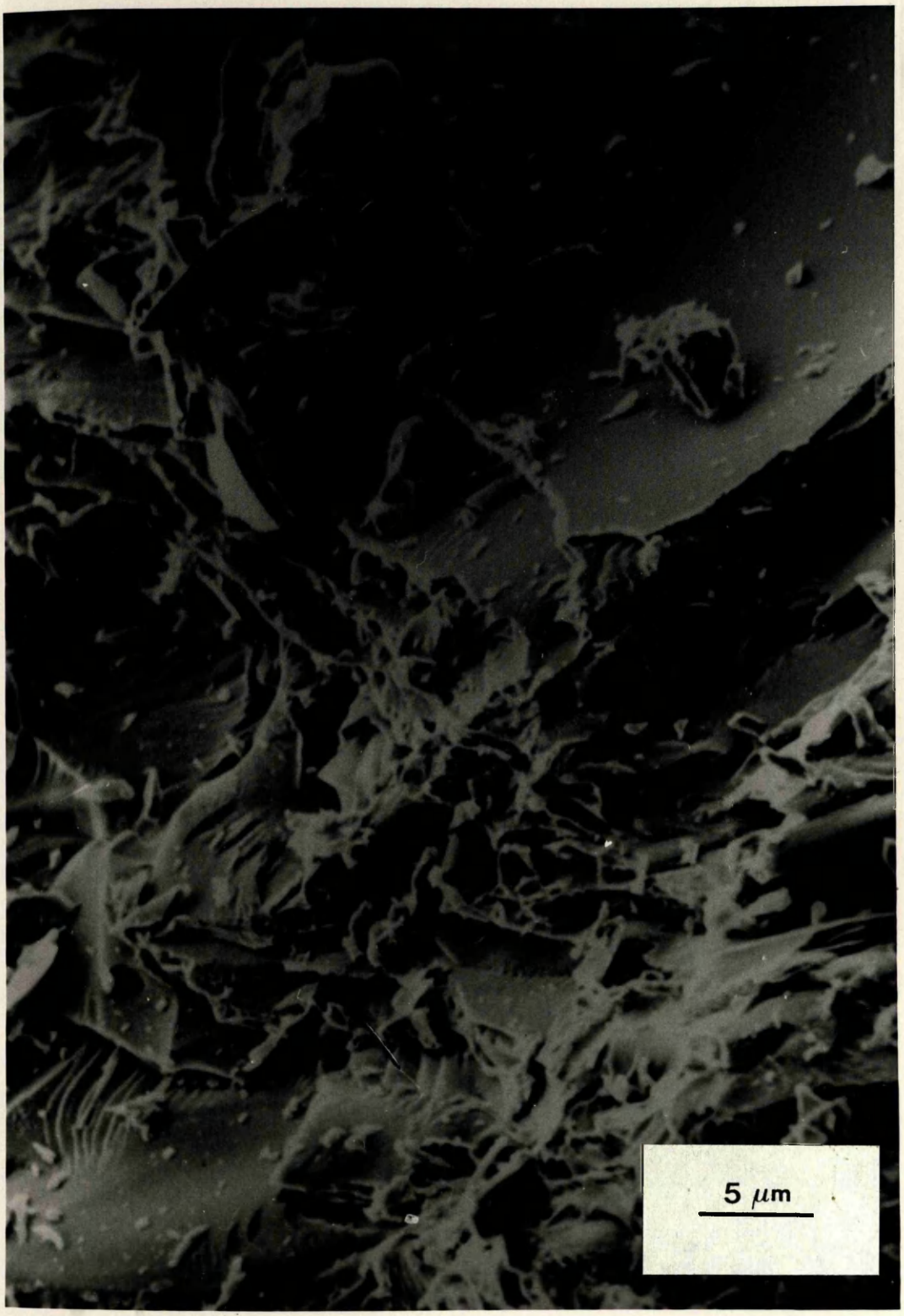

Figure 6.3 : SEM of the Anthra 800_3 and Anthra 800_{20} samples showing a smooth external surface and lamellar layers.

Figure 6.4: SEM of the Anthra$_1$ sample displaying a smooth external surface with large cracks.

6.2.3- POWDER X-RAY DIFFRACTION ANALYSIS (XRD)

One broad peak was evident from both the Anthra 800_3 and Anthra 800_{20} x-ray diffraction traces (figure 6.5). The peak, in both cases, was centered on (29.8°) 0.348nm and fell within the interplanar spacings range (40.4-17.0°) 0.259-0.606nm.

The $Anthra_1$ x-ray diffraction trace exhibited three peaks within the interplanar spacings range (40.0-16.0°) 0.262-0.643nm (figure 6.6). The most intense peak was centered on (21.1°) 0.513nm. The second and third peaks, in order of decreasing intensity, were centered on (25.6°) 0.404nm and (28.6°) 0.362nm respectively.

6.3.- EFFECT OF POTASSIUM ON CARBONISED ANTHRACENE

6.3.1- TRANSMISSION ELECTRON MICROSCOPY (TEM)

After exposure to potassium vapour, the Anthra 800_3K and Anthra $800_{20}K$ samples both exhibited a non-graphitised carbon structure (L_a=1-5.5nm) with lattice spacings in the range 0.34-0.48nm and a typical value of 0.36nm (L_c=0.7-4nm). Both samples also exhibited a long-range ordered structure (L_a=6-27nm) with interplanar spacings of 0.35nm (L_c=2.5-9nm).

The $Anthra_1K$ sample revealed three different types of microstructure. A non-graphitised carbon structure (L_a=1-4nm) with lattice spacings in the range 0.34-0.48nm and a typical value of 0.36nm (L_c=0.7-3.5nm), a long-range ordered structure (L_a=5-24nm) with interplanar spacings in

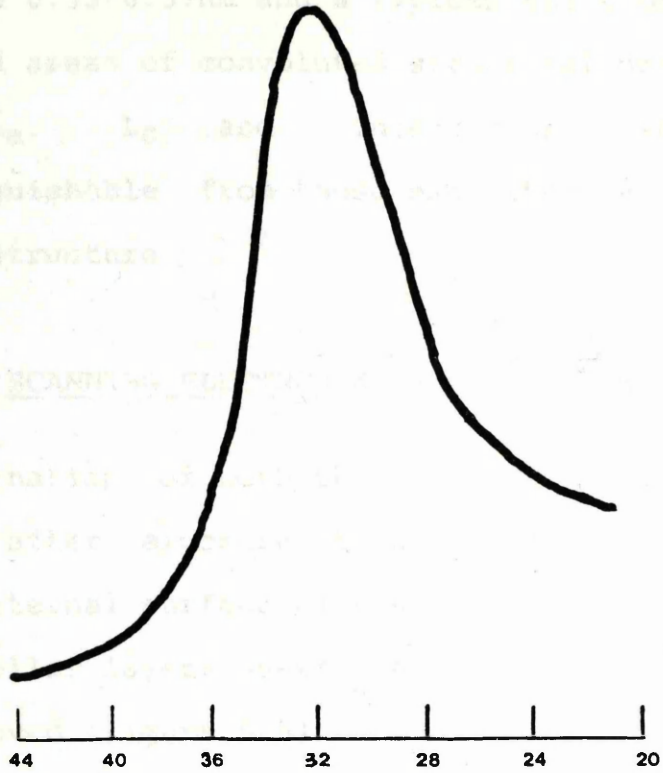

Figure 6.5: XRD trace representative of the Anthra 800_3 and Anthra 800_{20} samples.

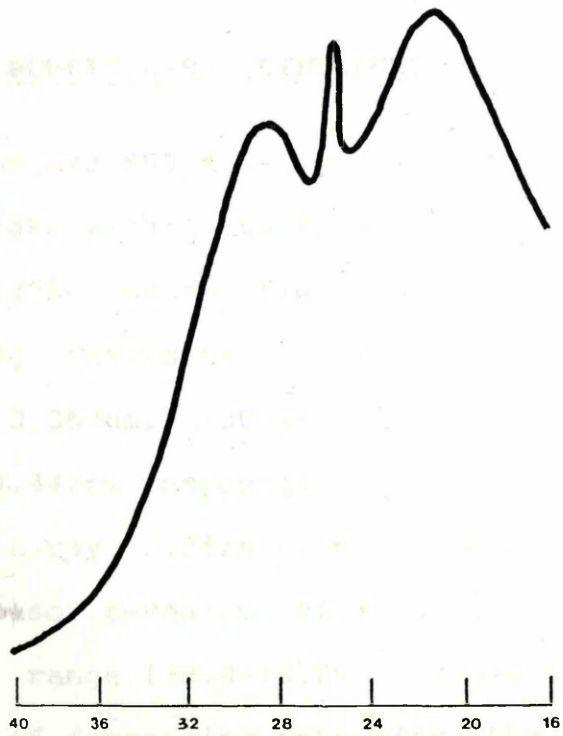

Figure 6.6: XRD trace of the $Anthra_1$ sample.

the range 0.33-0.37nm and a typical value of 0.34nm (L_c=2-11nm) and areas of convoluted structural order (figure 6.7) with L_a, L_c and interplanar spacing values indistinguishable from those exhibited by the long-range ordered structure.

6.3.2- SCANNING ELECTRON MICROSCOPY (SEM)

Examination of both the Anthra 800_3 and Anthra 800_{20} samples after exposure to potassium vapour revealed a smooth external surface displaying large cracks and sheet-like lamellar layers where the smooth external surface had been removed (figure 6.8).

The $Anthra_1K$ sample exhibited a smooth external surface displaying large cracks and holes leading to the interior (figure 6.9).

6.3.3- POWDER X-RAY DIFFRACTION ANALYSIS (XRD)

The Anthra 800_3K x-ray diffraction trace revealed five sharp peaks within the interplanar spacings range (38.0-16.0°) 0.275-0.643nm (figure 6.10). The peaks, in order of decreasing intensity, were centered on (29.4°) 0.353nm, (28.2°) 0.367nm, (30.4°) 0.341nm, (27.4°) 0.378nm and (23.3°) 0.443nm respectively.

The x-ray diffraction trace for the Anthra $800_{20}K$ sample also revealed five peaks within an interplanar spacings range (38.0-16.0°) 0.275-0.643nm (figure 6.11). In order of decreasing intensity, the most intense peak was centered (30.2°) 0.344nm. Of the four peaks remaining,

Figure 6.7: HREM of the Anthra$_1$K sample showing the convoluted and long-range structural order (0.33-0.37nm).

Figure 6.8: SEM of the Anthra 800_3K and Anthra $800_{20}K$ samples displaying a smooth external surface with large cracks and sheet-like lamellar layers.

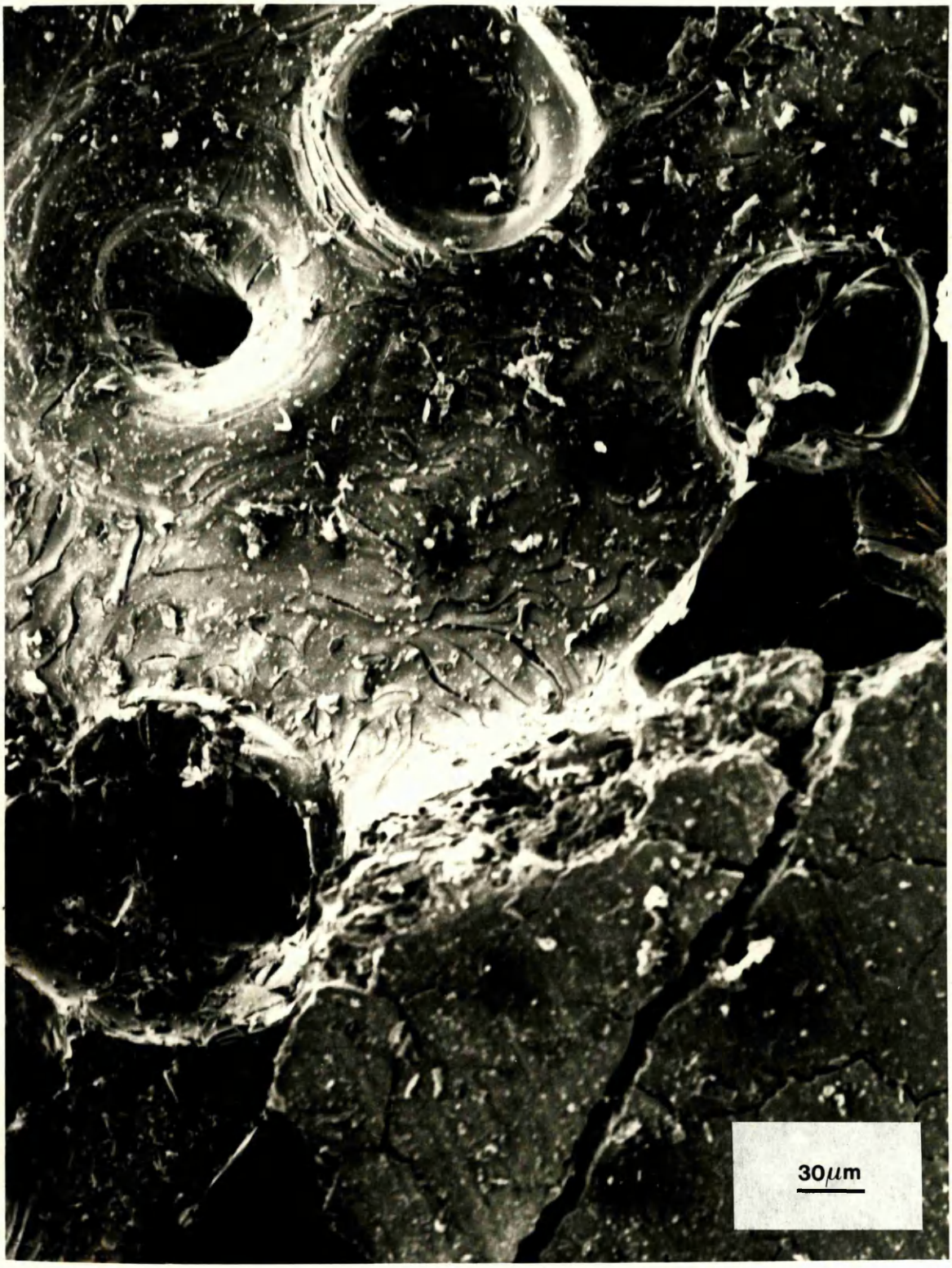

Figure 6.9: SEM of the Anthra 800₁K sample showing the large cracks and holes leading to the interior.

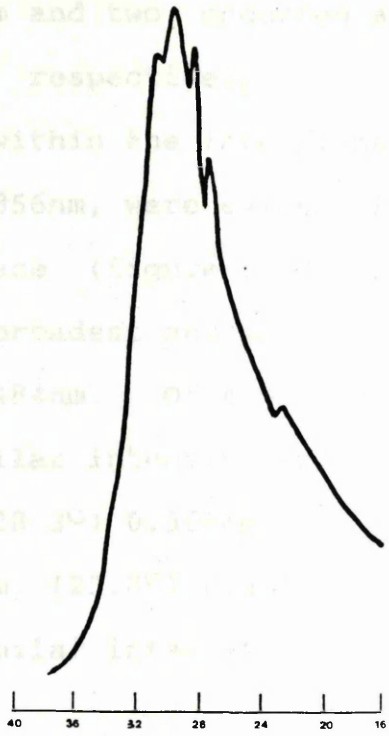

Figure 6.10: XRD trace of the Anthra 800_3K sample.

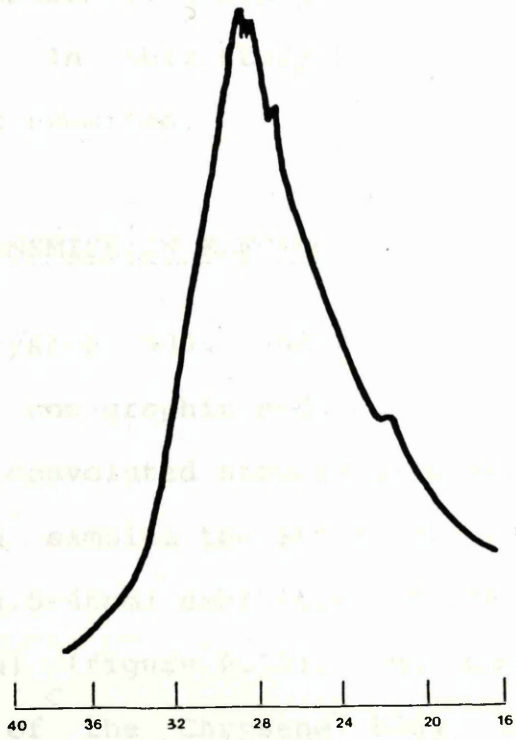

Figure 6.11: XRD trace of the Anthra 800_{20}K sample.

two exhibited a similar intensity at (29.8°) 0.348nm and (29.4°) 0.353nm and two occurred at (27.0°) 0.383nm and (21.6°) 0.478nm respectively.

Six peaks, within the interplanar spacings range (40.0-12.0°) 0.262-0.856nm, were evident from the $Anthra_1K$ x-ray diffraction trace (figure 6.12). In order of decreasing intensity, the broadest and most intense peak was centered on (21.3°) 0.484nm. Of the five peaks remaining, two exhibited a similar intensity and were centered at (29.9°) 0.347nm and (28.3°) 0.366nm with the three centered at (26.6°) 0.389nm, (25.8°) 0.401nm and (25.1°) 0.412nm also displaying a similar intensity.

6.4- ANALYSIS OF CARBONISED CHRYSENE

Graphitisation of chrysene at 3000°C is known to result in the formation of a non-graphitising carbon (Sharkey et al., 1966). In this study two carbonised samples were prepared and examined.

6.4.1- TRANSMISSION ELECTRON MICROSCOPY (TEM)

The Chrysene 800_3 and Chrysene 800_{20} samples both revealed a non-graphitised carbon structure and areas exhibiting convoluted structural order.

In both samples the areas of convoluted structural order (L_a=6.5-46nm) exhibited lattice spacings of 0.34nm (L_c=3.2-12nm) (figure 6.13). The non-graphitised carbon structure of the Chrysene 800_3 sample (L_a=1-4.5nm) exhibited lattice spacings in the range 0.33-0.42nm with

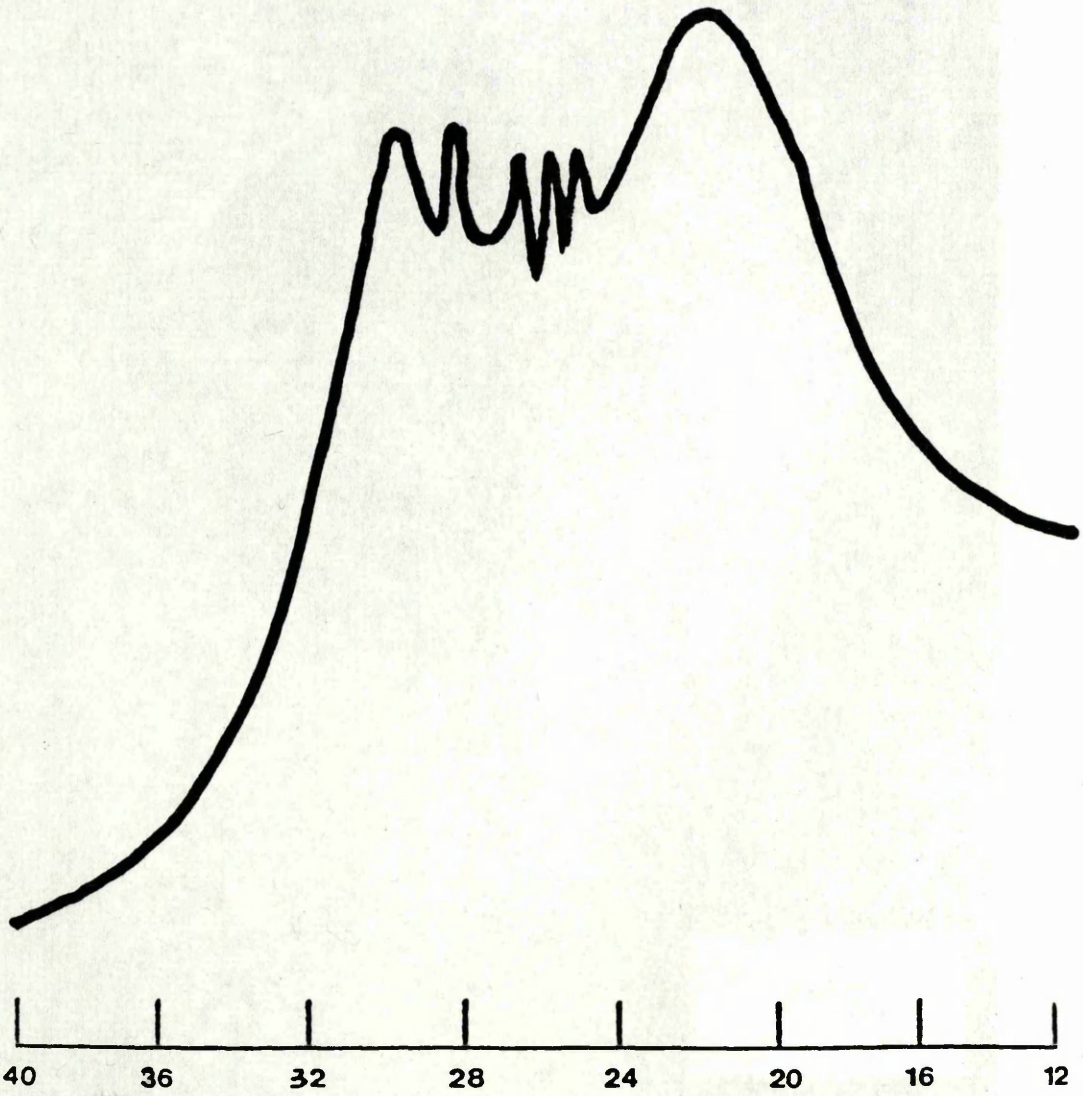

Figure 6.12: XRD trace of the Anthra$_1$K sample.

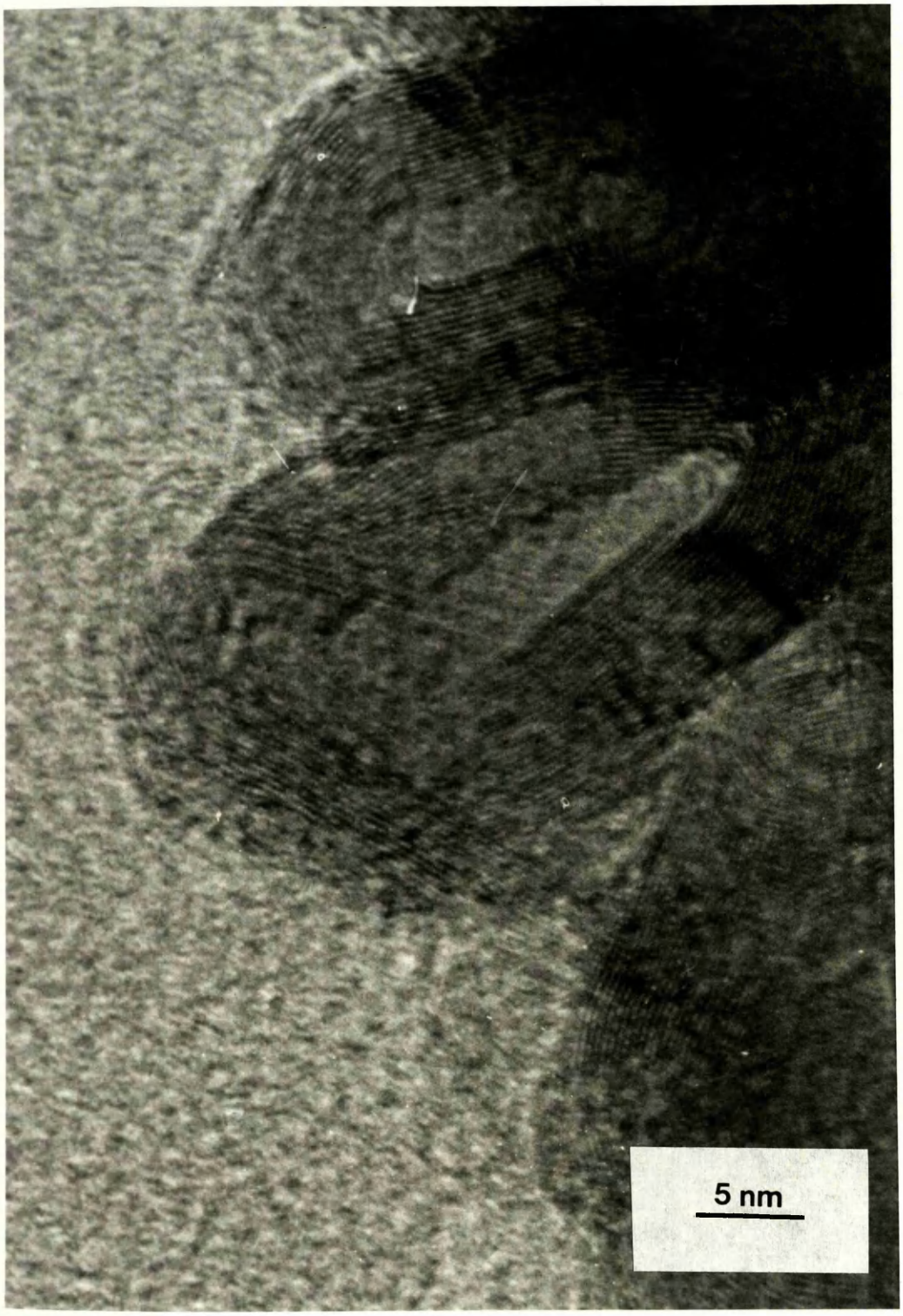

Figure 6.13: HREM of the convoluted structural order exhibited by both the Chrysene 800_3 and Chrysene 800_{20} samples (0.34nm).

a typical value of 0.39nm (L_c=0.66-3nm) (figure 6.14). The non-graphitised carbon structure of the Chrysene 800_{20} sample (L_a=1-5nm) revealed interplanar spacings in the range 0.34-0.48nm with a typical value of 0.44nm (L_c=0.34-3nm).

6.4.2- SCANNING ELECTRON MICROSCOPY (SEM)

Examination of both the Chrysene 800_3 and Chrysene 800_{20} samples by SEM revealed a smooth external surface exhibiting deep cracks and holes (figure 6.15). The sample also revealed sheet-like lamellar layers where the smooth external surface had been removed (figure 6.16).

6.4.3- POWDER X-RAY DIFFRACTION ANALYSIS (XRD)

The Chrysene 800_3 sample exhibited six sharp peaks within the interplanar spacings range (36.0-16.0^o) 0.290-0.643nm (figure 6.17). The most intense peak of the x-ray diffraction trace was centered at (29.4^o) 0.353nm. The remaining peaks, in order of decreasing intensity, were centered at (28.7^o) 0.361nm, (30.5^o) 0.340nm, (28.0^o) 0.370nm, (25.9^o) 0.399nm and (20.4^o) 0.505nm, with the latter two peaks exhibiting a similar intensity.

The x-ray diffraction trace for the Chrysene 800_{20} sample exhibited two broad peaks within the interplanar spacings range (40.8-15.8^o) 0.257-0.651nm (figure 6.18). The most intense peak of the trace was centered on (30.0^o) 0.346nm with the remaining peak centered at (22.0^o) 0.469nm.

Figure 6.14: HREM of the Chrysene 800_3 sample showing the non-graphitised carbon structure (0.39nm).

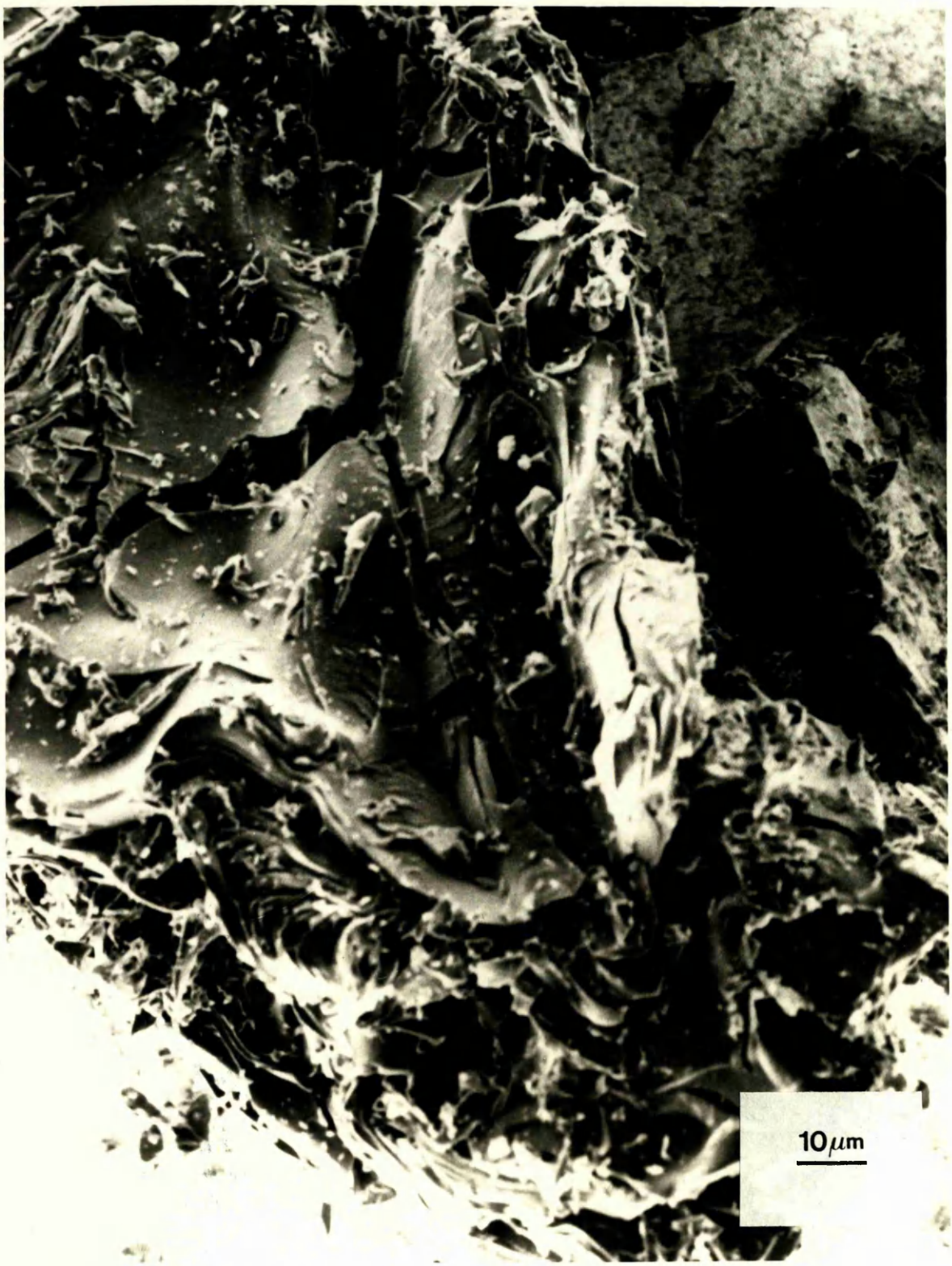

Figure 6.15: SEM of the Chrysene 800_3 and Chrysene 800_{20} samples revealing a smooth external surface with cracks and holes.

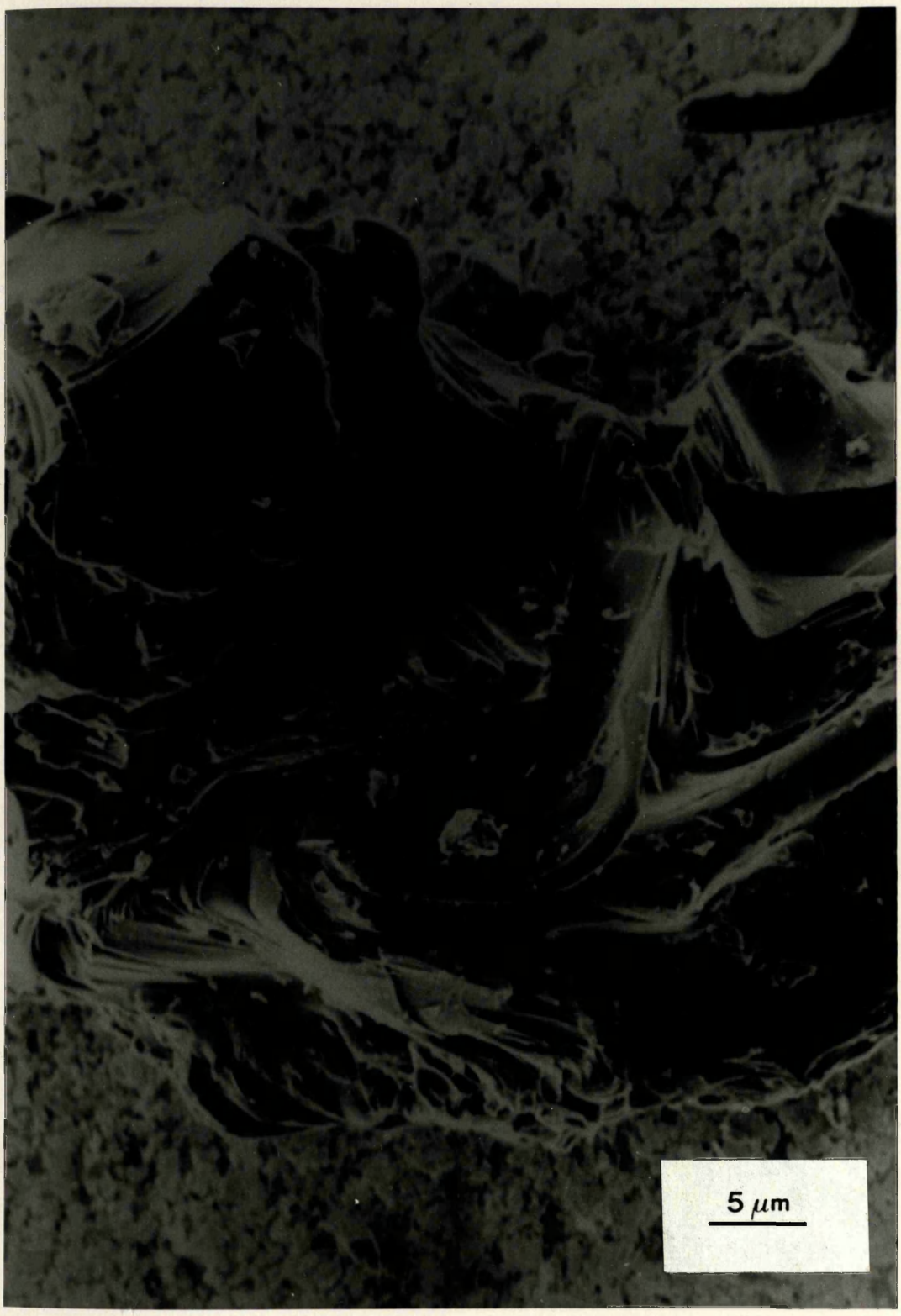

Figure 6.16: SEM of the Chrysene 800_3 and Chrysene 800_{20} samples showing the sheet-like lamellar layers.

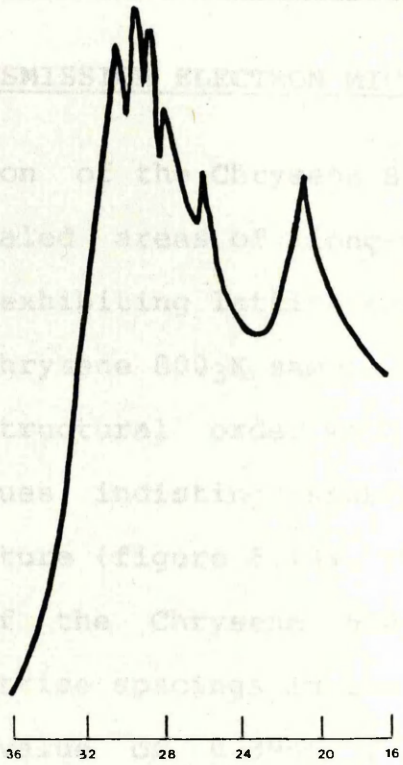

Figure 6.17: XRD trace of the Chrysene 800_3 sample.

Figure 6.18: XRD trace of the Chrysene 800_{20} sample.

6.5- EFFECT OF POTASSIUM ON CARBONISED CHRYSENE

6.5.1- TRANSMISSION ELECTRON MICROSCOPY (TEM)

Examination of the Chrysene 800_3K and Chrysene $800_{20}K$ samples revealed areas of long-range ordered structure (L_a=5-50nm) exhibiting lattice spacings of 0.34nm (L_c=3-15nm). The Chrysene 800_3K sample also displayed areas of convoluted structural order with L_a, L_c and interplanar spacing values indistinguishable from the long-range ordered structure (figure 6.19). The non-graphitised carbon structure of the Chrysene 800_3K sample (L_a=1-3.5nm) exhibited lattice spacings in the range 0.34-0.56nm with a typical value of 0.39nm (L_c=0.68-3nm). The non-graphitised carbon structure of the Chrysene $800_{20}K$ sample (L_a=1-4nm) revealed interplanar spacings in the range 0.34-0.48nm with a typical value of 0.44nm (L_c=0.34-3.5nm).

6.5.2- SCANNING ELECTRON MICROSCOPY (SEM)

Examination of the both the Chrysene 800_3K and Chrysene $800_{20}K$ samples revealed a structure similar to that exhibited by the Chrysene 800_3 and Chrysene 800_{20} samples. A smooth external surface exhibiting deep cracks, holes and shhet-like lamellar layers where the smooth external surface had been removed (figure 6.15 and figure 6.16) respectively.

6.5.3- POWDER X-RAY DIFFRACTION ANALYSIS (XRD)

The Chrysene 800_3K x-ray diffraction trace exhibited

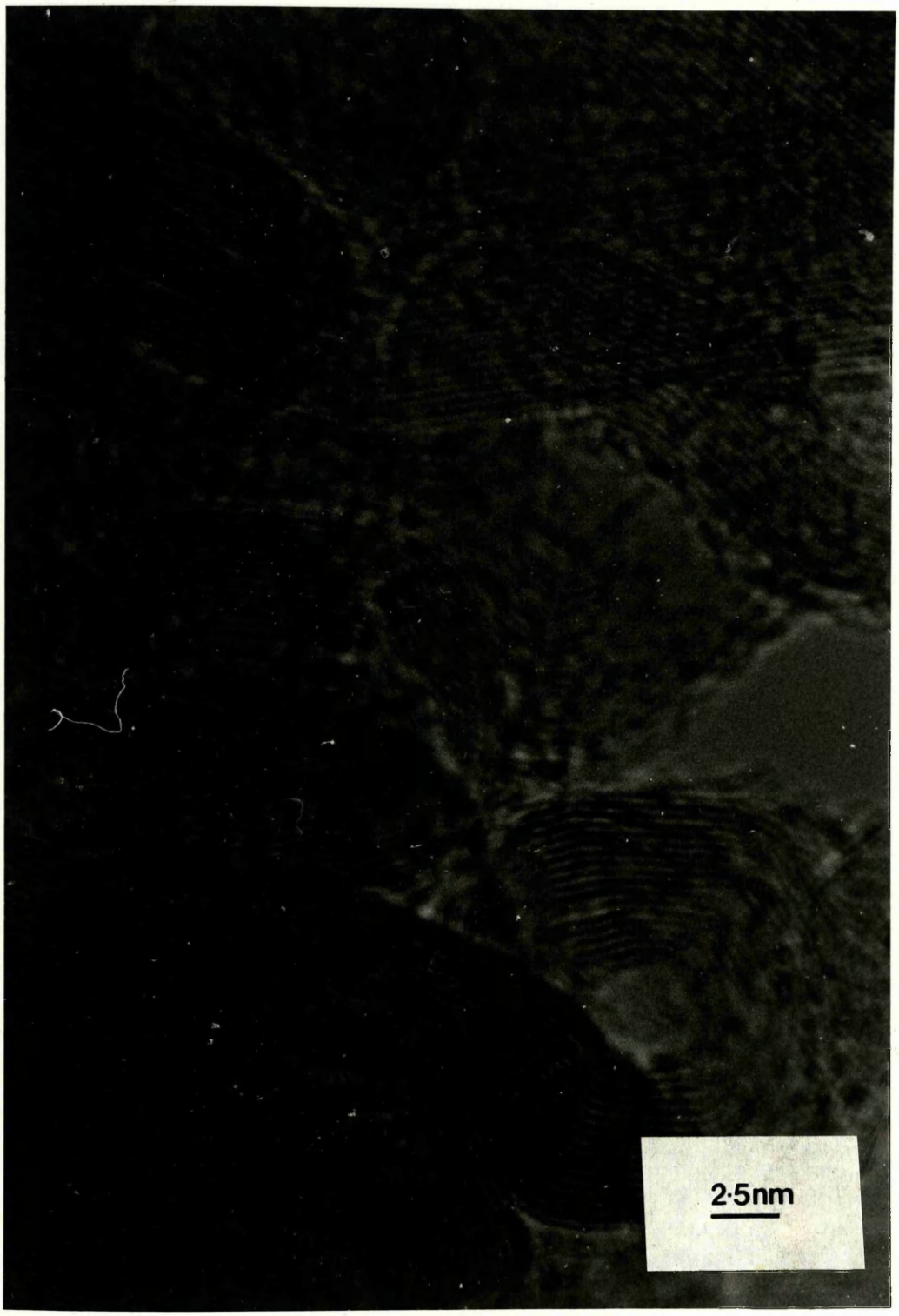

Figure 6.19: HREM exhibiting the long-range and convoluted structural order displayed by the Chrysene 800_3K sample (0.34nm).

eleven peaks within the interplanar spacings range (36.0-16.0°) 0.290-0.643nm (figure 6.20). Three peaks of similar intensity were centered on (30.5°) 0.340nm, (29.9°) 0.347nm and (29.1°) 0.356nm. The remaining peaks, in order of decreasing relative intensity, were centered on (28.5°) 0.364nm, (27.3°) 0.379nm, (25.7°) 0.402nm, (24.7°) 0.419nm, (22.0°) 0.469nm, (21.6°) 0.478nm, (20.9°) 0.494nm and (19.8°) 0.521nm with the two peaks occurring at (22.0°) 0.469nm and (21.6°) 0.478nm displaying a similar intensity.

The x-ray diffraction trace for the Chrysene $800_{20}K$ sample revealed three broad peaks within the interplanar spacings range (40.4-15.8°) 0.259-0.651nm (figure 6.21). The peak of greatest intensity was centered on (29.8°) 0.348nm with the remaining peaks, in order of decreasing intensity, centered on (23.0°) 0.449nm and (21.2°) 0.487nm respectively.

6.6- ANALYSIS OF CARBONISED FLUORANTHENE

Graphitisation of fluoranthene at 3000°C is known to result in the formation of a graphitising carbon (Fitzer et al., 1971). In this study two carbonised samples were prepared and examined.

6.6.1- TRANSMISSION ELECTRON MICROSCOPY (TEM)

Analysis of the Fluor 800_3 sample revealed areas of well-ordered long-range structure (L_a=5-75nm) with interplanar spacings of 0.33nm (L_c=3-25nm) (figure 6.22). In addition areas of convoluted structural order became

Figure 6.20: XRD trace of the Chrysene 800_3K sample.

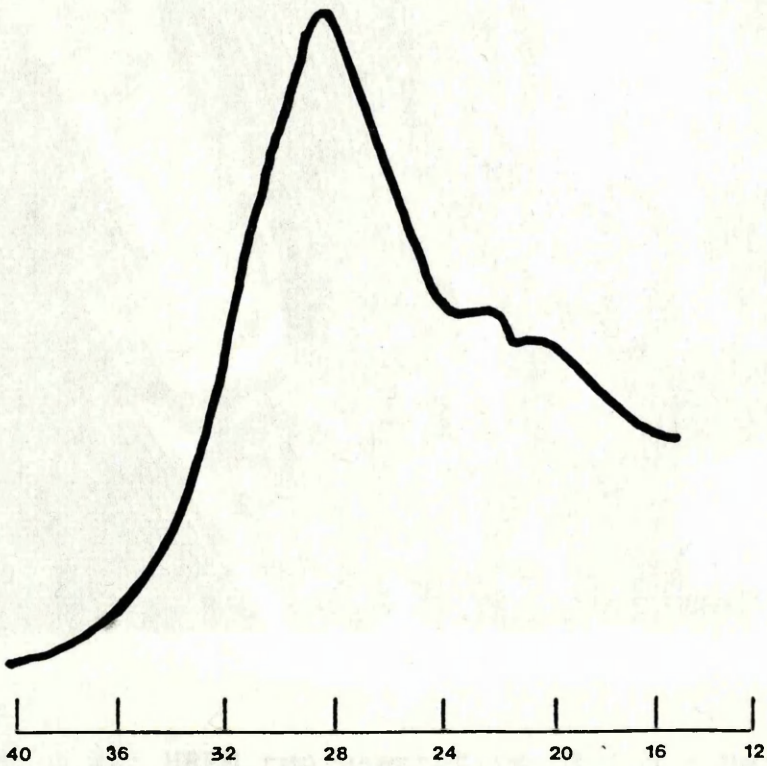

Figure 6.21: XRD trace of the Chrysene $800_{20}K$ sample.

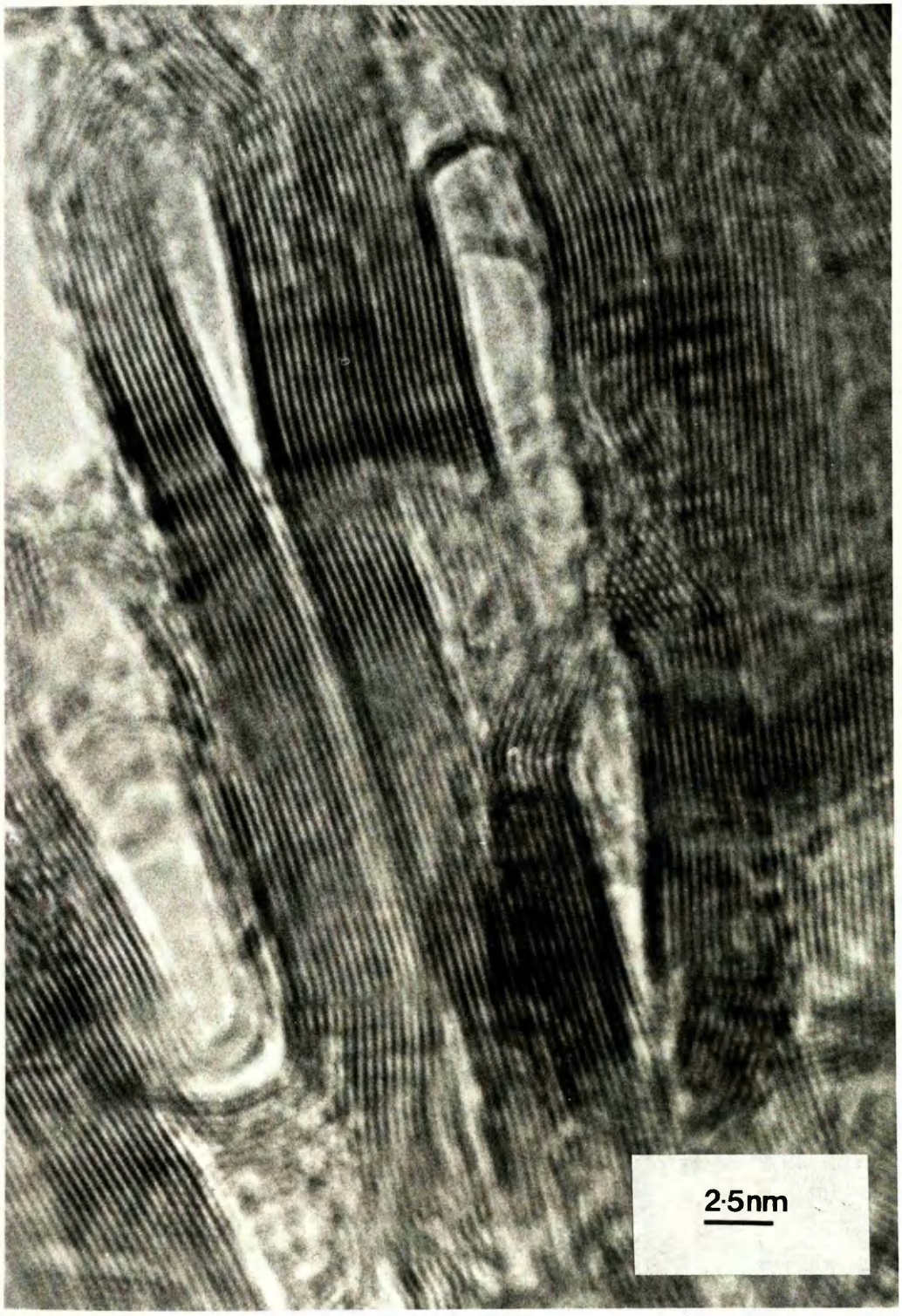

Figure 6.22: HREM representative of the long-range ordered structure (0.33nm) exhibited by the Fluor 800_3, Fluor 800_3K and Fluor $800_{20}K$ samples.

apparent, with L_a, L_c and interplanar spacings values indistinguishable from the long-range ordered structure. The non-graphitised carbon structure (L_a=1-8nm) exhibited lattice spacings within the range 0.34-0.52nm and a typical value of 0.37nm (L_c=0.34-4nm).

Examination of the Fluor 800_{20} sample revealed a non-graphitised carbon structure (L_a=1-6nm) with lattice spacings of between 0.35-0.52nm and a typical value of 0.39nm (L_c=0.35-3.5nm).

6.6.2- SCANNING ELECTRON MICROSCOPY (SEM)

Examination of both the Fluor 800_3 and Fluor 800_{20} samples revealed a smooth external surface with large holes leading to the interior and development of sheet-like lamellar layers visible along the fractured surface (figure 6.23).

6.6.3- POWDER X-RAY DIFFRACTION ANALYSIS (XRD)

The x-ray diffraction trace for the Fluor 800_3 sample revealed two broad peaks within the interplanar spacings range (40.6-15.8^o) 0.258-0.651nm (figure 6.24). The most intense peak of the trace was centered on (22.0^o) 0.469nm with the remaining peak centered at (29.0^o) 0.358nm.

The Fluro 800_{20} x-ray diffraction trace exhibited two peaks within the interplanar spacings range (40.0-16.0^o) 0.262-0.643nm (figure 6.25). The most intense peak of the trace was centered on (21.6^o) 0.478nm with the remaining peak centered at (19.5^o) 0.529nm.

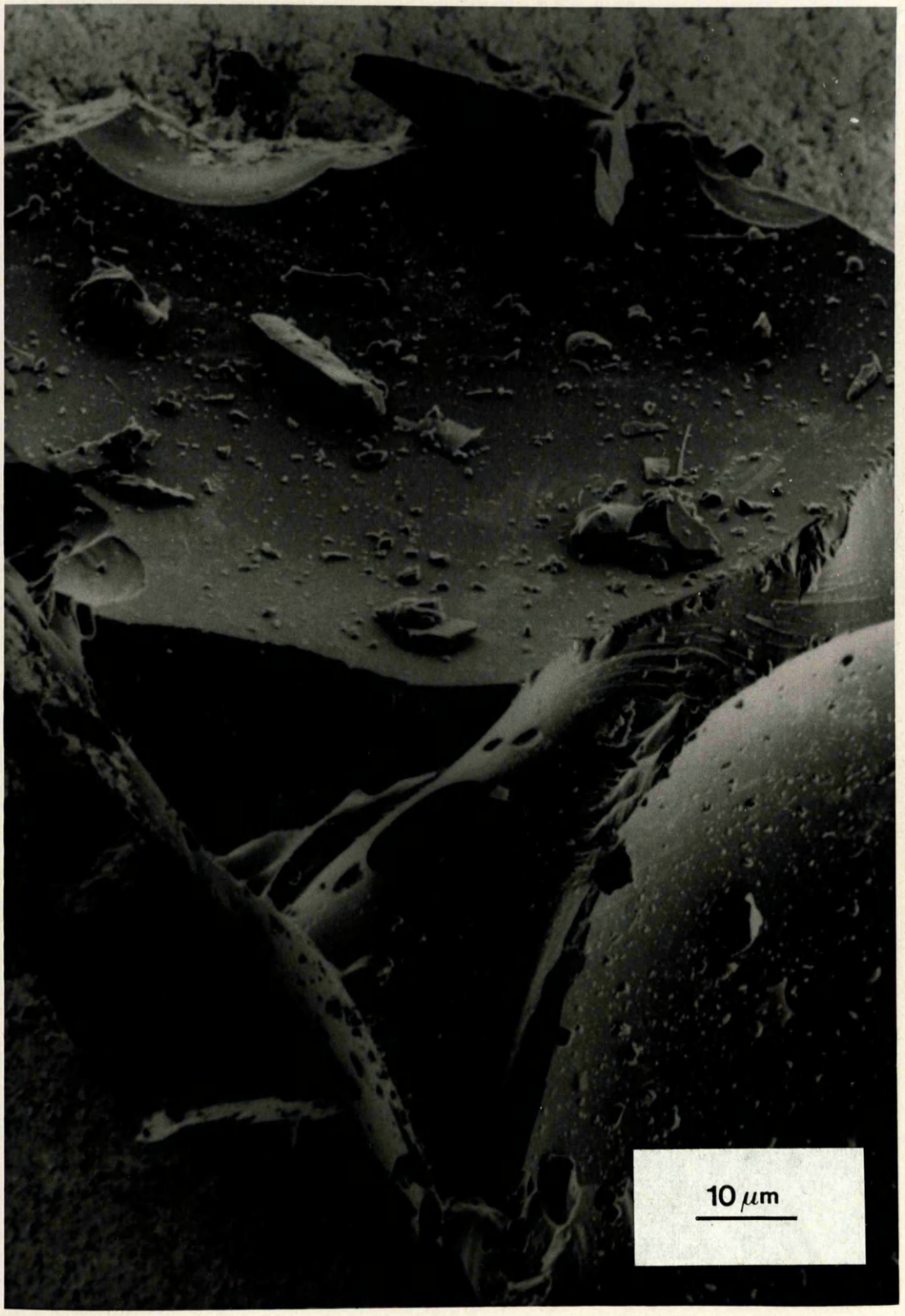

Figure 6.23: SEM of the Fluro 800_3 and Fluro 800_{20} samples revealing the smooth external surface with large holes and sheet-like lamellar layers.

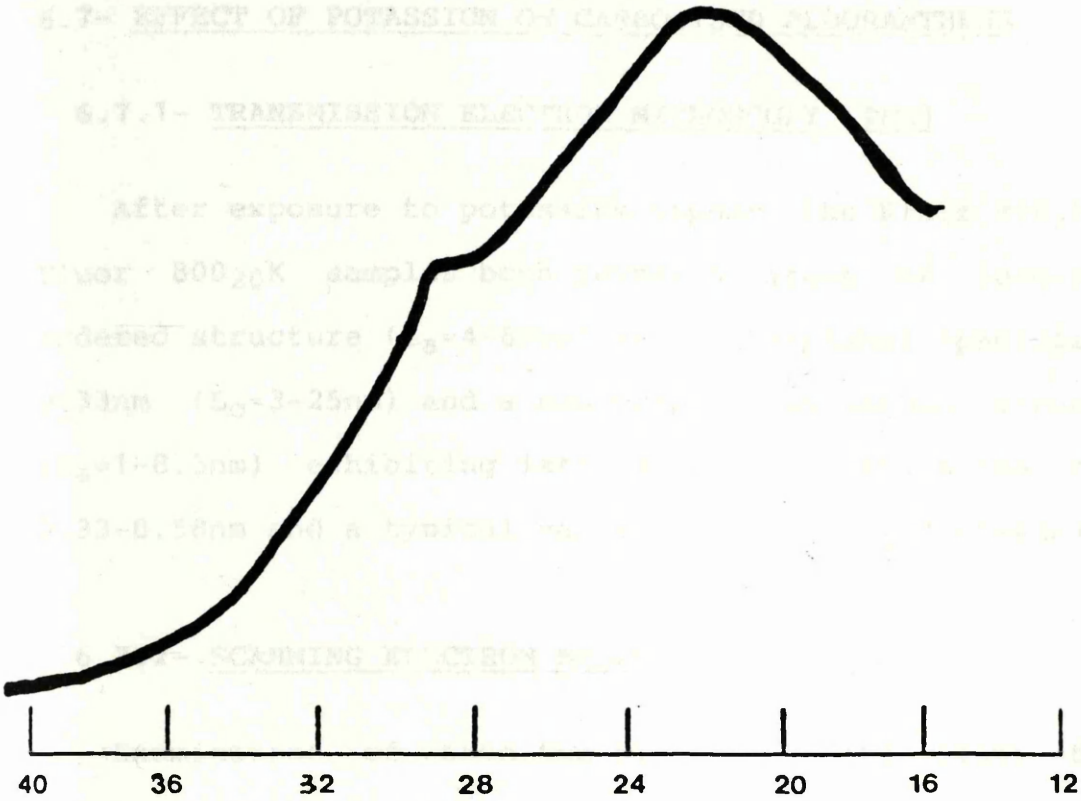

Figure 6.24: XRD trace of the Fluor 800_3 sample.

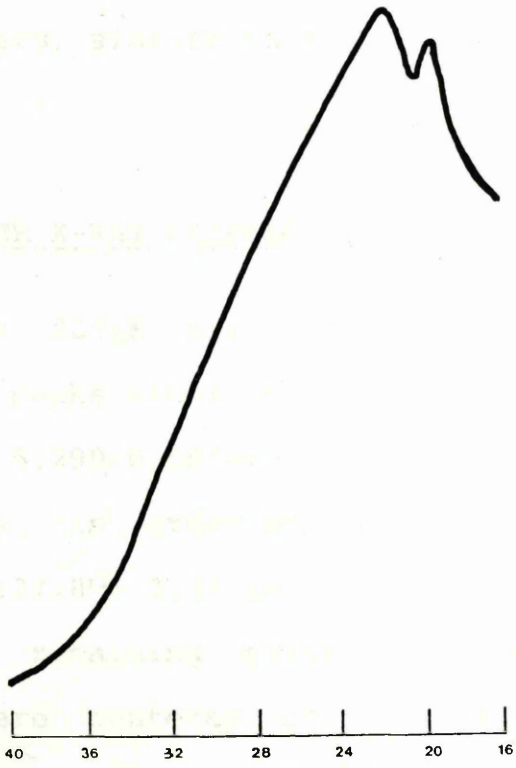

Figure 6.25: XRD trace of the Fluor 800_{20} sample.

6.7- EFFECT OF POTASSIUM ON CARBONISED FLUORANTHENE

6.7.1- TRANSMISSION ELECTRON MICROSCOPY (TEM)

After exposure to potassium vapour, the Fluor 800_3K and Fluor $800_{20}K$ samples both revealed areas of long-range ordered structure (L_a=4-60nm) with interplanar spacings of 0.33nm (L_c=3-25nm) and a non-graphitised carbon structure (L_a=1-8.5nm) exhibiting lattice spacings within the range 0.33-0.58nm and a typical value of 0.37nm (L_c=0.66-4nm).

6.7.2- SCANNING ELECTRON MICROSCOPY (SEM)

Examination of both the Fluor 800_3 and Fluor 800_{20} samples after exposure to potassium vapour revealed a smooth external surface with large holes leading to the interior and the continued development of sheet-like lamellar layers, similar to the structure shown in figure 6.23.

6.7.3- POWDER X-RAY DIFFRACTION ANALYSIS (XRD)

The Fluor 800_3K x-ray diffraction trace exhibited twenty sharp peaks within the interplanar spacings range (36.0-15.8^o) 0.290-0.651nm) (figure 6.26). The three most intense peaks, in order of decreasing intensity, were centered on (27.8^o) 0.373nm, (28.8^o) 0.360nm and (27.3^o) 0.379nm. The remaining peaks, in order of decreasing intensity, were centered on (33.9^o) 0.307nm, (32.2^o) 0.323nm, (31.4^o) 0.331nm, (30.8^o) 0.337nm, (30.1^o) 0.345nm, (26.6^o) 0.389nm, (25.9^o) 0.399nm, (25.3^o) 0.409nm, (24.7^o)

Figure 6.26: XRD trace of the Fluor 800_3K sample.

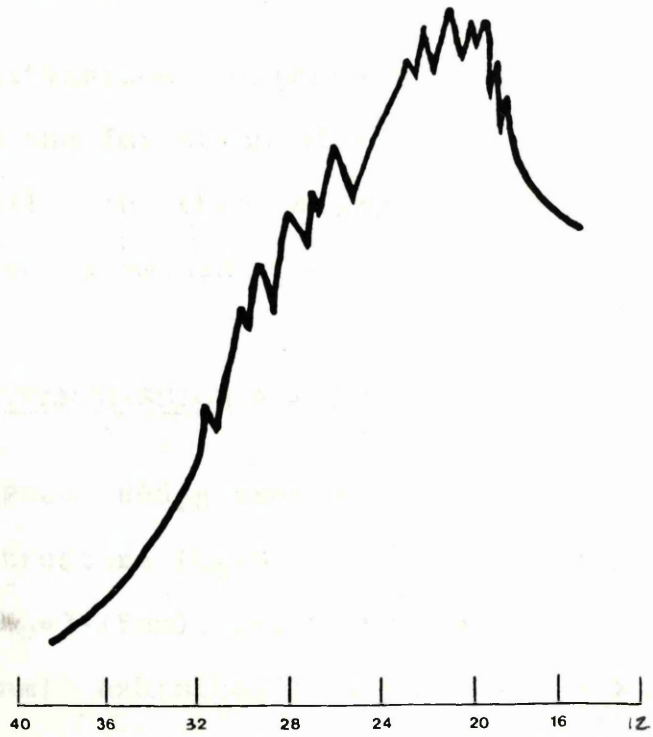

Figure 6.27: XRD trace of the Fluor 800_{20}K sample.

0.419nm, (24.1°) 0.429nm, (23.7°) 0.436nm, (22.7°) 0.455nm, (21.2°) 0.487nm, (20.3°) 0.508nm, (19.5°) 0.528nm, (18.2°) 0.566nm and (17.7°) 0.582nm respectively.

The x-ray diffraction trace for the Fluor 800_{20}K sample revealed thirteen peaks within the interplanar spacings range (38.2-14.7°) 0.274-0.700nm (figure 6.27). The five most intense peaks, in order of decreasing intensity, were centered on (20.7°) 0.498nm, (22.2°) 0.465nm, (22.8°) 0.453nm, (19.8°) 0.521nm and (19.2°) 0.537nm, with the latter two peaks exhibiting a similar intensity. The remainder of the peaks, in order of decreasing intensity, were centered on (31.7°) 0.328nm, (30.0°) 0.346nm, (29.2°) 0.355nm, (27.6°) 0.375nm, (26.5°) 0.391nm, (25.9°) 0.399nm, (18.9°) 0.545nm and (18.3°) 0.563nm.

6.8- ANALYSIS OF CARBONISED PHENANTHRENE

Graphitisation of phenanthrene at 3000°C is known to result in the formation of a graphitising carbon (Kinney et al., 1957). In this study one carbonised sample was prepared and examined.

6.8.1- TRANSMISSION ELECTRON MICROSCOPY (TEM)

The Phen 800_{20} sample revealed areas of long-range ordered structure (L_a=5-35nm) with interplanar spacings of 0.37nm (L_c=3-15nm). The non-graphitised carbon structure (L_a=1-3.5nm) exhibited lattice spacings within the range 0.34-0.52nm and a typical value of 0.46nm (L_c=0.34-4.2nm).

6.8.2- SCANNING ELECTRON MICROSCOPY (SEM)

Examination of the Phen 800_{20} sample by SEM revealed a smooth external surface exhibiting evidence of pitting and small holes leading to the interior (figure 6.28).

6.8.3- POWDER X-RAY DIFFRACTION ANALYSIS (XRD)

The Phen 800_{20} x-ray diffraction trace revealed two broad peaks within the interplanar spacings range (40.0-14.0^{o}) 0.262-0.735nm (figure 6.29). The two peaks were centered at (22.0^{o}) 0.469nm and (26.6^{o}) 0.389nm, with the latter being the less intense.

6.9- EFFECT OF POTASSIUM ON CARBONISED PHENANTHRENE

6.9.1- TRANSMISSION ELECTRON MICROSCOPY (TEM)

Examination of the Phen 800_{20}K sample revealed a long-range ordered structure (L_a=4-37nm) exhibiting interplanar spacings of 0.37nm (L_c=4-12nm). The non-graphitised carbon structure (L_a=1-4.5nm) revealed lattice spacings within the range 0.34-0.48nm and a typical value of 0.41nm (L_c=0.68-3.5nm).

6.9.2- SCANNING ELECTRON MICROSCOPY (SEM)

The Phen 800_{20}K sample revealed a structure similar to that exhibited by the Phen 800_{20} sample. A smooth external surface revealing evidence of pitting and small holes leading to the interior (figure 6.28).

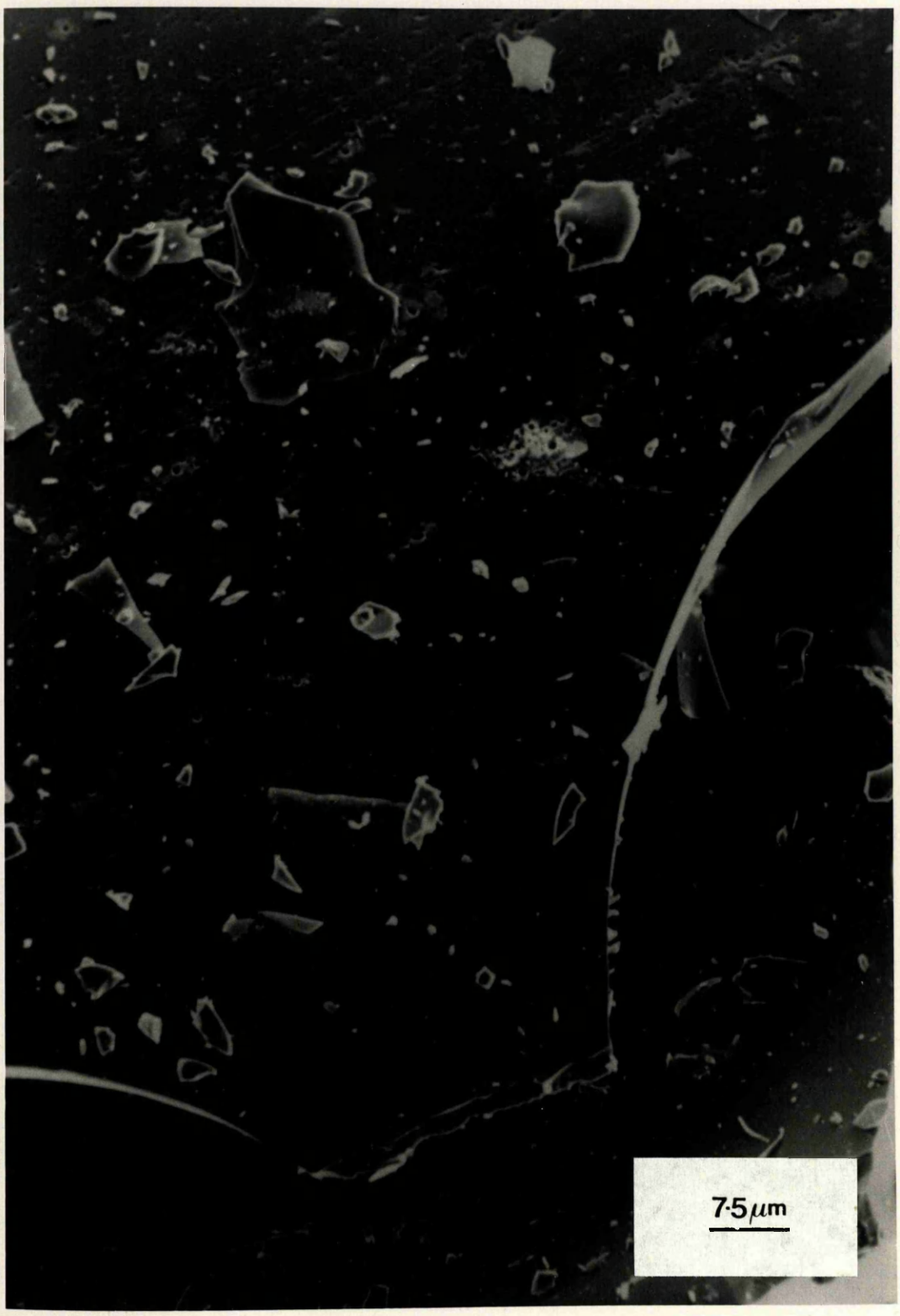

Figure 6.28: SEM of the Phen 800_{20} sample exhibiting the smooth external surface with evidence of pitting and holes.

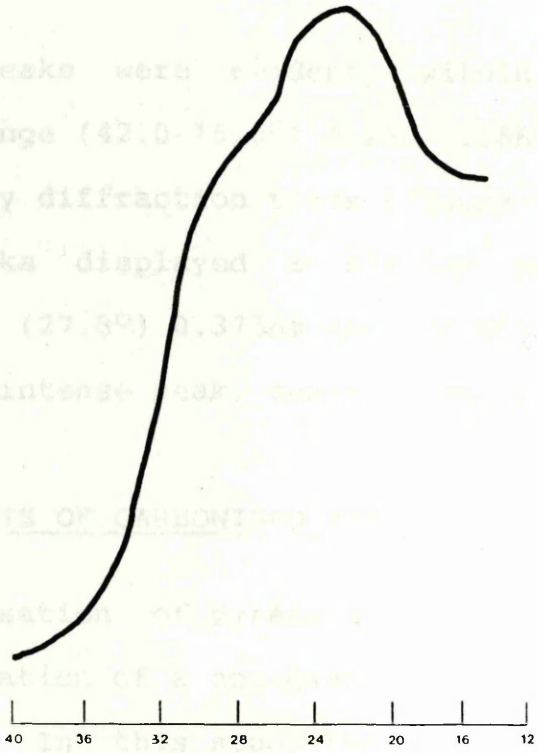

Figure 6.29: XRD trace of the Phen 800_{20} sample.

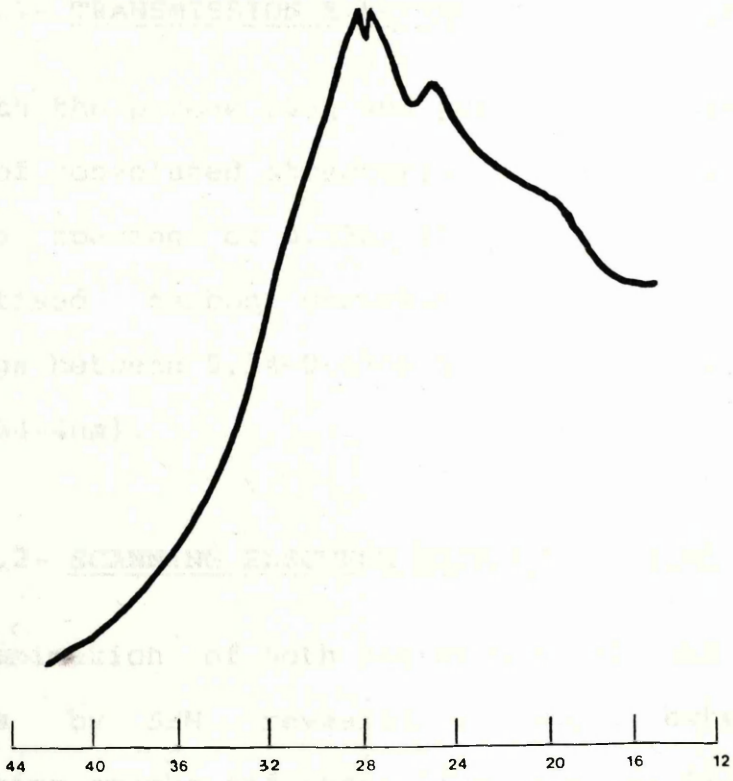

Figure 6.30: XRD trace of the Phen $800_{20}K$ sample.

6.9.3- POWDER X-RAY DIFFRACTION ANALYSIS (XRD)

Three peaks were evident, within the interplanar spacings range (42.0-15.0°) 0.250-0.686nm, from the Phen $800_{20}K$ x-ray diffraction trace (figure 6.30). The two most intense peaks displayed a similar intensity and were centered on (27.8°) 0.373nm and (28.2°) 0.367nm with the third, less intense peak, centered on (25.0°) 0.414nm.

6.10- ANALYSIS OF CARBONISED PYRENE

Graphitisation of pyrene at 3000°C is known to result in the formation of a non-graphitising carbon (Sharkey et al., 1966). In this study two carbonised samples were prepared and examined.

6.10.1- TRANSMISSION ELECTRON MICROSCOPY (TEM)

Both the pyrene 800_3 and pyrene 800_{20} samples exhibited areas of convoluted structural development (L_a=6-26nm) with lattice spacings of 0.33nm (L_c=1.5-4nm) and areas of non-graphitised carbon structure (L_a=1-5nm) with lattice spacings between 0.34-0.47nm and a typical value of 0.38nm (L_c=0.34-4nm).

6.10.2- SCANNING ELECTRON MICROSCOPY (SEM)

Examination of both the Pyrene 800_3 and Pyrene 800_{20} samples by SEM revealed a smooth external surface exhibiting cracks and sheet-like lamellar layers visible in the areas where the smooth external surface have been

removed (figure 6.31).

6.10.3- POWDER X-RAY DIFFRACTION ANALYSIS (XRD)

The x-ray diffraction trace for the Pyrene 800_3 sample revealed five peaks within the interplanar spacings range (36.0-14.0°) 0.290-0.735nm (figure 6.32). The sharpest, most intense peak was centered at (30.4°) 0.341nm, with the four less intense peaks centered on (30.8°) 0.337nm, (26.8°) 0.386nm, (22.8°) 0.452nm and (34.4°) 0.303nm respectively.

The Pyrene 800_{20} x-ray diffraction trace exhibited four peaks within the interplanar spacings range (36.0-14.4°) 0.290-0.714nm (figure 6.33). The sharpest, most intense peak was centered on (29.8°) 0.348nm. The remaining peaks, in order of decreasing intensity, were centered on (27.2°) 0.381nm, (22.2°) 0.465nm and (34.4°) 0.303nm respectively.

6.11- EFFECT OF POTASSIUM ON CARBONISED PYRENE

6.11.1- TRANSMISSION ELECTRON MICROSCOPY (TEM)

Analysis of the pyrene 800_3 and pyrene 800_{20} samples after exposure to potassium vapour revealed areas of long-range ordered structure (figure 6.34) and areas of convoluted structural development (L_a=5-26nm) with lattice spacings of 0.33nm (L_c=1.5-4nm) and areas of non-graphitised carbon structure (L_a=1-4.5nm, L_c=0.34-4.5nm) with lattice spacings between 0.34-0.43nm and 0.34-0.41 for the pyrene 800_3K and pyrene 800_{20}K samples respectively, with both exhibiting a typical value of 0.38nm.

Figure 6.31: SEM of the Pyrene 800_3 and Pyrene 800_{20} samples revealing a smooth external surface, cracks and sheet-like lamellar layers.

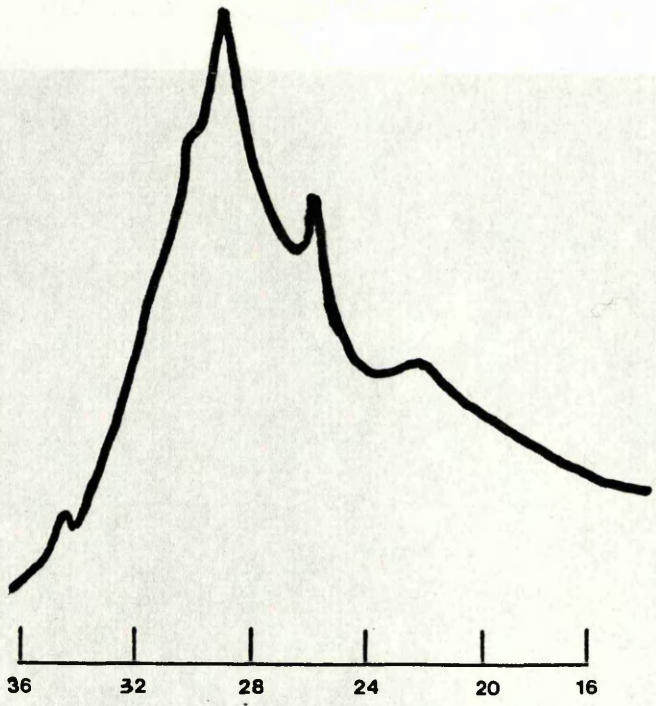

Figure 6.32: XRD trace of the Pyrene 800_3 sample.

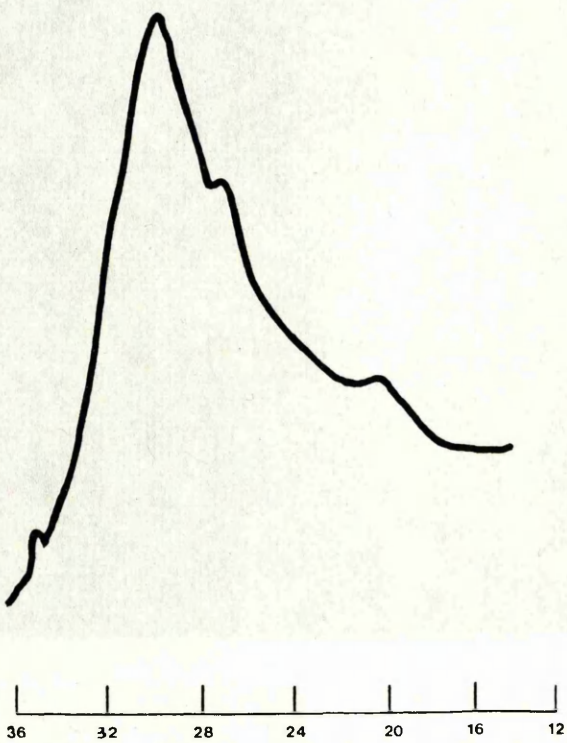

Figure 6.33: XRD trace of the Pyrene 800_{20} sample.

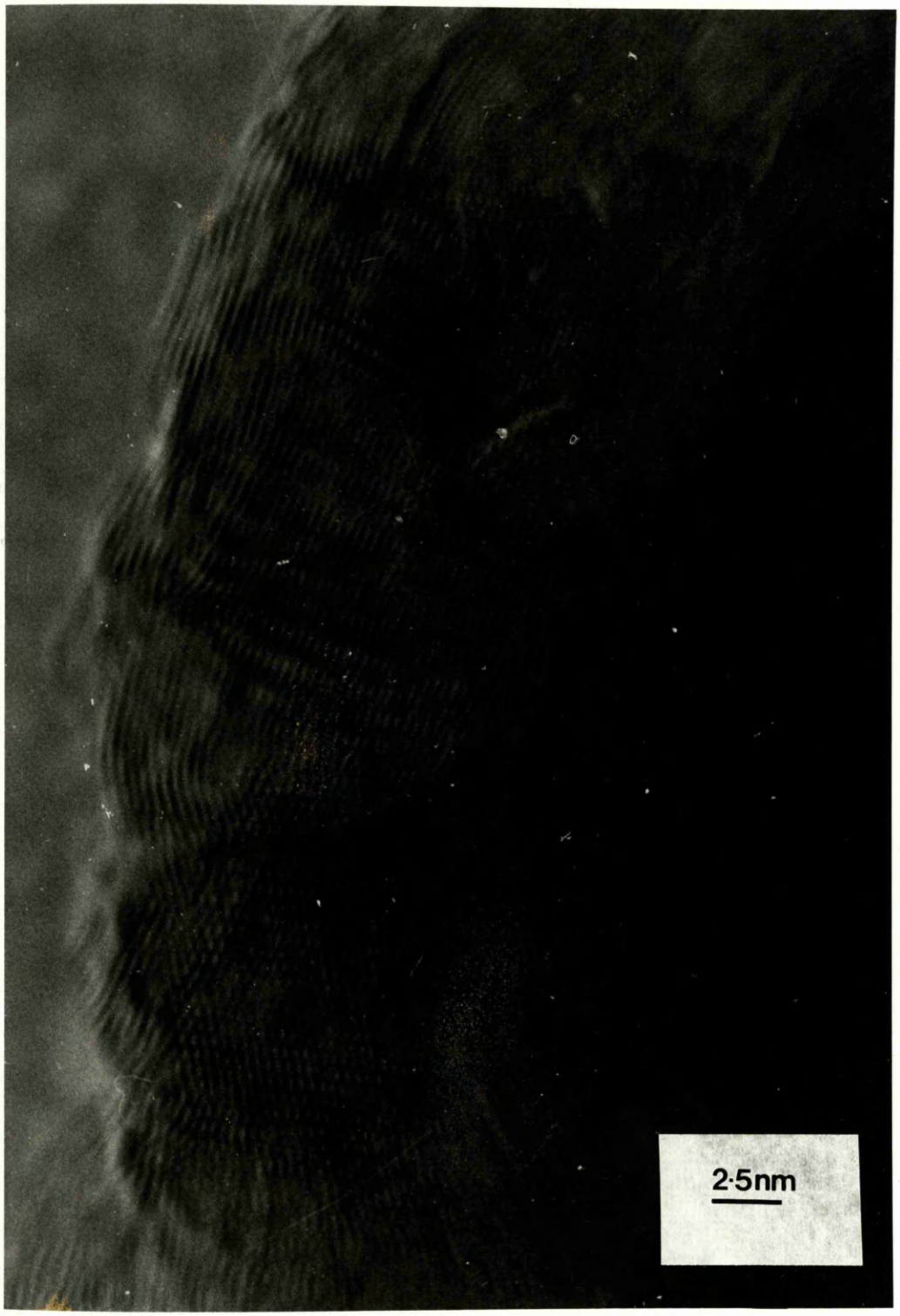

Figure 6.34: HREM representative of the long-range ordered structue (0.33nm) exhibited by the Pyrene 800_3K and Pyrene $800_{20}K$ samples.

6.11.2- SCANNING ELECTRON MICROSCOPY (SEM)

After exposure to potassium vapour the Pyrene 800_3K and Pyrene $800_{20}K$ samples continued to exhibit a smooth external surface displaying cracks. The Pyrene 800_3K sample however revealed increased cracking across the external surface as a result of exposure to potassium vapour (figure 6.35).

6.11.3- POWDER X-RAY DIFFRACTION ANALYSIS (XRD)

The x-ray diffraction trace for the Pyrene 800_3K sample exhibited five peaks within the interplanar spacings range (36.0-16.0^o) 0.290-0.643nm (figure 6.36). The peaks, in order of decreasing relative intensity, were centered on (30.1^o) 0.345nm, (29.5^o) 0.352nm, (30.7^o) 0.338nm, (26.7^o) 0.388nm and (34.4^o) 0.303nm respectively.

Three peaks were evident, within the interplanar spacings range (44.0-18.0^o) 0.239-0.572nm, from the Pyrene $800_{20}K$ x-ray diffraction trace (figure 6.37). The most intense peak was centered on (34.0^o) 0.306nm, with the remaining peaks, in order of decreasing intensity, centered on (32.2^o) 0.323nm and (25.4^o) 0.407nm respectively.

6.12- ANALYSIS OF CARBONISED p-TERPHENYL

Graphitisation of p-terphenyl at 3000°C is known to result in the formation of a non-graphitising carbon (Fitzer et al., 1971). In this study two carbonised samples were prepared and examined.

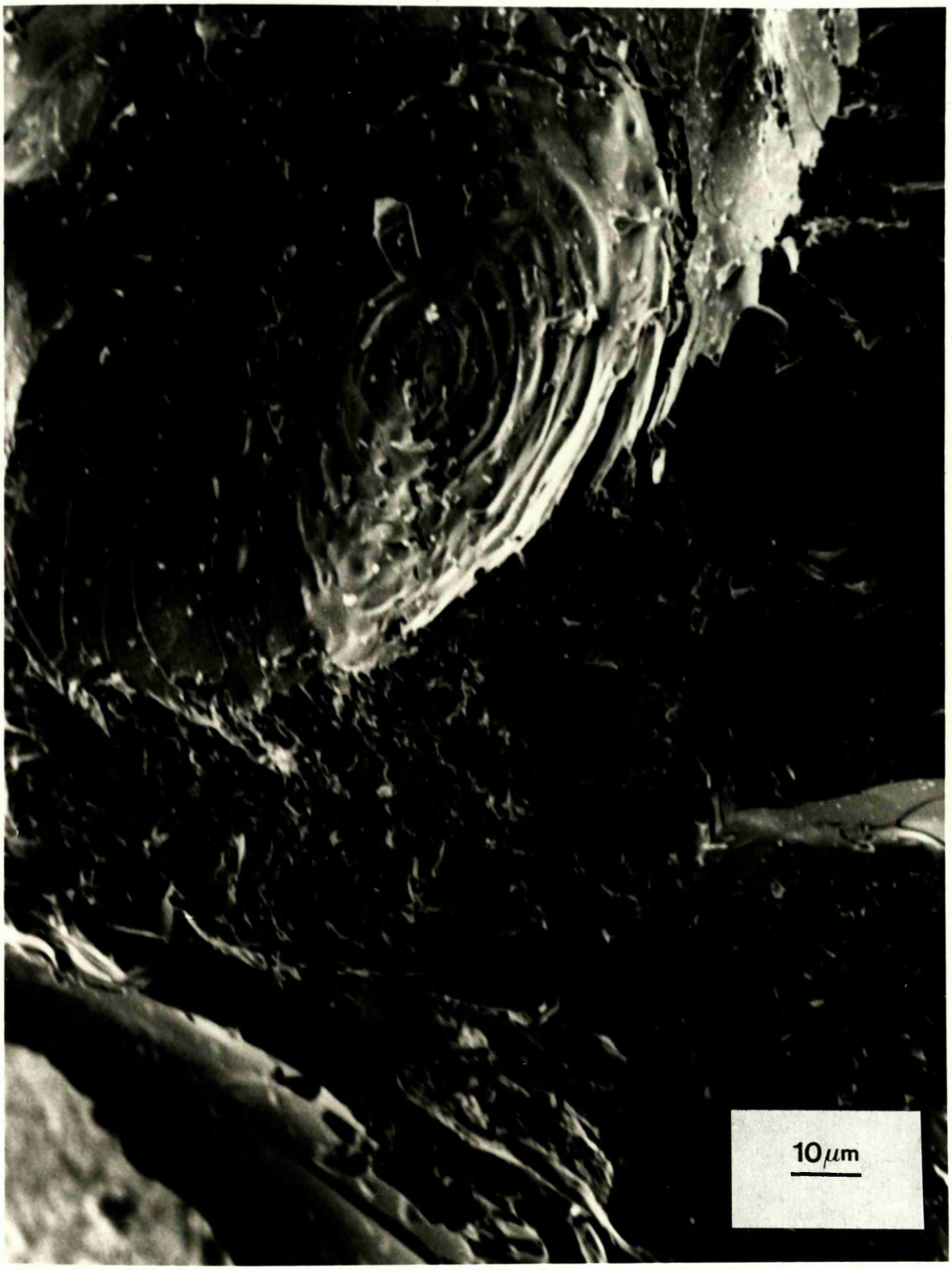

Figure 6.35: SEM of the Pyrene 8003K sample exhibiting the increased cracking across the external surface.

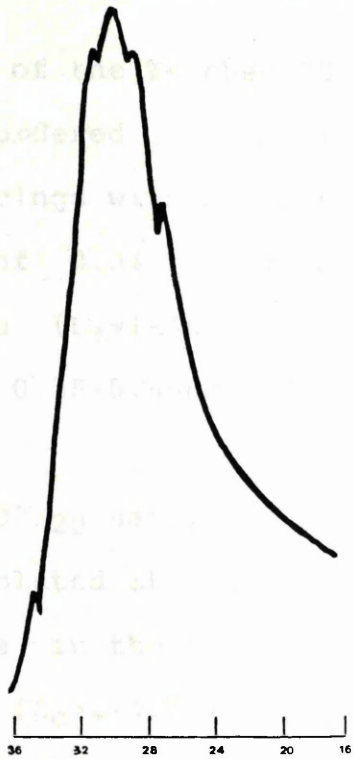

Figure 6.36: XRD trace of the Pyrene 800_3K sample.

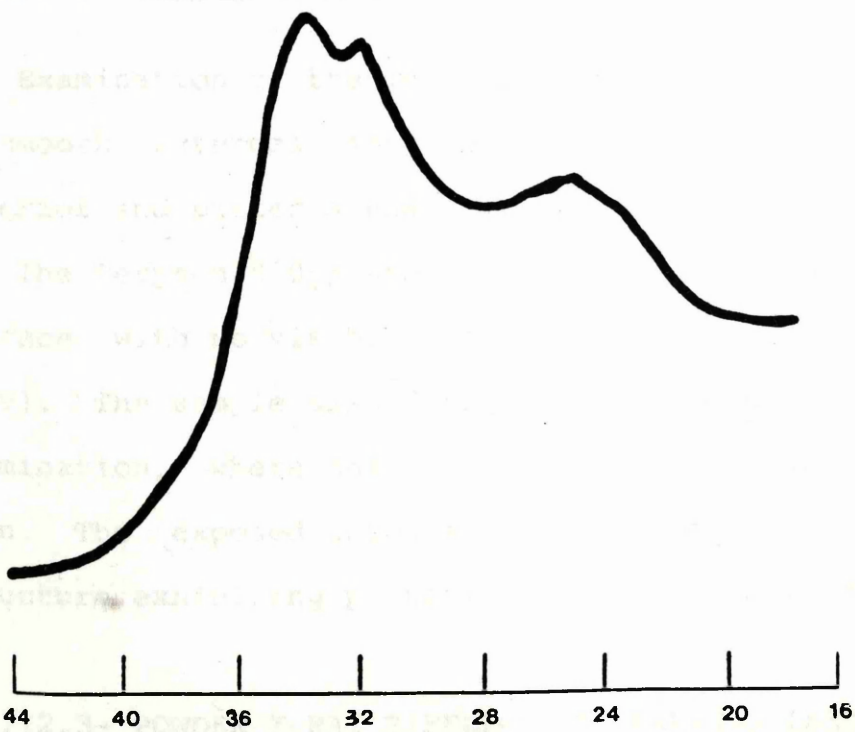

Figure 6.37: XRD trace of the Pyrene $800_{20}K$ sample.

6.12.1- TRANSMISSION ELECTRON MICROSCOPY (TEM)

Examination of the Terphen 800_3 sample revealed areas of long-range ordered structure (L_a=4-18nm) exhibiting interplanar spacings within the range 0.32-0.39nm with a typical value of 0.34 (L_c=2-5nm). The non-graphitised carbon structure (L_a=1-4nm) revealed lattice spacings within the range 0.35-0.49nm and a typical value of 0.44nm (L_c=0.4-3nm).

The Terphen 800_{20} sample revealed areas of long-range order and convoluted structural order (L_a=3-15nm) with lattice spacings in the range 0.33-0.39nm and a typical value of 0.35nm (L_c=2-4.5nm). The non-graphitised carbon structure (L_a=1-4.5nm) revealed lattice spacings of between 0.35-0.49nm with a typical value of 0.44nm (L_c=0.4-3nm).

6.12.2- SCANNING ELECTRON MICROSCOPY (SEM)

Examination of the Terphen 800_3 sample by SEM revealed a smooth external surface with cracks, holes to the interior and pitted areas (figure 6.38).

The Terphen 800_{20} sample revealed a smooth external surface with no visible pitting, holes or cracks (figure 6.39). The sample also displayed an internal surface for examination, where one of the smooth structures had split open. The exposed internal surface revealed a crumpled structure exhibiting pitted areas and holes (figure 6.40).

6.12.3- POWDER X-RAY DIFFRACTION ANALYSIS (XRD)

The x-ray diffraction trace for the Terphen 800_3 sample

Figure 6.38: SEM of the Terphen 800_3 sample showing a smooth external surface with cracks, holes and pitted areas.

Figure 6.39: SEM of the Terphen 800_{20} sample revealing a smooth external surface.

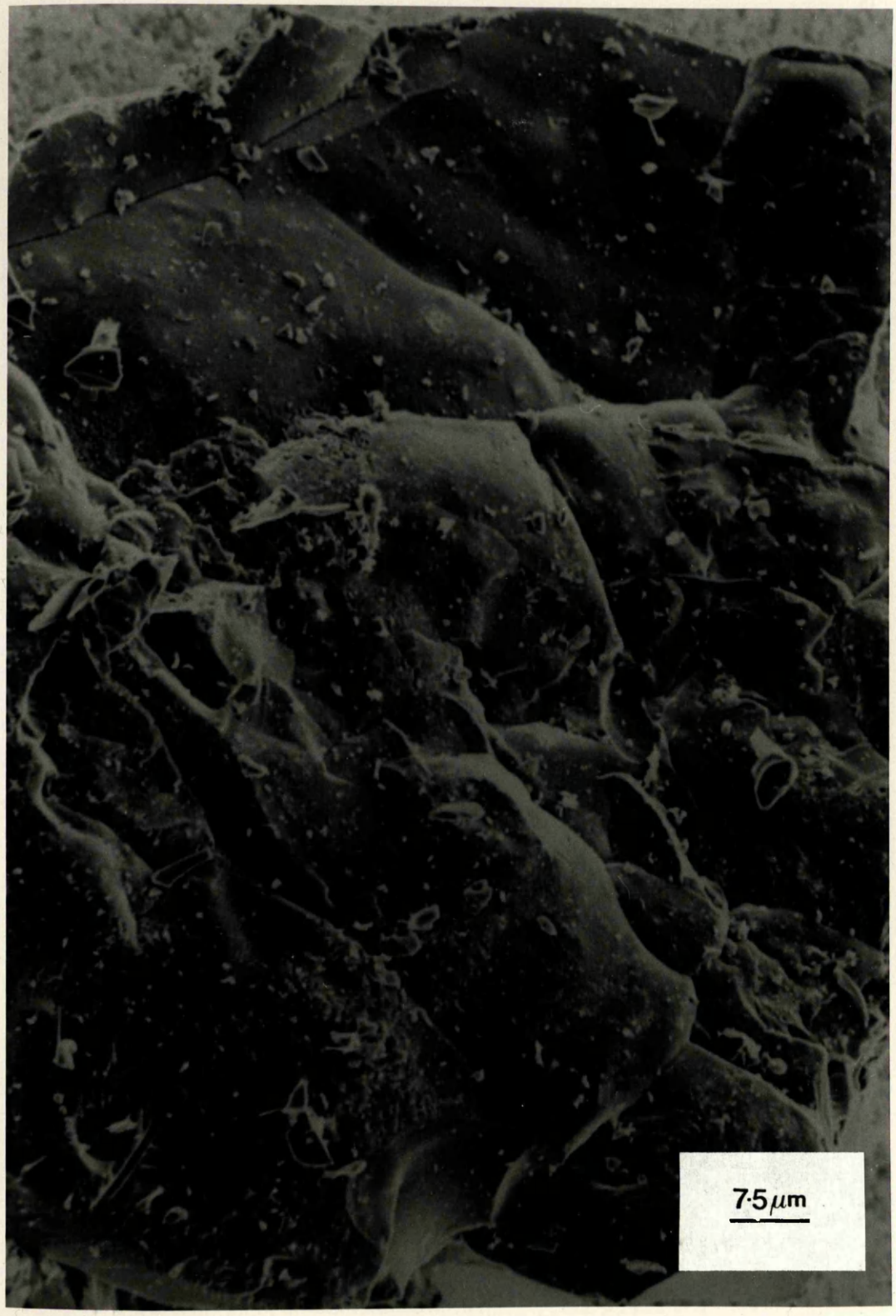

Figure 6.40: SEM of the Terphen 800_{20} sample displaying a crumpled internal surface with evidence of pitting and holes.

revealed two peaks, within the interplanar spacings range (40.0-14.6°) 0.262-0.704nm (figure 6.41). The sharpest and most intense peak was centered on (31.2°) 0.333nm, with the broader, less intense peak centered on (23.0°) 0.449nm.

The Terphen 800_{20} x-ray diffraction trace exhibited three peaks within the interplanar spacings range (42.6-12.8°) 0.246-0.803nm (figure 6.42). The most intense peak was centered on (23.2°) 0.445nm. The second and third peaks, in order of decreasing intensity, were centered on (31.1°) 0.334nm and (29.0°) 0.356nm respectively.

6.13- EFFECT OF POTASSIUM ON CARBONISED p-TERPHENYL

6.13.1- TRANSMISSION ELECTRON MICROSCOPY (TEM)

After exposure to potassium vapour the Terphen 800_3 and Terphen 800_{20} samples both revealed areas of long-range order, non-graphitised carbon and convoluted structural order. In both samples the long-range ordered structure (L_a=4-16nm) exhibited lattice spacings within the range 0.33-0.37nm and with a typical value of 0.34nm (L_c=2.5-6nm), values that were indistinguishable from the observed convoluted structural order. A non-graphitised carbon structure with lattice spacings of between 0.35-0.55nm, typical value of 0.48nm (L_a=1-6nm, L_c=0.7-3.7nm) and 0.35-0.49nm, typical value of 0.44nm (L_a=1-4.5nm, L_c=0.4-3.5nm) were exhibited by the Terphen 800_3K and Terphen 800_{20}K samples respectively.

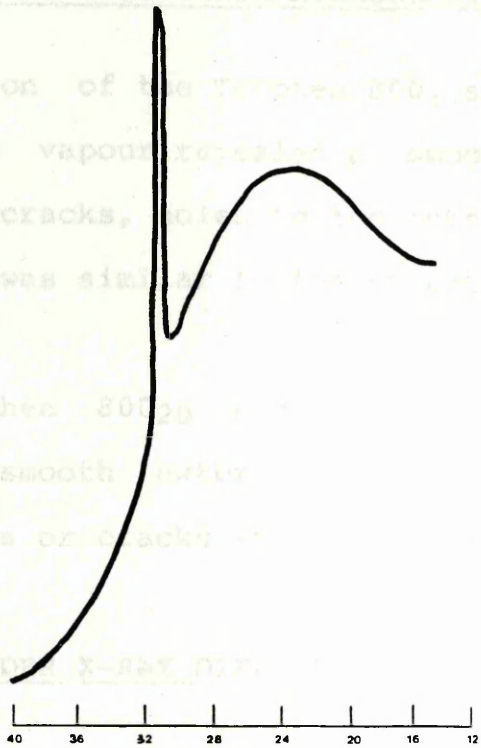

Figure 6.41: XRD trace of the Terphen 800_3 sample.

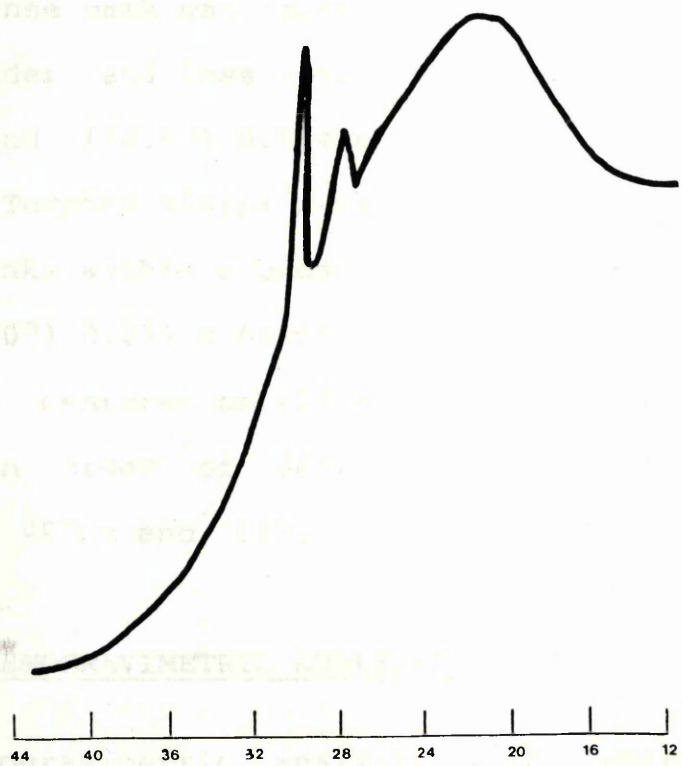

Figure 6.42: XRD trace of the Terphen 800_{20} sample.

6.13.2- SCANNING ELECTRON MICROSCOPY (SEM)

Examination of the Terphen 800_3 sample after exposure to potassium vapour revealed a smooth external surface exhibiting cracks, holes to the interior and evidence of pitting and was similar to the structure shown in figure 6.38.

The Terphen 800_{20} and Terphen $800_{20}K$ samples both revealed a smooth external surface with no visible pitting, holes or cracks (figure 6.39).

6.13.3- POWDER X-RAY DIFFRACTION ANALYSIS (XRD)

Three peaks were evident from the Terphen 800_3K x-ray diffraction trace (figure 6.43). Within the interplanar spacings range (39.6-16.0^o) 0.264-0.643nm, the sharpest and most intense peak was centered on (31.0^o) 0.335nm, with the two broader and less intense peaks centered on (22.2^o) 0.465nm and (18.6^o) 0.554nm respectively.

The Terphen $800_{20}K$ x-ray diffraction trace exhibited three peaks within a broad range of interplanar spacings (44.0-16.0^o) 0.239-0.643nm (figure 6.44). The most intense peak was centered on (24.8^o) 0.416nm with the remaining peaks, in order of decreasing intensity, centered on (20.8^o) 0.495nm and (31.4^o) 0.330nm respectively.

6.14- THERMOGRAVIMETRIC ANALYSIS (TGA)

Thermogravimetric analysis of the carbonised samples (prepared via a closed carbonisation system) both before and after exposure to potassium vapour, revealed a similar

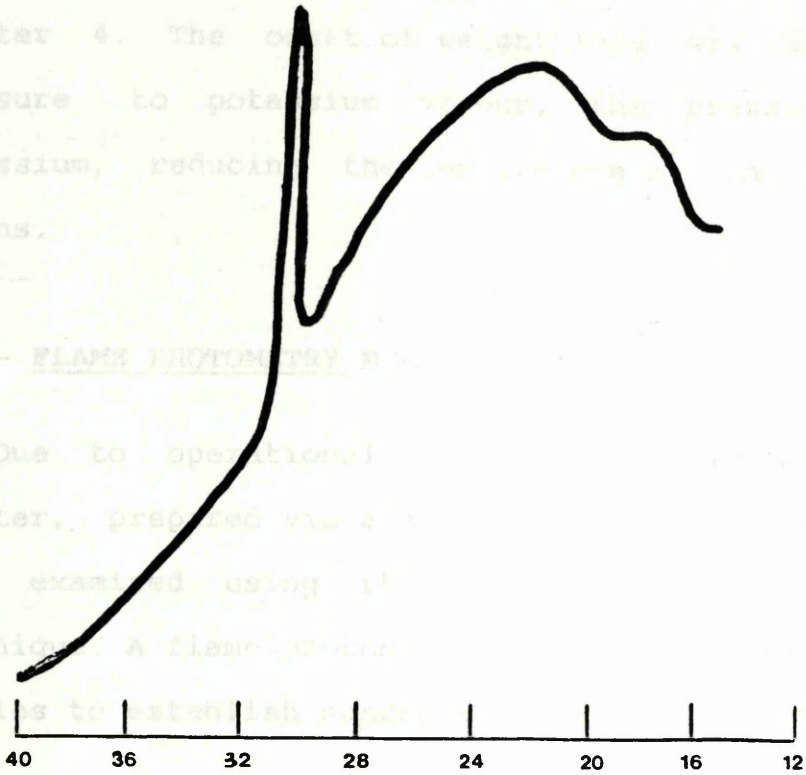

Figure 6.43: XRD trace of the Terphen 800_3K sample.

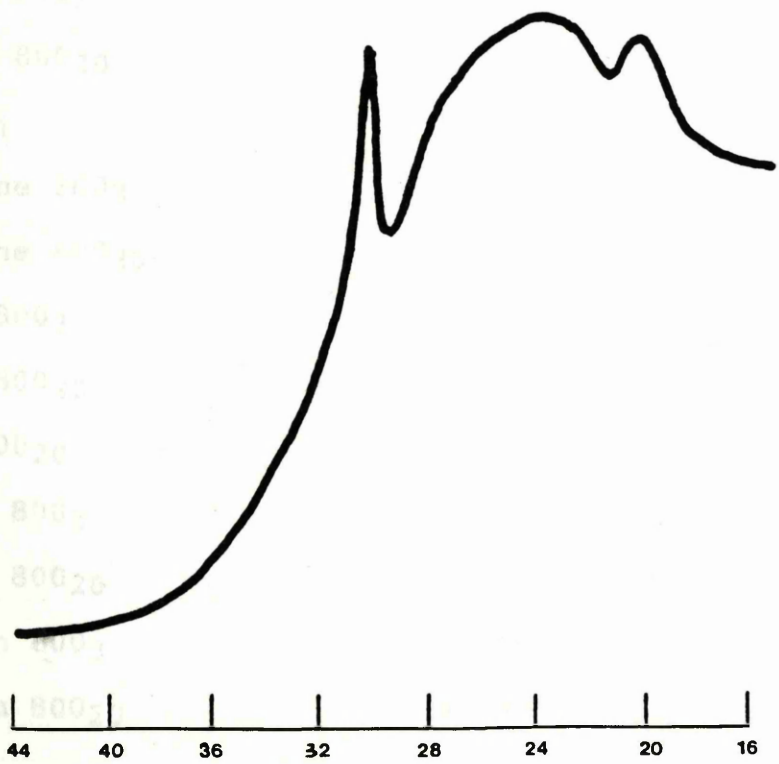

Figure 6.44: XRD trace of the Terphen $800_{20}K$ sample.

trend to that observed for the carbonised samples in chapter 4. The onset of weight loss was altered after exposure to potassium vapour, the presence of the potassium, reducing the temperature at which combustion begins.

6.15- FLAME PHOTOMETRY MEASUREMENTS

Due to operational problems, the samples from this chapter, prepared via a closed carbonisation system, were not examined using the potassium uptake measurement technique. A flame photometry study was carried out on the samples to establish susceptibility to alkai attack.

SAMPLE	K CONC. (mg) per 100mg of sample
Anthra 800_3	2.392
Anthra 800_{20}	1.490
$Anthra_1$	4.803
Chrysene 800_3	5.970
Chrysene 800_{20}	0.865
Fluor 800_3	4.166
Fluor 800_{20}	2.357
Phen 800_{20}	6.184
Pyrene 800_3	11.732
Pyrene 800_{20}	3.066
Terphen 800_3	9.640
Terphen 800_{20}	5.538

Table 6.2 Flame photometry potassium concentrations for the aromatic hydrocarbons carbonised via a closed carbonisation system.

6.16- EFFECT OF INERT CARRIER GASES

A selection of the carbonised samples were exposed to potassium vapour using different inert carrier gases, argon and nitrogen. Examination of each sample , by HREM and XRD, did not reveal any salient microstructural differences when an alternative carrier gas was used, indeed examination of the samples revealed no obvious structural carrier gas dependence.

6.17- SUMMARY OF RESULTS

A summary of the TEM and XRD results obtained for the compounds carbonised via the closed carbonisation system, both before and after exposure to potassium vapour, are shown in table 6.3.

SAMPLE	MICROSTRUCTURE	L_a(nm)	L_c(nm)	d(nm)	XRD(nm)
Anthra 800_3	S.R.O	1-7	0.7-2.5	0.35 (0.33-0.39)	0.348
Anthra 800_{20}	S.R.O	1-7	0.7-2.5	0.35 (0.33-0.39)	0.348
$Anthra_1$	S.R.O	1-4.5	0.7-3	0.36 (0.34-0.41)	0.513 0.404
	L.R.O	5-17	2-13	0.34 (0.33-0.37)	0.362
Anthra 800_3K	S.R.O	1-5.5	0.7-4	0.36 (0.34-0.48)	0.353 0.367
	L.R.O	6-27	2.5-9	0.35	0.341 0.378 0.443
Anthra 800_{20}K	S.R.O	1-5.5	0.7-4	0.36 (0.34-0.48)	0.344 0.348
	L.R.O	6-27	2.5-9	0.35	0.353 0.383 0.478

SAMPLE	MICROSTRUCTURE	L_a(nm)	L_c(nm)	d(nm)	XRD(nm)
$Anthra_1K$	S.R.O	1-4	0.7-35	0.36	0.484
				(0.34-0.48)	0.347
	L.R.O	5-24	2-11	0.34	0.366
	& ribbon			(0.33-0.37)	0.389
					0.401
					0.412
Chrysene 800_3	S.R.O	1-4.5	0.66-3	0.39	0.353
				(0.33-0.42)	0.361
	ribbon	6.5-46	3.2-12	0.34	0.340
					0.370
					0.399
					0.505
Chrysene 800_{20}	S.R.O	1-5	0.34-3	0.44	0.346
				(0.34-0.48)	0.469
	L.R.O	6.5-46	3.2-12	0.34	
	& ribbon				
Chrysene 800_3K	S.R.O	1-3.5	0.68-3	0.39	(a)
				(0.34-0.56)	
	L.R.O	5-50	3-15	0.34	
	& ribbon				
Chrysene $800_{20}K$	S.R.O	1-4	0.34-3.5	0.44	0.348
				(0.34-0.48)	0.449
	L.R.O	5-50	3-15	0.34	0.487
Fluor 800_3	S.R.O	1-8	0.34-4	0.37	0.469
				(0.34-0.52)	0.358
	L.R.O	5-75	3-25	0.33	
	& ribbon				
Fluor 800_{20}	S.R.O	1-6	0.35-3.5	0.39	0.478
				(0.35-0.52)	0.529
Fluor 800_3K	S.R.O	1-8.5	0.66-4	0.37	(b)
				(0.33-0.58)	
	L.R.O	4-60	3-25	0.33	
Fluor $800_{20}K$	S.R.O	1-8.5	0.66-4	0.37	(c)
				(0.33-0.58)	
	L.R.O	4-60	3-25	0.33	
Phen 800_{20}	S.R.O	1-3.5	0.34-4.2	0.46	0.469
				(0.34-0.52)	0.389
	L.R.O	5-35	3-15	0.37	
Phen $800_{20}K$	S.R.O	1-4.5	0.68-3.5	0.41	0.373
				(0.34-0.48)	0.367
	L.R.O	4-37	4-12	0.37	0.414

SAMPLE	MICROSTRUCTURE	L_a(nm)	L_c(nm)	d(nm)	XRD(nm)
Pyrene 800_3	S.R.O	1-5	0.34-4	0.38	0.341
				(0.34-0.47)	0.337
	ribbon	6-26	1.5-4	0.33	0.386
					0.452
					0.303
Pyrene 800_{20}	S.R.O	1-5	0.34-4	0.38	0.348
				(0.34-0.47)	0.381
	ribbon	6-26	1.5-4	0.33	0.465
					0.303
Pyrene 800_3K	S.R.O	1-4.5	0.34-4.5	0.38	0.345
				(0.34-0.43)	0.352
	L.R.O	5-26	1.5-4	0.33	0.338
	& ribbon				0.388
					0.303
Pyrene 800_{20}K	S.R.O	1-4.5	0.34-4.5	0.38	0.306
				(0.34-0.41)	0.32.323
	L.R.O	5-26	1.5-4	0.33	0.407
	& ribbon				
Terphen 800_3	S.R.O	1-4	0.4-3	0.44	0.333
				(0.35-0.49)	0.449
	L.R.O	4-18	2-5	0.34	
				(0.32-0.39)	
Terphen 800_{20}	S.R.O	1-4.5	0.4-3	0.44	0.445
				(0.35-0.49)	0.334
	L.R.O	3-15	2-4.5	0.35	0.356
	& ribbon			(0.33-0.39)	
Terphen 800_3K	S.R.O	1-6	0.7-3.7	0.48	0.335
				(0.35-0.55)	0.465
	L.R.O	4-16	2.5-6	0.34	0.554
	& ribbon			(0.33-0.37)	
Terphen 800_{20}K	S.R.O	1-4.5	0.4-3.5	0.44	0.416
				(0.35-0.49)	0.495
	L.R.O	4-16	2.5-6	0.34	0.330
	& ribbon			(0.33-0.37)	

(a) 0.340, 0.347, 0.356, 0.364, 0.379, 0.402, 0.419, 0.469, 0.478, 0.494, 0.521.

(b) 0.373, 0.360, 0.379, 0.307, 0.323, 0.331, 0.337, 0.345, 0.389, 0.399, 0.409, 0.419, 0.429, 0.436, 0.455, 0.487, 0.508, 0.528, 0.566, 0.582.

(c) 0.498, 0.465, 0.453, 0.521, 0.537, 0.328, 0.346, 0.355, 0.375, 0.391, 0.399, 0.545, 0.563.

Table 6.3 Summary of the TEM and XRD results for the aromatic hydrocarbons carbonised via a closed carbonisation system.

CHAPTER SEVEN

DISCUSSION OF THE RESULTS FOR THE SAMPLES PREPARED VIA A CLOSED CARBONISATION SYSTEM

7.1- INTRODUCTION

Preparation of these samples required charring to a temperature of 550°C under their own vapour pressure (Lewis and Edstrom, 1961) as such materials merely volatilise leaving no carbonaceous residue in an open system.

Analysis of the results presented for the samples prepared via a closed carbonisation system will be discussed individually with a comparison of any overall group relevance.

7.2- CARBONISED ANTHRACENE SAMPLES

The Anthra 800_3 and Anthra 800_{20} XRD trace revealed a single peak, exhibiting a wide range of carbon lattice spacings. The interplanar spacings, centered on 0.348nm, were consistent with the non-graphitised carbon structure observed for both samples by HREM, 0.35nm (0.33-0.39nm). Examination of the $Anthra_1$ sample by XRD revealed a trace exhibiting three overlapping peaks. The interplanar spacings centered around, two of the peaks, 0.362nm and 0.404nm, would be accounted for by both the non-graphitised carbon structure 0.36nm (0.34-0.41nm) and the long-range ordered structure 0.34nm (0.33-0.37nm) observed by HREM, the relative peak heights of the 0.404nm spacing compared to the 0.362nm spacing corresponding to the greater abundance of the non-graphitised carbon structure within this sample. The largest peak, corresponding to the 0.513nm interplanar spacing was not detected by HREM examination of the sample.

After exposure to potassium vapour, XRD analysis of all three samples: Anthra 800_3K, Anthra $800_{20}K$ and $Anthra_1K$, revealed sharper peaks for the carbon-carbon interplanar spacings than was evident from the corresponding unexposed samples, indicating a more ordered arrangement of the carbon layer planes and confirming the structural ordering observed by HREM. Microstructural analysis of the Anthra 800_3K and Anthra $800_{20}K$ samples revealed that on exposure to potassium vapour areas of the carbonised structure experienced changes that resulted in the formation of a long-range ordered structure, previously undetected by HREM, and an expanded non-graphitised carbon structure.

XRD analysis of the $Anthra_1K$ sample was consistent with the non-graphitised, convoluted and long-range structural order observed by HREM. The 0.484nm peak corresponding to the expanded non-graphitised lattice spacings 0.34-0.48nm detected by HREM. Although undetected by HREM, the $Anthra_1$ sample did reveal a 0.513nm interplanar spacings peak on the XRD trace, thus, the expanded non-graphitised carbon structure, exhibited after exposure to potassium vapour can not, for the $Anthra_1K$ sample, be regarded as developing as a result of intercalation or a residue compound.

SEM examination of the Anthra 800_3 and Anthra 800_{20} samples revealed remarkably little variance in macrostructure with both exhibiting a smooth external structure displaying no detectable cracks or pores and sheet-like lamellar layers. The samples, after exposure to potassium vapour, continued to reveal a comparable macrostructure except that the smooth external surface now

exhibited cracks. The macrostructure of the Anthra$_1$K sample appeared more susceptible to alterations of the samples structure on exposure to potassium vapour. However, of the three anthracene samples, this one displayed a higher affinity for potassium according to the flame photometry results and could thus be expected to show a macro and microstructure that had been changed or altered more significantly, by exposure to potassium, than the Anthra 800$_3$ and the Anthra 800$_{20}$ samples.

7.3- CARBONISED CHRYSENE SAMPLES

Examination of the Chrysene 800$_3$ sample by XRD revealed a trace exhibiting six overlapping peaks. The interplanar spacings centered around all but one of the peaks, 0.505nm, were consistent with the non-graphitised carbon structure 0.39nm (0.33-0.42nm) and the convoluted structural order (0.34nm) observed by HREM. The peak corresponding to the 0.505nm interplanar spacing remained undetected by HREM examination of the sample. After exposure to potassium vapour analysis of the Chrysene 800$_3$K sample, by XRD, confirmed the structural modifications observed using HREM, the interplanar spacings centered around all of the peaks, coincided with the expanded short-range ordered structure 0.39nm (0.34-0.56nm) and the long-range and convoluted structural order (0.34nm). Again however, as in the case of the Anthra$_1$ sample, this expanded non-graphitised carbon structure can not be regarded as developing as a result of intercalation or a residue compound as the trace of the

unexposed sample did reveal a peak corresponding to a 0.505nm interplanar spacing.

The XRD study of the exposed and unexposed Chrysene 800_{20} sample revealed a very similar trace for both samples. The trace for the unexposed Chrysene 800_{20} sample agreed with the non-graphitised, convoluted and long-range structural order observed by HREM examination. The peak centered at 0.346nm corresponding to the 0.34nm convoluted and long-range structural order and encompassing the non-graphitised carbon structure 0.44nm (0.34-0.48nm) with the 0.469nm trace peak arising as a result of the non-graphitised carbon structure. The resultant XRD trace after exposure of the sample to potassium vapour revealed an increased peak definition, the difference being that the 0.469nm peak (non-graphitised carbon structure) displayed by the unexposed Chrysene 800_{20} sample had become split into two peaks of decreasing intensity centered at 0.449nm and 0.487nm respectively. The 0.348nm lattice spacing peak was still dominant and would be accounted for by the presence of both the short 0.44 (0.34-0.48nm) and the long-range 0.34nm ordered structures.

SEM examination of both the exposed and unexposed Chrysene 800_3 and Chrysene 800_{20} samples revealed all the samples to exhibit similarities in their general morphology. This aspect of macrostructure similarity in the chrysene samples differs significantly from the anthracene samples when the difference in the flame photometry potassium measurements are taken into consideration. The Chrysene 800_3 sample displayed a seven times greater

potassium uptake concentration than the Chrysene 800_{20} sample, with no apparent additional effects to the macrostructure of the material, whereas a doubling of the potassium taken up in the $Anthra_1$ sample causes a detectable difference in the macrostructure of the sample.

Both the macro and microstructural evidence from this study indicates that the anthracene samples (graphitisng carbon) appeared more susceptible to alterations of the samples structure on exposure to potassium vapour than the chrysene samples (non-graphitising carbon).

7.4- CARBONISED FLUORANTHENE SAMPLES

The Fluor 800_3 and Fluor 800_{20} XRD traces both revealed a double peak within a wide range of carbon lattice spacings. The Fluor 800_3 trace revealed interplanar spacings centered on 0.469nm and 0.358nm and would be accounted for by the non-graphitised carbon structure 0.37nm (0.34-52nm) observed by HREM. Convoluted and long-range structural order (0.33nm), detected by HREM, were absent from the XRD trace, it must therefore be concluded that the signals from these regions are not sufficiently intense to result in individual peak definition and that they are encompassed within the XRD interplanar spacings range for the sample. X-ray diffraction analysis of the Fluor 800_{20} sample revealed interplanar spacings centered on 0.478nm and 0.529nm, consistent with the non-graphitised carbon structure 0.37nm (0.34-0.52nm) observed by HREM.

After exposure to potassium vapour the Fluor 800_3 and

Fluor 800_{20} samples both revealed sharper, more intense peaks for the carbon-carbon interplanar spacings than was evident from the corresponding unexposed samples, indicating a more ordered arrangement of the carbon layer planes. The long-range ordered structure, observed in both samples after exposure to potassium vapour by HREM, gave a sufficently intense signal to be revealed by the XRD traces.

SEM examination of both the exposed and unexposed Fluor 800_3 and Fluor 800_{20} samples revealed the smooth external surface of all the materials and their similarities in pore structure, size and general morphology. This aspect of macrostructure similarity, in the fluoranthene samples, is the same as that exhibited by the chrysene samples, although their is not such an obvious difference in the flame photometry potassium measurements between the exposed and unexposed fluoranthene samples.

The macrostructural evidence from this study indicates that the anthracene samples (graphitisng carbon) appeared more susceptible to alterations of the samples structure on exposure to potassium vapour than the chrysene samples (non-graphitising carbon) and the fluoranthene samples (graphitising carbon). The microstructural evidence indicates that the anthracene samples (graphitisng carbon) and the fluoranthene samples (graphitising carbon) appeared more susceptible to alterations of the samples structure on exposure to potassium vapour than the chrysene samples (non-graphitising carbon).

7.5- CARBONISED PHENANTHRENE SAMPLE

The x-ray diffraction trace of the Phen 800_{20} sample revealed interplanar spacings centered on 0.469nm and 0.389nm, accounted for by the non-graphitised carbon structure 0.46nm (0.34-52nm) observed by HREM. However, microstructural examination of the sample also revealed a long-range ordered structure (0.37nm), it must therefore be concluded that the signals from these regions are not sufficiently intense to register individual peak definition and are encompassed within the XRD interplanar spacings range of the sample.

After exposure to potassium vapour analysis of the Phen 800_{20} sample by HREM revealed a non-graphitised carbon structure that exhibited interplanar spacings with both a reduced typical value and overall lattice spacings range. Areas of long-range ordered structure, with a lattice spacings value that was unaltered were also detected. From the XRD trace, the interplanar spacings centered around two peaks, 0.373nm and 0.367nm, would be accounted for by both the non-graphitised carbon structure 0.41nm (0.34-0.48nm) and the long-range ordered structure 0.37nm with the 0.414nm interplanar spacings peak arising as a result of the non-graphitised carbon structure.

SEM examination of both the exposed and unexposed Phen 800_{20} samples revealed their similarities in pore structure, size and general morphology. This aspect of macrostructure similarity, both before and after exposure to potassium vapour, for the phenanthrene samples is the

same as that exhibited by the chrysene and fluoranthene samples, although no comparison can be made for the flame photometry potassium measurements as only one sample was examined before and after potassium exposure in this study.

The macrostructural evidence from this study, indicates that the anthracene samples (graphitisng carbon) appeared more susceptible to alterations of the samples structure on exposure to potassium vapour than the chrysene samples (non-graphitising carbon), the fluoranthene samples (graphitising carbon) and the phenanthrene sample (graphitising carbon). The microstructural evidence indicates that the anthracene samples (graphitisng carbon) the fluoranthene samples (graphitising carbon), and the phenanthrene sample (graphitising carbon) appeared more susceptible to alterations of the samples structure on exposure to potassium vapour than the chrysene samples (non-graphitising carbon).

7.6- CARBONISED PYRENE SAMPLES

Microstructural analysis of both the Pyrene 800_3 and Pyrene 800_{20} samples, before exposure to potassium vapour, displayed a non-graphitised carbon structure and areas of convoluted structural order. After exposure to potassium vapour, the samples revealed areas of the carbonised structure experienced changes resulting in the formation of a long-range ordered structure, previously undetected by HREM. The XRD traces from both the exposed and unexposed samples confirmed the structural modifications observed by

HREM and revealed peaks with interplanar spacings consistent with the non-graphitised carbon structure and the convoluted and long-range structural order observed by HREM.

SEM examination of the Pyrene 800_3 and Pyrene 800_{20} samples revealed remarkably little variance in macrostructure with both exhibiting a smooth external structure displaying cracks and sheet-like lamellar layers. After exposure to potassium vapour, the Pyrene 800_{20} sample continued to reveal a comparable macrostructure, with the Pyrene 800_3 sample exhibiting an increased cracking across the external surface with a larger proportion of the internal structure visible.

This aspect of macrostructural appearance for the pyrene samples is similar to that exhibited by the anthracene samples, with the Pyrene 800_3 sample displaying a higher affinity for potassium according to the flame photometry results than the corresponding Pyrene 800_{20} sample. The Pyrene 800_3 sample could thus be expected to show a macro and microstructure that had been changed or altered more significantly, by exposure to potassium, than the Pyrene 800_{20} sample.

The macrostructural evidence from this study, indicates that the anthracene samples (graphitisng carbon) and pyrene (non-graphitising carbon) appeared more susceptible to alterations of the samples structure on exposure to potassium vapour than the chrysene samples (non-graphitising carbon), the fluoranthene samples (graphitising carbon) and the phenanthrene sample

(graphitising carbon). The microstructural evidence indicates that the anthracene samples (graphitisng carbon), the fluoranthene samples (graphitising carbon) and the phenanthrene sample (graphitising carbon) appeared more susceptible to alterations of the samples structure on exposure to potassium vapour than the chrysene samples (non-graphitising carbon) and the pyrene samples (non-graphitising carbon).

7.7- CARBONISED p-TERPHENYL SAMPLES

Microstructural analysis of the Terphen 800_3 sample revealed a non-graphitised carbon structure and areas exhibiting long-range order. After exposure to potassium vapour, the sample displayed areas of convoluted structural order in addition to the long and short-range ordered structures. Both the exposed and unexposed Terphen 800_3 samples revealed a very similar XRD trace, with the peaks centered at 0.333nm and 0.335nm respectively, corresponding to the long-range ordered structure. The 0.449nm peak, arising due to the existence of the non-graphitised carbon structure 0.44nm (0.35-0.49nm), revealed a double peak centered at 0.465nm and 0.554nm after potassium exposure.

Examination of both the exposed and unexposed Terphen 800_{20} samples, by HREM, revealed a non-graphitised carbon structure and areas exhibiting convoluted and long-range structural order. The XRD traces from both the exposed and unexposed samples confirming the slight structural modifications observed by HREM revealing peaks with

interplanar spacings consistent with the non-graphitised carbon structure and the convoluted and long-range structural order.

SEM examination of the Terphen 800_3 and Terphen 800_{20} samples revealed a macrostructure with both exhibiting a smooth external structure and the Terphen 800_3 sample displaying cracks and pitting. Both samples, after exposure to potassium vapour, continued to reveal a macrostructure comparable with that of the unexposed samples.

This aspect of macrostructure appearance for the terphenyl samples is similar to that exhibited by the anthracene samples, with the Terphen 800_3 sample displaying an increased affinity for potassium according to the flame photometry results than the corresponding Terphen 800_{20} sample. The Terphen 800_3 sample could thus be expected to show a macro and microstructure that had been changed or altered more significantly, by exposure to potassium, than the Terphen 800_{20} sample.

The macrostructural evidence from this study, indicates that the anthracene samples (graphitising carbon), the pyrene samples (non-graphitising carbon) and the terphenyl samples (non-graphitising carbon) appeared more susceptible to alterations of the samples structure on exposure to potassium vapour than the chrysene samples (non-graphitising carbon), the fluoranthene samples (graphitising carbon) and the phenanthrene sample (graphitising carbon). The microstructural evidence indicates that the anthracene samples (graphitisng carbon),

the fluoranthene samples (graphitising carbon) and the phenanthrene sample (graphitising carbon) appeared more susceptible to alterations of the samples structure on exposure to potassium vapour than the chrysene samples (non-graphitising carbon), the pyrene samples (non-graphitising carbon) and the terphenyl samples (non-graphitising carbon).

7.8- FLAME PHOTOMETRY MEASUREMENTS

Flame photometry measurements were undertaken to determine which, if any, of the carbonised samples, prepared via a closed carbonisation system, was more susceptible to alkali attack.

Comparisons made between the same carbonised material, prepared under different temperature conditions (altered heating rates, same final temperature and soak period at this temperature), revealed that the anthracene, chrysene, fluoranthene, pyrene and terphenyl samples prepared at a heating rate of 3°C/min exhibit a higher potassium concentration, to varying degrees, than the corresponding 20°C/min preparation. In the case of the anthracene samples an additional carbonised material, $Anthra_1$, was prepared with a heating rate of 1°C/min. This carbon, as expected, exhibited an even higher potassium concentration than the sample prepared at 3°C/min. This comparison was unable to be made for the phenanthrene carbon as only one sample, 20°C/min, was prepared.

7.9- EFFECTS OF INERT CARRIER GASES

In order to determine if the type of inert carrier gas used, altered or had any significant effect on the microstructure of the carbonised samples after exposure to potassium vapour, various inert carrier gases were used when exposing the carbonised materials to potassium vapour.

Examination of the potassium exposed carbonised materials, by HREM and XRD, revealed no significant differences in any of the microstructural forms and appeared to be independent of the carrier gas used. As reported in chapter five, the effects of the non-reacting carrier gases on coke properties can be profound but this is thought to be more significant in the macrostructural properties of the materials.

7.10- THERMOGRAVIMETRIC ANALYSIS (TGA)

Thermogravimetric analysis of the carbonised samples both before and after exposure to potassium vapour revealed a trend similar to that observed for the carbonised samples in chapter five. The onset of weight loss was altered after exposure to potassium vapour, the presence of the potassium reducing the temperature at which combustion began, reflecting the catalytic influence that the potassium has on the carbonised materials

7.11- CONCLUSIONS

The variety and diversity of each carbonised material

was established with the occurrence of differing carbon structures, even before exposure to potassium vapour. Thus, each sample was prepared and analysed several times in order to obtain reproducible results and establish a characteristic representation of the samples due to the heterogeneity of the material.

Overall the XRD traces from the carbonised samples, both before and after exposure to potassium vapour were consistent with the HREM observations and indicated that exposure to potassium vapour resulted in a structure that was more ordered than that exhibited by the unexposed samples. The resultant structural changes, as reported in chapter five, are probably a consequence of potassium penetration into the carbonised microstructure and the subsequent collapse of these expanded lattice planes to a more ordered structure.

From the HREM, XRD and SEM investigations, the graphitisable and non-graphitisable carbonised materials all show some evidence of susceptibility to potassium vapour. The presence of potassium, influences their structural development, by creating areas of long-range and convoluted structural ordering within the carbon matrix, changing their lattice spacing values and altering their macrostructures.

In general, according to the microstructural examination, the carbonised material arising from the graphitising carbons appears more susceptible to potassium than the corresponding non-graphitisng samples. This contrasts with the observations from the study in chapters

four and five where the non-graphitising carbon was considered to be the more susceptible. However, it must be remembered that the carbonised PVA sample (graphitising carbon) gave such an ordered structure to begin with, that it was difficult to determine if the potassium vapour had any significant effect on the structure.

The potassium uptake and flame photometry measurements undertaken to determine which, if any, of the two initial carbonised samples was more susceptible to potassium vapour inferred that the non-graphitised sample was the more susceptible. With the potassium uptake measurements technique, obvious differences between the measured values did arise, as compared to the flame photometry results which revealed similar values and thus a general trend. For the carbonised materials, prepared via a closed carbonisation sytem, the flame photometry results infer that the carbonised materials arising from the non-graphitised carbons 'take-up' more potassium than the corresponding 'graphitising' carbonised materials but that the microstructure of these 'non-graphitised' carbonised materials are the least affected by the presence of potassium.

Due to the inconclusive nature of the macrostructural study on the carbonised materials, prepared via a closed carbonisation procedure, the differences observed between the graphitising and non-graphitising carbon macrostructures could possibly arise as a result of the carbonised materials being prepared and exposed under different inert carrier gas conditions, which has

previously been reported (Shevlin, 1987) as having an effect on the macrostructural properties of coke samples. This could also account for the carbonised sucrose sample exhibiting such a profound macrostructural difference after exposure to potassium vapour and thus have no bearing on the susceptibility of the carbonised material to potassium vapour as was deduced in chapter five.

CHAPTER EIGHT

RESULTS FOR THE SAMPLES PREPARED VIA AN OPEN CARBONISATION SYSTEM

8.1- INTRODUCTION

The results reported in this chapter were obtained for the group of compounds carbonised via an open carbonisation system (table 8.1) and their subsequent exposure to potassium vapour. These samples were studied by a variety of techniques to allow analysis of the microstructural aspects of the different carbonised materials and the subsequent changes induced therein. Due to the number of samples involved a tabulated summary of the TEM and XRD results, both before and after exposure to potassium vapour, is shown for each individual group of samples.

COMPOUND	HEATING RATE	FINAL TEMP	SOAK PERIOD	ATM	CODE
Acenaphthylene	3°C/min	800°C	2hr	N_2	Acenap 800_3
Acenaphthylene	20°C/min	800°C	2hr	N_2	Acenap 800_{20}
Acenaphthylene	1°C/min	800°C	2hr	Ar	$Acenap_A$
Acenaphthylene	1°C/min	800°C	15hr	Ar	$Acenap_B$
Acenaphthylene	1°C/min	1100°C	2hr	Ar	$Acenap_{E1}$
Acenaphthylene	1°C/min	1100°C	15hr	Ar	$Acenap_{E2}$
Acenaphthylene	3°C/min	800°C	2hr	Ar	$Acenap_{E5}$
Acenaphthylene	3°C/min	800°C	15hr	Ar	$Acenap_{E8}$
Acenaphthylene	3°C/min	1100°C	2hr	Ar	$Acenap_{E3}$
Acenaphthylene	3°C/min	1100°C	15hr	Ar	$Acenap_{E4}$
Acenaphthylene	10°C/min	800°C	2hr	Ar	$Acenap_{E6}$
Acenaphthylene	10°C/min	800°C	15hr	Ar	$Acenap_{E7}$
Decacylene	3°C/min	800°C	2hr	N_2	Deca 800_3
Decacylene	20°C/min	800°C	2hr	N_2	Deca 800_{20}

COMPOUND	HEATING RATE	FINAL TEMP	SOAK PERIOD	ATM	CODE
Decacylene	1°C/min	800°C	2hr	Ar	$Deca_3$
Decacylene	1°C/min	800°C	15hr	Ar	$Deca_1$
Decacylene	1°C/min	1100°C	2hr	Ar	$Deca_8$
Decacylene	1°C/min	1100°C	15hr	Ar	$Deca_7$
Decacylene	3°C/min	800°C	2hr	Ar	$Deca_{12}$
Decacylene	3°C/min	800°C	15hr	Ar	$Deca_9$
Decacylene	3°C/min	1100°C	2hr	Ar	$Deca_{10}$
Decacylene	3°C/min	1100°C	15hr	Ar	$Deca_{11}$
Decacylene	10°C/min	800°C	2hr	Ar	$Deca_5$
Decacylene	10°C/min	800°C	15hr	Ar	$Deca_6$
Dibenzanthrone	1°C/min	800°C	2hr	Ar	$Dibenz_5$
Dibenzanthrone	1°C/min	800°C	15hr	Ar	$Dibenz_1$
Dibenzanthrone	1°C/min	1100°C	2hr	Ar	$Dibenz_8$
Dibenzanthrone	1°C/min	1100°C	15hr	Ar	$Dibenz_7$
Dibenzanthrone	3°C/min	800°C	2hr	Ar	$Dibenz_{16}$
Dibenzanthrone	3°C/min	800°C	15hr	Ar	$Dibenz_9$
Dibenzanthrone	3°C/min	1100°C	2hr	Ar	$Dibenz_{15}$
Dibenzanthrone	3°C/min	1100°C	15hr	Ar	$Dibenz_{14}$
Dibenzanthrone	10°C/min	800°C	2hr	Ar	$Dibenz_{10}$
Dibenzanthrone	10°C/min	800°C	15hr	Ar	$Dibenz_{11}$
PVA	1°C/min	800°C	2hr	Ar	PVA_2
PVA	1°C/min	800°C	15hr	Ar	PVA_1
Sucrose	1°C/min	800°C	2hr	Ar	SUC_1
Sucrose	1°C/min	800°C	15hr	Ar	SUC_2
Sucrose	3°C/min	800°C	15hr	Ar	SUC_{E1}

Table 8.1 The conditions of preparation for the aromatic hydrocarbons carbonised via an open carbonisation system.

Examination of the carbonised samples by HREM, both before and after exposure to potassium vapour, revealed non-graphitised carbon structures, long-range ordered structures and areas exhibiting convoluted structural development. Generally these structures are represented by figures throughout chapters 4 and 6 and thus only a selection will be exhibited in this chapter.

8.2- ANALYSIS OF CARBONISED ACENAPHTHYLENE

Graphitisation of acenaphthylene at 3000°C is known to result in the formation of a graphitising carbon (Fitzer et al., 1971). In this study twelve carbonised samples were prepared and examined.

8.2.1- TRANSMISSION ELECTRON MICROSCOPY (TEM)

The Acenap 800_3 sample revealed a non-graphitising carbon structure (L_a=1-4.5nm) with lattice spacings in the range 0.34-0.48nm and a typical value of 0.43nm (L_c=0.34-3nm).

A non-graphitising carbon structure was displayed by the Acenap 800_{20} sample (L_a=1-7nm) with lattice spacings in the range 0.34-0.49nm and a typical value of 0.39nm (L_c=0.68-4.2nm).

The $Acenap_A$ sample exhibited two distinct types of microstructure, a non-graphitised carbon structure (L_a=1-5nm) with interplanar spacings in the range 0.39-0.68nm and a typical value of 0.45nm (L_c=0.4-3.5nm), and areas of long-range ordered structure (L_a=25-76nm) with

lattice spacings of between 0.31-0.36nm (figure 8.1) and a typical value of 0.34nm (L_c=2-29nm).

Examination of the $Acenap_B$ sample revealed a non-graphitised carbon structure (L_a=1-5.5nm) with lattice spacings in the range 0.34-0.58nm and a typical value of 0.41nm (L_c=0.34-4.8nm).

Analysis of the $Acenap_{E1}$ sample revealed both a non-graphitised carbon structure (L_a=1-4nm) with interplanar spacings in the range 0.34-0.49nm and a typical value of 0.41nm (L_c=0.34-2.5nm), and areas of long-range ordered structure (L_a=10-36nm) with lattice spacings of between 0.31-0.36nm and a typical value of 0.34nm (L_c=4.5-13nm).

The $Acenap_{E2}$ sample exhibited areas of ordered long-range structure (L_a=13-21nm) with lattice spacings of 0.34nm (L_c=10-20nm) and areas of short-range ordered structure (L_a=1-2.5nm) with lattice spacings in the range 0.35-0.61nm (figure 8.2) and a typical value of 0.48nm (L_c=0.7-1.5nm).

A non-graphitising carbon structure was displayed by the $Acenap_{E5}$ sample (L_a=1-6nm) with lattice spacings in the range 0.34-0.49nm and a typical value of 0.39nm (L_c=0.4-3.4nm).

Examination of the $Acenap_{E8}$ sample revealed a long-range ordered structure and areas of convoluted structural order (L_a=9-29nm) with interplanar spacings in the range 0.33-0.39nm, and a typical value of 0.35nm (L_c=4-21nm). The non-graphitised carbon structure (L_a=1-3.5nm) showed lattice spacings of between 0.34-0.52nm with a typical value of 0.41nm (L_c=0.68-2nm).

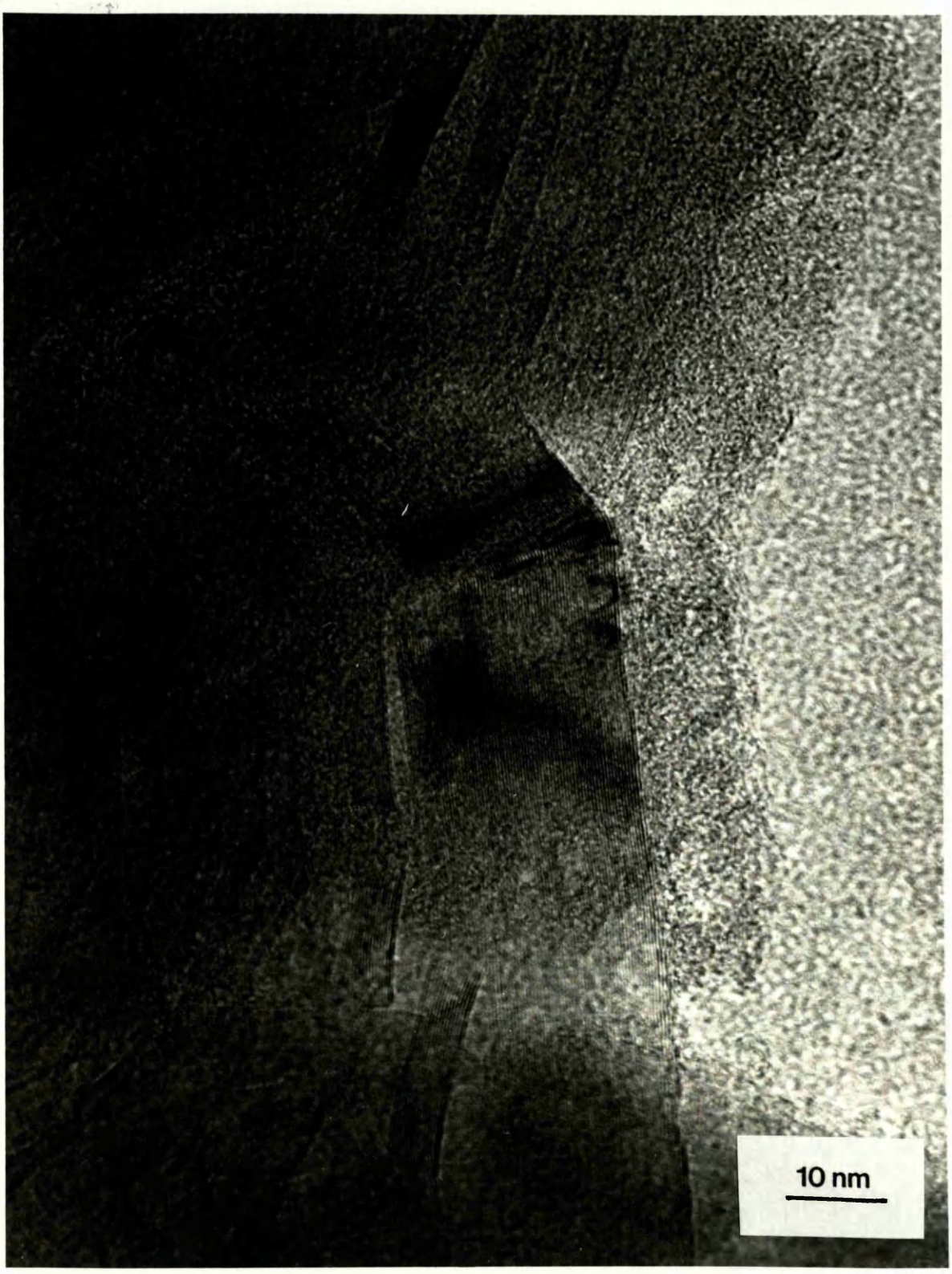

Figure 8.1: HREM of the $Acenap_A$ sample showing the long-range ordered structure (0.31-0.36nm).

Figure 8.2: HREM of the Acenap$_{E2}$ sample showing the non-graphitised carbon structure (0.35-0.61nm).

Three types of structure were displayed by the $Acenap_{E3}$ sample, a long-range ordered structure, a non-graphitised carbon structure and areas exhibiting convoluted structural development. The convoluted and long-range ordered structure revealed similar L_a=21-43nm and L_c=8.5-26nm values with lattice spacings in the range 0.31-0.39nm, and a typical value of 0.35nm. The non-graphitised carbon structure (L_a=1-4.5nm) showed lattice spacings of between 0.35-0.48nm with a typical value of 0.40nm (L_c=0.34-1.5nm).

Analysis of the $Acenap_{E4}$ sample revealed areas of extensively well-ordered long-range structure (L_a=17-65nm) with interplanar spacings of between 0.31-0.36nm, and a typical value of 0.34nm (L_c=4-8.5nm). The short-range ordered structure (L_a=1-3.3nm) revealed lattice spacings within the range 0.35-0.57nm, and a typical value of 0.44nm (L_c=0.7-2.6nm).

The $Acenap_{E6}$ sample exhibited a non-graphitised carbon structure (L_a=1-5nm) with interplanar spacings in the range 0.35-0.55nm and a typical value of 0.48nm (L_c=0.7-3.5nm). The sample also revealed areas of long-range ordered structure (L_a=11-34nm) with lattice spacings of 0.34nm (L_c=6-23nm).

A non-graphitising carbon structure (L_a=1-4.5nm) with lattice spacings in the range 0.34-0.54nm and a typical value of 0.39nm (L_c=0.34-3nm) was revealed by the $Acenap_{E7}$ sample.

8.2.2- SCANNING ELECTRON MICROSCOPY (SEM)

Examination of the acenaphthylene samples by SEM

revealed a smooth external surface exhibiting cracks (figure 8.3) and two types of lamellar layer structure; sheet-like lamellar layers (figure 8.4) and a smooth, folded, flow-like lamellar surface (figure 8.5). Table 8.2 summarises the SEM structure exhibited by each of the acenaphthylene samples.

SAMPLE	STRUCTURE EXHIBITED
Acenap 800_3	smooth, folded, flow-like lamellar surface
Acenap 800_{20}	sheet-like lamellar layers
$Acenap_A$	sheet-like lamellar layers
$Acenap_B$	sheet-like lamellar layers
$Acenap_{E1}$	sheet-like lamellar layers
$Acenap_{E2}$	sheet-like lamellar layers
$Acenap_{E5}$	smooth, folded, flow-like lamellar surface
$Acenap_{E8}$	sheet-like lamellar layers
$Acenap_{E3}$	smooth, folded, flow-like lamellar surface
$Acenap_{E4}$	sheet-like lamellar layers
$Acenap_{E6}$	smooth, folded, flow-like lamellar surface
$Acenap_{E7}$	smooth, folded, flow-like lamellar surface

Table 8.2 SEM structures exhibited by each of the carbonised acenaphthylene samples.

8.2.3- POWDER X-RAY DIFFRACTION ANALYSIS (XRD)

The Acenap 800_3 x-ray diffraction trace exhibited three peaks within the interplanar spacings range (41.8-15.6^o) 0.251-0.660nm (figure 8.6). The sharpest, most intense peak was centered at (30.4^o) 0.341nm with the two remaining

Figure 8.3: SEM showing a smooth external surface with deep cracks, exhibited by both the acenaphthylene and decacylene samples.

Figure 8.4: SEM revealing the sheet-like lamellar layers exhibited by some of the acenaphthylene and decacylene samples.
(Acenap 800_{20}, $Acenap_{E1}$, $Acenap_{E2}$, $Acenap_{E8}$, $Acenap_{E4}$, Deca 800_3, Deca 800_{20}, $Deca_1$, $Deca_8$, $Deca_7$, $Deca_{11}$, $Deca_6$).

Figure 8.5: SEM displaying the smooth, folded, flow-like lamellar surface exhibited by some of the acenaphthylene and decacylene samples.
(Acenap 800_3, $Acenap_{E5}$, $Acenap_{E3}$, $Acenap_{E6}$, $Acenap_{E7}$, $Deca_3$, $Deca_{12}$, $Deca_9$, $Deca_{10}$, $Deca_5$).

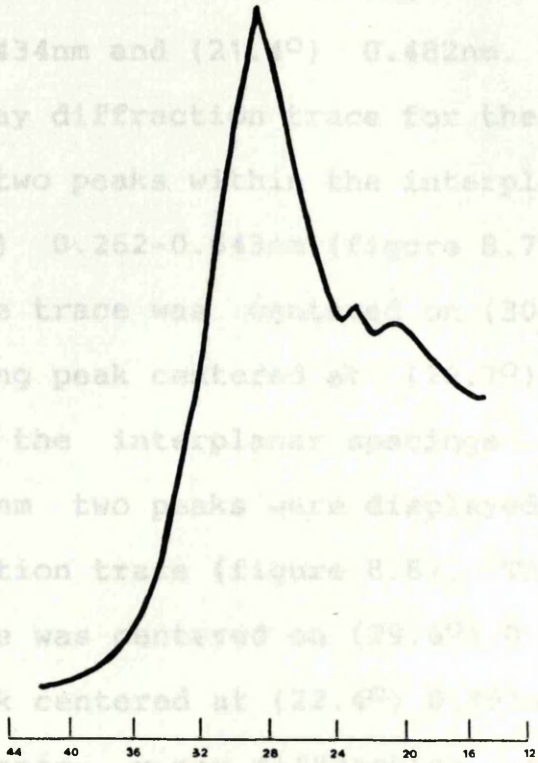

Figure 8.6: XRD trace of the Acenap 800_3 sample.

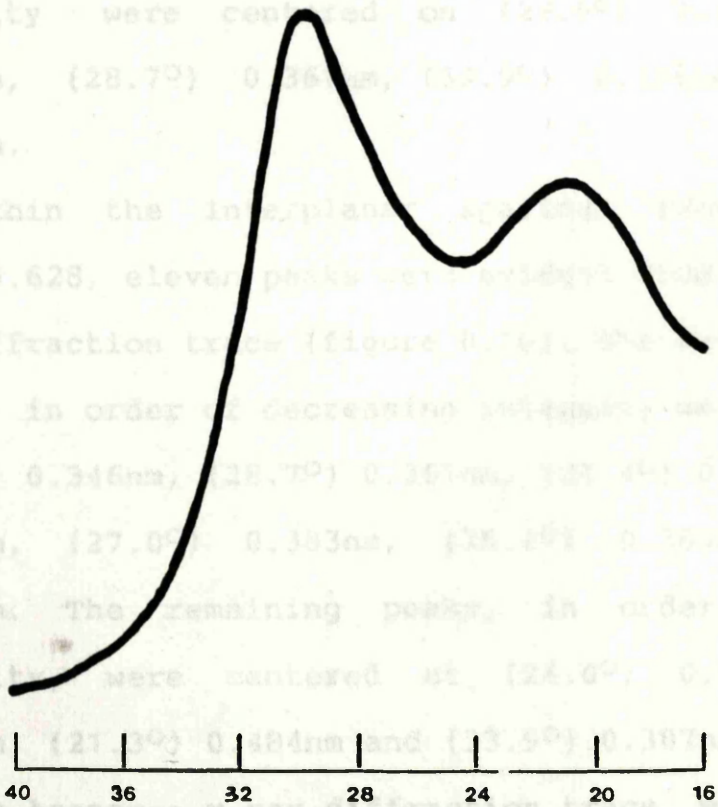

Figure 8.7: XRD trace of the Acenap 800_{20} sample.

peaks, in order of decreasing intensity, centered at (23.8°) 0.434nm and (21.4°) 0.482nm.

The x-ray diffraction trace for the Acenap 800_{20} sample exhibited two peaks within the interplanar spacings range (40.0-16.0°) 0.262-0.643nm (figure 8.7). The most intense peak of the trace was centered on (30.0°) 0.346nm with the remaining peak centered at (20.7°) 0.498nm.

Within the interplanar spacings range (42.2-14.6°) 0.249-0.704nm two peaks were displayed for the $Acenap_A$ x-ray diffraction trace (figure 8.8). The most intense peak of the trace was centered on (29.6°) 0.350nm with the less intense peak centered at (22.4°) 0.461nm.

The $Acenap_B$ x-ray diffraction trace exhibited five peaks within the interplanar spacings range (40.0-16.0°) 0.262-0.643 (figure 8.9). The peaks, in order of decreasing intensity were centered on (29.9°) 0.347nm, (30.4°) 0.341nm, (28.7°) 0.361nm, (30.9°) 0.336nm, and (20.6°) 0.501nm.

Within the interplanar spacings range (38.6-16.4°) 0.271-0.628, eleven peaks were evident from the $Acenap_{E1}$ x-ray diffraction trace (figure 8.10). The seven most intense peaks, in order of decreasing intensity were centered on (30.0°) 0.346nm, (28.7°) 0.361nm, (31.4°) 0.331nm, (27.8°) 0.373nm, (27.0°) 0.383nm, (26.6°) 0.389nm and (25.0°) 0.414nm. The remaining peaks, in order of decreasing intensity, were centered at (24.0°) 0.431nm, (23.0°) 0.449nm, (21.3°) 0.484nm and (33.9°) 0.307nm respectively.

The $Acenap_{E2}$ x-ray diffraction trace, with interplanar spacings in the range (40.0-12.0°) 0.262-0.856nm, exhibited

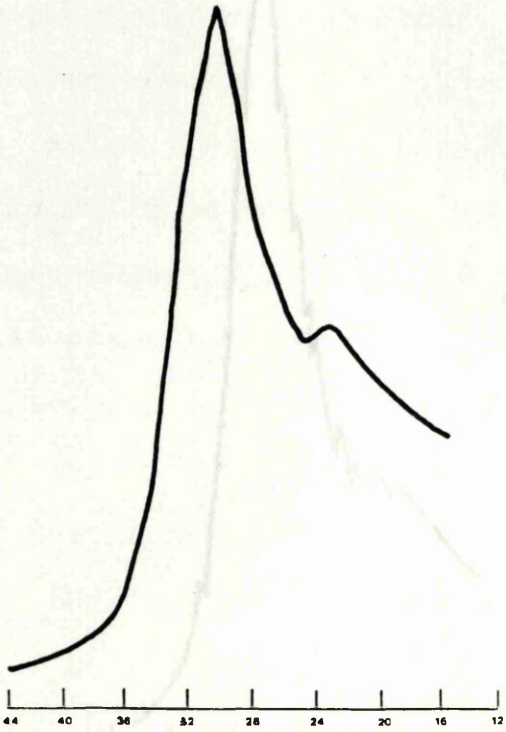

Figure 8.8: XRD trace of the $Acenap_A$ sample.

Figure 8.9: XRD trace of the $Acenap_B$ sample.

Figure 8.10: XRD trace of the $Acenap_{E1}$ sample.

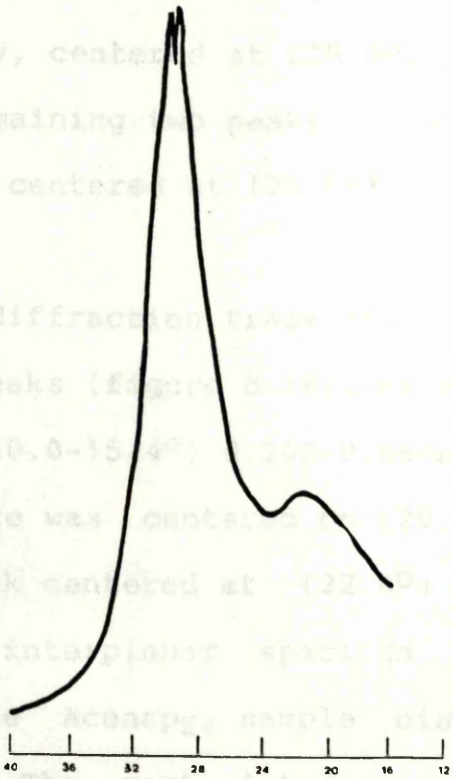

Figure 8.11: XRD trace of the $Acenap_{E2}$ sample.

three peaks (figure 8.11). Two of the peaks, occurring within close proximity of each other, exhibited a similar intensity and were centered at (30.2°) 0.344nm and (29.7°) 0.349nm. The third, less intense peak, was broader and centered at (21.3°) 0.484nm.

The $Acenap_{E5}$ x-ray diffraction trace, with interplanar spacings in the range (41.4-15.2°) 0.253-0.677nm, exhibited three peaks (figure 8.12). Two of the peaks, occurring within close proximity of each other, exhibited a similar intensity and were centered at (30.4°) 0.341nm and (28.8°) 0.360nm. The third, less intense peak, was broader and centered at (20.8°) 0.495nm.

Five peaks were evident from the $Acenap_{E8}$ x-ray diffraction trace (figure 8.13), within the interplanar spacings range (35.6-20.0°) 0.293-0.515nm. The most intense peak was centered at (30.0°) 0.346nm with two peaks, of similar intensity, centered at (28.9°) 0.359nm and (31.0°) 0.335nm. The remaining two peaks, in order of decreasing intensity were centered at (26.5°) 0.391nm and (25.6°) 0.404nm.

The x-ray diffraction trace for the $Acenap_{E3}$ sample exhibited two peaks (figure 8.14). Within the interplanar spacings range (40.0-15.4°) 0.262-0.668nm, the most intense peak of the trace was centered on (29.8°) 0.348nm with the remaining peak centered at (22.0°) 0.469nm.

Within the interplanar spacings range (40.0-12.0°) 0.262-0.856nm the $Acenap_{E4}$ sample displayed four peaks (figure 8.15). The most intense peak of the x-ray diffraction trace was centered at (29.6°) 0.350nm with the

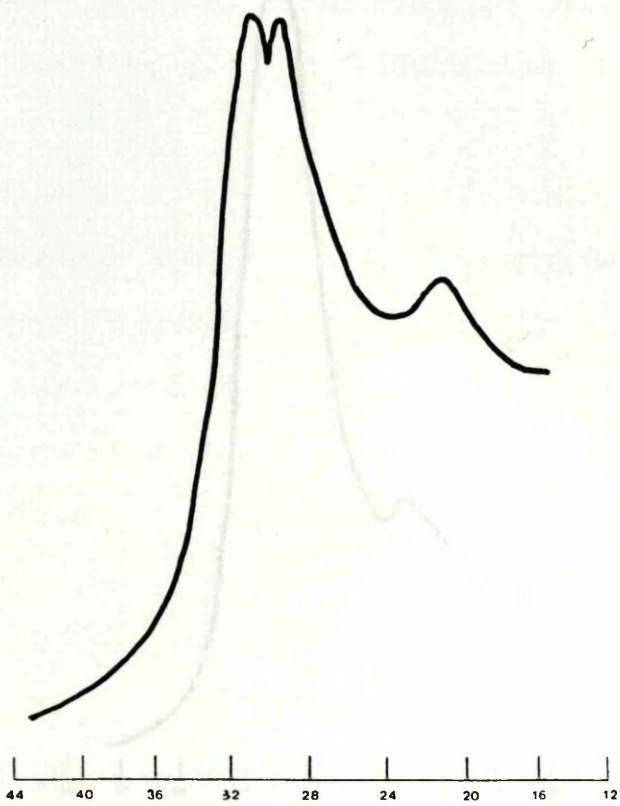

Figure 8.12: XRD trace of the $Acenap_{E5}$ sample.

Figure 8.13: XRD trace of the $Acenap_{E8}$ sample.

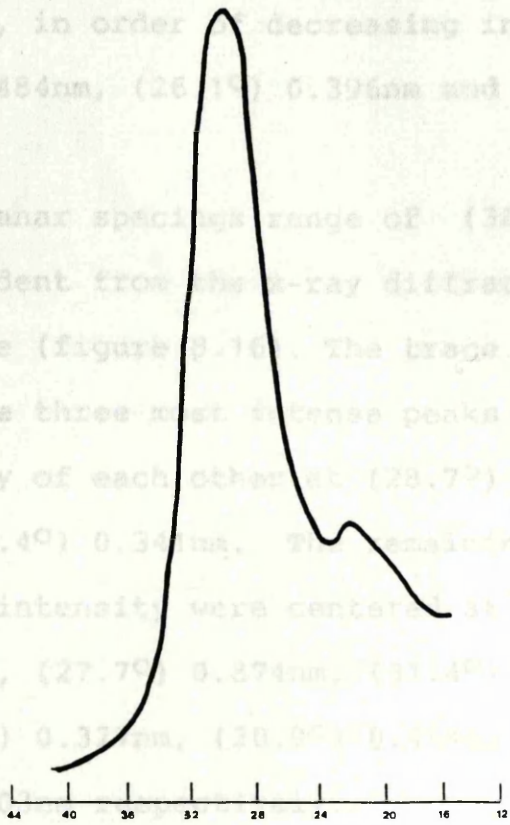

Figure 8.14: XRD trace of the $Acenap_{E3}$ sample.

Figure 8.15: XRD trace of the $Acenap_{E4}$ sample.

remaining peaks, in order of decreasing intensity, centered at (21.3°) 0.484nm, (26.1°) 0.396nm and (25.7°) 0.402nm respectively.

An interplanar spacings range of (36.0-16.0°) 0.290-0.643nm was evident from the x-ray diffraction trace of the $Acenap_{E6}$ sample (figure 8.16). The trace revealed twelve peaks, with the three most intense peaks centered within close proximity of each other at (28.7°) 0.361nm, (29.7°) 0.349nm and (30.4°) 0.341nm. The remaining peaks, in order of decreasing intensity were centered at (30.9°) 0.336nm, (28.3°) 0.366nm, (27.7°) 0.374nm, (31.4°) 0.331nm, (27.0°) 0.383nm, (31.8°) 0.327nm, (20.9°) 0.494nm, (32.8°) 0.317nm and (34.4°) 0.303nm respectively.

Within the interplanar spacings range (37.4-17.0°) 0.279-0.606, twelve peaks were exhibited for the x-ray diffraction trace of the $Acenap_{E7}$ sample (figure 8.17). Two peaks, of similar intensity, and within close proximity of each other were centered at (30.1°) 0.345nm and (29.7°) 0.349nm. The remaining peaks, in order of decreasing intensity, were centered at (29.2°) 0.355nm, (28.7°) 0.361nm, (31.0°) 0.335nm, (28.3°) 0.366nm, (26.3°) 0.393nm, (25.9°) 0.407nm, (24.2°) 0.427nm, (22.0°) 0.469nm, (25.2°) 0.410nm and (19.1°) 0.540nm respectively.

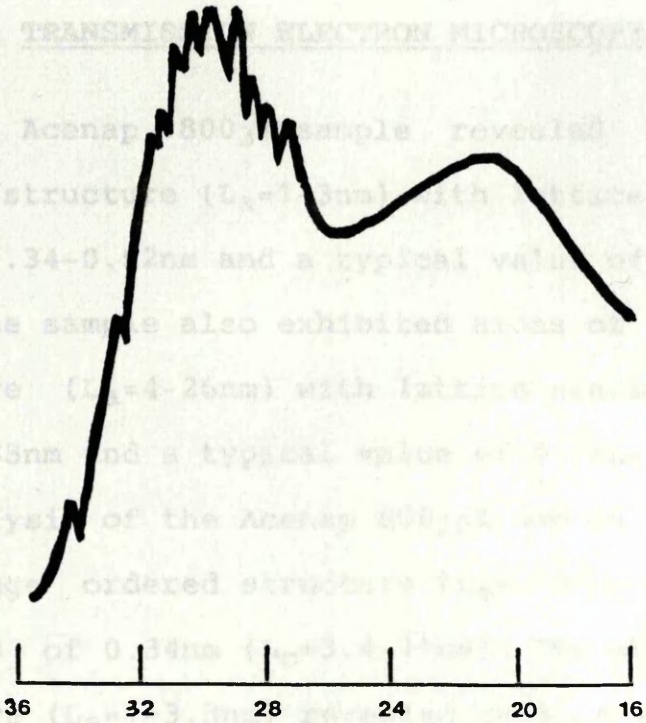

Figure 8.16: XRD trace of the $Acenap_{E6}$ sample.

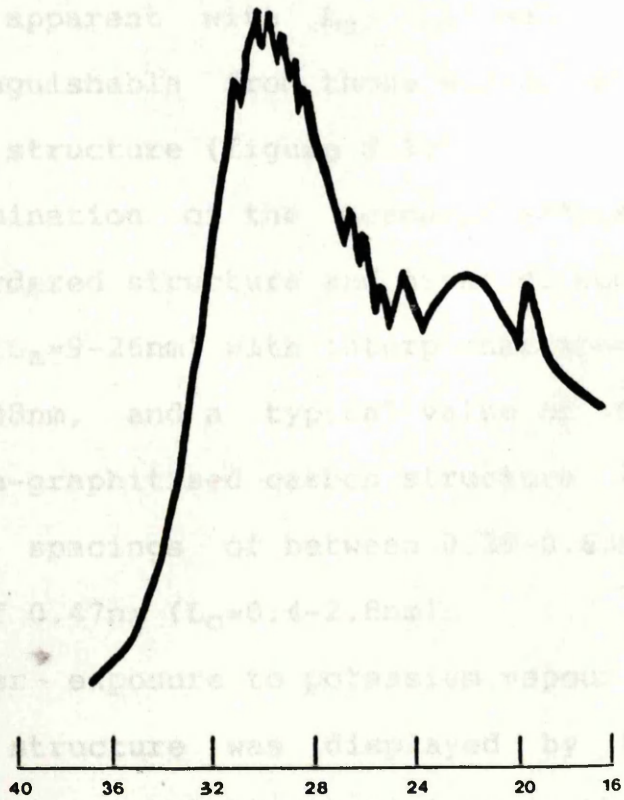

Figure 8.17: XRD trace of the $Acenap_{E7}$ sample.

8.3- EFFECT OF POTASSIUM ON CARBONISED ACENAPHTHYLENE

8.3.1- TRANSMISSION ELECTRON MICROSCOPY (TEM)

The Acenap 800_3K sample revealed a non-graphitised carbon structure (L_a=1-3nm) with lattice spacings in the range 0.34-0.52nm and a typical value of 0.43nm (L_c=0.68-3nm). The sample also exhibited areas of long-range ordered structure (L_a=4-26nm) with lattice spacings in the range 0.33-0.38nm and a typical value of 0.34nm (L_c=3-14nm).

Analysis of the Acenap $800_{20}K$ sample revealed areas of long-range ordered structure (L_a=7-37nm) with interplanar spacings of 0.34nm (L_c=3.4-11nm). The short-range ordered structure (L_a=1-3.3nm) revealed lattice spacings within the range 0.59-0.74nm, and a typical value of 0.67nm (L_c=0.6-3nm). In addition areas of convoluted structural order became apparent with L_a, L_c and interplanar spacings indistinguishable from those exhibited by the long-range ordered structure (figure 8.18).

Examination of the $Acenap_AK$ sample revealed a long-range ordered structure and areas of convoluted structural order (L_a=9-26nm) with interplanar spacings in the range 0.31-0.38nm, and a typical value of 0.35nm (L_c=4-19nm). The non-graphitised carbon structure (L_a=1-3.7nm) showed lattice spacings of between 0.39-0.63nm with a typical value of 0.47nm (L_c=0.4-2.8nm).

After exposure to potassium vapour a non-graphitising carbon structure was displayed by the $Acenap_B$ sample (L_a=1-6nm) with lattice spacings in the range 0.34-0.48nm and a typical value of 0.41nm (L_c=0.34-3.4nm).

Figure 8.18: HREM of the Acenap 800_{20}K sample showing the convoluted and long-range structural order (0.34nm).

The $Acenap_{E1}K$ sample revealed a non-graphitised carbon structure (L_a=1-5nm) with lattice spacings in the range 0.34-0.54nm and a typical value of 0.44nm (L_c=0.68-4.8nm).

A non-graphitised carbon structure was exhibited by the $Acenap_{E2}K$ sample (L_a=1-3.5nm) with interplanar spacings in the range 0.34-0.48nm and a typical value of 0.42nm (L_c=0.68-3.5nm). The sample also revealed areas of long-range ordered structure (L_a=7-34nm) with lattice spacings of 0.34nm (L_c=3-18nm).

Examination of the $Acenap_{E5}$ sample, after exposure to potassium vapour, revealed a non-graphitised carbon structure (L_a=1-5nm) with lattice spacings in the range 0.34-0.66nm and a typical value of 0.54nm (L_c=0.34-4.3nm).

The $Acenap_{E8}K$ sample revealed a long-range ordered structure and areas of convoluted structural order (L_a=8-24nm) with interplanar spacings in the range 0.33-0.39nm, and a typical value of 0.35nm (L_c=4-19nm). The non-graphitised carbon structure (L_a=1-3.5nm) showed lattice spacings of between 0.34-0.51nm with a typical value of 0.41nm (L_c=0.68-2nm).

Analysis of the $Acenap_{E3}K$ sample revealed a non-graphitised carbon structure (L_a=1-4nm) with interplanar spacings in the range 0.34-0.51nm and a typical value of 0.37nm (L_c=0.34-3.2nm), and areas of long-range ordered structure (L_a=10-36nm) with lattice spacings of 0.34nm (L_c=5-13nm).

After exposure to potassium vapour a non-graphitising carbon structure was displayed by the $Acenap_{E4}$ sample (L_a=1-6nm) with lattice spacings in the range 0.34-0.51nm

and a typical value of 0.44nm (L_c=0.34-4nm).

Analysis of the $Acenap_{E6}K$ sample revealed areas of long-range ordered structure (L_a=9-47nm) with interplanar spacings of between 0.34-0.39nm and a typical value of 0.35nm (L_c=4-17nm). The short-range ordered structure (L_a=1-3nm) revealed lattice spacings within the range 0.36-0.54nm, and a typical value of 0.42nm (L_c=0.72-4nm). In addition areas of convoluted structural order became apparent with L_a, L_c and interplanar spacings indistinguishable from those exhibited by the long-range ordered structure.

A non-graphitised carbon structure was exhibited by the $Acenap_{E7}K$ sample (L_a=1-3.5nm) with interplanar spacings in the range 0.34-0.48nm and a typical value of 0.39nm (L_c=0.68-3.5nm). The sample also revealed areas of long-range ordered structure (L_a=6-30nm) with lattice spacings of 0.34nm (L_c=3-18nm).

8.3.2- SCANNING ELECTRON MICROSCOPY (SEM)

Examination of the acenaphthylene samples after exposure to potassium vapour continued to reveal a smooth layer structure, sheet-like lamellar layers and a smooth, folded, flow-like lamellar surface. However, exposure to the potassium vapour had not only increased the extent of cracking across the samples surface (figure 8.19) but also resulted in the development of large holes (figure 8.20). Table 8.3 summarises the SEM structure exhibited by each of the acenaphthylene samples.

SAMPLE	STRUCTURE EXHIBITED
Acenap 800_3K	sheet-like lamellar layers
Acenap $800_{20}K$	sheet-like lamellar layers
$Acenap_AK$	sheet-like lamellar layers
$Acenap_BK$	sheet-like lamellar layers
$Acenap_{E1}K$	sheet-like lamellar layers
$Acenap_{E2}K$	sheet-like lamellar layers
$Acenap_{E5}K$	smooth, folded, flow-like lamellar surface
$Acenap_{E8}K$	sheet-like lamellar layers
$Acenap_{E3}K$	sheet-like lamellar layers
$Acenap_{E4}K$	sheet-like lamellar layers
$Acenap_{E6}K$	smooth, folded, flow-like lamellar surface
$Acenap_{E7}K$	smooth, folded, flow-like lamellar surface

Table 8.3 SEM structures exhibited by each of the acenaphthylene samples after exposure to potassium vapour.

8.3.3- POWDER X-RAY DIFFRACTION ANALYSIS (XRD)

Examination of the Acenap 800_3K sample by x-ray diffraction revealed a trace with interplanar spacings in the range (34.6-16.0°) 0.301-0.643nm (figure 8.21) and two peaks, in order of decreasing intensity, centered at (29.6°) 0.350nm and (28.6°) 0.362nm.

The Acenap $800_{20}K$ sample exhibited four peaks within the interplanar spacings range (40.0-16.0°) 0.262-0.643nm (figure 8.22). The most intense peak of the XRD trace was centered at (29.7°) 0.349nm with the remaining peaks, in order of decreasing intensity, centered at (28.9°) 0.359nm, (30.6°) 0.339nm and (28.3°) 0.366nm respectively.

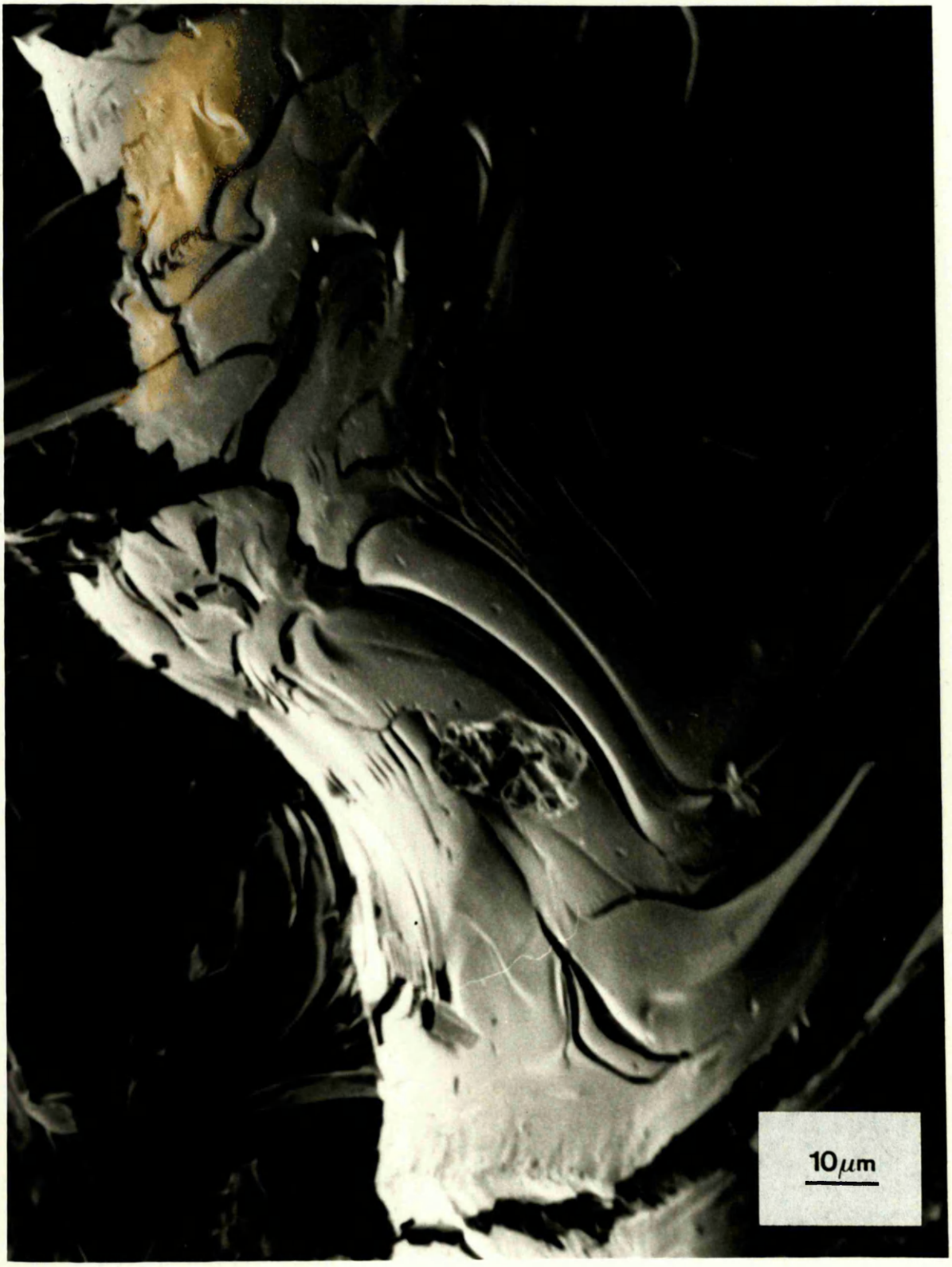

Figure 8.19: SEM exhibiting the increased cracking across the external surface of both the acenaphthylene and decacylene samples after exposure to potassium vapour.

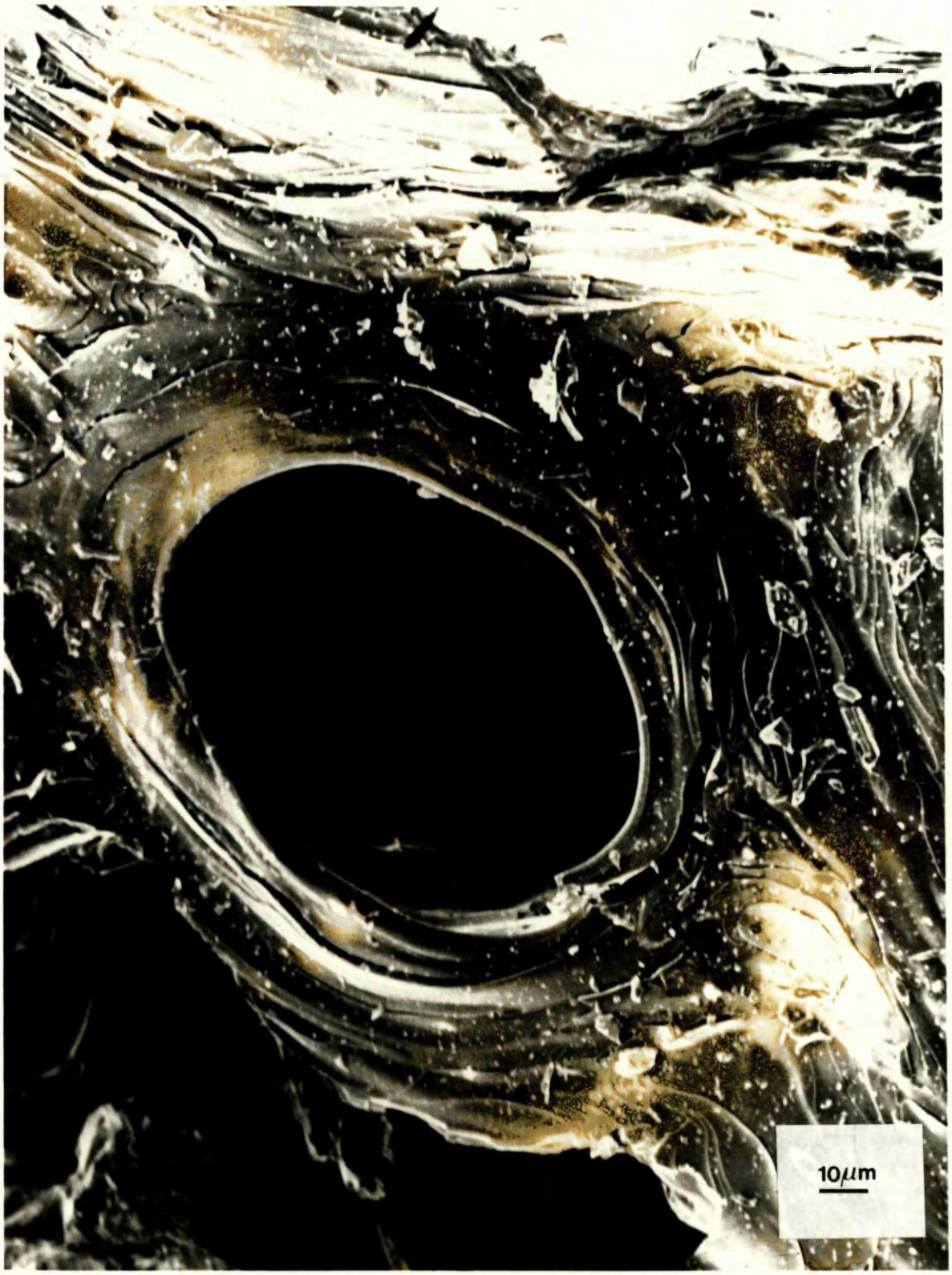

Figure 8.20: SEM revealing the development of holes in the external surface of the acenaphthylene samples after exposure to potassium vapour.

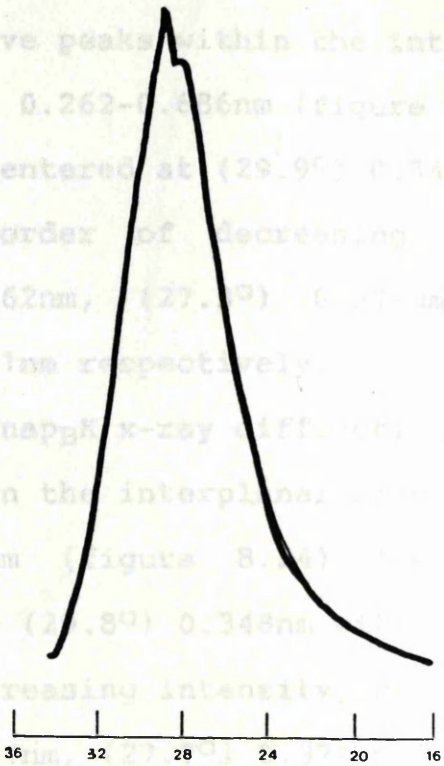

Figure 8.21: XRD trace of the Acenap 800_3K sample.

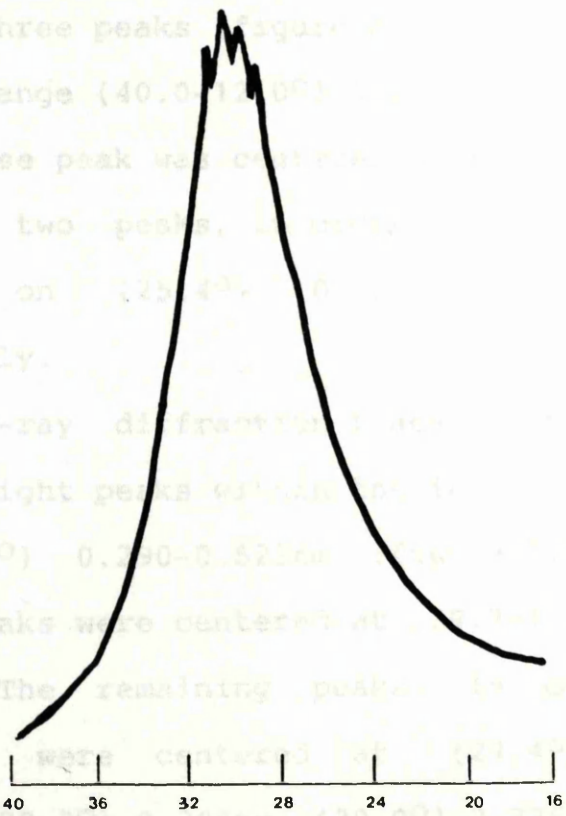

Figure 8.22: XRD trace of the Acenap 800_{20}K sample.

The x-ray diffraction trace of the $Acenap_AK$ sample revealed five peaks within the interplanar spacings range (40.0-15.0°) 0.262-0.686nm (figure 8.23). The most intense peak was centered at (29.9°) 0.347nm with the remaining peaks, in order of decreasing intensity, centered at (28.6°) 0.362nm, (27.3°) 0.379nm, (26.5°) 0.391nm and (21.9°) 0.471nm respectively.

The $Acenap_BK$ x-ray diffraction trace exhibited seven peaks within the interplanar spacings range (37.7-18.0°) 0.277-0.572nm (figure 8.24). The most intense peak was centered at (29.8°) 0.348nm with the remaining peaks, in order of decreasing intensity, centered on (30.4°) 0.341nm, (31.1°) 0.334nm, (27.7°) 0.374nm, (25.4°) 0.407nm, (25.0°) 0.414nm and (21.4°) 0.482nm respectively.

Examination of the $Acenap_{E1}K$ x-ray diffraction trace revealed three peaks (figure 8.25). Within the interplanar spacings range (40.0-12.0°) 0.262-0.856nm the broadest and most intense peak was centered at (28.8°) 0.360nm with the remaining two peaks, in order of decreasing intensity, centered on (25.4°) 0.407nm and (18.7°) 0.551nm respectively.

The x-ray diffraction trace of the $Acenap_{E2}K$ sample revealed eight peaks within the interplanar spacings range (36.0-19.7°) 0.290-0.523nm (figure 8.26). The two most intense peaks were centered at (29.7°) 0.349nm and (30.4°) 0.341nm. The remaining peaks, in order of decreasing intensity, were centered at (29.4°) 0.353nm, (28.7°) 0.361nm, (28.3°) 0.366nm, (30.9°) 0.336nm, (25.3°) 0.409nm and (24.7°) 0.419nm.

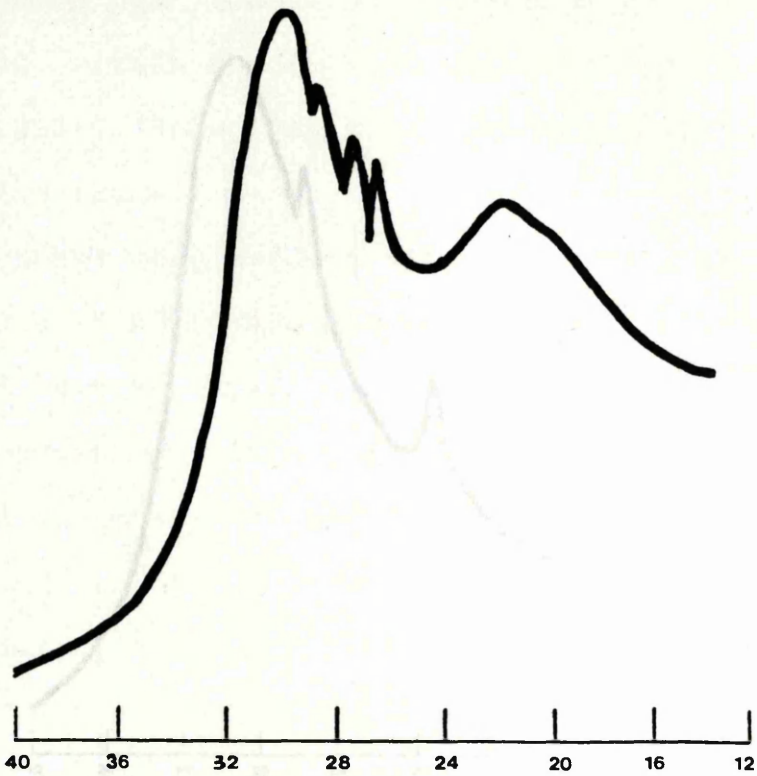

Figure 8.23: XRD trace of the $Acenap_AK$ sample.

Figure 8.24: XRD trace of the $Acenap_BK$ sample.

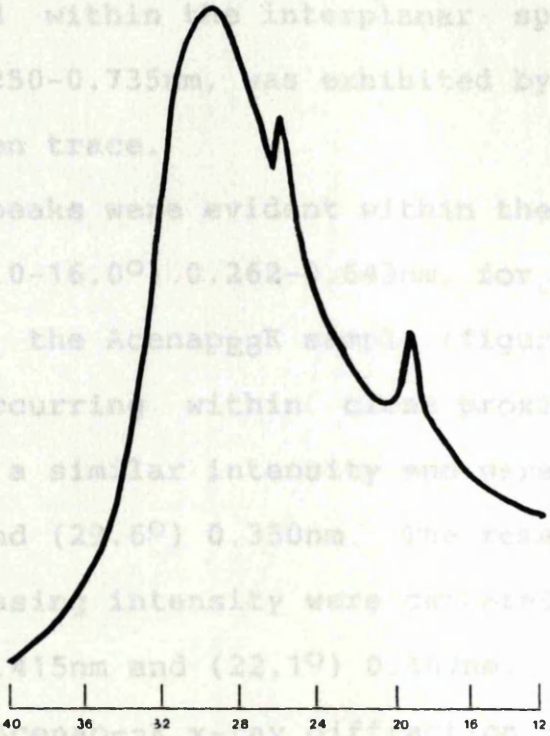

Figure 8.25: XRD trace of the $Acenap_{E1}K$ sample.

Figure 8.26: XRD trace of the $Acenap_{E2}K$ sample.

One broad peak, centered at (30.0°) 0.345nm (figure 8.27) and within the interplanar spacings range (42.0-14.0°) 0.250-0.735nm, was exhibited by the $Acenap_{E5}K$ x-ray diffraction trace.

Five peaks were evident within the interplanar spacings range (40.0-16.0°) 0.262-0.643nm, for the x-ray diffraction trace of the $Acenap_{E8}K$ sample (figure 8.28). Two of the peaks, occurring within close proximity of each other exhibited a similar intensity and were centered at (30.1°) 0.345nm and (29.6°) 0.350nm. The remaining peaks, in order of decreasing intensity were centered at (28.4°) 0.365nm, (24.9°) 0.415nm and (22.1°) 0.467nm.

The $Acenap_{E3}K$ x-ray diffraction trace exhibited five peaks within the interplanar spacings range (40.0-12.0°) 0.262-0.856nm (figure 8.29). The broadest and most intense peak was centered at (27.9°) 0.371nm with the remaining peaks, in order of decreasing intensity, centered on (25.4°) 0.407nm, (30.9°) 0.336nm, (24.0°) 0.431nm and (20.4°) 0.505nm respectively.

Seven peaks were evident within the interplanar spacings range (38.6-17.4°) 0.271-0.592nm, for the x-ray diffraction trace of the $Acenap_{E4}K$ sample (figure 8.30). The three most intense peaks were centered within close proximity of each other at (28.5°) 0.364nm, (29.3°) 0.354nm and (30.0°) 0.346nm. The remaining peaks, in order of decreasing intensity were centered at (27.9°) 0.371nm, (27.2°) 0.381nm, (26.2°) 0.395nm and (23.4°) 0.414nm.

The $Acenap_{E6}K$ x-ray diffraction trace exhibited four peaks within the interplanar spacings range (40.0-14.0°)

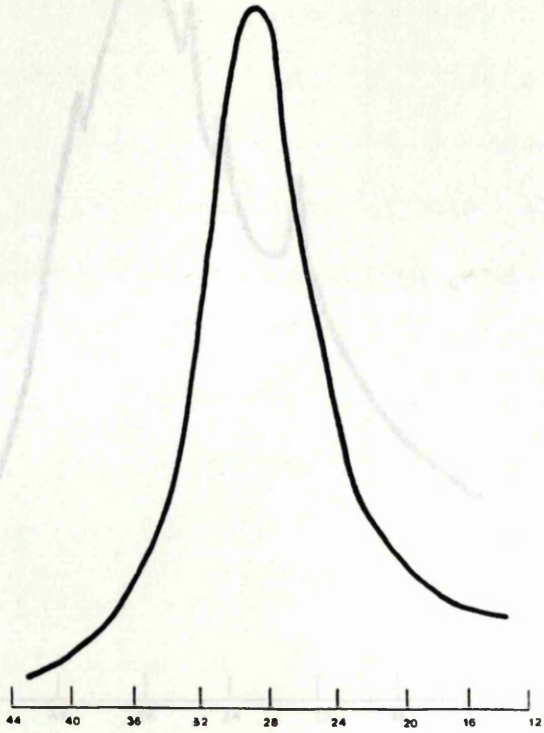

Figure 8.27: XRD trace of the $Acenap_{E5}K$ sample.

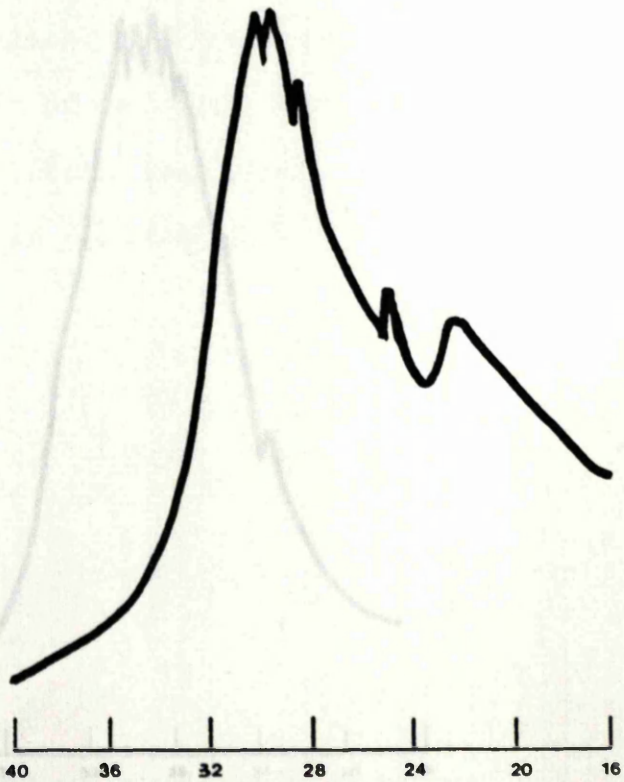

Figure 8.28: XRD trace of the $Acenap_{E8}K$ sample.

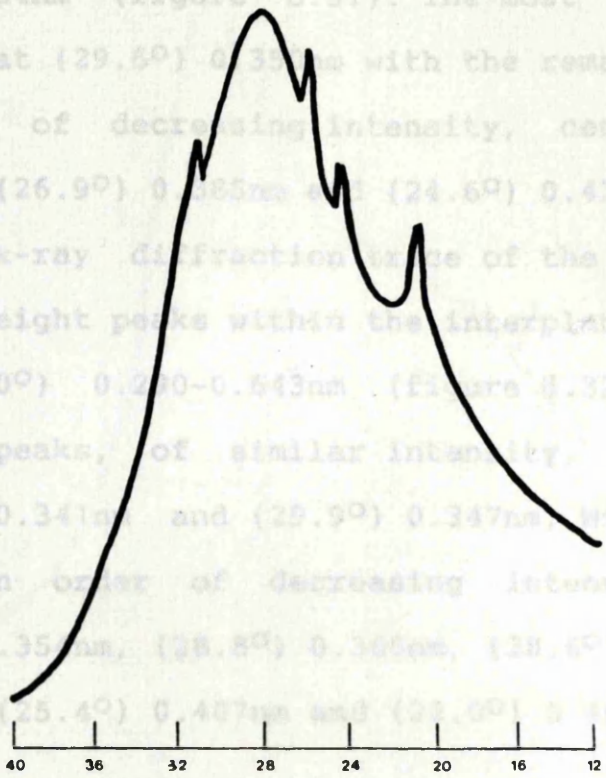

Figure 8.29: XRD trace of the $Acenap_{E3}K$ sample.

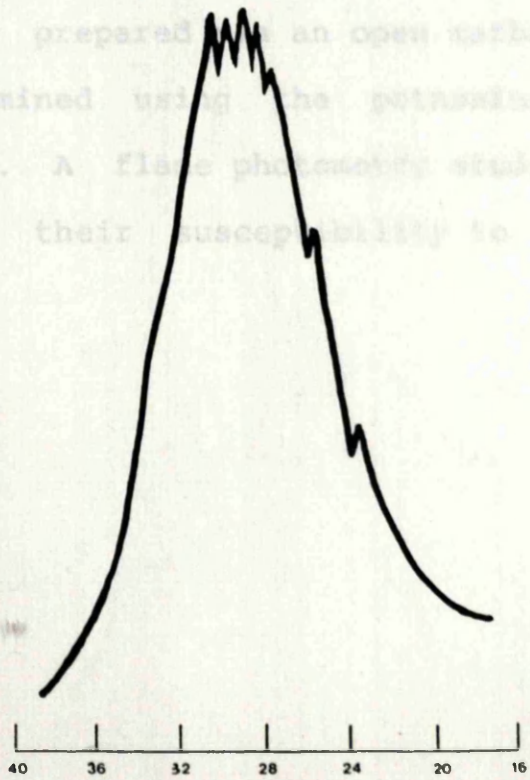

Figure 8.30: XRD trace of the $Acenap_{E4}K$ sample.

0.262-0.734nm (figure 8.31). The most intense peak was centered at (29.6°) 0.350nm with the remaining three peaks, in order of decreasing intensity, centered on (27.8°) 0.373nm, (26.9°) 0.385nm and (24.6°) 0.420nm respectively.

The x-ray diffraction trace of the $Acenap_{E7}K$ sample revealed eight peaks within the interplanar spacings range (36.0-16.0°) 0.290-0.643nm (figure 8.32). The two most intense peaks, of similar intensity, were centered at (30.4°) 0.341nm and (29.9°) 0.347nm. With the remaining peaks, in order of decreasing intensity, centered at (29.3°) 0.354nm, (28.8°) 0.360nm, (28.6°) 0.362nm, (27.9°) 0.371nm, (25.4°) 0.407nm and (22.0°) 0.469nm respectively.

8.3.4- FLAME PHOTOMETRY MEASUREMENTS

Due to operational problems, the acenaphthylene samples, prepared via an open carbonisation system, were not examined using the potassium uptake measurement technique. A flame photometry study was carried out to establish their susceptibility to alkali attack (table 8.4).

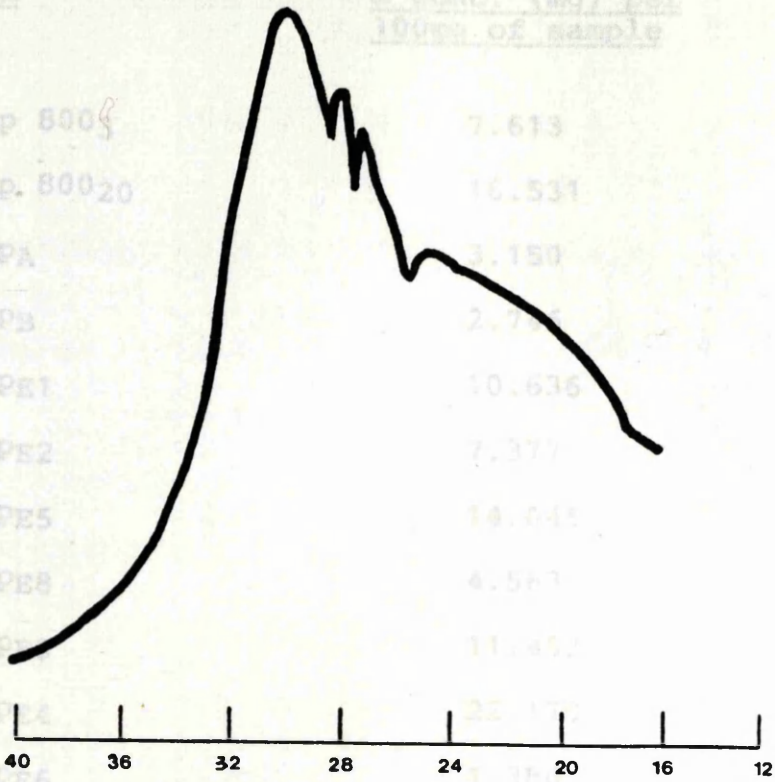

Figure 8.31: XRD trace of the $Acenap_{E6}K$ sample.

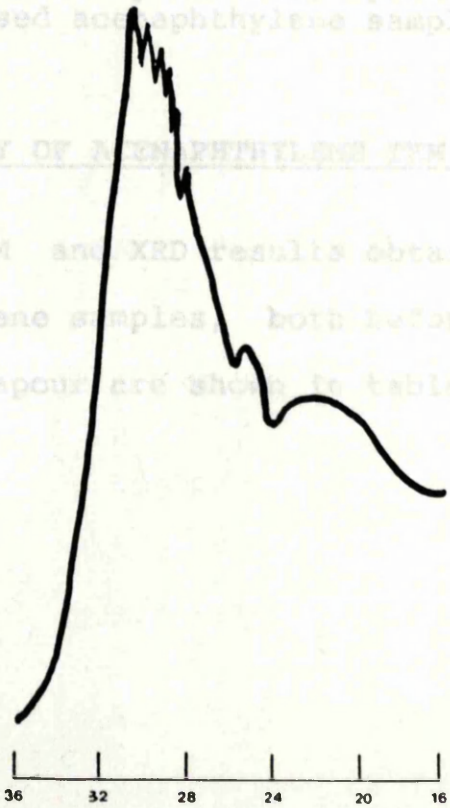

Figure 8.32: XRD trace of the $Acenap_{E7}K$ sample.

SAMPLE	K CONC. (mg) per 100mg of sample
Acenap 800_3	7.613
Acenap 800_{20}	16.531
$Acenap_A$	3.150
$Acenap_B$	2.746
$Acenap_{E1}$	10.636
$Acenap_{E2}$	7.377
$Acenap_{E5}$	14.045
$Acenap_{E8}$	4.563
$Acenap_{E3}$	11.458
$Acenap_{E4}$	22.179
$Acenap_{E6}$	1.386
$Acenap_{E7}$	0.970

Table 8.4 Flame photometry potassium concentrations for the carbonised acenaphthylene samples.

8.4- SUMMARY OF ACENAPHTHYLENE TEM AND XRD RESULTS

The TEM and XRD results obtained for the carbonised acenaphthylene samples, both before and after exposure to potassium vapour are shown in table 8.5.

SAMPLE	MICROSTRUCTURE	L_a(nm)	L_c(nm)	d(nm)	XRD(nm)
Acenap 800_3	S.R.O	1-4.5	0.34-3	0.43 (0.34-0.48)	0.341 0.434 0.482
Acenap 800_{20}	S.R.O	1-7	0.68-4.2	0.39 (0.34-0.49)	0.346 0.498
$Acenap_A$	S.R.O	1-5	0.4-3.5	0.45 (0.39-0.68)	0.350 0.461
	L.R.O	25-76	2-29	0.34 (0.31-0.36)	
$Acenap_B$	S.R.O	1-5.5	0.34-4.8	0.41 (0.34-0.58)	0.347 0.341 0.361 0.336 0.501
$Acenap_{E1}$	S.R.O	1-4	0.34-2.5	0.41 (0.34-0.49)	(a)
	L.R.O	10-36	4.5-13	0.34 (0.31-0.36)	
$Acenap_{E2}$	S.R.O	1-2.5	0.4-1.5	0.48 (0.35-0.61)	0.344 0.349
	L.R.O	13-21	10-20	0.34	0.484
$Acenap_{E5}$	S.R.O	1-6	0.4-3.4	0.39 (0.34-0.49)	0.341 0.360 0.495
$Acenap_{E8}$	S.R.O	1-3.5	0.68-2	0.41 (0.34-0.52)	0.346 0.359
	L.R.O & ribbon	9-29	4-21	0.35 (0.33-0.39)	0.335 0.391 0.404
$Acenap_{E3}$	S.R.O	1-4.5	0.34-1.5	0.40 (0.35-0.48)	0.348 0.469
	L.R.O & ribbon	21-43	8.5-26	0.35 (0.31-0.39)	
$Acenap_{E4}$	S.R.O	1-3.3	0.7-2.6	0.44 (0.35-0.57)	0.350 0.484
	L.R.O	17-65	4-8.5	0.34 (0.31-0.36)	0.396 0.402
$Acenap_{E6}$	S.R.O	1-5	0.7-3.5	0.48 (0.35-0.55)	(b)
	L.R.O	11-34	6-23	0.34	
$Acenap_{E7}$	S.R.O	1-4.5	0.34-3	0.39 (0.34-0.54)	(c)

SAMPLE	MICROSTRUCTURE	L_a(nm)	L_c(nm)	d(nm)	XRD(nm)
Acenap 800_3K	S.R.O	1-3	0.68-3	0.43	0.350
				(0.34-0.52)	0.362
	L.R.O	4-26	3-14	0.34	
				(0.33-0.38)	
Acenap 800_{20}K	S.R.O	1-3.3	0.6-3	0.67	0.349
				(0.59-0.74)	0.359
	L.R.O	7-37	3.4-11	0.34	0.339
	& ribbon				0.366
Acenap$_A$K	S.R.O	1-3.7	0.4-2.8	0.47	0.347
				(0.39-0.63)	0.362
	L.R.O	9-26	4-19	0.35	0.379
	& ribbon			(0.31-0.38)	0.391
					0.471
Acenap$_B$K	S.R.O	1-6	0.34-3.4	0.41	(d)
				(0.34-0.48)	
Acenap$_{E1}$K	S.R.O	1-5	0.68-4.8	0.44	0.360
				(0.34-0.54)	0.407
					0.551
Acenap$_{E2}$K	S.R.O	1-3.5	0.68-3.5	0.42	(e)
				(0.34-0.48)	
	L.R.O	7-34	3-18	0.34	
Acenap$_{E5}$K	S.R.O	1-5	0.34-4.3	0.54	0.345
				(0.34-0.66)	
Acenap$_{E8}$K	S.R.O	1-3.5	0.68-2	0.41	0.345
				(0.34-0.51)	0.350
	L.R.O	8-24	4-19	0.35	0.365
	& ribbon			(0.33-0.39)	0.415
					0.467
Acenap$_{E3}$K	S.R.O	1-4	0.34-3.2	0.37	0.371
				(0.34-0.51)	0.407
	L.R.O	10-36	5-13	0.34	0.336
					0.431
					0.505
Acenap$_{E4}$K	S.R.O	1-6	0.34-4	0.44	(f)
				(0.34-0.51)	
Acenap$_{E6}$K	S.R.O	1-3	0.72-4	0.42	0.350
				(0.36-0.54)	0.373
	L.R.O	9-47	4-17	0.35	0.385
	& ribbon			(0.34-0.39)	0.420
Acenap$_{E7}$K	S.R.O	1-3.5	0.68-3.5	0.39	(g)
				(0.34-0.48)	
	L.R.O	6-30	3-18	0.34	

(a) 0.346, 0.361, 0.331, 0.373, 0.383, 0.389, 0.414, 0.431, 0.449, 0.484, 0.307.

(b) 0.361, 0.349, 0.341, 0.336, 0.366, 0.374, 0.381, 0.383, 0.327, 0.494, 0.317, 0.303.

(c) 0.345, 0.349, 0.355, 0.361, 0.335, 0.366, 0.393, 0.407, 0.427, 0.469, 0.410, 0.540.

(d) 0.348, 0.341, 0.334, 0.374, 0.407, 0.414, 0.482.

(e) 0.349, 0.341, 0.353, 0.361, 0.366, 0.336, 0.409, 0.419.

(f) 0.364, 0.354, 0.346, 0.371, 0.381, 0.395, 0.414.

(g) 0.341, 0.347, 0.354, 0.360, 0.362, 0.371, 0.407, 0.469.

S.R.O - short-range order
L.R.O - long-range order

Table 8.5 Summary of TEM and XRD results for the carbonised acenaphthylene samples.

8.5- ANALYSIS OF CARBONISED DECACYLENE

Graphitisation of decacylene at 3000°C is known to result in the formation of a graphitising carbon (Fitzer et al., 1971). In this study twelve carbonised samples were prepared and examined.

8.5.1- TRANSMISSION ELECTRON MICROSCOPY (TEM)

A non-graphitised carbon structure was exhibited by the Deca 800_3 sample (L_a=1-3.5nm) with interplanar spacings in the range 0.41-0.56nm and a typical value of 0.48nm (L_c=0.82-3.5nm). The sample also revealed areas of long-range ordered structure (L_a=6-30nm) with lattice spacings of between 0.32-0.36nm and a typical value of 0.34nm (L_c=3-18nm).

The Deca 800_{20} sample revealed a short-range ordered structure (L_a=1-3nm) with lattice spacings in the range 0.36-0.47nm and a typical value of 0.43nm (L_c=0.36-4nm).

The $Deca_3$ sample revealed areas of both long and short-range order. The long-range ordered structure (L_a=7-49nm) exhibited interplanar spacings in the range 0.32-0.37nm, with a typical value of 0.34nm (L_c=4-31nm). The short-range ordered structure (L_a=1-4nm) showed lattice spacings of between 0.35-0.49nm and a typical value of 0.41nm (L_c=0.7-2.5nm). Also present were areas of convoluted structural order with L_a, L_c and interplanar spacings that were indistinguishable from the values exhibited by the long-range ordered structure.

Analysis of the $Deca_1$ sample revealed a short-range ordered structure (L_a=1-3nm) with lattice spacings in the range 0.35-0.49nm and a typical value of 0.45nm (L_c=0.7-3.8nm).

The $Deca_8$ sample revealed a non-graphitised carbon structure (L_a=1-4.5nm) with lattice spacings in the range 0.34-0.50nm and with a typical value of 0.41nm (L_c=0.68-4.2nm).

Examination of the $Deca_7$ sample revealed areas of both long and short-range order. The long-range ordered structure (L_a=4-60nm) exhibited interplanar spacings in the range 0.31-0.40nm and a typical value of 0.34nm (L_c=4-84nm) (figure 8.33). The short-range ordered structure (L_a=1-5nm) showed lattice spacings of between 0.51-0.72nm and a typical value of 0.64nm (L_c=0.5-2.5nm). Also present were areas of convoluted structural order with L_a, L_c and

Figure 8.33: HREM of the Deca7 sample showing the extensive long-range ordered structure (0.34nm).

interplanar spacings that were indistinguishable from the values exhibited by the long-range ordered structure.

The $Deca_{12}$ sample exhibited a long-range ordered structure (L_a=10-75nm) with lattice spacings in the range 0.30-0.35nm and a typical value of 0.34nm (L_c=5-28nm). The short-range ordered structure (L_a=1-5nm) exhibited lattice spacings of between 0.40-0.49nm with a typical value of 0.45nm (L_c=0.8-4nm).

Analysis of the $Deca_9$ sample revealed areas of short-range ordered structure (L_a=1-4nm) with lattice spacings in the range 0.40-0.52nm and a typical value of 0.45nm (L_c=0.4-2nm). The long-range ordered structure (L_a=5-31nm) revealed lattice spacings within the range 0.31-0.35nm and a typical value of 0.34nm (L_c=3-12nm).

The $Deca_{10}$ sample exhibited areas of convoluted structural development and extensively ordered long-range structure (L_a=5-155nm) with lattice spacings of between 0.32-0.37nm and a typical value of 0.34nm (L_c=7-39nm). Analysis of the short-range ordered structure (L_a=1-2nm) revealed lattice spacings in the range 0.40-0.64nm with a typical value of 0.48nm (L_c=0.8-4.5nm).

A non-graphitised carbon structure was exhibited by the $Deca_{11}$ sample (L_a=1-3.5nm) with interplanar spacings in the range 0.41-0.54nm and a typical value of 0.48nm (L_c=0.82-5nm). The sample also revealed areas of long-range ordered structure (L_a=5-25nm) with lattice spacings of 0.34nm (L_c=4-11nm).

The $Deca_5$ sample exhibited a long-range ordered structure (L_a=8-45nm) with lattice spacings in the range

0.32-0.37nm and a typical value of 0.34nm (L_c=5-37nm). The short-range ordered structure (L_a=1-5nm) exhibited interplanar spacings in the range 0.41-0.54nm with a typical value of 0.48nm (L_c=0.8-4.5nm).

Analysis of the $Deca_6$ sample revealed areas of short-range ordered structure (L_a=1-4nm) with lattice spacings in the range 0.32-0.52nm and a typical value of 0.43nm (L_c=0.64-4nm). The long-range ordered structure (L_a=9-20nm) revealed lattice spacings within the range 0.31-0.37nm and a typical value of 0.34nm (L_c=4-12nm).

8.5.2- SCANNING ELECTRON MICROSCOPY (SEM)

As previously observed by the acenaphthylene samples (figure 8.3, 8.4 and 8.5), examination of the decacylene samples by SEM revealed a smooth external surface exhibiting cracks and two differing lamellar structures; sheet-like lamellar layers and a smooth, folded, flow-like lamellar surface. Table 8.6 summaries the SEM structure exhibited by each of the decacylene samples.

SAMPLE	STRUCTURE EXHIBITED
$Deca\ 800_3$	sheet-like lamellar layers
$Deca\ 800_{20}$	sheet-like lamellar layers
$Deca_3$	smooth, folded, flow-like lamellar surface
$Deca_1$	sheet-like lamellar layers
$Deca_8$	sheet-like lamellar layers
$Deca_7$	sheet-like lamellar layers
$Deca_{12}$	smooth, folded, flow-like lamellar surface
$Deca_9$	smooth, folded, flow-like lamellar surface

SAMPLE	STRUCTURE EXHIBITED
$Deca_{10}$	smooth, folded, flow-like lamellar surface
$Deca_{11}$	sheet-like lamellar layers
$Deca_5$	smooth, folded, flow-like lamellar surface
$Deca_6$	sheet-like lamellar layers

Table 8.6 SEM structures exhibited by each of the carbonised decacylene samples.

8.5.3- POWDER X-RAY DIFFRACTION ANALYSIS (XRD)

The Deca 800_3 x-ray diffraction trace exhibited nine peaks within the interplanar spacings range (36.0-15.8°) 0.290-0.651nm (figure 8.34). The most intense peak, was centered at (29.6°) 0.350nm. The remaining peaks, in order of decreasing intensity, were centered at (30.4°) 0.341nm, (31.2°) 0.333nm, (21.5°) 0.480nm, (19.8°) 0.521nm, (25.6°) 0.404nm, (24.5°) 0.422nm, (23.2°) 0.445nm and (18.0°) 0.572nm, with two of these peaks, (24.5°) 0.422nm and (23.2°) 0.445nm exhibiting a similar intensity.

The x-ray diffraction trace for the Deca 800_{20} sample exhibited two peaks (figure 8.35). Within the interplanar spacings range (41.2-13.2°) 0.254-0.779nm, the most intense peak was centered at (29.6°) 0.350nm with the remaining peak centered at (22.0°) 0.469nm.

Examination of the $Deca_3$ sample revealed an x-ray diffraction trace with one broad peak (figure 8.36) centered on (30.0°) 0.346nm and within an interplanar spacings range of (40.4-18.0°) 0.259-0.572nm.

The $Deca_1$ x-ray diffraction trace exhibited three peaks

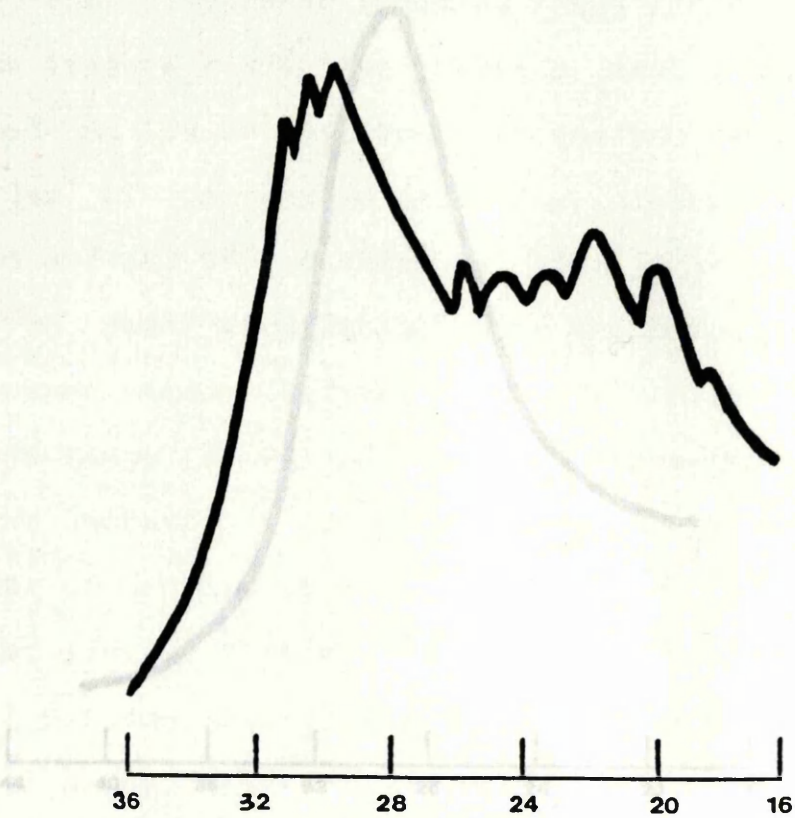

Figure 8.34: XRD trace of the Deca 800_3 sample.

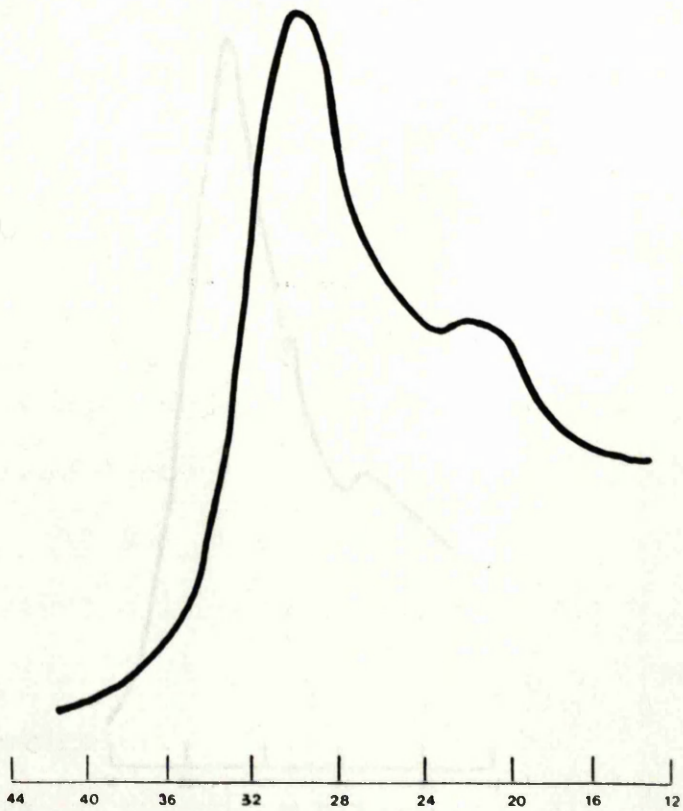

Figure 8.35: XRD trace of the Deca 800_{20} sample.

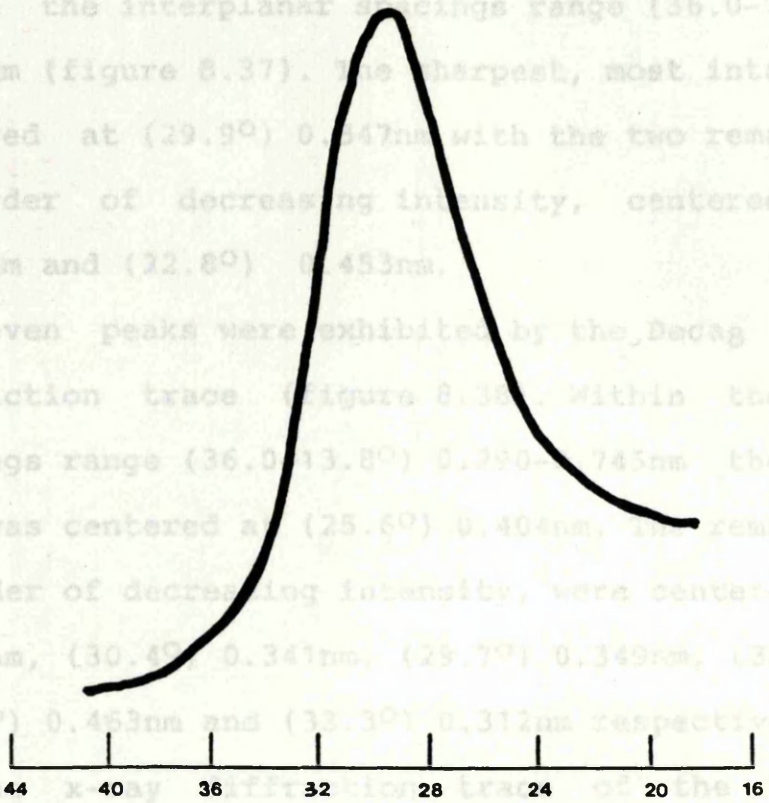

Figure 8.36: XRD trace of the $Deca_3$ sample.

Figure 8.37: XRD trace of the $Deca_1$ sample.

within the interplanar spacings range (36.0-17.0°) 0.290-0.606nm (figure 8.37). The sharpest, most intense peak was centered at (29.9°) 0.347nm with the two remaining peaks, in order of decreasing intensity, centered at (24.4°) 0.424nm and (22.8°) 0.453nm.

Seven peaks were exhibited by the $Deca_8$ sample x-ray diffraction trace (figure 8.38). Within the interplanar spacings range (36.0-13.8°) 0.290-0.745nm the most intense peak was centered at (25.6°) 0.404nm. The remaining peaks, in order of decreasing intensity, were centered at (24.5°) 0.422nm, (30.4°) 0.341nm, (29.7°) 0.349nm, (32.2°) 0.323nm, (22.3°) 0.463nm and (33.3°) 0.312nm respectively.

The x-ray diffraction trace of the $Deca_7$ sample exhibited four peaks within the interplanar spacings range (36.0-16.0°) 0.290-0.643nm (figure 8.39). The most intense peak was centered at (29.8°) 0.348nm. The remaining peaks, in order of decreasing intensity, were centered at (29.0°) 0.358nm, (22.6°) 0.457nm and (20.1°) 0.513nm respectively.

The $Deca_9$ sample exhibited six peaks within the interplanar spacings range (36.0-13.8°) 0.290-0.745nm (figure 8.40). The most intense peak, of the x-ray diffraction trace, was centered at (29.6°) 0.350nm. The remaining peaks, in order of decreasing intensity, were centered at (30.8°) 0.337nm, (21.4°) 0.482nm, (22.8°) 0.453nm, (19.9°) 0.518nm and (23.7°) 0.436nm, with two of these peaks, (22.8°) 0.453nm and (19.9°) 0.518nm exhibiting a similar intensity.

The x-ray diffraction trace for the $Deca_{10}$ sample (figure 8.41) revealed a broad peak, centered at (30.0°)

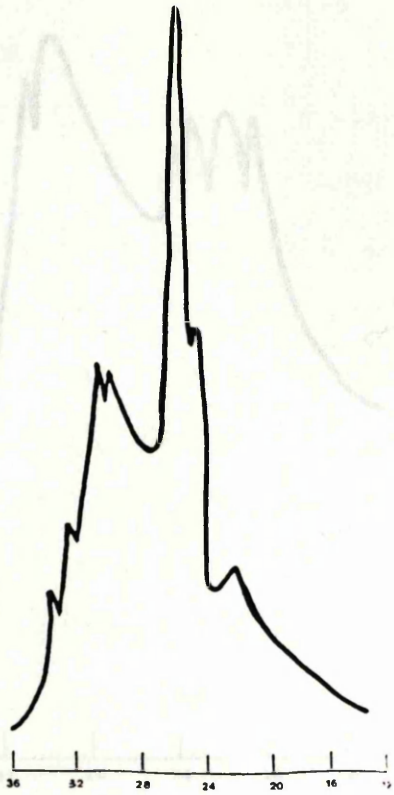

Figure 8.38: XRD trace of the $Deca_8$ sample.

Figure 8.39: XRD trace of the $Deca_7$ sample.

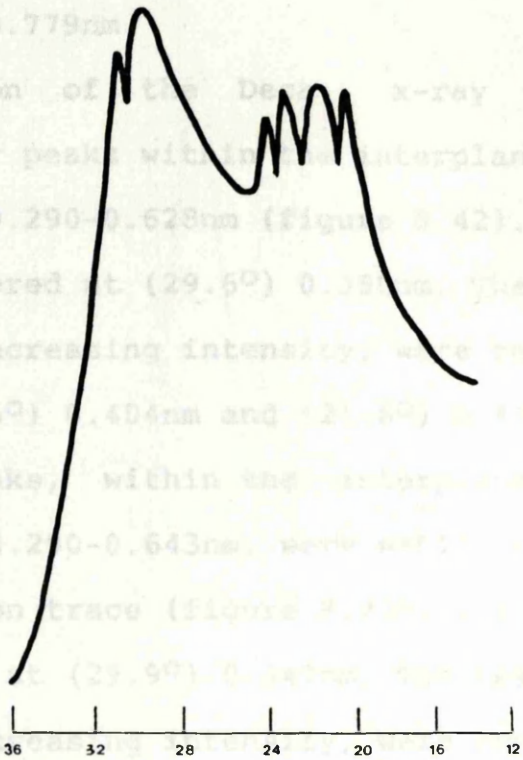

Figure 8.40: XRD trace of the $Deca_9$ sample.

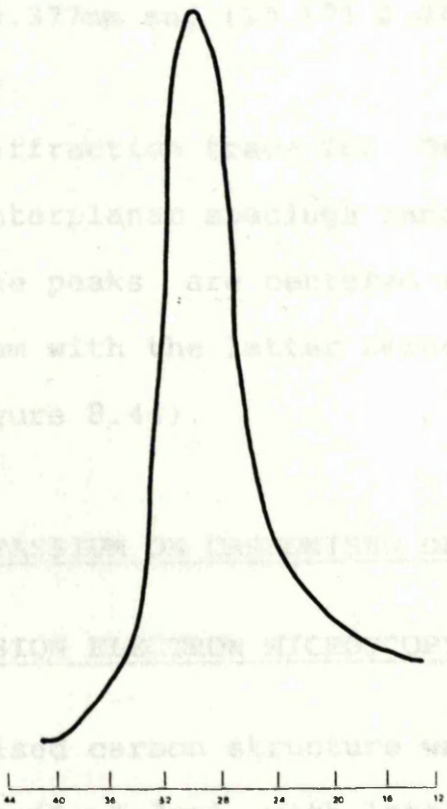

Figure 8.41: XRD trace of the $Deca_{10}$ sample.

0.345nm, within an interplanar spacings range of (40.0-13.2°) 0.262-0.779nm.

Examination of the $Deca_{11}$ x-ray diffraction trace revealed four peaks within the interplanar spacings range (36.0-16.4°) 0.290-0.628nm (figure 8.42). The most intense peak was centered at (29.6°) 0.350nm. The remaining peaks, in order of decreasing intensity, were centered at (30.2°) 0.344nm, (25.6°) 0.404nm and (21.6°) 0.478nm respectively.

Seven peaks, within the interplanar spacings range (36.0-16.0°) 0.290-0.643nm, were exhibited by the $Deca_5$ x-ray diffraction trace (figure 8.43). The most intense peak, was centered at (29.9°) 0.347nm. The remaining peaks, in order of decreasing intensity, were centered at (29.0°) 0.358nm, (30.9°) 0.336nm, (21.2°) 0.487nm, (27.5°) 0.377nm, (23.1°) 0.447nm and (19.3°) 0.534nm, with two of these peaks, (27.5°) 0.377nm and (23.1°) 0.447nm exhibiting a similar intensity.

The x-ray diffraction trace for $Deca_6$ revealed two peaks within an interplanar spacings range of (42.4-14.0°) 0.248-0.735nm. The peaks are centered at (30.0°) 0.345nm and (21.4°) 0.482nm with the latter being the smallest and least intense (figure 8.44).

8.6- EFFECT OF POTASSIUM ON CARBONISED DECACYLENE

8.6.1- TRANSMISSION ELECTRON MICROSCOPY (TEM)

A non-graphitised carbon structure was exhibited by the Deca 800_3K sample (L_a=1-3nm) with lattice spacings in the range 0.34-0.42nm and a typical value of 0.41nm (L_c=0.68-

Figure 8.42: XRD trace of the $Deca_{11}$ sample.

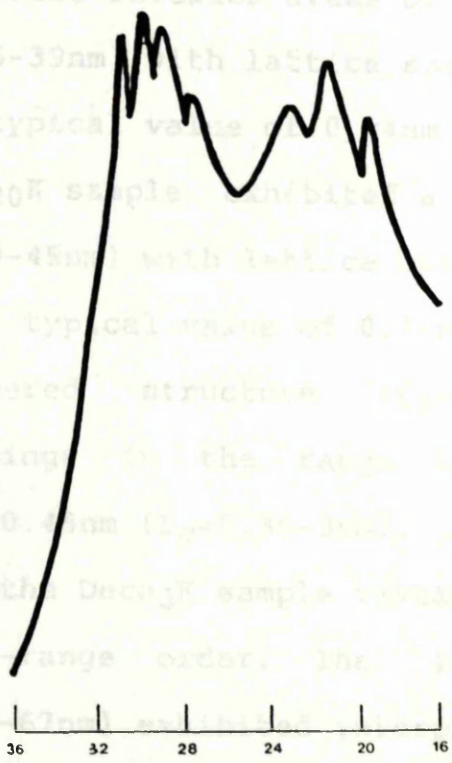

Figure 8.43: XRD trace of the $Deca_5$ sample.

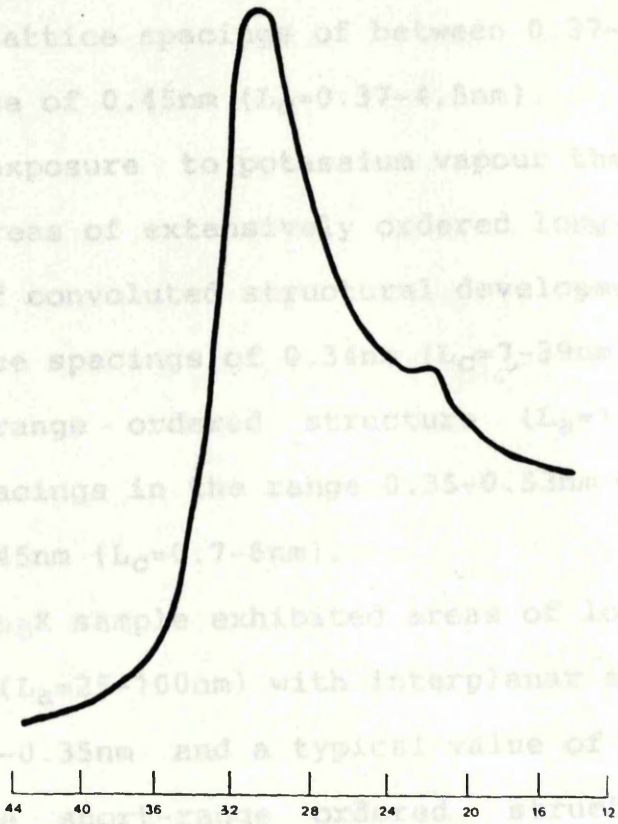

Figure 8.44: XRD trace of the $Deca_6$ sample.

4nm). The sample also revealed areas of long-range ordered structure (L_a=15-39nm) with lattice spacings in the range 0.32-0.36 and a typical value of 0.34nm (L_c=4-20nm).

The Deca 800_{20}K sample exhibited a long-range ordered structure (L_a=10-45nm) with lattice spacings in the range 0.32-0.37nm and a typical value of 0.34nm (L_c=5-27nm). The short-range ordered structure (L_a=1-5nm) exhibited interplanar spacings in the range 0.36-0.45nm with a typical value of 0.45nm (L_c=0.36-3nm).

Analysis of the $Deca_3$K sample revealed areas of both long and short-range order. The long-range ordered structure (L_a=14-67nm) exhibited interplanar spacings in the range 0.32-0.37nm with a typical value of 0.34nm (L_c=6-37nm). The short-range ordered structure (L_a=1-6nm)

exhibited lattice spacings of between 0.37-0.52nm with a typical value of 0.45nm (L_c=0.37-4.5nm).

After exposure to potassium vapour the $Deca_1$ sample exhibited areas of extensively ordered long-range structure and areas of convoluted structural development (L_a=8-55nm) with lattice spacings of 0.34nm (L_c=7-39nm). Analysis of the short-range ordered structure (L_a=1-5nm) revealed lattice spacings in the range 0.35-0.53nm with a typical value of 0.45nm (L_c=0.7-6nm).

The $Deca_8K$ sample exhibited areas of long-range ordered structure (L_a=25-100nm) with interplanar spacings in the range 0.32-0.35nm and a typical value of 0.33nm (L_c=7-28nm). The short-range ordered structure (L_a=1-5nm) revealed lattice spacings within the range 0.33-0.43nm and a typical value of 0.37nm (L_c=0.66-8nm).

A non-graphitised carbon structure was exhibited by the $Deca_7K$ sample (L_a=1-4nm) with lattice spacings in the range 0.35-0.47nm and a typical value of 0.37nm (L_c=0.7-5.5nm). The sample also revealed areas of long-range ordered structure (L_a=12-34nm) with lattice spacings in the range 0.31-0.38 and a typical value of 0.34nm (L_c=4-15nm).

After exposure to potassium vapour the $Deca_9$ sample exhibited a long-range ordered structure (L_a=6-75nm) with lattice spacings in the range 0.33-0.37nm and a typical value of 0.34nm (L_c=2-24nm). The short-range ordered structure (L_a=1-5nm) exhibited interplanar spacings in the range 0.38-0.53nm with a typical value of 0.43nm (L_c=0.76-5nm).

Analysis of the $Deca_{10}K$ sample revealed areas of both

long and short-range order. The long-range ordered structure (L_a=6-42nm) exhibited interplanar spacings with a typical value of 0.34nm (L_c=4-14nm). The short-range ordered structure (L_a=1-6nm) exhibited lattice spacings of between 0.39-0.48nm with a typical value of 0.41nm (L_c=0.39-8nm). Also present were areas of convoluted structural order with L_a, L_c and interplanar spacings that were indistinguishable from the values exhibited by the long-range ordered structure.

Examination of the $Deca_{11}K$ sample exhibited areas of ordered long-range structure (L_a=13-40nm) with lattice spacings in the range 0.32-0.37 with a typical value of 0.34nm (L_c=3-21nm). Analysis of the short-range ordered structure (L_a=1-3nm) revealed lattice spacings in the range 0.36-0.49nm with a typical value of 0.41nm (L_c=0.36-4.5nm).

The $Deca_5K$ sample exhibited areas of long-range ordered structure (L_a=8-27nm) with interplanar spacings of 0.34nm (L_c=5-13nm). The short-range ordered structure (L_a=1-4.5nm) revealed lattice spacings within the range 0.35-0.56nm and a typical value of 0.37nm (L_c=0.7-3nm). Also present were areas of convoluted structural order with L_a, L_c and interplanar spacings that were indistinguishable from the values exhibited by the long-range ordered structure.

Analysis of the $Deca_6K$ sample revealed areas of convoluted structural order and areas exhibiting a long-range ordered structure (figure 8.45) (L_a=25-125nm) with interplanar spacings in the range 0.33-0.36nm and a typical value of 0.34nm (L_c=4-50nm). The short-range ordered structure (L_a=1-7nm) exhibited lattice spacings of between 0.33-0.42nm with a typical value of 0.38nm (L_c=0.66-6nm).

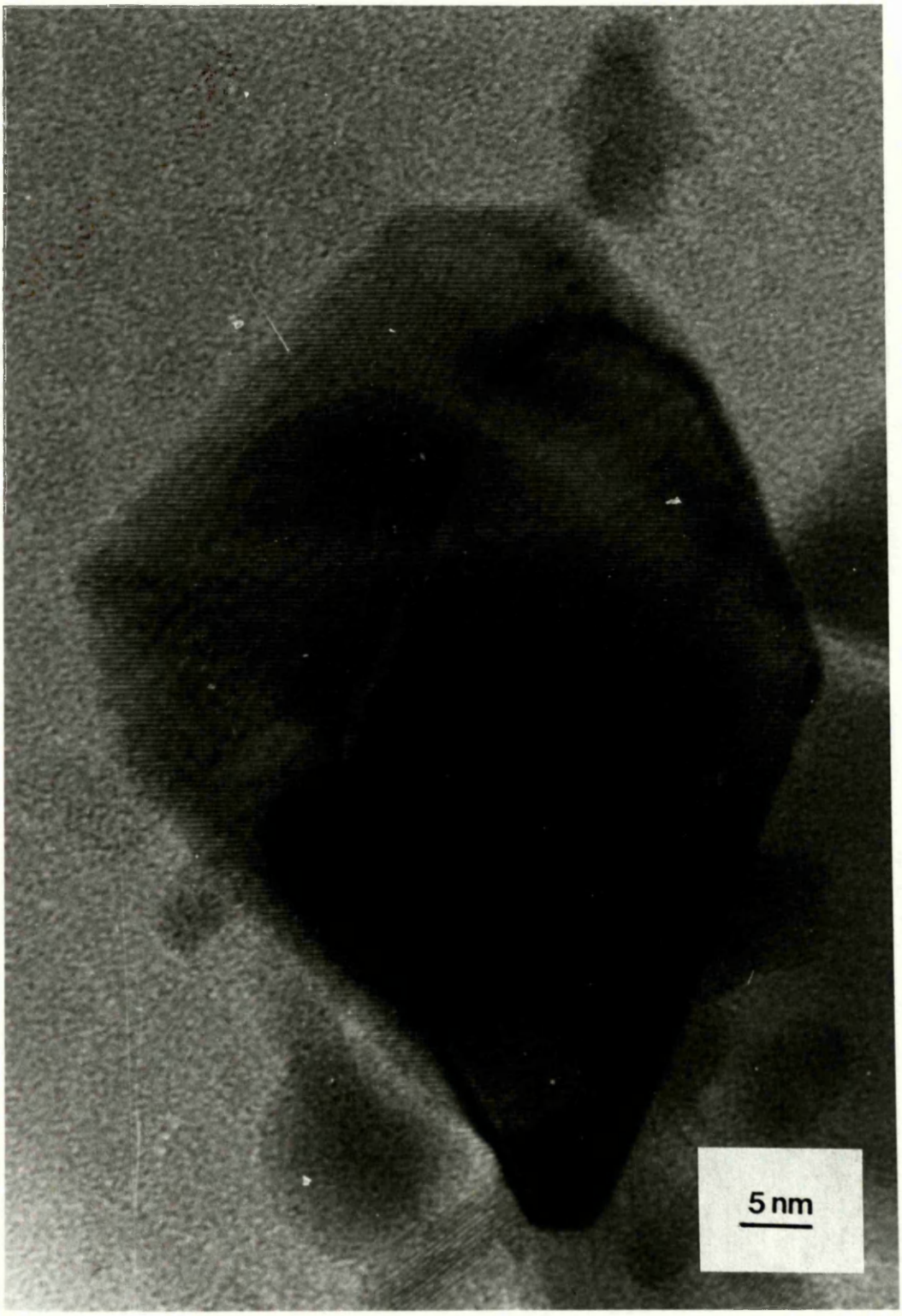

Figure 8.45: HREM of the $Deca_6K$ sample showing the long-range ordered structure (0.34nm).

8.6.2- SCANNING ELECTRON MICROSCOPY (SEM)

After exposure to potassium vapour the decacylene samples exhibited three surface structures. A smooth external surface (figure 8.3), a structure revealing an increase in the extent of external surface cracking (figure 8.19) and a rough nodular surface displaying cracks, holes and pitting (figure 8.46). The samples also revealed the two differing lamellar structures; sheet-like lamellar layers and a smooth, folded, flow-like lamellar surface. Table 8.7 summaries the SEM structure exhibited by each of the decacylene samples.

8.6.3- POWDER X-RAY DIFFRACTION ANALYSIS (XRD)

Within the interplanar spacings range (37.8-17.0^{o}) 0.276-0.606nm, six peaks were exhibited for the x-ray diffraction trace of the Deca 800_3K sample (figure 8.47). The most intense peak was centered at (30.1^{o}) 0.345nm with two peaks, of similar intensity, centered at (29.6^{o}) 0.350nm and (30.9^{o}) 0.336nm. The remaining three peaks, in order of decreasing intensity, were centered at (31.4^{o}) 0.331nm, (28.7^{o}) 0.361nm and (26.1^{o}) 0.396nm respectively.

Six peaks were evident, within the interplanar spacings range (36.0-20.0^{o}) 0.290-0.515nm, from the Deca 800_{20}K sample x-ray diffraction trace (figure 8.48). Two peaks, of similar intensity, were centered within close proximity of each other at (29.4^{o}) 0.350nm and (29.9^{o}) 0.347nm. The remaining peaks, in order of decreasing intensity, were centered at (28.3^{o}) 0.366nm, (27.2^{o}) 0.381nm, (26.6^{o}) 0.389nm and (26.1^{o}) 0.396nm respectively.

SAMPLE	STRUCTURE EXHIBITED
Deca 800_3K	sheet-like lamellar layers smooth surface
Deca $800_{20}K$	sheet-like lamellar layers smooth surface
$Deca_3K$	sheet-like lamellar layers cracked surface
$Deca_1K$	sheet-like lamellar layers smooth surface
$Deca_8K$	sheet-like lamellar layers nodular surface
$Deca_7K$	sheet-like lamellar layers nodular surface
$Deca_{12}K$	------
$Deca_9K$	smooth, folded, flow-like lamellar surface cracked surface
$Deca_{10}K$	smooth, folded, flow-like lamellar surface smooth surface
$Deca_{11}K$	sheet-like lamellar layers smooth surface
$Deca_5K$	smooth, folded, flow-like lamellar surface smooth surface
$Deca_6K$	sheet-like lamellar layers nodular surface

Table 8.7 SEM structures exhibited by each of the carbonised decacylene samples after exposure to potassium vapour.

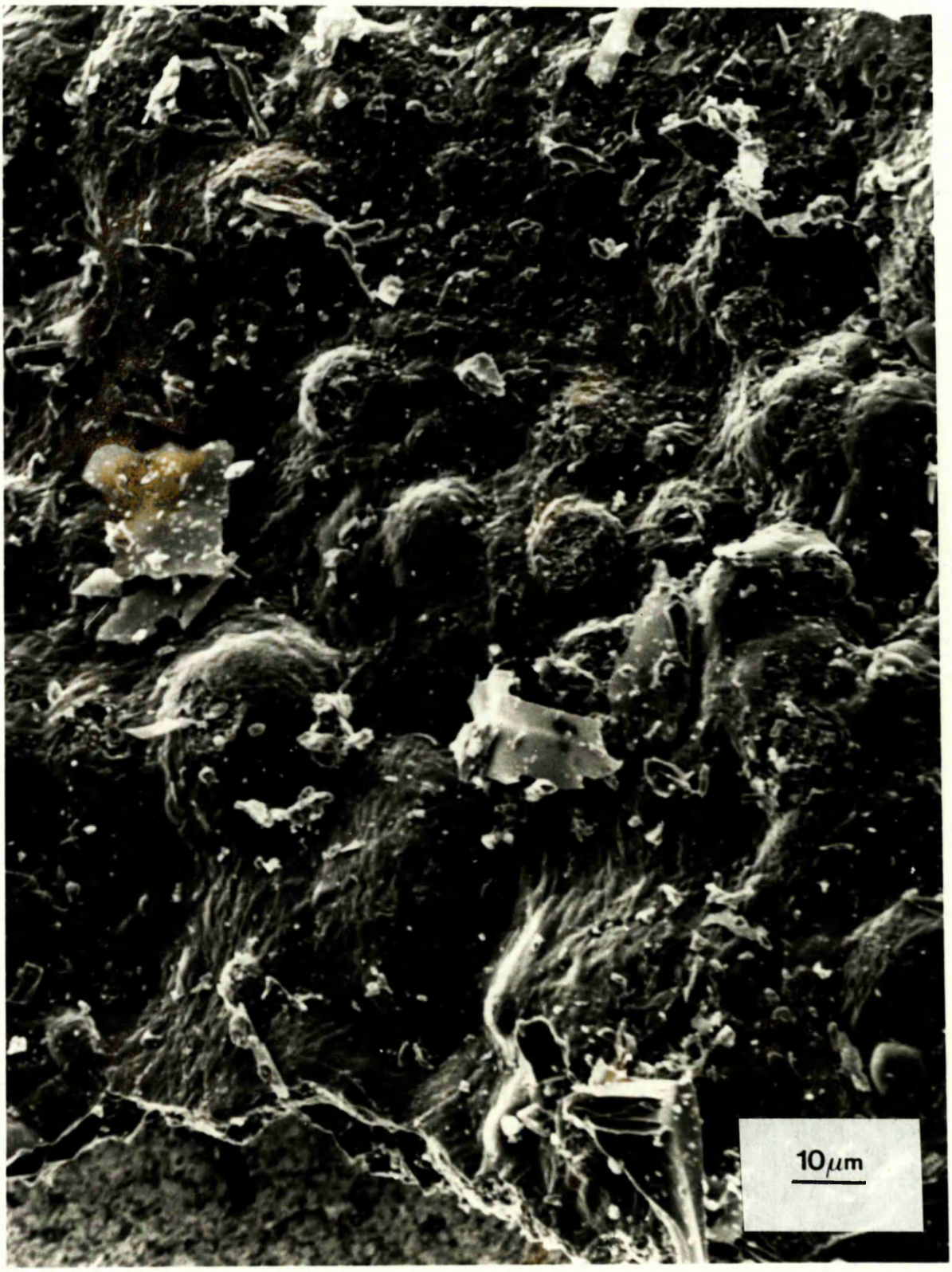

Figure 8.46: SEM showing the rough nodular surface with cracks, holes and pitting, exhibited by the decacylene samples after exposure to potassium vapour.

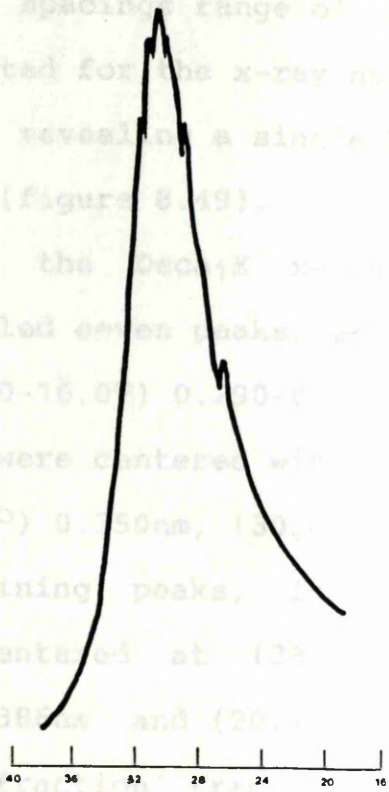

Figure 8.47: XRD trace of the Deca 800_3K sample.

Figure 8.48: XRD trace of the Deca $800_{20}K$ sample.

An interplanar spacings range of (42.6-16.0°) 0.246-0.643nm was exhibited for the x-ray diffraction trace of the $Deca_3K$ sample, revealing a single broad peak centered at (28.6°) 0.362nm (figure 8.49).

Examination of the $Deca_1K$ x-ray diffraction trace (figure 8.50) revealed seven peaks, within the interplanar spacings range (36.0-16.0°) 0.290-0.643nm. Three peaks, of similar intensity, were centered within close proximity of each other at (29.6°) 0.350nm, (30.0°) 0.346nm and (30.4°) 0.341nm. The remaining peaks, in order of decreasing intensity, were centered at (28.5°) 0.364nm, (27.2°) 0.381nm, (26.8°) 0.386nm and (20.1°) 0.513nm respectively.

The x-ray diffraction trace of the $Deca_8K$ sample revealed nine peaks within the interplanar spacings range (37.6-17.6°) 0.278-0.585nm (figure 8.51). The most intense peak was centered at (25.6°) 0.404nm, with two peaks of similar intensity centered at (29.8°) 0.348nm and (30.5°) 0.340nm. The remaining peaks, in order of decreasing intensity, were centered at (24.4°) 0.424nm, (28.7°) 0.361nm, (31.3°) 0.332nm, (32.2°) 0.323nm, (33.2°) 0.313nm and (33.7°) 0.309nm respectively.

The $Deca_7K$ x-ray diffraction trace exhibited eight peaks within the interplanar spacings range (36.0-20.0°) 0.290-0.515nm (figure 8.52). The most intense peak was centered at (29.8°) 0.348nm. The remaining peaks, in order of decreasing intensity, were centered at (30.4°) 0.341nm, (30.8°) 0.337nm, (26.9°) 0.385nm, (26.5°) 0.391nm, (26.1°) 0.396nm, (33.0°) 0.315nm and (23.0°) 0.449nm respectively.

The x-ray diffraction trace of the $Deca_9K$ sample

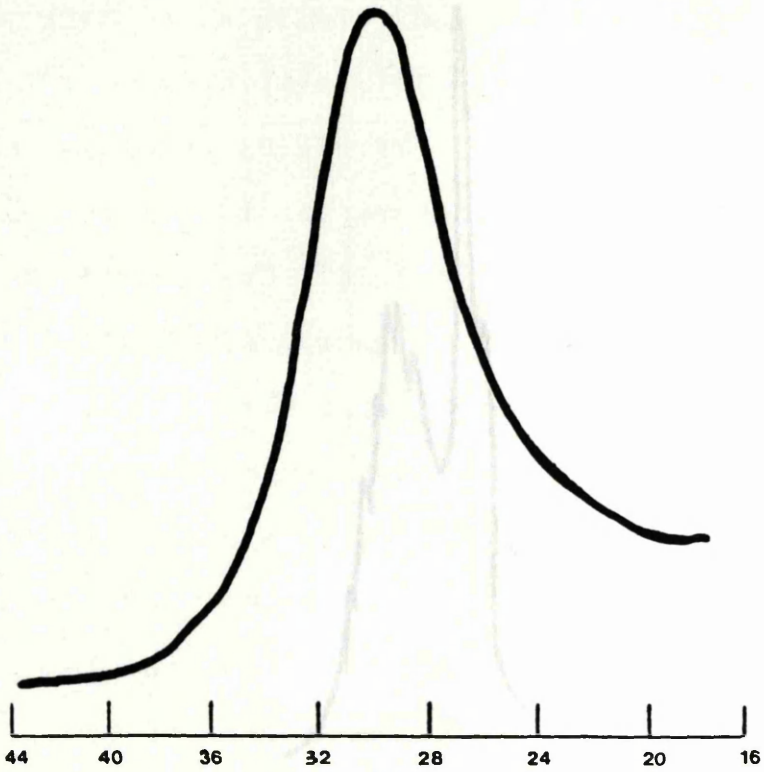

Figure 8.49: XRD trace of the $Deca_3K$ sample.

Figure 8.50: XRD trace of the $Deca_1K$ sample.

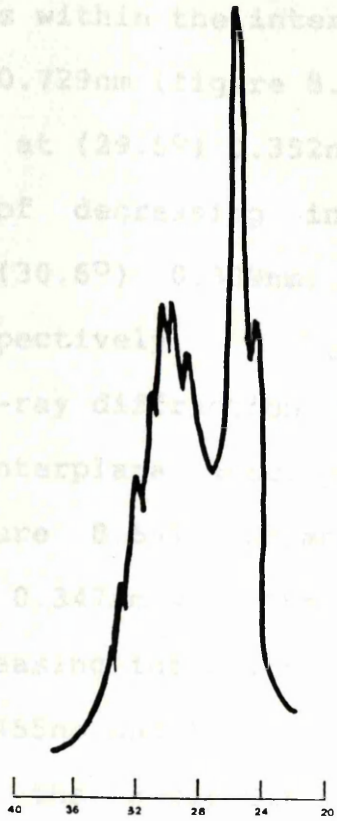

Figure 8.51: XRD trace of the $Deca_8K$ sample.

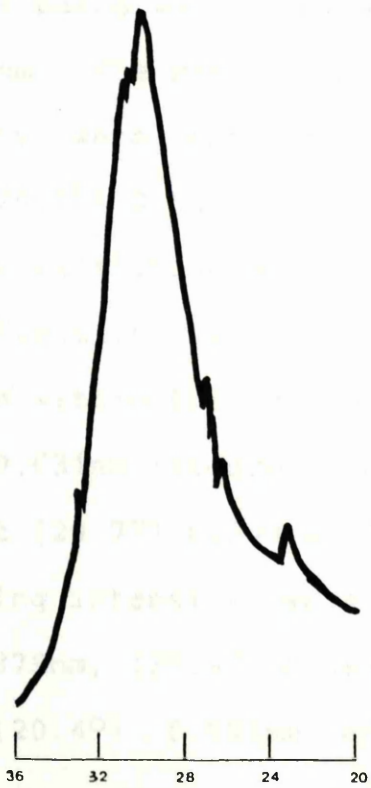

Figure 8.52: XRD trace of the $Deca_7K$ sample.

revealed five peaks within the interplanar spacings range (36.2-14.1°) 0.288-0.729nm (figure 8.53). The most intense peak was centered at (29.5°) 0.352nm with the remaining peaks, in order of decreasing intensity, centered at (28.7°) 0.361nm, (30.6°) 0.339nm, (21.5°) 0.480nm and (19.4°) 0.531nm respectively.

The $Deca_{10}K$ x-ray diffraction trace exhibited four peaks within the interplanar spacings range (40.0-20.4°) 0.262-0.505nm (figure 8.54). The most intense peak was centered at (29.9°) 0.347nm with the remaining three peaks, in order of decreasing intensity, centered on (25.7°) 0.402nm, (22.7°) 0.455nm and (21.4°) 0.482nm respectively.

Examination of the x-ray diffraction trace of the $Deca_{11}K$ sample revealed six peaks within the interplanar spacings range (37.4-17.4°) 0.279-0.592nm (figure 8.55). The two most intense peaks were centered at (29.9°) 0.347nm and (25.5°) 0.406nm. The remaining peaks in order of decreasing intensity were centered at (26.3°) 0.393nm, (26.0°) 0.398nm, (20.5°) 0.503nm and (21.1°) 0.489nm with the latter two peaks exhibiting similar intensity.

The x-ray diffraction trace of the $Deca_5K$ sample revealed eight peaks within the interplanar spacings range (36.0-16.3°) 0.290-0.631nm (figure 8.56). The most intense peak was centered at (29.7°) 0.349nm. The remaining peaks, in order of decreasing intensity, were centered at (30.4°) 0.341nm, (27.6°) 0.375nm, (25.9°) 0.399nm, (25.0°) 0.414nm, (24.0°) 0.431nm, (20.4°) 0.505nm and (19.3°) 0.534nm respectively.

Seven peaks, within the interplanar spacings range

Figure 8.53: XRD trace of the $Deca_9K$ sample.

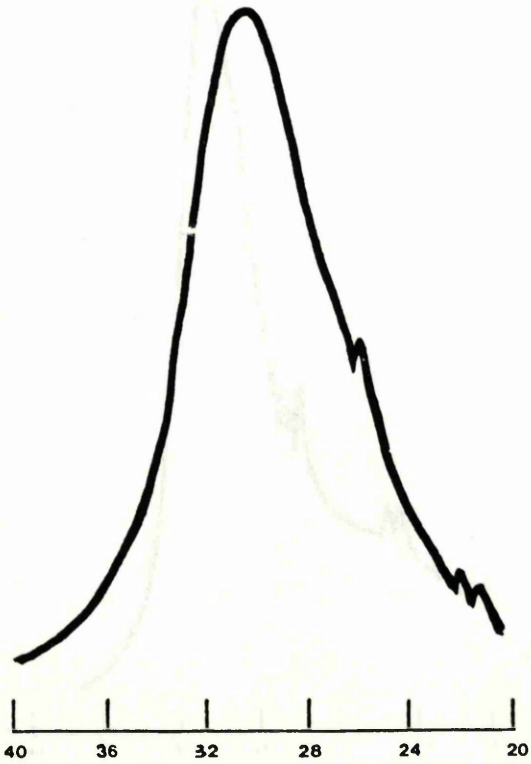

Figure 8.54: XRD trace of the $Deca_{10}K$ sample.

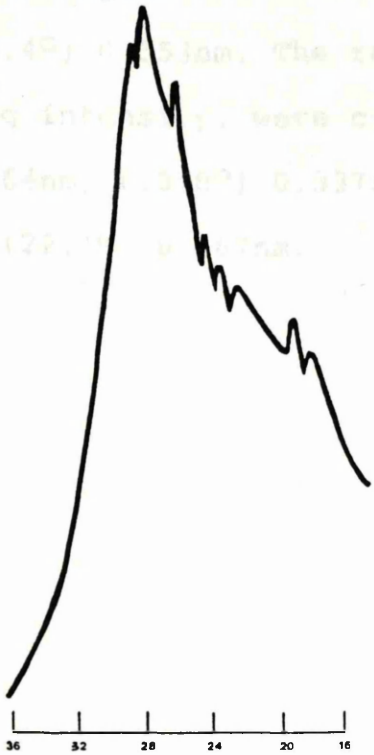

Figure 8.55: XRD trace of the $Deca_{11}K$ sample.

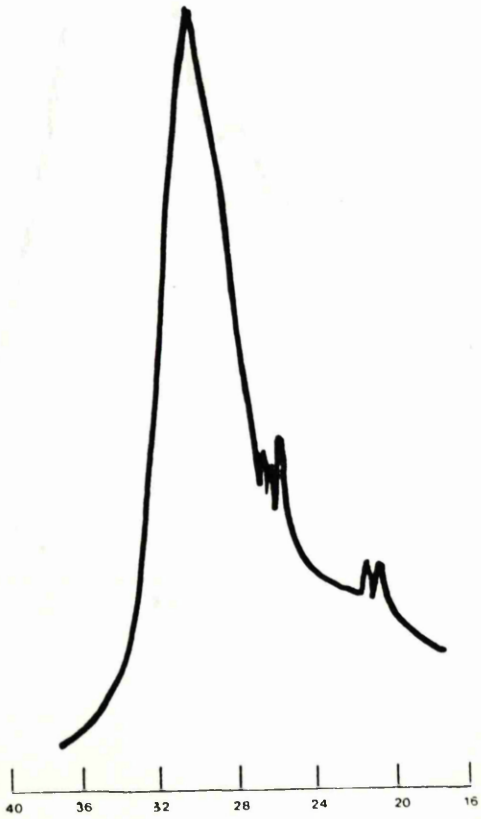

Figure 8.56: XRD trace of the $Deca_5K$ sample.

(36.1-15.8°) 0.289-0.651nm, were exhibited by the $Deca_6K$ x-ray diffraction trace (figure 8.57). The most intense peak was centered at (29.4°) 0.353nm. The remaining peaks, in order of decreasing intensity, were centered at (30.0°) 0.346nm, (28.5°) 0.364nm, (30.8°) 0.337nm, (27.8°) 0.373nm, (25.2°) 0.410nm and (22.1°) 0.467nm.

Figure 8.57: XRD trace of the $Deca_6K$ sample.

8.6.4- FLAME PHOTOMETRY MEASUREMENTS

Due to operational problems, the decacylene samples, prepared via an open carbonisation system were not examined using the potassium uptake measurement technique. A flame photometry study was carried out to establish their susceptibility to alkali attack.

SAMPLE	K CONC. (mg) per 100mg of sample
Deca 800_3	4.423
Deca 800_{20}	5.654
$Deca_3$	1.747
$Deca_1$	3.707
$Deca_8$	7.000
$Deca_7$	2.288
$Deca_{12}$	----
$Deca_9$	11.256
$Deca_{10}$	4.772
$Deca_{11}$	5.036
$Deca_5$	7.669
$Deca_6$	6.463

Table 8.8 Flame photometry potassium concentrations for the carbonised decacylene samples.

8.7- SUMMARY OF DECACYLENE RESULTS

The TEM and XRD results obtained for the carbonised decacylene samples, both before and after exposure to potassium vapour are shown in table 8.9.

SAMPLE	MICROSTRUCTURE	L_a(nm)	L_c(nm)	d(nm)	XRD(nm)
Deca 800_3	S.R.O	1-3.5	0.82-3.5	0.48 (0.41-0.56)	(a)
	L.R.O	6-30	3-18	0.34 (0.32-0.36)	
Deca 800_{20}	S.R.O	1-3	0.36-4	0.43 (0.36-0.47)	0.350 0.469
$Deca_3$	S.R.O	1-4	0.7-2.5	0.41 (0.35-0.49)	0.346
	L.R.O & ribbon	7-49	4-31	0.34 (0.32-0.37)	
$Deca_1$	S.R.O	1-3	0.7-3.8	0.45 (0.35-0.49)	0.347 0.424 0.453
$Deca_8$	S.R.O	1-4.5	0.68-4.2	0.41 (0.34-0.50)	(b)
$Deca_7$	S.R.O	1-5	0.5-2.5	0.64 (0.51-0.72)	0.348 0.358
	L.R.O & ribbon	4-60	4-84	0.34 (0.31-0.40)	0.457 0.513
$Deca_{12}$	S.R.O	1-5	0.8-4	0.45 (0.40-0.49)	----
	L.R.O	10-75	5-28	0.34 (0.30-0.35)	
$Deca_9$	S.R.O	1-4	0.4-2	0.45 (0.40-0.52)	0.350 0.337
	L.R.O	5-31	3-12	0.34 (0.31-0.35)	0.482 0.453 0.518 0.436
$Deca_{10}$	S.R.O	1-2	0.8-4.5	0.48 (0.40-0.64)	0.345
	L.R.O & ribbon	5-155	7-39	0.34 (0.32-0.37)	
$Deca_{11}$	S.R.O	1-3.5	0.82-5	0.48 (0.41-0.54)	0.350 0.344
	L.R.O	5-25	4-11	0.34	0.404 0.478
$Deca_5$	S.R.O	1-5	0.8-4.5	0.48 (0.41-0.54)	(c)
	L.R.O	8-45	5-37	0.34 (0.32-0.37)	
$Deca_6$	S.R.O	1-4	0.64-4	0.43 (0.32-0.52)	0.345 0.482
	L.R.O	9-20	4-12	0.34 (0.31-0.37)	

SAMPLE	MICROSTRUCTURE	L_a(nm)	L_c(nm)	d(nm)	XRD(nm)
Deca 800_3K	S.R.O	1-3	0.68-4	0.41	0.396
				(0.34-0.42)	0.361
	L.R.O	15-39	4-20	0.34	0.350
				(0.32-0.36)	0.345
					0.336
					0.331
Deca 800_{20}K	S.R.O	1-5	0.36-3	0.39	0.396
				(0.36-0.45)	0.389
	L.R.O	10-45	5-27	0.34	0.381
				(0.32-0.37)	0.366
					0.350
					0.347
Deca$_3$K	S.R.O	1-6	0.3-4.5	0.45	0.362
				(0.37-0.52)	
	L.R.O	14-67	6-37	0.34	
				(0.32-0.37)	
Deca$_1$K	S.R.O	1-5	0.7-6	0.45	0.513
				(0.35-0.53)	0.386
	L.R.O	8-55	7-39	0.34	0.381
	& ribbon				0.364
					0.350
					0.346
					0.341
Deca$_8$K	S.R.O	1-5	0.66-8	0.37	(d)
				(0.33-0.43)	
	L.R.O	25-100	7-28	0.33	
				(0.32-0.35)	
Deca$_7$K	S.R.O	1-4	0.7-5.5	0.37	(e)
				(0.35-0.47)	
	L.R.O	12-34	4-15	0.34	
				(0.31-0.38)	
Deca$_{12}$K			--------		
Deca$_9$K	S.R.O	1-5	0.76-5	0.43	0.352
				(0.38-0.53)	0.361
	L.R.O	6-75	2-24	0.34	0.339
				(0.33-0.37)	0.480
					0.531
Deca$_{10}$K	S.R.O	1-6	0.39-8	0.41	0.482
				(0.39-0.48)	0.455
	L.R.O	6-42	4-15	0.34	0.402
	& ribbon				0.347
Deca$_{11}$K	S.R.O	1-3	0.36-4.5	0.41	0.503
				(0.36-0.49)	0.489
	L.R.O	13-40	3-21	0.34	0.406
				(0.32-0.37)	0.398
					0.393
					0.347

SAMPLE	MICROSTRUCTURE	L_a(nm)	L_c(nm)	d(nm)	XRD(nm)
$Deca_5K$	S.R.O	1-4.5	0.7-3	0.37 (0.35-0.56)	(f)
	L.R.O	8-27	5-13	0.34	
$Deca_6K$	S.R.O	1-7	0.66-6	0.38 (0.33-0.42)	0.353 0.346 0.364 0.337 0.373 0.410 0.467
	L.R.O & ribbon	25-125	4-50	0.34 (0.33-0.36)	

S.R.O - short-range order
L.R.O - long-range order

(a) 0.350, 0.341, 0.333, 0.480, 0.521, 0.404, 0.422, 0.445, 0.572.

(b) 0.404, 0.422, 0.341, 0.349, 0.323, 0.463, 0.312.

(c) 0.347, 0.358, 0.336, 0.487, 0.377, 0.447, 0.534.

(d) 0.309, 0.404, 0.348, 0.340, 0.424, 0.361, 0.332, 0.323, 0.313.

(e) 0.449, 0.396, 0.391, 0.385, 0.348, 0.341, 0.337, 0.315.

(f) 0.349, 0.341, 0.375, 0.399, 0.414, 0.431, 0.505, 0.534.

Table 8.9 Summary of TEM and XRD results for the carbonised decacylene samples.

8.8- ANALYSIS OF CARBONISED DIBENZANTHRONE

Graphitisation of dibenzanthrone at 3000°C is known to result in the formation of a graphitising carbon (Kipling et al., 1964). In this study ten carbonised samples were prepared and examined.

8.8.1- TRANSMISSION ELECTRON MICROSCOPY (TEM)

The $Dibenz_5$ sample exhibited a non-graphitised carbon

structure (L_a=1-5.5nm) with lattice spacings in the range 0.38-0.67nm and a typical value of 0.56nm (L_c=0.38-2.5nm). The sample also exhibited areas of convoluted structural order and areas of long-range ordered structure (L_a=14-58nm) with lattice spacings of between 0.32-0.36nm and a typical value of 0.34nm (L_c=2-17nm).

Analysis of the $Dibenz_1$ sample revealed a non-graphitised carbon structure (L_a=1-5nm) with lattice spacings in the range 0.36-0.48nm (figure 8.58) and a typical value of 0.40nm (L_c=0.72-3nm).

Examination of the $Dibenz_8$ sample revealed areas of both long and short-range order. The long-range ordered structure (L_a=9-35nm) exhibited interplanar spacings in the range 0.32-0.36nm and a typical value of 0.34nm (L_c=3-10nm). The short-range ordered structure (L_a=1-3nm) showed lattice spacings of between 0.36-0.57nm and a typical value of 0.49nm (L_c=0.72-5nm).

A non-graphitised carbon structure was exhibited by the $Dibenz_7$ sample (L_a=1-3.5nm) with interplanar spacings in the range 0.39-0.63nm and a typical value of 0.46nm (L_c=0.4-4.5nm). The sample also revealed areas of convoluted structural order and areas exhibiting a long-range ordered structure (L_a=6-30nm) with lattice spacings of between 0.33-0.41nm and a typical value of 0.36nm (L_c=3-9nm).

$Dibenz_{16}$ exhibited a short-range ordered structure (L_a=1-4.5nm) with lattice spacings in the range 0.39-0.58nm and a typical value of 0.48nm (L_c=0.78-3nm).

The $Dibenz_9$ sample revealed areas of both long and

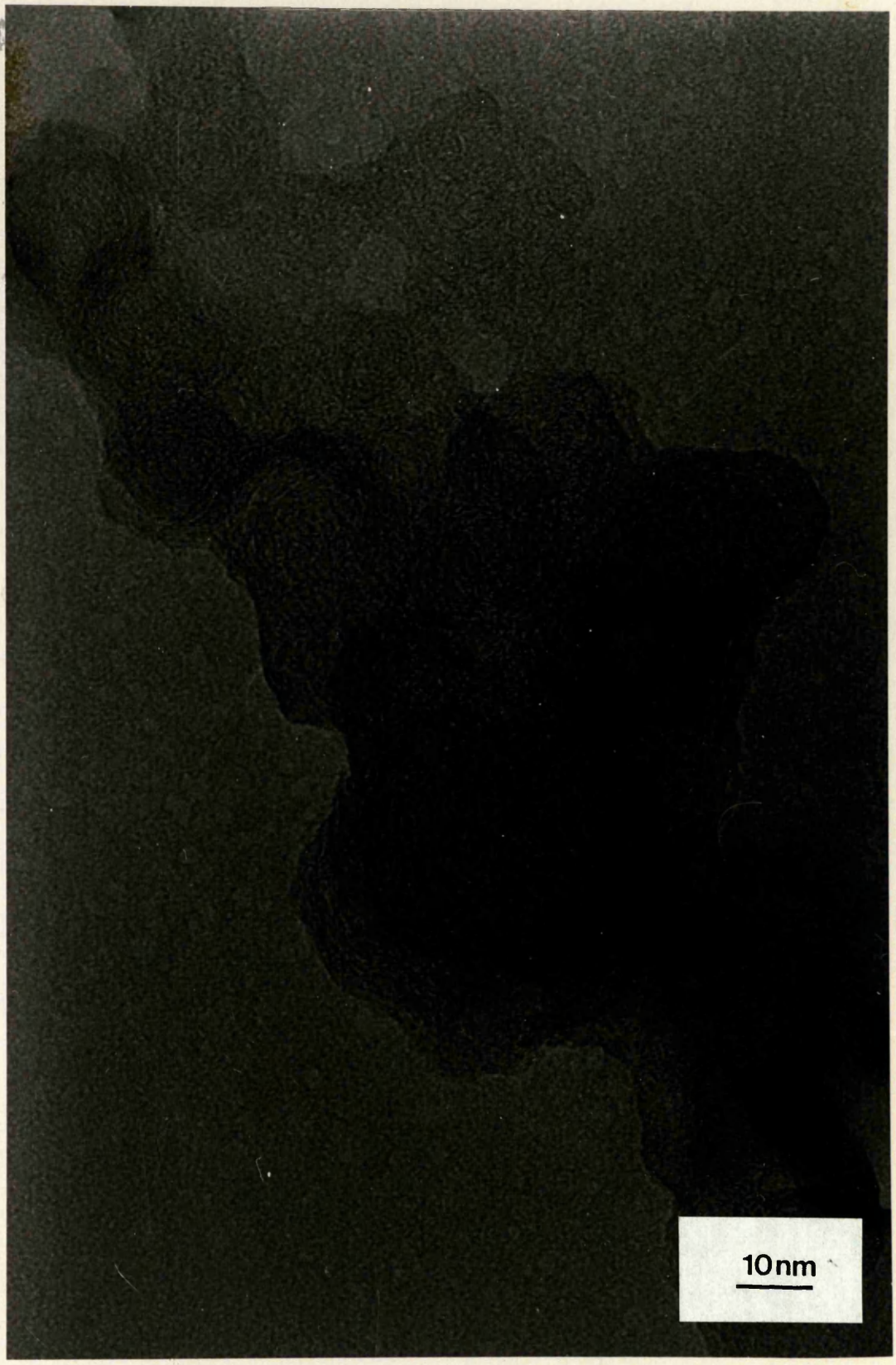

Figure 8.58: HREM of the Dibenz$_1$ sample revealing the non-graphitised carbon structure (0.36-0.48nm).

short-range order. The long-range ordered structure (L_a=7-49nm) exhibited interplanar spacings of 0.34nm (L_c=4-14nm). The short-range ordered structure (L_a=1-4nm) showed lattice spacings of between 0.36-0.44nm and a typical value of 0.40nm (L_c=0.7-2.5nm).

Examination of the $Dibenz_{15}$ sample revealed areas of both long and short-range order. The long-range ordered structure (L_a=4-23nm) exhibited interplanar spacings of 0.34nm (L_c=2-8nm). The short-range ordered structure (L_a=1-4.5nm) showed lattice spacings of between 0.37-0.59nm and a typical value of 0.48nm (L_c=0.74-3.5nm).

Analysis of the $Dibenz_{14}$ sample revealed a non-graphitised carbon structure (L_a=1-5nm) with lattice spacings in the range 0.36-0.64nm and a typical value of 0.49nm (L_c=0.36-5nm).

$Dibenz_{10}$ exhibited a non-graphitised carbon structure (L_a=1-6nm) with lattice spacings in the range 0.39-0.67nm and a typical value of 0.51nm (L_c=0.4-2nm) and areas of long-range ordered structure (L_a=14-45nm) with lattice spacings of between 0.32-0.36nm and a typical value of 0.34nm (L_c=2-15nm). Also present were areas of convoluted structural order with L_a, L_c and interplanar spacings that were indistinguishable from the values exhibited by the long-range ordered structure.

The $Dibenz_{11}$ sample revealed a short-range ordered structure (L_a=1-3nm) with lattice spacings in the range 0.36-0.48nm and a typical value of 0.40nm (L_c=0.72-4nm).

8.8.2- SCANNING ELECTRON MICROSCOPY (SEM)

The dibenzanthrone samples, when examination by SEM, revealed two very contrasting surfaces. One showed a rough surface exhibiting large holes leading to the interior (figure 8.59). The second type of structure was a ramifying, chambered structure (figure 8.60) with figure 8.61 revealing the internal surface of the ramifying chambered structure. Table 8.10 summarises the SEM structures exhibited by each of the dibenzanthrone samples.

SAMPLE	STRUCTURE EXHIBITED
$Dibenz_5$	ramifying chambered structure
$Dibenz_1$	large holes leading to the interior
$Dibenz_8$	ramifying chambered structure
$Dibenz_7$	ramifying chambered structure
$Dibenz_{16}$	ramifying chambered structure
$Dibenz_9$	ramifying chambered structure
$Dibenz_{15}$	ramifying chambered structure
$Dibenz_{14}$	large holes leading to the interior
$Dibenz_{10}$	large holes leading to the interior
$Dibenz_{11}$	large holes leading to the interior

Table 8.10 SEM structures exhibited by each of the carbonised dibenzanthrone samples.

8.8.3- POWDER X-RAY DIFFRACTION ANALYSIS (XRD)

Within the interplanar spacings range (38.0-17.0^{o}) 0.275-0.606, twelve peaks were evident from the $Dibenz_5$ x-ray diffraction trace (figure 8.62). The peaks, in order of

Figure 8.59: SEM displaying the rough surface and holes leading to the interior exhibited by the $Dibenz_1$, $Dibenz_{14}$, $Dibenz_{10}$ and $Dibenz_{11}$ samples.

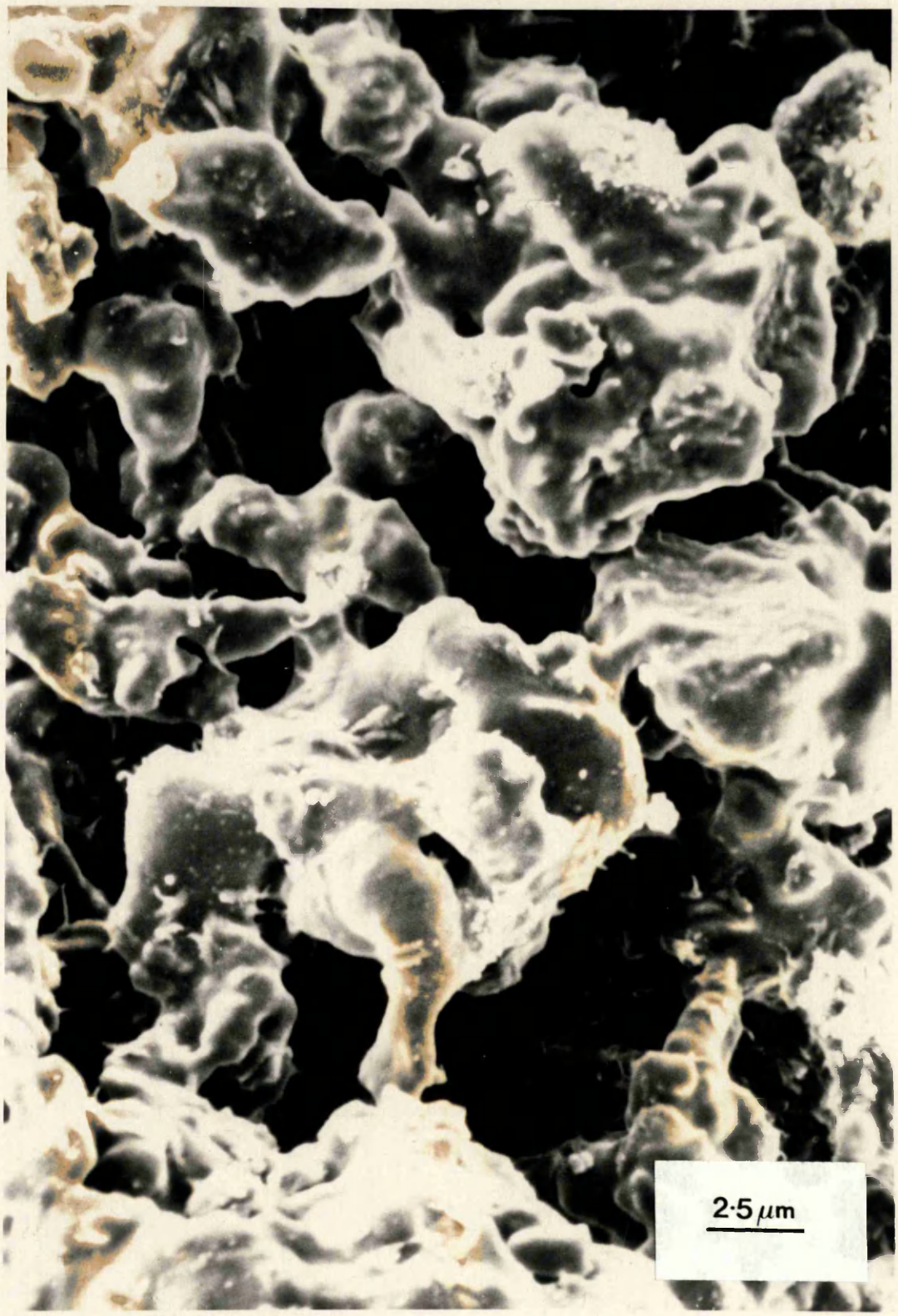

Figure 8.60: SEM showing the ramifying chambered structure exhibited by the $Dibenz_5$, $Dibenz_8$, $Dibenz_7$, $Dibenz_{16}$, $Dibenz_9$ and $Dibenz_{15}$ samples.

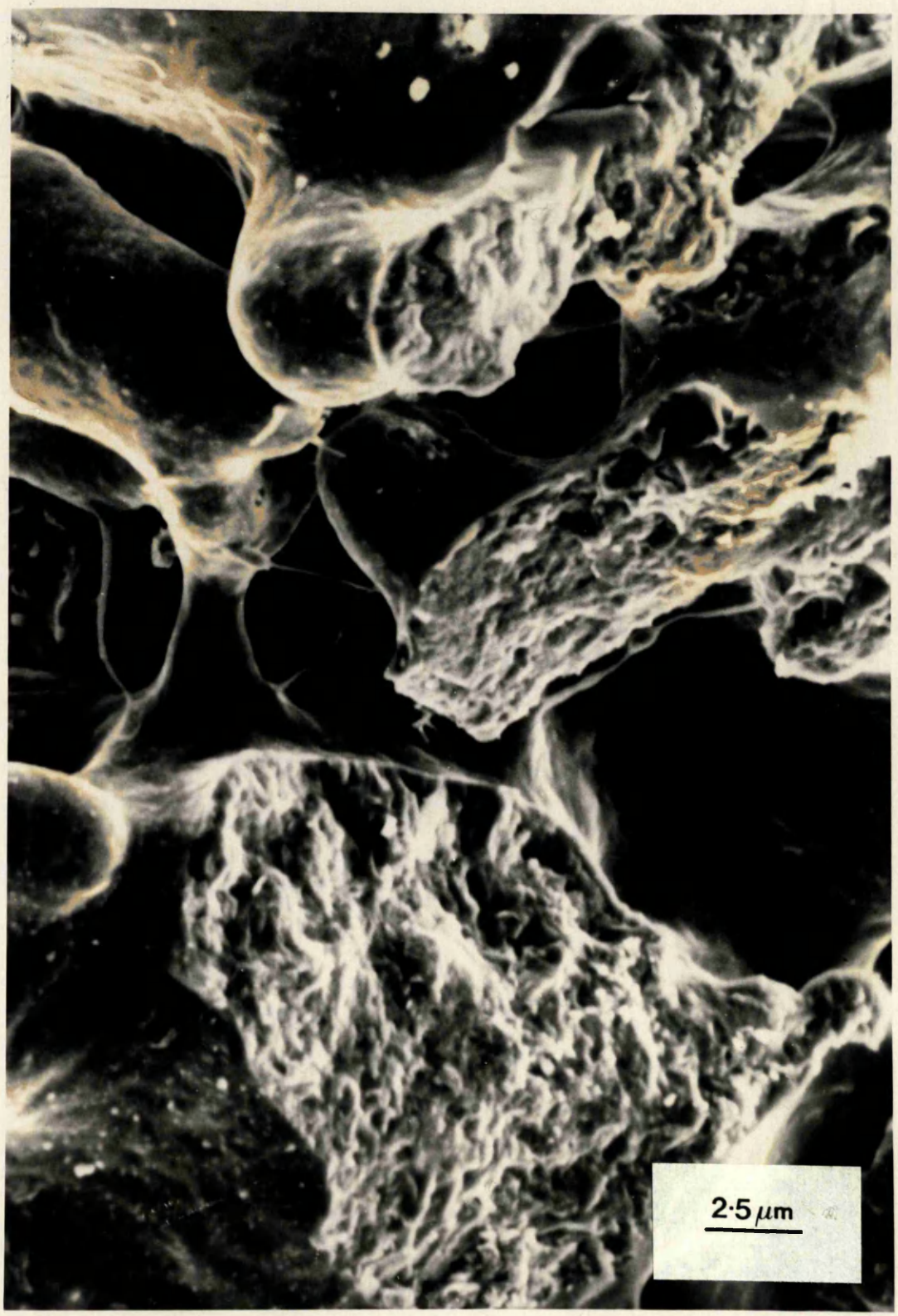

Figure 8.61: SEM revealing the internal surface of the ramifying chambered structure.

Figure 8.62: XRD trace of the Dibenz$_5$ sample.

Figure 8.63: XRD trace of the Dibenz$_1$ sample.

decreasing intensity were centered on (28.6°) 0.362nm, (28.2°) 0.367nm, (29.2°) 0.355nm, (27.2°) 0.381nm, (26.7°) 0.388nm, (26.0°) 0.398nm, (30.0°) 0.346nm, (31.0°) 0.335nm, (24.6°) 0.420nm, (21.6°) 0.478nm, (31.9°) 0.326nm and (33.4°) 0.312nm. Within this group of twelve, (26.7°) 0.388nm and (26.0°) 0.398nm exhibited a similar intensity, as did the peaks occurring at (24.6°) 0.420nm and (21.6°) 0.478nm.

The x-ray diffraction trace of the $Dibenz_1$ sample revealed seven peaks within the interplanar spacings range (38.2-20.0°) 0.274-0.515nm (figure 8.63). The most intense peak was centered at (29.3°) 0.354nm with the remaining peaks, in order of decreasing intensity, centered at (30.3°) 0.345nm, (28.3°) 0.366nm, (27.2°) 0.381nm, (26.2°) 0.395nm, (25.2°) 0.410nm and (24.6°) 0.420nm respectively.

Examination of the x-ray diffraction trace obtained for the $Dibenz_8$ sample revealed fifteen peaks within the interplanar spacings range (35.2-17.8°) 0.296-0.579nm (figure 8.64). The most intense peak was centered at (25.6°) 0.404nm with the remaining peaks, in order of decreasing intensity, centered at (30.2°) 0.344nm, (30.6°) 0.339nm, (31.0°) 0.335nm, (29.6°) 0.350nm, (28.9°) 0.359nm, (28.2°) 0.367nm, (28.0°) 0.370nm, (27.6°) 0.375nm, (27.0°) 0.383nm, (26.5°) 0.391nm, (24.5°) 0.422nm, (22.3°) 0.463nm, (19.9°) 0.518nm and (19.3°) 0.534nm, with two of these peaks, (31.0°) 0.335nm and (30.6°) 0.339nm exhibiting a similar intensity.

The $Dibenz_7$ x-ray diffraction trace exhibited fourteen peaks within the interplanar spacings range (36.0-17.6°)

Figure 8.64: XRD trace of the Dibenz$_8$ sample.

Figure 8.65: XRD trace of the Dibenz$_7$ sample.

0.290-0.585nm (figure 8.65). The most intense peak, was centered at (30.8°) 0.337nm. The remaining peaks, in order of decreasing intensity, were centered at (30.2°) 0.344nm, (29.5°) 0.352nm, (28.4°) 0.365nm, (28.0°) 0.370nm, (27.2°) 0.381nm, (25.8°) 0.401nm, (26.7°) 0.388nm, (24.8°) 0.417nm, (22.8°) 0.453nm, (21.6°) 0.478nm, (20.8°) 0.496nm, (19.6°) 0.526nm and (18.4°) 0.560nm, with two of these peaks, (21.6°) 0.478nm and (20.8°) 0.496nm exhibiting a similar intensity.

Within the interplanar spacings range (36.0-16.6°) 0.290-0.620, twelve peaks were evident from the $Dibenz_{16}$ x-ray diffraction trace (figure 8.66). The eight most intense peaks, in order of decreasing intensity were centered on (28.4°) 0.365nm, (28.9°) 0.359nm, (27.9°) 0.371nm, (29.6°) 0.350nm, (27.2°) 0.381nm, (30.7°) 0.338nm, (30.1°) 0.345nm and (31.1°) 0.334nm. The remaining peaks, in order of decreasing intensity, were centered at (25.8°) 0.401nm, (23.8°) 0.434nm, (19.8°) 0.521nm and (18.6°) 0.554nm respectively.

The $Dibenz_9$ x-ray diffraction trace exhibited three peaks within the interplanar spacings range (39.0-16.6°) 0.268-0.620nm (figure 8.67). The most intense peak was centered at (25.6°) 0.404nm with the remaining peaks, in order of decreasing intensity, centered at (28.8°) 0.360nm and (31.0°) 0.335nm respectively.

The x-ray diffraction trace for the $Dibenz_{15}$ sample exhibited four peaks within the interplanar spacings range (44.0-14.0°) 0.239-0.735nm (figure 8.68). The sharpest and most intense peak was centered at (31.1°) 0.332nm. The

Figure 8.66: XRD trace of the Dibenz$_{16}$ sample.

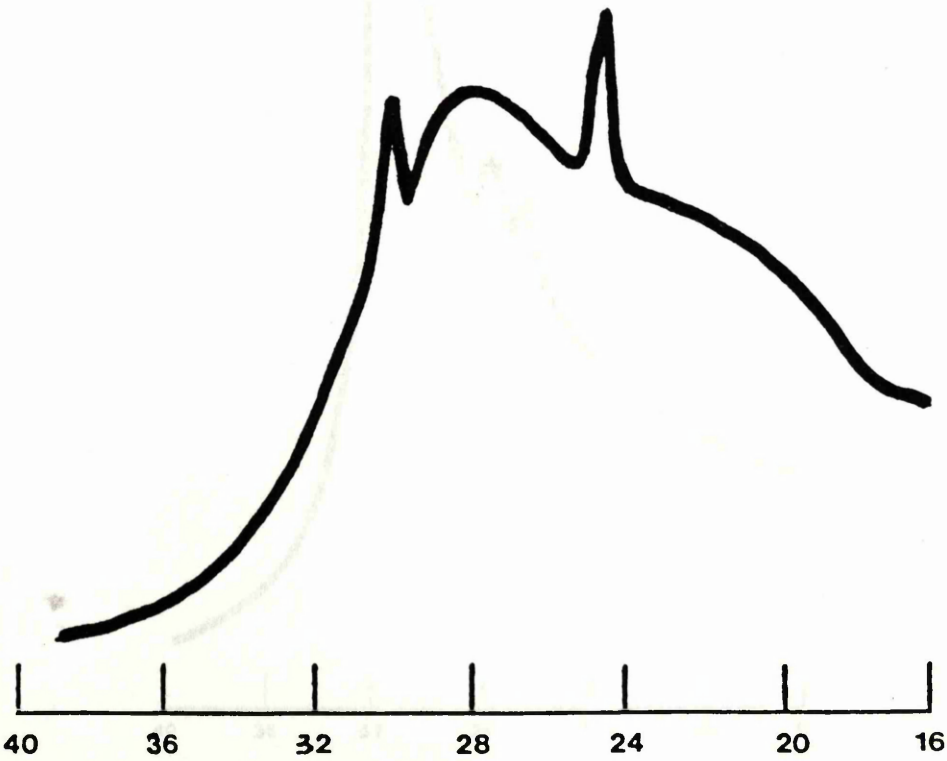

Figure 8.67: XRD trace of the Dibenz$_{9}$ sample.

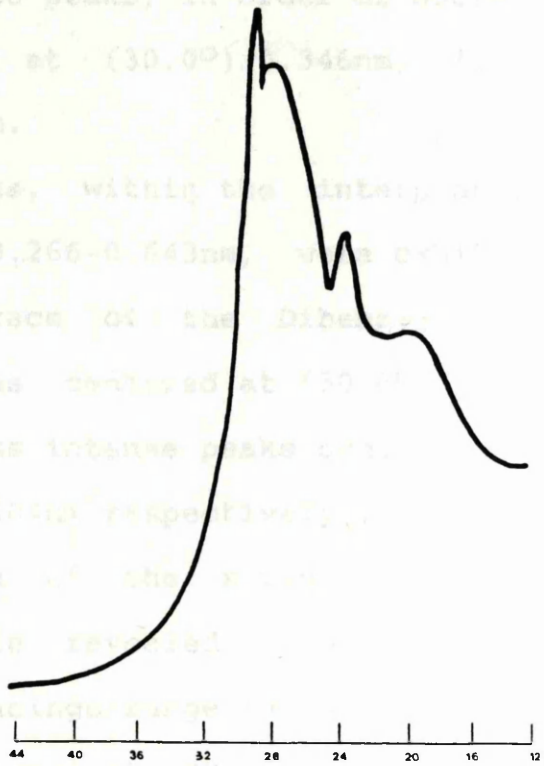

Figure 8.68: XRD trace of the Dibenz$_{15}$ sample.

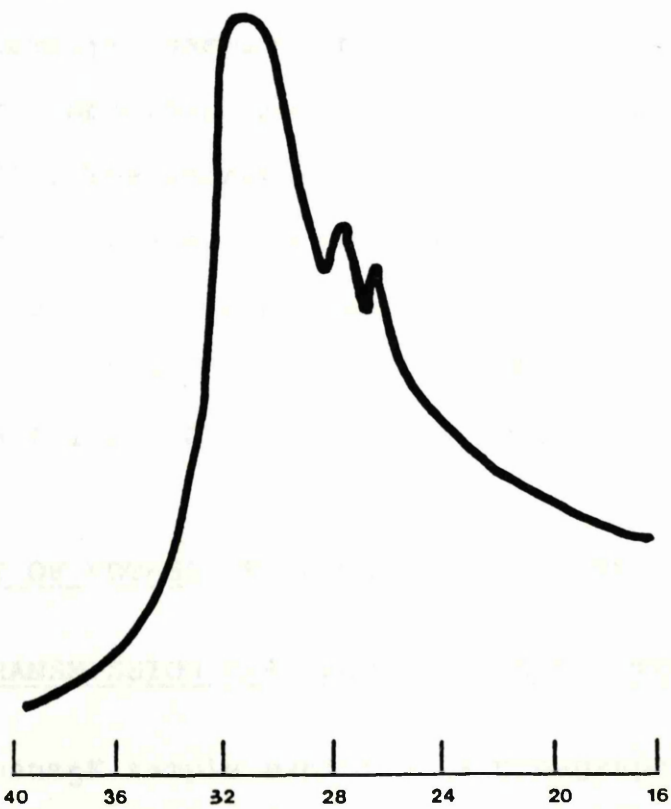

Figure 8.69: XRD trace of the Dibenz$_{14}$ sample.

remaining three peaks, in order of decreasing intensity, were centered at (30.0°) 0.346nm, (25.6°) 0.404nm and (21.2°) 0.486nm.

Three peaks, within the interplanar spacings range (39.4-16.0°) 0.266-0.643nm, were exhibited by the x-ray diffraction trace of the $Dibenz_{14}$ sample. The most intense peak was centered at (30.8°) 0.337nm with the two smaller and less intense peaks centered at (26.8°) 0.386nm and (25.6°) 0.404nm respectively (figure 8.69).

Examination of the x-ray diffraction trace of the $Dibenz_{10}$ sample revealed two broad peaks within the interplanar spacings range (41.4-15.4°) 0.253-0.668nm. The peaks were centered at (28.6°) 0.362nm and (22.0°) 0.469nm, the latter exhibiting a slightly smaller peak intensity (figure 8.70).

The $Dibenz_{11}$ sample exhibited five peaks within the interplanar spacings range (36.0-16.0°) 0.290-0.643nm (figure 8.71). The sharpest and most intense peak of the x-ray diffraction trace, was centered at (25.6°) 0.404nm. The remaining peaks in order of decreasing intensity were centered at (21.4°) 0.482nm, (27.8°) 0.373nm, (30.4°) 0.341nm and (32.6°) 0.319nm respectively.

8.9- EFFECT OF POTASSIUM ON CARBONISED DIBENZANTHRONE

8.9.1- TRANSMISSION ELECTRON MICROSCOPY (TEM)

The $Dibenz_5K$ sample exhibited a non-graphitised carbon structure (L_a=1-7nm) with lattice spacings in the range 0.39-0.62nm and a typical value of 0.56nm (L_c=0.78-3nm) and

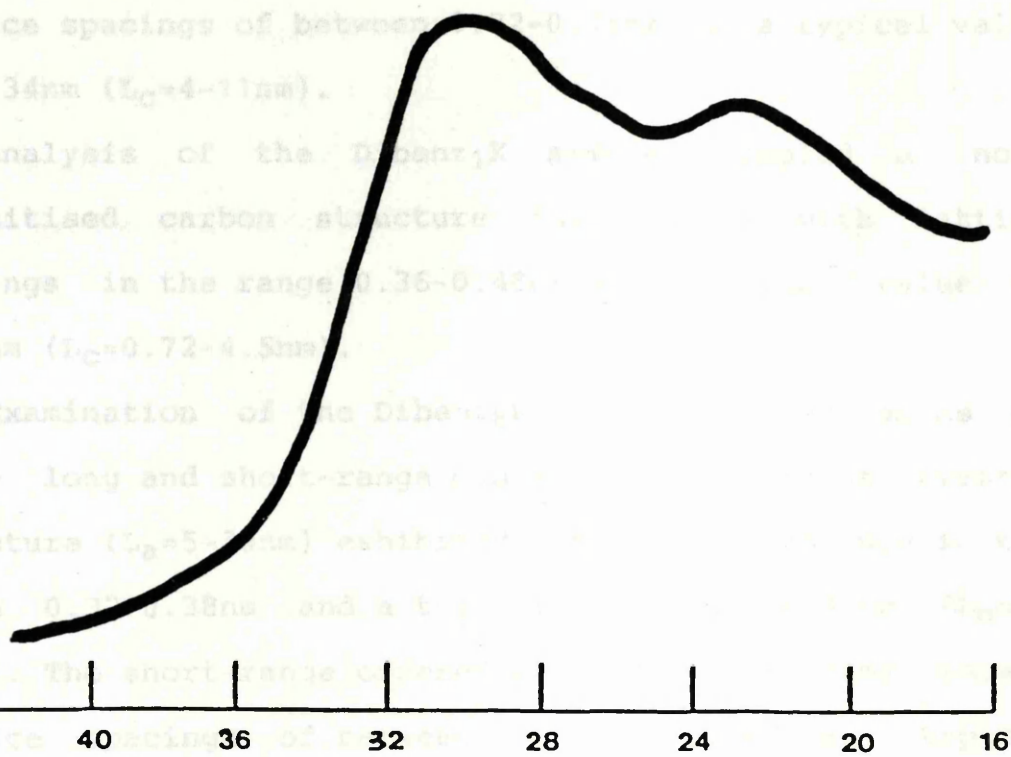

Figure 8.70: XRD trace of the $Dibenz_{10}$ sample.

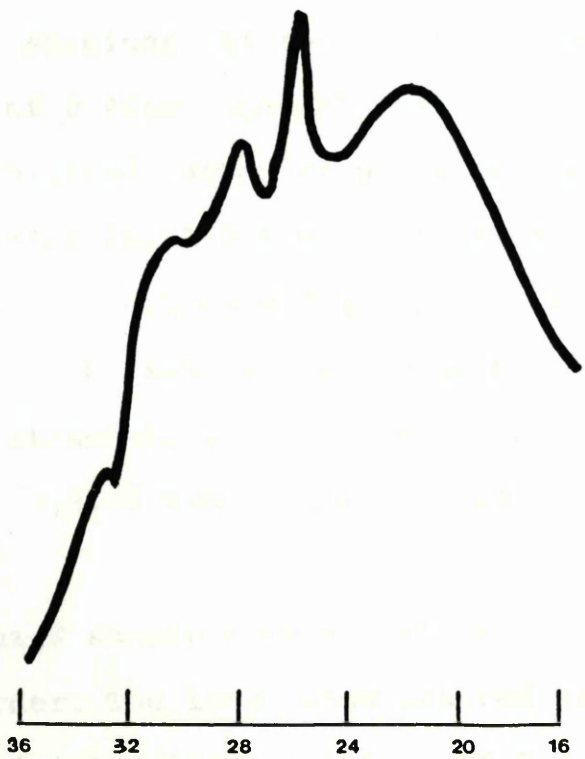

Figure 8.71: XRD trace of the $Dibenz_{11}$ sample.

areas of long-range ordered structure (L_a=9-39nm) with lattice spacings of between 0.32-0.36nm and a typical value of 0.34nm (L_c=4-11nm).

Analysis of the Dibenz$_1$K sample revealed a non-graphitised carbon structure (L_a=1-5.5nm) with lattice spacings in the range 0.36-0.48nm and a typical value of 0.42nm (L_c=0.72-4.5nm).

Examination of the Dibenz$_8$K sample revealed areas of both long and short-range order. The long-range ordered structure (L_a=5-39nm) exhibited interplanar spacings in the range 0.32-0.38nm and a typical value of 0.34nm (L_c=3-12nm). The short-range ordered structure (L_a=1-4nm) showed lattice spacings of between 0.35-0.48nm and a typical value of 0.40nm (L_c=0.7-3.5nm).

After exposure to potassium vapour the Dibenz$_7$ sample exhibited a short-range ordered structure (L_a=1-3.5nm) with lattice spacings in the range 0.39-0.54nm and a typical value of 0.46nm (L_c=0.39-3nm).

A non-graphitised carbon structure was exhibited by the Dibenz$_{16}$K sample (L_a=1-3.5nm) with interplanar spacings in the range 0.37-0.64nm and a typical value of 0.48nm (L_c=0.74-4nm). The sample also revealed areas of long-range ordered structure (L_a=10-45nm) with lattice spacings of between 0.32-0.37nm and a typical value of 0.34nm (L_c=2-12nm).

The Dibenz$_9$K sample revealed areas of both long and short-range order. The long-range ordered structure (L_a=4-24nm) exhibited interplanar spacings of 0.34nm (L_c=2-9nm). The short-range ordered structure (L_a=1-4nm) showed lattice

spacings of between 0.37-0.52nm and a typical value of 0.40nm (L_c=0.72-2.5nm).

Examination of the $Dibenz_{15}K$ sample revealed areas of convoluted structural order and areas exhibiting a long-range ordered structure (L_a=7-36nm) exhibited interplanar spacings of 0.35nm (L_c=4-10nm). The short-range ordered structure (L_a=1-6nm) showed lattice spacings of between 0.37-0.52nm (figure 8.72) and a typical value of 0.46nm (L_c=0.74-6nm).

Analysis of the $Dibenz_{14}$ sample after exposure to potassium vapour revealed a non-graphitised carbon structure (L_a=1-3.5nm) with lattice spacings in the range 0.36-0.48nm and a typical value of 0.41nm (L_c=0.36-4.5nm). the sample also exhibited areas of convoluted structural order (L_a=2-8nm) with interplanar spacings in the range 0.32-0.37nm and a typical value of 0.34nm (L_c=3-6nm.)

After exposure to potassium vapour the $Dibenz_{10}$ sample exhibited a non-graphitised carbon structure (L_a=1-5nm) with lattice spacings in the range 0.39-0.58nm and a typical value of 0.44nm (L_c=0.78-5nm) and areas of long-range ordered structure (L_a=11-39nm) with lattice spacings of between 0.32-0.36nm and a typical value of 0.34nm (L_c=2-6nm).

The $Dibenz_{11}K$ sample revealed a non-graphitised carbon structure (L_a=1-6nm) with lattice spacings in the range 0.36-0.48nm and a typical value of 0.40nm (L_c=0.36-4nm).

8.9.2- SCANNING ELECTRON MICROSCOPY (SEM)

The dibenzanthrone samples revealed two very

Figure 8.72: HREM of the Dibenz$_{15}$K sample showing the non-graphitised carbon structure (0.37-0.52nm).

contrasting surfaces after exposure to potassium vapour. The structures, similar to those exhibited by the dibenzanthrone samples prior to potassium vapour exposure, revealed a rough surface exhibiting large holes leading to the interior (figure 8.59) and a ramifying, chambered structure (figure 8.60). Table 8.11 summarises the SEM structures exhibited by each of the dibenzanthrone samples.

SAMPLE	STRUCTURE EXHIBITED
$Dibenz_5K$	large holes leading to the interior
$Dibenz_1K$	large holes leading to the interior
$Dibenz_8K$	ramifying chambered structure
$Dibenz_7K$	ramifying chambered structure
$Dibenz_{16}K$	ramifying chambered structure
$Dibenz_9K$	ramifying chambered structure
$Dibenz_{15}K$	large holes leading to the interior
$Dibenz_{14}K$	large holes leading to the interior
$Dibenz_{10}K$	large holes leading to the interior
$Dibenz_{11}K$	large holes leading to the interior

Table 8.11 SEM structures exhibited by each of the carbonised dibenzanthrone samples after exposure to potassium vapour.

8.9.3- POWDER X-RAY DIFFRACTION ANALYSIS (XRD)

Within the interplanar spacings range (35.6-16.0^{o}) 0.293-0.643, eighteen peaks were evident from the $Dibenz_5K$ x-ray diffraction trace (figure 8.73). The seven most intense peaks, in order of decreasing intensity were centered on (28.3^{o}) 0.366nm, (27.5^{o}) 0.377nm, (29.9^{o})

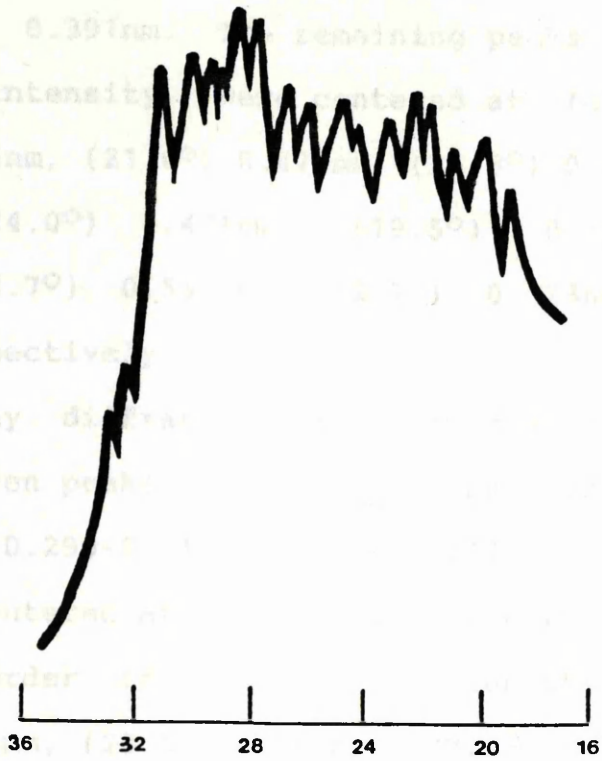

Figure 8.73: XRD trace of the Dibenz$_5$K sample.

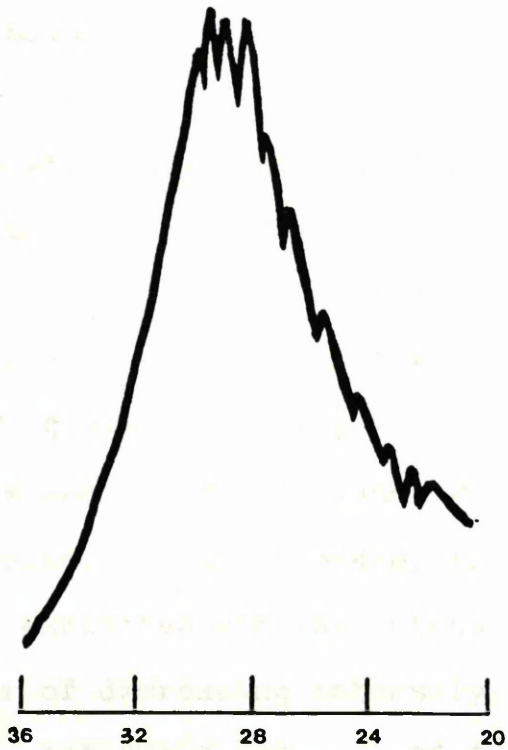

Figure 8.74: XRD trace of the Dibenz$_1$K sample.

0.347nm, (29.3°) 0.354nm, (31.0°) 0.345nm, (28.9°) 0.359nm and (26.5°) 0.391nm. The remaining peaks, in order of decreasing intensity, were centered at (22.1°) 0.467nm, (24.9°) 0.415nm, (21.6°) 0.478nm, (25.8°) 0.401nm, (23.0°) 0.449nm, (24.0°) 0.431nm, (19.5°) 0.529nm, (20.7°) 0.498nm, (18.7°) 0.551nm, (32.2°) 0.323nm and (32.9°) 0.316nm respectively.

The x-ray diffraction trace of the $Dibenz_1K$ sample revealed eleven peaks within the interplanar spacings range (36.0-20.0°) 0.290-0.515nm (figure 8.74). The most intense peak was centered at (30.0°) 0.346nm with the remaining peaks, in order of decreasing intensity, centered at (29.2°) 0.355nm, (28.5°) 0.364nm, (30.4°) 0.341nm, (27.8°) 0.373nm, (27.0°) 0.383nm, (25.8°) 0.401nm, (24.6°) 0.420nm, (23.6°) 0.438nm, (22.8°) 0.453nm and (22.0°) 0.469nm with two of these peaks, (29.2°) 0.355nm and (28.5°) 0.364nm exhibiting a similar intensity.

Within the interplanar spacings range (34.6-21.6°) 0.301-0.478, sixteen peaks were evident from the $Dibenz_8K$ x-ray diffraction trace (figure 8.75). The eight most intense peaks, in order of decreasing intensity were centered on (25.6°) 0.404nm, (30.8°) 0.337nm, (29.8°) 0.348nm, (30.2°) 0.344nm, (29.4°) 0.353nm, (28.7°) 0.361nm, (28.2°) 0.367nm and (27.8°) 0.373nm. Within this group of eight, three peaks, (30.2°) 0.344nm, (29.8°) 0.348nm and (29.4°) 0.353nm exhibited similar intensity. The remaining peaks, in order of decreasing intensity, were centered at (27.1°) 0.382nm, (26.2°) 0.395nm, (26.9°) 0.385nm, (24.9°) 0.415nm, (24.2°) 0.427nm, (32.2°) 0.323, (33.0°) 0.315nm

Figure 8.75: XRD trace of the Dibenz$_8$K sample.

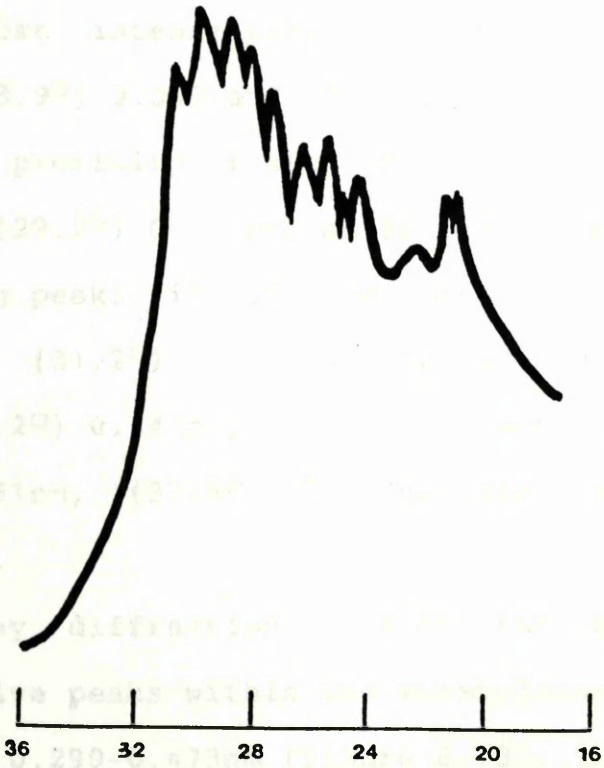

Figure 8.76: XRD trace of the Dibenz$_7$K sample.

and (33.5°) 0.311nm respectively.

Twelve peaks, within an interplanar spacings range of (36.0-17.5°) 0.290-0.588nm, were exhibited by the x-ray diffraction trace of the $Dibenz_7K$ sample (figure 8.76). The most intense peak was centered at (29.8°) 0.348nm with the remaining peaks, in order of decreasing intensity, centered at (28.8°) 0.360nm, (28.2°) 0.367nm, (30.8°) 0.337nm, (27.4°) 0.378nm, (25.4°) 0.407nm, (26.3°) 0.393nm, (24.4°) 0.424nm, (21.2°) 0.487nm, (21.0°) 0.491nm, (24.9°) 0.415nm and (22.2°) 0.465nm. Two of the peaks, occurring within close proximity of each other, exhibited a similar intensity and were centered at (21.2°) 0.487nm and (21.0°) 0.491nm.

Thirteen peaks, within an interplanar spacings range of (34.8-20.0°) 0.299-0.515nm, were revealed by the x-ray diffraction trace of the $Dibenz_{16}K$ sample (figure 8.77). Of the four most intense peaks, (29.8°) 0.348nm, (29.2°) 0.355nm, (28.9°) 0.359 and (28.5°) 0.364nm, all centered within close proximity of each other, two peaks, (29.8°) 0.348nm and (29.2°) 0.355nm, exhibited a similar intensity. The remaining peaks, in order of decreasing intensity were centered on (31.2°) 0.333nm, (27.8°) 0.373nm, (27.4°) 0.378nm, (30.2°) 0.343nm, (25.6°) 0.404nm, (26.3°) 0.393nm, (24.0°) 0.431nm, (32.8°) 0.317nm and (34.0°) 0.306nm respectively.

The x-ray diffraction trace of the $Dibenz_9K$ sample revealed twelve peaks within the interplanar spacings range (36.0-21.8°) 0.290-0.473nm (figure 8.78). The most intense peak was centered at (28.4°) 0.365nm with the remaining

Figure 8.77: XRD trace of the Dibenz$_{16}$K sample.

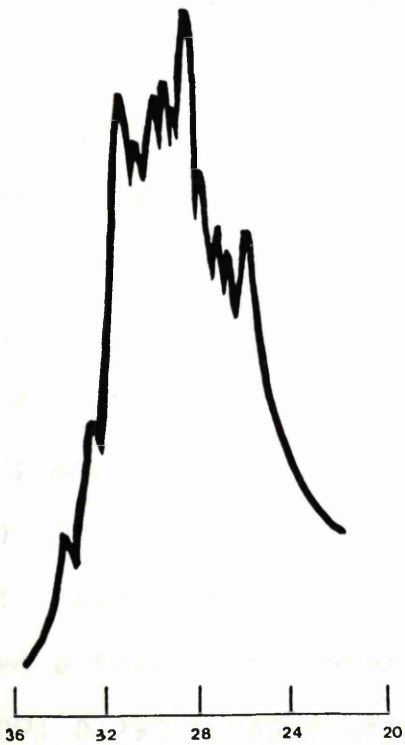

Figure 8.78: XRD trace of the Dibenz$_{9}$K sample.

peaks, in order of decreasing intensity, centered at (29.1°) 0.356nm, (31.1°) 0.334nm, (29.7°) 0.349nm, (28.8°) 0.360nm, (30.3°) 0.342nm, (27.7°) 0.374nm, (26.8°) 0.386nm, (25.6°) 0.404nm, (26.4°) 0.392nm, (32.7°) 0.318nm and (33.8°) 0.308nm respectively.

Four peaks, within an interplanar spacings range (43.2-14.0°) 0.243-0.735nm (figure 8.79), were exhibited by the x-ray diffraction trace of the $Dibenz_{15}K$ sample. The sharpest and most intense peak was centered at (25.6°) 0.404nm. The three remaining peaks were centered at (31.2°) 0.332nm, (29.2°) 0.355nm and (28.4°) 0.364nm with respectively decreasing intensities.

The x-ray diffraction trace for the $Dibenz_{14}K$ sample revealed three peaks within the interplanar spacings range (40.2-16.0°) 0.260-0.643nm (figure 8.80). The most intense peak of the trace was centered at (25.6°) 0.404nm. The remaining two peaks, in order of decreasing intensity, were centered at (30.6°) 0.339nm and (22.0°) 0.469nm.

The $Dibenz_{10}K$ x-ray diffraction trace exhibited five peaks within the range of interplanar spacings (36.0-20.0°) 0.290-0.515nm (figure 8.81). The most intense peak was centered at (28.3°) 0.366nm with two peaks, of similar intensity, centered at (29.6°) 0.350nm and (31.0°) 0.335nm. The remaining two peaks, with decreasing intensity were centered at (25.8°) 0.401nm and (23.5°) 0.440nm.

Examination of the $Dibenz_{11}K$ sample by x-ray diffraction revealed a trace with interplanar spacings in the range (36.0-16.0°) 0.290-0.643nm (figure 8.82) and two peaks, of similar intensity, centered at (27.9°) 0.371nm and (21.6°) 0.478nm.

Figure 8.79: XRD trace of the Dibenz$_{15}$K sample.

Figure 8.80: XRD trace of the Dibenz$_{14}$K sample.

Figure 8.81: XRD trace of the $Dibenz_{10}K$ sample.

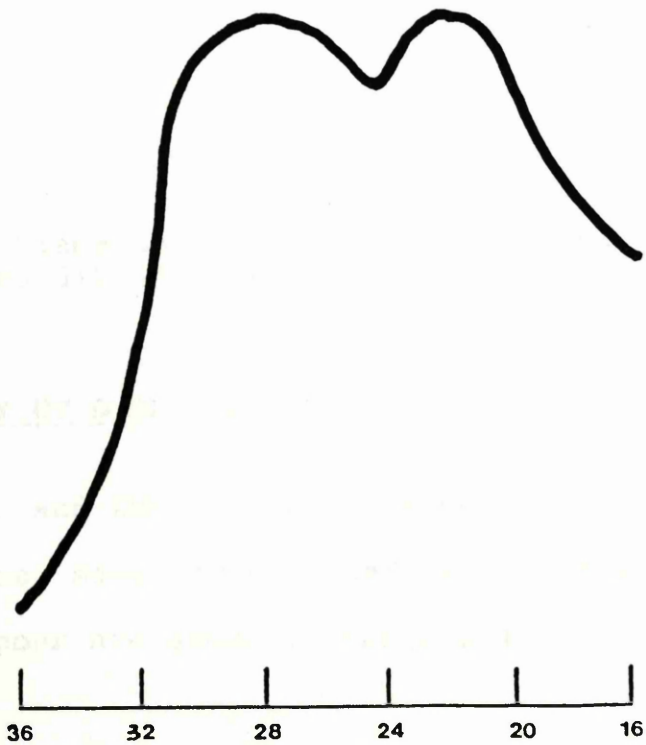

Figure 8.82: XRD trace of the $Dibenz_{11}K$ sample.

8.9.4- FLAME PHOTOMETRY MEASUREMENTS

Due to operational problems, the dibenzanthrone samples, prepared via an open carbonisation system were not examined using the potassium uptake measurement technique. A flame photometry study was carried out to establish their susceptibility to alkali attack.

SAMPLE	K CONC. (mg) per 100mg of sample
$Dibenz_5$	8.922
$Dibenz_1$	8.144
$Dibenz_8$	1.891
$Dibenz_7$	5.104
$Dibenz_{16}$	4.420
$Dibenz_9$	7.110
$Dibenz_{15}$	4.664
$Dibenz_{14}$	2.966
$Dibenz_{10}$	4.863
$Dibenz_{11}$	2.190

Table 8.12 Flame photometry potassium concentrations for the carbonised dibenzanthrone samples.

8.10- SUMMARY OF DIBENZANTHRONE RESULTS

The TEM and XRD results obtained for the carbonised dibenzanthrone samples, both before and after exposure to potassium vapour are shown in table 8.13.

SAMPLE	MICROSTRUCTURE	L_a(nm)	L_c(nm)	d(nm)	XRD(nm)
Dibenz$_5$	S.R.O	1-5.5	0.38-2.5	0.56 (0.38-0.67)	(a)
	L.R.O & ribbon	14-58	2-17	0.34 (0.32-0.36)	
Dibenz$_1$	S.R.O	1-5	0.72-3	0.40 (0.36-0.48)	(b)
Dibenz$_8$	S.R.O	1-3	0.72-5	0.49 (0.36-0.57)	(c)
	L.R.O	9-35	3-10	0.34 (0.32-0.36)	
Dibenz$_7$	S.R.O	1-3.5	0.4-4.5	0.46 (0.39-0.63)	(d)
	L.R.O & ribbon	6-30	3-9	0.36 (0.33-0.41)	
Dibenz$_{16}$	S.R.O	1-4.5	0.78-3	0.48 (0.39-0.58)	(e)
Dibenz$_9$	S.R.O	1-4	0.7-2.5	0.40 (0.36-0.44)	0.404 0.360
	L.R.O	7-49	4-14	0.34	0.335
Dibenz$_{15}$	S.R.O	1-4.5	0.74-3.5	0.48 (0.37-0.59)	0.332 0.346
	L.R.O	4-23	2-8	0.34	0.404 0.486
Dibenz$_{14}$	S.R.O	1-5	0.36-5	0.49 (0.36-0.64)	0.337 0.386 0.404
Dibenz$_{10}$	S.R.O	1-6	0.4-2	0.51 (0.39-0.67)	0.469 0.362
	L.R.O & ribbon	14-45	2-15	0.34 (0.32-0.36)	
Dibenz$_{11}$	S.R.O	1-3	0.72-4	0.40 (0.36-0.48)	0.404 0.482 0.373 0.341 0.319
Dibenz$_5$K	S.R.O	1-7	0.78-3	0.56 (0.39-0.62)	(f)
	L.R.O	9-39	4-11	0.34 (0.32-0.36)	
Dibenz$_1$K	S.R.O	1-5.5	0.72-4.5	0.42 (0.36-0.48)	(g)

SAMPLE	MICROSTRUCTURE	L_a(nm)	L_c(nm)	d(nm)	XRD(nm)
Dibenz$_8$K	S.R.O	1-4	0.7-3.5	0.40 (0.35-0.48)	(h)
	L.R.O	5-39	3-12	0.34 (0.32-0.38)	
Dibenz$_7$K	S.R.O	1-3.5	0.39-3	0.46 (0.39-0.54)	(i)
Dibenz$_{16}$K	S.R.O	1-3.5	0.74-4	0.48 (0.37-0.64)	(j)
	L.R.O	10-45	2-12	0.34 (0.32-0.37)	
Dibenz$_9$K	S.R.O	1-4	0.72-2.5	0.40 (0.36-0.49)	(k)
	L.R.O	4-24	2-9	0.34	
Dibenz$_{15}$K	S.R.O	1-6	0.74-6	0.46 (0.37-0.52)	0.404 0.332
	L.R.O & ribbon	7-36	4-10	0.35	0.355 0.364
Dibenz$_{14}$K	S.R.O	1-3.5	0.36-4.5	0.41 (0.36-0.48)	0.404 0.339
	ribbon	2-8	3-6	0.34 (0.32-0.37)	0.469
Dibenz$_{10}$K	S.R.O	1-5	0.78-5	0.44 (0.39-0.58)	0.366 0.350
	L.R.O	11-39	2-6	0.34 (0.32-0.36)	0.335 0.401 0.440
Dibenz$_{11}$K	S.R.O	1-6	0.36-4	0.40 (0.36-0.48)	0.371 0.478

S.R.O - short-range order
L.R.O - long-range order

(a) 0.362, 0.367, 0.355, 0.381, 0.388, 0.398, 0.346, 0.335, 0.420, 0.478, 0.326, 0.312.

(b) 0.354, 0.345, 0.366, 0.381, 0.395, 0.410, 0.420.

(c) 0.404, 0.344, 0.339, 0.335, 0.350, 0.359, 0.367, 0.370, 0.375, 0.383, 0.391, 0.422, 0.463, 0.518, 0.534.

(d) 0.337, 0.344, 0.352, 0.365, 0.370, 0.381, 0.401, 0.388, 0.417, 0.453, 0.478, 0.496, 0.526, 0.560.

(e) 0.365, 0.359, 0.371, 0.350, 0.381, 0.336, 0.345, 0.344, 0.401, 0.434, 0.521, 0.554.

(f) 0.366, 0.377, 0.347, 0.354, 0.345, 0.359, 0.391, 0.467, 0.415, 0.478, 0.401, 0.449, 0.431, 0.529, 0.498, 0.551, 0.323, 0.316.

(g) 0.346, 0.355, 0.364, 0.341, 0.373, 0.383, 0.401, 0.420, 0.438, 0.453, 0.469.

(h) 0.404, 0.337, 0.348, 0.344, 0.353, 0.361, 0.367, 0.373, 0.382, 0.395, 0.385, 0.415, 0.427, 0.323, 0.315, 0.311.

(i) 0.348, 0.360, 0.367, 0.337, 0.378, 0.407, 0.393, 0.424, 0.487, 0.491, 0.415, 0.465.

(j) 0.348, 0.355, 0.359, 0.364, 0.333, 0.373, 0.378, 0.343, 0.404, 0.393, 0.431, 0.317, 0.306.

(k) 0.365, 0.356, 0.334, 0.349, 0.360, 0.342, 0.374, 0.386, 0.404, 0.392, 0.318, 0.308.

Table 8.13 Summary of TEM and XRD results for the carbonised dibenzanthrone samples.

8.11- ANALYSIS OF CARBONISED POLYVINYL ACETATE

Graphitisation of polyvinyl acetate at 3000°C is known to result in the formation of a graphitising carbon. In this study two carbonised samples were prepared and examined.

8.11.1- TRANSMISSION ELECTRON MICROSCOPY (TEM)

Both the PVA_2 and PVA_1 samples exhibited areas of long-range ordered structure (L_a=9-63nm) with lattice spacings in the range 0.33-0.35nm (L_c=3-14nm). Examination of the short-range ordered structure, exhibited by the PVA_2 sample (L_a=1-5nm) revealed lattice spacings in the range 0.35-0.48nm and a typical value of 0.40nm (L_c=0.7-3.5nm). Analysis of the PVA_1 sample revealed a non-graphitised carbon structure (L_a=1-5nm) with lattice spacings in the

range 0.35-0.46nm and a typical value of 0.42nm (L_c=0.7-3.5nm).

8.11.2- SCANNING ELECTRON MICROSCOPY (SEM)

Examination of both the PVA_2 and PVA_1 by SEM revealed areas with a smooth external surface displaying cracks and pitting (figure 4.17). As with the PVA(800) sample (figure 4.18), where the smooth exterior surface had been removed, the sample exhibited a flow-like lamellar surface. Indeed all three samples revealed a very similar structure.

8.11.3- POWDER X-RAY DIFFRACTION ANALYSIS (XRD)

Six peaks, within the interplanar spacings range (36.0-17.4^o) 0.290-0.592nm, were exhibited by the x-ray diffraction trace for the PVA_2 sample (figure 8.83). The peaks, in order of decreasing intensity, were centered on (25.8^o) 0.401nm, (27.4^o) 0.378nm, (29.4^o) 0.353nm, (24.0^o) 0.431nm, (31.2^o) 0.333nm and (36.8^o) 0.284nm.

The x-ray diffraction trace of the PVA_1 sample exhibited four peaks within an interplanar spacings range (36.0-16.0^o) 0.290-0.643nm (figure 8.84). The peaks, in order of decreasing intensity, were centered at (29.4^o) 0.353nm, (25.6^o) 0.404nm, (34.4^o) 0.303nm and (36.8^o) 0.284nm.

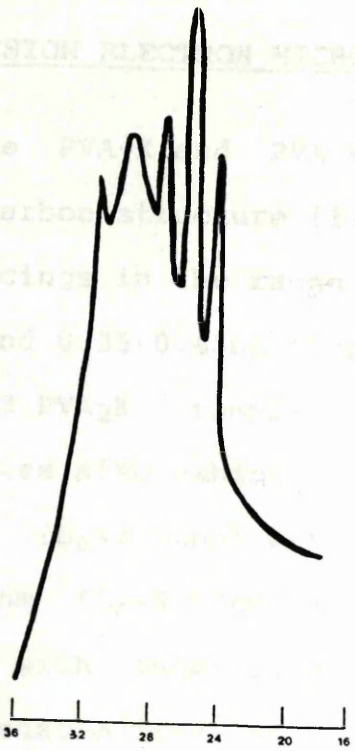

Figure 8.83: XRD trace of the PVA_2 sample.

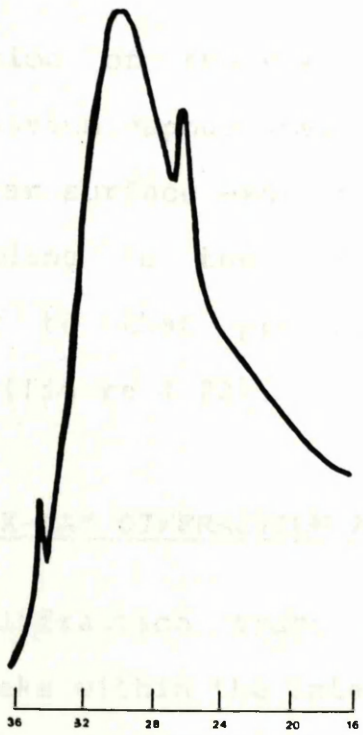

Figure 8.84: XRD trace of the PVA_1 sample.

8.12- EFFECT OF POTASSIUM ON CARBONISED POLYVINYL ACETATE

8.12.1- TRANSMISSION ELECTRON MICROSCOPY (TEM)

Analysis of the PVA_2K and PVA_1K samples revealed a non-graphitised carbon structure (figure 8.85) (L_a=1-6nm) with lattice spacings in the range 0.35-0.68nm (typical value of 0.54nm) and 0.35-0.48nm (typical value of 0.40nm) for the PVA_1K and PVA_2K samples respectively (L_c=0.7-4.5nm). The samples also exhibited areas of long-range ordered structure (L_a=8-52nm) with lattice spacings of between 0.33-0.35nm (L_c=4-17nm) and areas of convoluted structural order with interplanar spacings, L_a and L_c values indistinguishable from the values of the long-range ordered structure.

8.12.2- SCANNING ELECTRON MICROSCOPY (SEM)

SEM examination of the PVA_2 and PVA_1 samples after exposure to potassium vapour revealed a smooth, folded, flow-like lamellar surface exhibiting cracks, fractures, large holes leading to the interior and evidence of porosity similar to that previously exhibited by the PVA(800)K sample (figure 4.22).

8.12.3- POWDER X-RAY DIFFRACTION ANALYSIS (XRD)

The x-ray diffraction trace for the PVA_2K sample revealed seven peaks within the interplanar spacings range (36.0-15.4^o) 0.290-0.668nm (figure 8.86). The peaks, in order of decreasing intensity, were centered at (25.8^o)

Figure 8.85: HREM representative of the non-graphitising carbon structure exhibited by the PVA_1K and PVA_2K samples.

Figure 8.86: XRD trace of the PVA_2K sample.

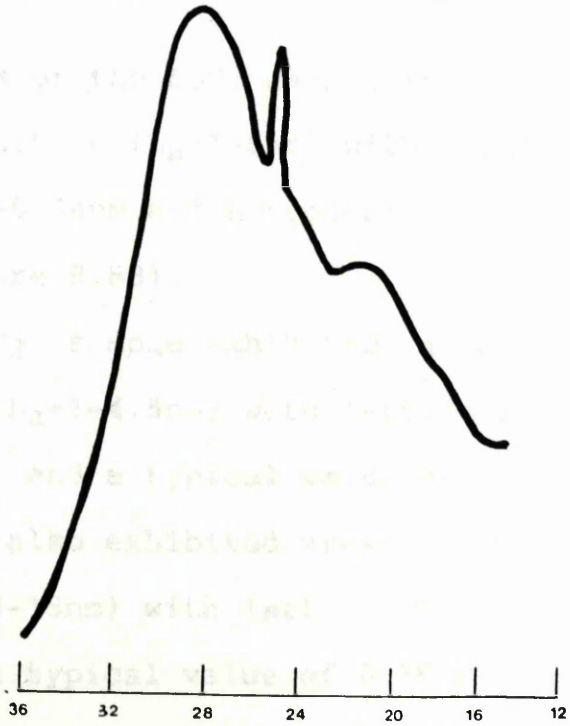

Figure 8.87: XRD trace of the PVA_1K sample.

0.400nm, (24.2°) 0.427nm, (27.4°) 0.377nm, (28.8°) 0.359nm, (31.2°) 0.333nm, 921.8°) 0.473nm and (36.8°) 0.284nm respectively.

The PVA_1K x-ray diffraction trace revealed four peaks within the interplanar spacings range (36.0-15.2°) 0.290-0.677nm (figure 8.87). The most intense peak was centered at (29.2°) 0.355nm, the remaining peaks, in order of decreasing intensity, were centered at (25.8°) 0.400nm, (22.0°) 0.469nm and (36.8°) 0.284nm respectively.

8.13- ANALYSIS OF CARBONISED SUCROSE

Graphitisation of sucrose at 3000°C is known to result in the formation of a non-graphitising carbon. In this study two carbonised samples were prepared and examined.

8.13.1- TRANSMISSION ELECTRON MICROSCOPY (TEM)

Analysis of the SUC_1 sample revealed a non-graphitised carbon structure (L_a=1-5nm) with lattice spacings in the range 0.36-0.54nm and a typical value of 0.47nm (L_c=0.36-3.5nm) (figure 8.88).

The SUC_2 sample exhibited a non-graphitised carbon structure (L_a=1-4.5nm) with lattice spacings in the range 0.38-0.54nm and a typical value of 0.47nm (L_c=0.38-2nm). The sample also exhibited areas of convoluted structural order (L_a=4-18nm) with lattice spacings of between 0.33-0.39nm and a typical value of 0.36nm (L_c=2-11nm).

Analysis of the SUC_{E1} sample revealed a non-graphitised carbon structure (L_a=1-3nm) with lattice spacings in the

Figure 8.88: HREM of the short-range ordered structure exhibited by the SUC_1 sample (0.36-0.54nm).

range 0.38-0.54nm and a typical value of 0.48nm (L_c=0.76-4nm). The sample also exhibited areas of long-range ordered structure (L_a=2-11nm) with lattice spacings of between 0.33-0.38nm and a typical value of 0.35nm (L_c=2-6.5nm) (figure 8.89).

8.13.2- SCANNING ELECTRON MICROSCOPY (SEM)

Examination of the SUC_1, SUC_2 and SUC_{E1} samples by SEM, revealed a very smooth external surface with no detectable surface cracks or porosity, similar to the structure exhibited by the SUC(800) sample (figure 4.9).

8.13.3- POWDER X-RAY DIFFRACTION ANALYSIS (XRD)

The SUC_1 sample revealed an x-ray diffraction trace with one broad peak (figure 8.90) centered on (21.8°) 0.473nm within an interplanar spacings range of (40.0-16.0°) 0.262-0.643nm.

One broad peak, within the interplanar spacings range (38.0-15.6°) 0.275-0.660nm and centered at (21.2°) 0.487nm (figure 8.91), was exhibited by the x-ray diffraction trace of the SUC_2 sample.

The x-ray diffraction trace for the SUC_{E1} sample exhibited two peaks within the interplanar spacings range (36.0-14.0°) 0.290-0.734nm. The most intense peak was centered at (21.5°) 0.480nm with the sharper, less intense peak centered at (31.3°) 0.312nm (figure 8.92).

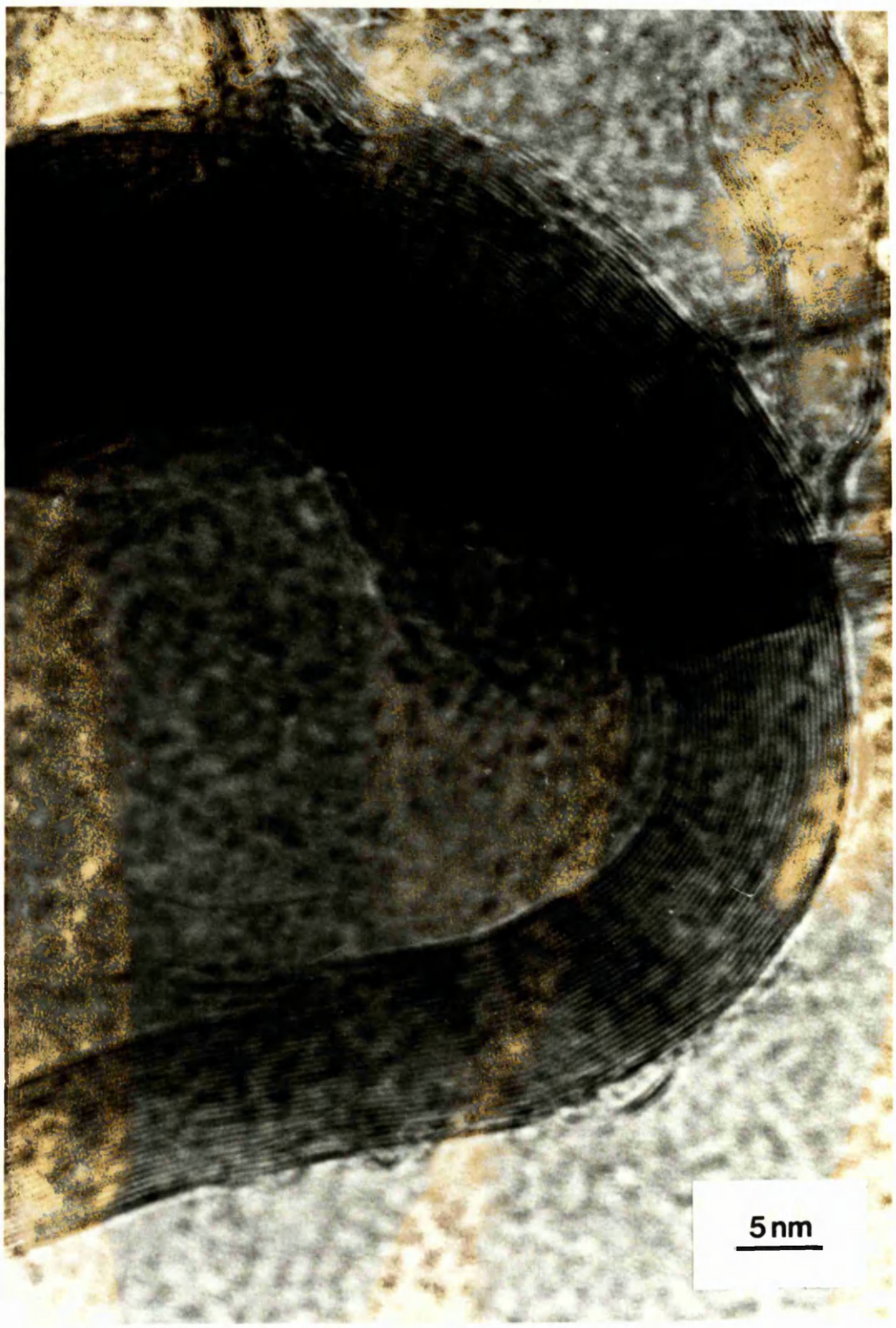

Figure 8.89: HREM of the long-range structural order exhibited by the SUC_{E1} sample (0.33-0.38nm).

Figure 8.90: XRD trace of the SUC_1 sample.

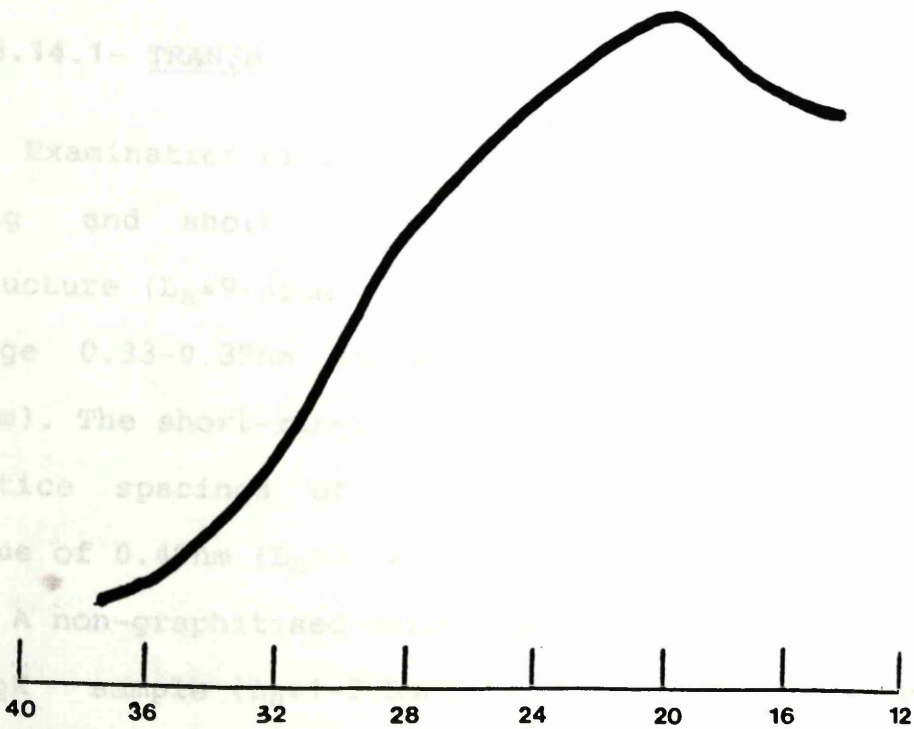

Figure 8.91: XRD trace of the SUC_2 sample.

Figure 8.92: XRD trace of the SUC_{E1} sample.

8.14- EFFECT OF POTASSIUM ON CARBONISED SUCROSE

8.14.1- TRANSMISSION ELECTRON MICROSCOPY (TEM)

Examination of the SUC_1K sample revealed areas of both long and short-range order. The long-range ordered structure (L_a=9-35nm) exhibited interplanar spacings in the range 0.33-0.39nm and a typical value of 0.36nm (L_c=3-10nm). The short-range ordered structure (L_a=1-3nm) showed lattice spacings of between 0.36-0.74nm and a typical value of 0.49nm (L_c=0.72-3.6nm).

A non-graphitised carbon structure was exhibited by the SUC_2K sample (L_a=1-3.5nm) with interplanar spacings in the range 0.38-0.53nm and a typical value of 0.47nm

(L_c=0.76-2.8nm).

Analysis of the $SUC_{E1}K$ sample revealed a non-graphitised carbon structure (L_a=1-4nm) exhibiting lattice spacings of between 0.37-0.71nm and a typical value of 0.48nm (L_c=0.37-3.4nm). The sample also revealed areas of convoluted structural order and areas exhibiting a long-range ordered structure (L_a=6-20nm) with lattice spacings of between 0.33-0.39nm and a typical value of 0.36nm (L_c=3-7nm).

8.14.2- SCANNING ELECTRON MICROSCOPY (SEM)

After exposure to potassium vapour the SUC_1, SUC_2 and SUC_{E1} samples continued to exhibit a structure similar to that of the original smooth external outer surface.

8.14.3- POWDER X-RAY DIFFRACTION ANALYSIS (XRD)

The SUC_1K sample exhibited seven peaks within the interplanar spacings range (36.0-12.0^o) 0.290-0.856nm. The most intense peak of the x-ray diffraction trace was centered at (21.9^o) 0.471nm (figure 8.93). The remaining peaks, in order of decreasing intensity, were centered at (20.0^o) 0.515nm, (25.8^o) 0.399nm, (28.4^o) 0.365nm, (14.1^o) 0.729nm, (31.2^o) 0.333nm and (34.2^o) 0.304nm.

Figure 8.94, the SUC_2K x-ray diffraction trace, revealed two broad peaks within the interplanar spacings range (38.6-15.8^o) 0.271-0.651nm. The peaks in order of decreasing intensity were centered at (22.0^o) 0.469nm and (26.4^o) 0.392nm.

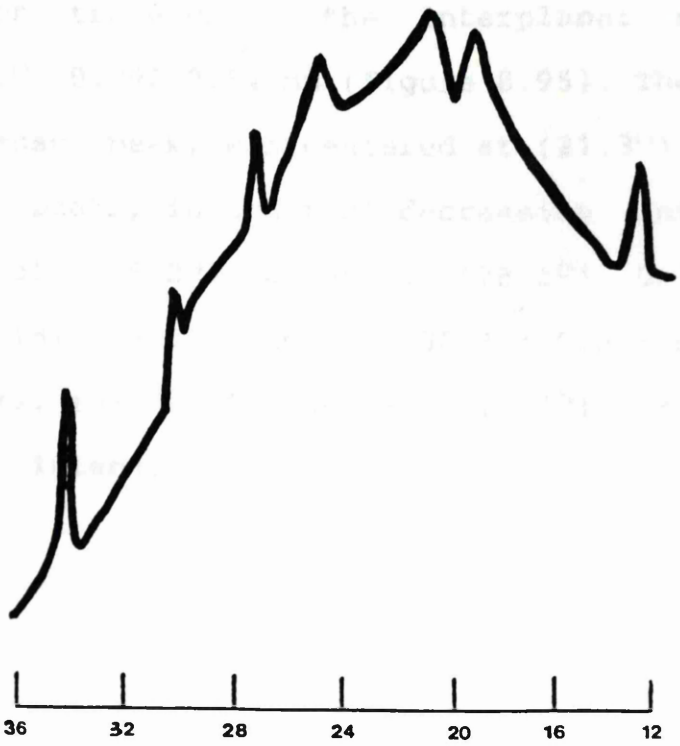

Figure 8.93: XRD trace of the SUC_1K sample.

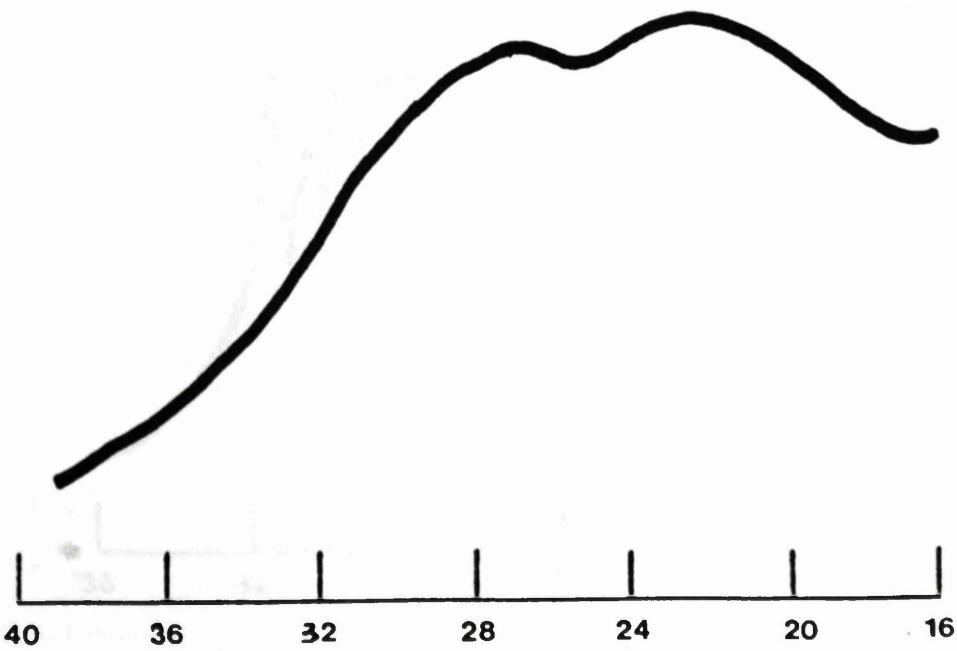

Figure 8.94: XRD trace of the SUC_2K sample.

Six peaks were exhibited by the $SUC_{E1}K$ x-ray diffraction trace within the interplanar spacings range (36.0-16.0°) 0.290-0.643nm (figure 8.95). The broadest and most intense peak, was centered at (21.3°) 0.484nm. The remaining peaks, in order of decreasing intensity, were centered at (26.2°) 0.395nm, (28.3°) 0.366nm, (29.4°) 0.353nm, (31.3°) 0.332nm and (30.3°) 0.343nm, with two of these peaks, (31.3°) 0.332nm and (29.4°) 0.353nm exhibiting a similar intensity.

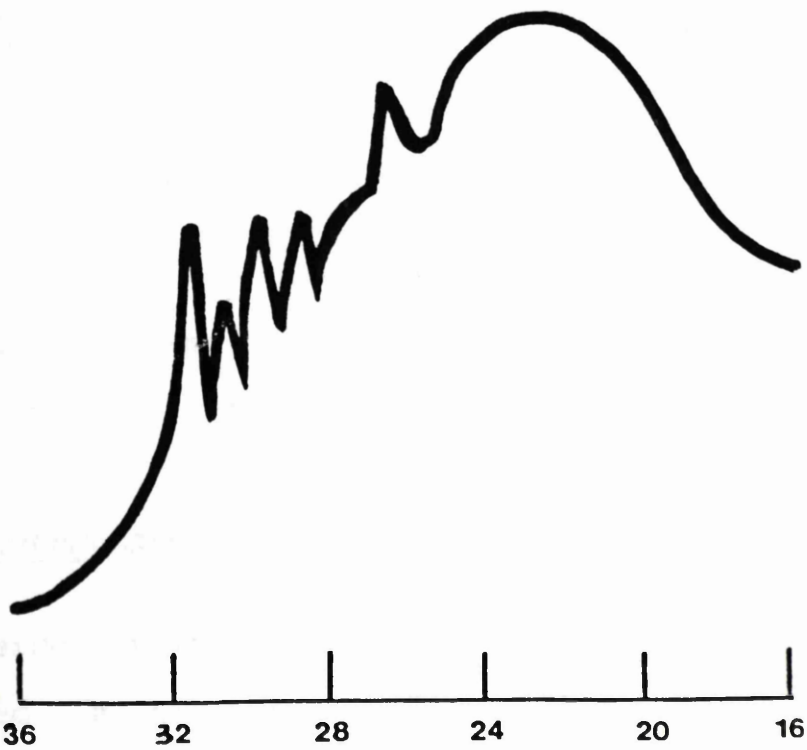

Figure 8.95: XRD trace of the $SUC_{E1}K$ sample.

8.14.4- FLAME PHOTOMETRY MEASUREMENTS

Due to operational problems, the PVA and sucrose samples, prepared via an open carbonisation system at Glasgow, were not examined using the potassium uptake measurement technique. A flame photometry study was carried out to establish their susceptibility to alkali attack.

SAMPLE	K CONC. (mg) per 100mg of sample
PVA_2	13.304
PVA_1	4.875
SUC_1	7.500
SUC_2	10.525
SUC_{E1}	18.710

Table 8.14 Flame photometry potassium concentrations for the carbonised PVA and sucrose samples.

8.15- SUMMARY OF PVA AND SUCROSE RESULTS

The TEM and XRD results obtained for the carbonised PVA and sucrose samples, both before and after exposure to potassium vapour are shown in table 8.15.

8.16- THERMOGRAVIMETRIC ANALYSIS (TGA)

Thermogravimetric analysis of the carbonised samples revealed a similar trend to that observed for the carbonised samples in chapters 4 and 6. The onset of weight loss was altered after exposure to potassium vapour, the presence of the potassium, reducing the temperature at which combustion commences.

SAMPLE	MICROSTRUCTURE	L_a(nm)	L_c(nm)	d(nm)	XRD(nm)
PVA_2	S.R.O	1-5	0.7-3.5	0.40	0.401
				(0.35-0.48)	0.378
	L.R.O	9-63	3-14	0.33-0.35	0.353
					0.431
					0.333
PVA_1	S.R.O	1-5	0.7-3.5	0.42	0.353
				(0.35-0.46)	0.404
	L.R.O	9-63	3-14	0.33-0.35	0.303
PVA_2K	S.R.O	1-6	0.7-4.5	0.40	0.400
				(0.35-0.48)	0.427
	L.R.O	8-52	4-17	0.33-0.35	0.377
	& ribbon				0.359
					0.333
					0.473
PVA_1K	S.R.O	1-6	0.7-4.5	0.54	0.355
				(0.35-0.68)	0.400
	L.R.O	8-52	4-17	0.33-0.35	0.469
SUC_1	S.R.O	1-5	0.36-3.5	0.47	0.473
				(0.36-0.54)	
SUC_2	S.R.O	1-4.5	0.38-2	0.47	0.487
				(0.38-0.54)	
	ribbon	4-18	2-11	0.36	
				(0.33-0.39)	
SUC_{E1}	S.R.O	1-3	0.76-4	0.48	0.480
				(0.38-0.54)	0.312
	L.R.O	2-11	2-6.5	0.35	
				(0.33-0.38)	
SUC_1K	S.R.O	1-3	0.72-3.6	0.49	0.471
				(0.36-0.74)	0.515
	L.R.O	9-35	3-10	0.36	0.399
				(0.33-0.39)	0.365
					0.729
					0.333
					0.304
SUC_2K	S.R.O	1-3.5	0.76-2.8	0.47	0.469
				(0.38-0.53)	0.392
$SUC_{E1}K$	S.R.O	1-4	0.37-3.4	0.48	0.484
				(0.37-0.71)	0.395
	L.R.O	6-20	3-7	0.36	0.366
	& ribbon			(0.33-0.39)	0.353
					0.332
					0.343

S.R.O - short-range order L.R.O - long-range order

Table 8.15 Summary of TEM and XRD results for the carbonised PVA and sucrose samples.

8.17- EFFECT OF INERT CARRIER GASES

A selection of the carbonised samples were prepared and exposed to potassium vapour using different inert carrier gases, argon and nitrogen. Examination of each sample, by HREM and XRD, both before and after exposure to potassium vapour, did not reveal any salient microstructural differences when an alternative carrier gas was used, indeed examination of the samples revealed no obvious structural carrier gas dependence.

CHAPTER NINE

DISCUSSION OF THE RESULTS FOR THE SAMPLES PREPARED VIA AN OPEN CARBONISATION SYSTEM

9.1- INTRODUCTION

Analysis of the results presented for the samples prepared via an open carbonisation system will be discussed individually with a comparison of any overall group relevance.

9.2- CARBONISED ACENAPHTHYLENE SAMPLES

Microstructural analysis of each of the carbonised acenaphthylene samples (graphitising carbon at 3000°C), before exposure to potassium vapour, revealed a non-graphitised carbon structure and areas of long-range ordered structure, with two of the samples also displaying convoluted structural order. The exhibited non-graphitised carbon structure revealed lattice spacings that encompassed a wide range of values. After exposure to potassium vapour some of the samples displayed a non-graphitised carbon structure with an increased lattice spacings range and were thus considered to be displaying an expanded carbon structure, regarded as developing as a result of intercalation or a residue compound. The samples also revealed areas of carbonised structure that had experienced changes, which resulted in the increased development of long-range and convoluted structural order.

The x-ray diffraction traces for the carbonised acenaphthylene samples from both the exposed and unexposed samples confirmed the structural modifications observed by HREM and revealed peaks with interplanar spacings consistent with the non-graphitised carbon structure and

the convoluted and long-range structural order detected by HREM. Generally, after exposure to potassium vapour the traces revealed sharper more intense peaks for the carbon-carbon interplanar spacings than was evident from the corresponding sample prior to exposure with potassium vapour, indicating a more ordered arrangement of the carbon layer planes. A wide range of lattice spacings were evident both before and after exposure to potassium vapour, in the latter not only did peaks become more prominent and evident, in the regions corresponding to the observed newly developed structural order, but some traces exhibited the peaks in a smaller range of 2θ values, also indicative of a more ordered particle size.

SEM examination of each of the acenaphthylene samples revealed remarkably little variance in macrostructure between all of the unexposed samples, each revealing a smooth external surface displaying cracks, the only apparent difference being the type of lamellar layer structure that each sample exhibited. The samples, after exposure to potassium vapour, revealed a macrostructure where the smooth external surface now exhibited large holes and an increased cracking across the samples surface. Some of the samples also exhibited an apparent conversion from the smooth, folded, flow-like lamellar internal structure to a sheet-like lamellar structure.

9.3- CARBONISED DECACYLENE SAMPLES

The carbonised decacylene sample, $deca_{12}$, was

accidentally destroyed during this research and was not able to be fully studied by all the examination techniques, thus, only a limited amount of information is available for this particular sample.

The XRD traces of the carbonised decacylene samples revealed a wide range of carbon lattice spacings that would be accounted for by the non-graphitised carbon structure, the long range ordered structue and the convoluted structural order observed by HREM. In some cases the non-graphitised carbon structure and the convoluted and long-range structural order detected by HREM, were absent from the XRD trace as individual peaks, it must therefore be concluded that the signals from these regions were not sufficiently intense to result in individual peak definition and that they were encompassed within the XRD interplanar spacings range for the sample.

After exposure to potassium vapour the carbonised decacylene samples, generally, revealed sharper, more intense peaks for the carbon-carbon interplanar spacings than was evident from the corresponding unexposed samples, indicating a more ordered arrangement of the carbon layer planes. Not only did peaks become more prominent and evident, in the regions corresponding to the observed newly developed structural order, but some traces exhibited the peaks in a smaller range of 2θ values, also indicative of a more ordered particle size.

Microstructural analysis of each of the unexposed carbonised decacylene samples (graphitising carbon at 3000°C), revealed a non-graphitised carbon structure and

areas of long-range and convoluted structural order. The areas of long-range ordered structure and the regions displaying the convoluted structural order exhibited interplanar spacings that were indistinguishable, with the non-graphitised carbon structure revealing lattice spacings that encompassed a wide range of values. After exposure to potassium vapour some of the samples displayed a non-graphitised carbon structure with an increased lattice spacings range and were thus considered to be displaying an expanded carbon structure, regarded as developing as a result of intercalation or a residue compound, other samples displayed a non-graphitised carbon structure exhibiting a reduced interplanar spacings range, these resultant structural changes, as previously reported in chapters five and seven, arising probably as a consequence of potassium penetration into the carbonised microstructure and the subsequent collapse of these expanded lattice planes to a more ordered structure. The samples also revealed areas of carbonised structure that had experienced changes, which resulted in the increased development of long-range and convoluted structural order.

As observed during the SEM study of the acenaphthylene samples, SEM examination of each of the decacylene samples revealed remarkably little variance in macrostructure between all of the unexposed samples, each revealing a smooth external surface displaying cracks, the only apparent difference being the type of lamellar layer structure that each sample exhibited. After exposure to potassium vapour, the carbonised samples revealed a

macrostructure where three external surfaces were now visible. Some samples continued to reveal a smooth, cracked, external surface, others exhibited a smooth external surface now displaying large holes and an increased cracking across the samples surface while others revealed a rough nodular surface with holes, cracks and pitting. Some of the samples also exhibited an apparent conversion from the smooth, folded, flow-like lamellar internal structure to a sheet-like lamellar structure. From this observation, a development of three macrostructures after potassium vapour exposure, the carbonised decacylene samples could possibly be more susceptible to alterations of the samples structure on exposure to potassium vapour than the carbonised acenaphthylene samples even thought they generally 'take-up' more potassium.

9.4- CARBONISED DIBENZANTHRONE SAMPLES

Examination of each of the unexposed carbonised dibenzanthrone samples (graphitising carbon at 3000°C), by HREM, revealed a non-graphitised carbon structure revealing interplanar spacings that encompassed a wide range of values. Areas of long-range and convoluted structural order were also detected with both exhibiting interplanar spacings that were indistinguishable. After exposure to potassium vapour some of the samples displayed a non-graphitised carbon structure with an increased lattice spacings range and were thus considered to be displaying an expanded carbon structure, regarded as developing as a

result of intercalation or a residue compound, other samples displayed a non-graphitised carbon structure exhibiting a reduced interplanar spacings range, these resultant structural changes, as previously reported in chapters five and seven, arising probably as a consequence of potassium penetration into the carbonised microstructure and the subsequent collapse of these expanded lattice planes to a more ordered structure. The samples also revealed areas of carbonised structure that had experienced changes, which resulted in the increased development of long-range and convoluted structural order.

SEM examination of each of the exposed and unexposed carbonised dibenzanthrone samples revealed that all the samples exhibited one of two external structures; a ramifying chambered structure or a rough surface exhibiting large holes leading to the interior, with some of the samples, after exposure to potassium vapour exhibiting an apparent conversion from the ramifying chambered structure to the large holes leading to the interior structure.

The x-ray diffraction traces for the carbonised dibenzanthrone samples from both the exposed and unexposed samples confirmed the structural modifications observed by HREM and revealed peaks with interplanar spacings consistent with the non-graphitised carbon structure and the convoluted and long-range structural order detected by HREM. Generally, after exposure to potassium vapour the traces revealed sharper more intense peaks for the carbon-carbon interplanar spacings than was evident from the corresponding sample prior to exposure with potassium

vapour, indicating a more ordered arrangement of the carbon layer planes. A wide range of lattice spacings were evident both before and after exposure to potassium vapour, in the latter however, not only did peaks become more prominent and evident, in the regions corresponding to the observed newly developed structural order, but some traces exhibited the peaks in a smaller range of 2θ values, also indicative of a more ordered particle size.

9.5- CARBONISED POLYVINYL ACETATE SAMPLES

Examination of the PVA_1 sample by XRD revealed a trace exhibiting three overlapping peaks. The interplanar spacings centered around, two of the peaks, 0.353nm and 0.404nm, would be accounted for by both the non-graphitised carbon structure 0.42nm (0.35-0.46nm) and the long-range ordered structure 0.33-0.35nm observed by HREM. The PVA_2 sample revealed a trace exhibiting five overlapping peaks, the interplanar spacings centered around all of the peaks, consistent with the non-graphitised carbon structure 0.40nm (0.35-0.48nm) and the long-range ordered structure 0.33-0.35nm detected by HREM.

Microstructural analysis of the PVA_1K and PVA_2K samples revealed that on exposure to potassium vapour areas of the carbonised structure experienced changes that resulted in the formation of a convoluted structure, previously undetected by HREM, and an expanded non-graphitised carbon structure for the PVA_2 sample, regarded as developing as a result of intercalation or a residue compound. XRD analysis

of the PVA_1K and PVA_2K samples were consistent with the non-graphitised, convoluted and long-range structural order revealed by HREM.

SEM examination of both the PVA_1 and the PVA_2 samples revealed remarkably little variance in macrostructure with both exhibiting a smooth external surface exhibiting cracks, some pitting and smooth folded flow-like lamellar layers where the smooth external surface had been removed. Both samples, after exposure to potassium vapour, continued to reveal a comparable macrostructure revealing where the smooth external structure had been removed a folded lamellar structure. Indeed the PVA_1, PVA_2 and the PVA(800) sample, examined in chapter four and five, both before and after exposure to potassium vapour, revealed a very similar macrostructure.

9.6- CARBONISED SUCROSE SAMPLES

Before exposure to potassium vapour, the SUC_1 and SUC_2 XRD traces revealed a single peak, exhibiting a wide range of carbon lattice spacings. The interplanar spacings, centered on 0.473nm and 0.487nm respectively, were consistent with the non-graphitised carbon structure observed for both samples by HREM. The convoluted structural order, detected by HREM, was absent from the SUC_2 XRD trace and it must therefore be concluded that the signals from these regions are not sufficiently intense to result in individual peak definition and that they are encompassed within the XRD interplanar spacings range for

the sample. HREM analysis of the SUC_{E1} sample revealed a carbonised matrix exhibiting a wide range of carbon lattice spacings arising as a result of the non-graphitised carbon structure and the long-range ordered structure, XRD analysis of the sample, exhibiting a trace consistent with the structures observed by HREM.

After exposure to potassium vapour, XRD analysis of all three samples: SUC_1K, SUC_2K and $SUC_{E1}K$, generally revealed sharper peaks for the carbon-carbon interplanar spacings than was evident from the corresponding unexposed samples, indicating a more ordered arrangement of the carbon layer planes and confirming the structural ordering observed by HREM. Microstructural analysis of the samples revealed that on exposure to potassium vapour areas of the carbonised structure experienced changes that resulted in the formation of a long-range ordered structure, previously undetected by HREM for the SUC_1K, an expanded non-graphitised carbon structure, displayed by both the SUC_1K and the $SUC_{E1}K$ samples, with the $SUC_{E1}K$ sample also exhibiting regions of convoluted structural order.

Both before and after exposure to potassium vapour, SEM examination of the macrostructure of the three carbonised sucrose samples, all revealed a very similar structure; a smooth external surface with no detectable surface cracks or porosity, comparable to the structure exhibited by the SUC(800) sample.

9.7- FLAME PHOTOMETRY MEASUREMENTS

Flame photometry measurements were undertaken to determine which, if any, of the carbonised samples prepared via an open carbonisation system, was more susceptible to alkali attack. Initially, comparisons were made between individual carbonised material, prepared at different temperatures and heating rates before any overall group relevance was established.

The acenaphthylene and decacylene samples, prepared by British Coal, revealed an opposite trend to the samples in chapter seven, with the carbonised samples prepared at a heating rate of 3°C/min exhibiting a lower potassium concentration, to varying degrees, than the corresponding 20°C/min preparation. Indeed, the equivalent 3°C/min acenaphthylene sample prepared at Glasgow University differed from the corresponding British Coal sample and exhibited a 50% higher potassium concentration with no apparent effect on the macrostructure of the sample. The lower potassium concentration, detected for the British Coal sample altered the appearance of the prepared sample causing a movement away from the original sheet-like lamellar layers visible in the unexposed sample to a smooth folded flow-like lamellar structure in the exposed sample. Further examination of the samples within each individual sample grouping, including the dibenzanthrone, PVA and sucrose samples, showed the flame photometry results to be largely inconclusive. This apparent lack of evidence or even, a general trend within this group of samples is

difficult to explain and it can only be surmised that it is due to or influenced by the sensitivity of the parent aromatic hydrocarbons to the preparation of the carbonised samples. For this reason it would be of benefit for British Coal to prepare and provide the same carbonised samples as was studied in chapter eight of this study, with Glasgow supplying the materials so that any differences arising were not due to the source of the materials, to determine if the samples prepared agreed with the already observed results. These samples, unfortunately, were not able to be supplied, and could not form part of this study.

9.8- EFFECTS OF INERT CARRIER GASES

In order to determine if the type of inert carrier gas used, altered or had any significant effect on the microstructure of the prepared carbonised materials and their subsequent exposure to potassium vapour, various inert carrier gases were used when preparing and exposing the carbonised materials to potassium vapour.

Examination of both the prepared and potassium exposed samples, by HREM and XRD, revealed no significant differences in any of the microstructural forms and appeared to be independent of the carrier gas used. As reported in chapter five, the effects of the non-reacting gases on coke properties can be profound, but this is thought to be more significant in the macrostructural properties of the material.

9.9- THERMOGRAVIMETRIC ANALYSIS (TGA)

Thermogravimetric analysis of the carbonised samples both before and after exposure to potassium vapour revealed the same trend as already observed in chapters five and seven. The onset of weight loss was altered after exposure to potassium vapour, the presence of the potassium causing the commencement of combustion to occur at a lower temperature, implying that the existence of the potassium is having a catalytic effect on the weight loss reaction.

9.10- CONCLUSIONS

The variety and diversity of each carbonised material was established with the occurence of differing carbon structures, even before exposure to potassium vapour. Thus, each sample was prepared and analysed several times in order to obtain reproducible results and establish a characteristic representation of the samples due to the heterogeneity of the material.

Overall the XRD traces from the carbonised samples both before and after exposure to potassium vapour were consistent with the HREM observations and indicated that exposure to potassium vapour resulted in a structure that was more ordered than that exhibited by the unexposed samples. The resultant structural changes, as previously reported in chapters five and seven, are probably a consequence of potassium penetration into the carbonised microstructure and the subsequent collapse of these expanded lattice planes to a more ordered structure.

In this section of the research all the samples studied, except one, would exhibit a graphitising carbon matrix at a temperature of 3000°C. Thus, it was difficult to ascertain which carbonised material group, graphitising or non-graphitising, if any, showed an increased susceptibility to potassium vapour. From the HREM, XRD and SEM investigations, the graphitisable and non-graphitisable carbonised materials all show some evidence of susceptibility to potassium vapour. The presence of potassium, influencing their structural development, by creating areas of long-range and convoluted structural ordering within the carbon matrix, changing their lattice spacing values and altering their macrostructures.

In general, according to the microstructural examination, the carbonised material arising from the graphitising carbons appears more susceptible to potassium than the corresponding non-graphitising sample. This contrasts with the observations from the study in chapters four and five where the non-graphitising carbon was considered to be the more susceptible but agrees with the observations from the study in chapters six and seven. Indeed, the decacylene carbonised materials appeared to exhibit a greater susceptibility to potassium vapour, than the other carbonised samples prepared from graphitisable carbons. The observed structural ordering occurred mainly in the L_a direction with a smaller increase in the measured L_c direction. The carbonised decacylene samples however, exhibited an increased expansion of the layer planes in both the L_a and L_c directions to a greater extent than was

observed for the other carbonised materials prepared via an open carbonisation system.

The flame photometry measurements undertaken to determine which, if any, of the carbonised samples, prepared via an open carbonisation sytem, was more susceptible to potassium were regarded as inconclusive for this study.

CHAPTER TEN

CONCLUSIONS

10.1- CONCLUSIONS

The overall aim of this study was to characterise any microstructural changes occurring to a selection of carbonised aromatic hydrocarbons after exposure to potassium vapour. The samples, known to give rise to graphitising and non-graphitising carbons at 3000°C, were first examined to determine their microstructure in order that any deviations from the original structure after exposure to potassium vapour could be determined. An examination of the relative uptake of potassium in each of the carbonised materials could determine which, if any, of the carbonised materials could be added to the blast furnace coke to preferentially absorb or be attacked by the potassium, with the purpose of reducing or eliminating the detrimental changes that occur in the structure of the blast furnace cokes due to recirculating alkali.

The present study has shown that structural changes are induced, by the presence of potassium vapour, in the structure of the carbonised samples. A comparison of the exposed and unexposed samples has revealed the formation of an expanded carbon matrix, due to the presence of a residue compound, and an ordering of the carbon structure to occur.

Franklin (1951), through her studies on graphitising and non-graphitising carbons, has shown that the two types of carbons have basically different structures and that the differences in structure are apparent from the earliest stages of carbonisation. The most striking difference appears in a comparison of the apparent stack height (L_c)

and the apparent layer size (L_a). For equal apparent layer sizes the apparent stack height is greater for a graphitising than a non-graphitising carbon; the layer stacking is more perfect in graphitising carbons than in non-graphitising carbons with a comparable layer structure. Non-graphitising carbons, on heating, develop a strong system of cross-linking, which immobilises the structure and unites the existing crystallites into a rigid mass that is randomly orientated and thus restricts the movement of single and groups of layers into the graphitic order.

XRD analysis of the carbonised samples, both before and after exposure to potassium vapour, were consistent with the HREM observations and indicated that exposure to potassium vapour resulted in a structure that was more ordered than that exhibited by the unexposed sample, with both the graphitising and non-graphitising carbonised materials showing evidence of susceptibility to potassium vapour. The presence of the potassium influencing their structural development by creating areas of long-range and convoluted structural ordering within the carbon matrix, changing their lattice spacing values and altering their macrostructure. For the majority of the carbonised samples, the observed structural ordering appeared mainly in the L_a direction with a smaller increase in the measured L_c direction. The carbonised decacylene samples (graphitising carbon) however, exhibited an increased expansion of the layer planes in both the L_a and L_c directions, to a greater extent than was observed for the other carbonised samples.

In order to determine the effects of alkali attack from

thermal effects, carbonised samples, that had previously only been heated to a temperature of 800°C, were heated in the absence of alkali to a temperature of 1100°C, a reduction of the turbostatic nature of carbon materials, by heat treatment, having been reported by several authors (Fishbach, 1971; Pacault, 1971; Robert et al., 1973; Oberlin, 1984). Analysis of a number of the carbonised materials heated to 1100°C revealed that structural ordering developed. However, the observed structural ordering was not as apparent as that produced in the corresponding potassium exposed samples. Obviously, an expanded carbon structure due to the presence of a potassium intercalated or residue compound would not be detected but some of the carbonised samples revealed such a wide range of carbon interplanar spacing values before exposure to potassium vapour, that large interplanar spacing values were still detected at the 'thermal effect' temperature. The temperature difference between the carbonisation temperature and the 'thermal effect' temperature was thus considered to be insufficent to reveal significant structural changes as a function of temperature alone.

A selection of the carbonised samples were also exposed to potassium vapour at below their original carbonisation temperatures, thus any structural changes observed would be due only to the chemical effects of the potassium vapour as the samples had previously been exposed to higher temperatures during carbonisation. These samples, did exhibit structural ordering, more so than the

corresponding thermal reaction, however, difficulties did arise due to the complexity of trying to quantify the levels of structural order and disorder observed for the carbonised materials.

Early studies (Platzer, 1960) concluded that potassium did not intercalate in non-graphitisable carbons which contain many cross-linkages, it was merely absorbed on the surface. This study also reported that graphitisable carbons formed intercalation compounds more readily, due to the ordered structure exhibited by these carbons. Subsequent studies (Berger et al., 1975) however, found potassium to intercalate in both graphitisable and non-graphitisable carbons, with the graphitisable carbons forming an intercalate more readily than the non-graphitisable carbons.

Bartlett and McQuillan (1982) reported that for reducing intercalants such as the alkai metals, interlayer cross-linking aids intercalation, due to a lowering of the fermi level and overcomes the mechanical stresses which are opposed to layer separation. This does not imply that it should necessarily intercalate more readily into non-graphitisable carbons, the ease of intercalation being determined by the accessibility of the basal planes to the intercalate and the ionisation potential of the intercalant as compared to the electron affinity of the carbon. Further studies on intercalation reported (Crespin et al., 1977) that intercalation/deintercalation cycles order the carbon structure by lowering the number of defects in the original material, the structural ordering occurring as a

result of the imperfections being 'smoothed out'.

During this study, after exposure to potassium vapour, a number of the carbonised materials, arising from both the graphitising and non-graphitising carbons, displayed expanded carbon structures that were detected by HREM. XRD analysis of the samples also indicated the presence of this expansion of the carbon lattices. However, no characteristic staging was observed by XRD and the expanded carbon structures were thus thought to be indicative of a residue compound rather than an intercalated material. Intercalated compounds are unstable and degrade when exposed to the atmosphere. In the present study such degradation could result on exposure of the sample to the atmosphere during the period of removal from the furnace to analysis by XRD or insertion into the microscope.

The fluid phase has been recognised as a primary requirement for obtaining well-ordered carbon residues. Only this fluid phase offers sufficient mobility of the reacting molecules during thermal decomposition to permit good preferred orientation. According to Brooks and Taylor (1968) in a temperature range between 400-500°C the mixture segregates into a mesophase and a fluid matrix. The mesophase consits of planar aromatic compounds and forms as spherical droplets exhibiting a considerable degree of molecular ordering. The molecular layers are arranged perpendicular to one diameter of the sphere but curved so that they are normal to the surface. Upon prolonged heating, the spheres coalesce and extended regions of uniform orientation may be formed. Brooks and Taylor (1968)

have shown that the formation of the well-ordered carbon residues during pyrolysis of well defined aromatic compounds proceeds by way of the mesophase. This inferior order can be explained by the smaller temperature range over which this material is in a fluid phase and demonstrates the effect of free mobility of the molecules upon pyrolysis and consequently upon the formation of a crystalline pre-order. The process can be thought of as proceeding by the initial formation of planar molecules and their subsequent parallel arrangement. These molecules then act as a nuclei for the preferential growth of the molecules having larger L_a values (>2.5nm) with the accumulation of such molecular structures initially detected as mesophase spherulites that accumulate and subsequently lead to the formation of a uniform mesophase. The rate of growth and coalescence of liquid crystals during a carbonisation are functions of the rate of heating, soaking time at the final HTT and the final HTT itself. All pyrolytic carbons consist of hexagonal structural units of carbon exhibiting various degrees of cross-linkage, with well-graphitisable carbons developing by the formation and accumulation of large planar aromatics in the fluid phase. Chemical cross-linking reaction and others increase the probability for the formation of poorly graphitising pyrolysis residues. The resulting graphitisability of the materials are also overshadowed by various sensitivities of the aromatics to fast heating and can be based not only on crystalline preorder, but also on stresses introduced into the carbon during pyrolysis prior

to graphitisation. Such stresses can lead to an extremely graphitic structure even in cases of carbons which are normally of low graphitisability. Thus for a better understanding of the structural order exhibited by the carbonised samples, it seemed necessary to carry out studies ensuring comparable physical conditions during pyrolysis. For this reason it would be of benefit for British Coal to prepare and provide the same carbonised samples as was studied in chapter eight of this study, with Glasgow supplying the materials so that any differences arising were not due to the source of the material, to determine if the samples prepared agreed with the already observed results. The results within this study exhibit differences which could be due to the physical conditions during pyrolysis. The carbonised PVA samples, examined in chapter eight and nine exhibited proportionally less long-range ordered structure than was exhibited by the PVA(800) sample studied in chapters four and five. The SUC(800) sample also exhibited differences, with the macrostructure of the sample revealing a profound alteration after exposure of the carbonised sample to potassium vapour.

The major pieces of information to arise from this study are:

1. All the carbonised materials examined developed, to some extent, layer structure ordering on heating. This development is heterogeneous, thus prior to graphitisation temperatures there are both ordered and disordered regions in the carbonised material.

2. Interlayer spacings evident prior to graphitisation, do not appear to be indicative of the final products graphitisability, although generally the graphitising carbons revealed a more extensive long-range ordered structure. The carbonisation conditions influence the extent of structural ordering observed.

3. In general, the presence of potassium reduced interlayer spacings (it was a graphitic promoter) or resulted in the formation of expanded interlayer spacings implying the formation of a intercalation or residue compound. These intercalated or residue compounds were considered to be intermediates between the disordered carbonised structure and the areas of enhanced localised ordering detected after exposure to potassium vapour. It also induced growth, in both graphitising and non-graphitising samples of the convoluted structure, particularly in areas which were not showing signs of incipient ordering.

REFERENCES

Abbe, E., Arch. Mikrosk. Anat. Entwicklungsmech., 9, 413 (1873).

Abraham, K.P. and Staffanson, L.I., Scand. J. Metallurgy, 4, 193 (1975).

Adair, R.R., Boult, E.H., Freeman, E.M., Jasienko, S. and Marsh, H., Carbon, 9, 763 (1971).

Agar, A.W., Br. J. Appl. Phys., 11, 185 (1960).

Agar, A.W., Techniques for Electron Microscopy (Kay, D.H., Ed.) 2nd Edn., Oxford: Blackwell p.1 (1965).

Ahmed, H., Electron Microsc. Anal. (Nixon, W.C., Ed.), London: Inst. Phys., Conf. Ser. No. 10, p.30 (1971).

Allpress, J.G., Hewat, F.A., Moodie, A.F. and Sanders, J.V., Acta. Crystallogr., A28, 528 (1972).

Amelinckx, S., Phil. Mag., 1, 269 (1956).

Amelinckx, S. and Delavignette, P., Nature, 185, 603 (1960(a)).

Amelinckx, S. and Delavignette, P., Proc. Eur. Conf. Elec. Micros., Delft, 1, 404 (1960(b)).

Amelinckx, S. and Delavignette, P., J. Appl. Phys., 31, 2126 (1960(c)).

Andrews, K.W., Dyson, D.J. and Keown, S.R., Interpretation of electron diffraction patterns (2nd Edn.), London: Hilger & Watt (1971).

Ardenne, M. von., Kolloid-z., 108, 195 (1944).

Armatorio, G.G., Kemner, W.F. and Hegedus, G.S., "Blast furnace operating problems with high alkali pellets", Presented at Chicago Regional Technical Meeting of AISI (1971).

Armaud, M. and Touzain, P., Mater. Sci. Eng., 31, 319 (1977).

Bacon, G.E., Acta. Crystallogr., 3, 137 (1950).

Bacon, G.E., Acta. Crystallogr., 4, 558 (1951).

Bacon, G.E., Acta. Crystallogr., 5, 392 (1952(a)).

Bacon, G.E., Acta. Crystallogr., 5, 492 (1952(b)).

Bacon, G.E., Acta. Crystallogr., 7, 359 (1954).

Bacon, G.E., AERE Report, M/R 2702, (1958).

Baker, C., Chou, Y.T. and Kelly, A., Phil. Mag., 6, 1305 (1961).

Baker, C., Gillin, L.M and Kelly, A., 2nd Int. Carbon and Graphite Conf., Society of Chemical Industry, London (1965).

Bartle, K.D., Collin, G., Stadelhofer, J.W. and Zander, M., J. Chem. Tech. Biotechnol., 29, 531 (1979).

Bartle, K.D. and Jones, D.W., Fuel, 48, 21 (1969).

Bartlett, N. and McQuillan, B.W., in Intercalation Chemistry (Whittingham, M.S. and Jacobson, A.J. Eds.), Academic Press: London pp. 19-54 (1982).

Batson, P.E., Chen, C.H. and Silcox, J., Proc. 34th Annu. Meet. Electron Microsc. Soc. Am. (Bailey, G.W., Ed.), Batson Rouge: Claitor, p.534 (1976).

Beeston, B.E.P., Practical Methods in Electron Microscopy: Electron diffraction and Optical Diffraction Techniques (Glauert, A.M., Ed.), Amsterdam: North Holland, Vol. 1, p.192 (1973).

Benedict, L.G. and Thompson, R.R., Int. J. of Coal Geology, 1, 19 (1980).

Beorchia, A. and Bonhomme, P., Optik, 39, 437 (1974).

Berger, D., Carton, B., Metrot, A. and Herold, A., Chemistry and Physics of Carbon (Walker, P.L. Jr, Ed), New York: Marcel Dekker, Vol.12, pp.1-37, (1975).

Bernal, J.D., Proc. Roy. Soc. (London), A106, 749 (1924).

Biscoe, J. and Warren, B.E., J. Appl. Phys., 13, 364 (1942).

Blayden, H.E., J. Chim. Phys. (Special Issue, Apr.), 15 (1969).

Blumer, G.P., Kleffner, H.W., Lucke, W. and Zander, M., Fuel, 59, 600 (1980).

Boehm, H.P. and Coughlin, R.W., Carbon, 2, 1 (1964).

Boehm, H.P. and Hoffman U., Z. Anorg. Allg. Chem., 278, 58 (1955).

Boersch, H. von., Annalen der Physik., (5), 27, 75 (1936).

Bollman, W., Phil Mag., 5, 621 (1960).

Bollman, W., Proc. 5th Carbon Conf., New York: Pergamon Press, Vol. 2, p.303 (1961).

Bollman, W., Proc. Eur. Reg. Conf. Electron Microscopy, Delft, p.330 (1961(a)).

Bollman, W., Proc. 1st Int. Conf. Properties of Reactor Materials, p.132 (1961(b)).

Borries, B. von and Ruska, E., Z. Wiss. Mikrosk. Tech., 56, 314 (1939).

Botham, J.C., Leeder, W.R. and Reeve, D.A., Symp. on Coal Evaluation, Calgary, Alberta (1974).

Boudouard, O., Bull. Soc. Chim. (Paris), 21, 465 and 712, (1899).

Boudouard, O., Bull. Soc. Chim. (Paris), 25, 227 and 833, (1901(a)).

Boudouard, O., Ann. Chim. Phys., 24, 1 (1901(b)).

Bouraoui, A. and Mering, J., Carbon, 1, 465 (1964).

Bovin, J-O., Wallenberg, L.R. and Smith, D.J., Electron Davisson, C. and Germer, L.H., Phys. Rev., 30, 705 (1927).

Brooks, J.D. and Taylor, G.H., Chemistry and Physics of Carbon (Walker, P.L. Jr, Ed.), New York: Marcel Dekker, Vol.4, p.243, (1968).

Crespin, M., Tchoubar, D., Gatineau, L., Beguin, F. and Setton, R., Carbon, 15, 303 (1977).

Debye, P. and Scherrer, P., Phys. Z., 18, 291 (1917).

Dickinson, E.M., Fuel, 59, 290 (1980).

Ebert, L.B., Annu. Rev. Mater. Sci., 6, 182 (1976).

Edington, J.W., Practical Electron Microscopy in Materials Science (1): The Operation and Calibration of the Electron Microscope, London: MacMillan (1974).

Edington, J.W., Practical Electron Microscopy in Materials Science (2): Electron Diffraction in the Electron Microscope, London: MacMillan (1975).

Edstrom, T. and Lewis, I.C., Carbon, 7, 85 (1969).

Edstrom, T. and Petro, B.A., J. Poly. Sci., Part C, 21, 171 (1968).

Eeles, W. T. and Wilson, A.J.C., Nature, 205, 66 (1965).

Eisenhandler, C.B. and Siegel B.M., J. Appl. Phys., 37 (2), 1613 (1966).

English, C.A. and Venables, J.A., Electron Microsc. Anal. (Nixon, W.C., Ed.), London: Inst. Phys., Conf. Ser. No. 10, p.40 (1971).

English, C.A. and Venables, J.A., Electron Microsc. Anal. (Nixon, W.C., Ed.), London: Inst. Phys., Conf. Ser. No. 14, p.172 (1972).

Ennos, A.E., Br. J. Appl. Phys., 4, 101 (1953).

Ergun, S., Carbon, 6, 141 (1968(a)).

Ergun, S., Chemistry and Physics of Carbon (Walker, P.L. Jr, Ed.), New York: Marcel Dekker, Vol. 3, p.211 (1968(b)).

Ergun, S. and Gifford, T.J., J. Appl. Crystallogr. 1, 313 (1968).

Ergun, S. and Gifford, T.J., J. Chim. Phys. (Special issue, Apr.), p.99 (1969).

Erickson, H.P., Advances in Optical and Electron Microscopy (Barer, R. and Cosslett, V.E., Eds.), London: Academic, Vol. 5, p.163 (1973).

Essen, C.G. van., Electron Microscopy and Microanalysis of Crystalline Materials (Belk, J.A., Ed.), London: Appl. Sci., p.99 (1979).

Evans, S. and Marsh, H., Carbon, 9, 733 and 747 (1971).

Everhart, T.E., J. Appl. Phys., 31 (2), 1483 (1960).

Everhart, T.E. and Hayes, T.L., Sci. Am., 226, 55 (1972).

Everhart, T.E., Wells, O.C. and Oatley, C.W., J. Electronics and Control, 7, 97 (1959).

Ewald, P.P., Sitzungsber Munch. Akad., 4, 7 (1914).

Fejes, P.L., Acta. Crystallogr., A33, 109 (1977).Qi15

Finch, G.I. and Wilman, H., Proc. Roy. Soc. (London), A155, 345 (1936).

Fischbach, D.B., Chemistry and Physics of Carbon (Walker, P.L. Jr., Ed.), New York: Marcel Dekker, Vol. 7 p.1 (1971).

Fisher, R.M., Szirmae, A. and Bain, E.C., Anal. Chem., 42, 362R (1970).

Fitzer, E., Mueller, K. and Schaefer, W., Chemistry and Physics of Carbon (Walker, P.L. Jr., Ed.), New York: Marcel Dekker, Vol. 7, p.237 (1971).

Fitzer, E. and Schlesinger, H., Carbon, 3, 247 (1965).

Frank, J., Optik, 38, 519 (1973).

Franke, F.H. and Meraikib, M., Carbon, 8, 423 (1970).

Franklin, R.E., Acta. Crystallogr., 3, 107 (1950).

Franklin, R.E., Acta. Crystallogr., 4, 253 (1951(a).

Franklin, R.E., Proc. Roy. Soc. (London), A209, 196 (1951(b)).

Fredenhagen, K. and Cadenbach, G., Z. Anorg. Chem., 158, 249 (1926).

Fredenhagen, K. and Suck, H., Z. Anorg. Chem., 178, 353 (1929).

Friedel, J., Dislocations, Oxford: Pergamon Press (1964).

Fryer, J.R., The Chemical Applications of Transmission Electron Microscopy, London: Academic (1979).

Fryer, J.R., Mol. Cryst. Liq. Cryst., 96, 275 (1983).

Fryer, J.R. and Holland, F., Proc. Roy. Soc. (London), A393, 353 (1984).

Fryer, J.R. and Smith, D.J., J. Microsc., 141, 3 (1986).

Geiss, R.H., Introduction to Analytical Electron Microscopy (Hren, J.J., Goldstein, J.I. and Joy, D.C., Eds.), New York: Plenum, p.43 (1979).

George, D.W.R. and Peart, J.A., Ironmaking Proc., 32, 40 (1973).

Gevers, R., Diffraction and Imaging Techniques in Material Science (Amelinckx, S., Gevers, R. and Landuyt, J. van., Eds.), Amsterdam: North Holland, Vol. 1, p.9 (1978).

Gilbert, J.B., Kipling, J.J., McEnaney, B. and Sherwood, J.N., Polymer, 3, 1 (1962).

Glaeser, R.M., Physical Aspects of Electron Microscopy and Microbeam Analysis (Siegel, B.M. and Beaman, D.R., Eds.), New York: Wiley, p.205 (1975).

Glauert, A.M., (Ed.), Practical Methods in Electron Microscopy, Amsterdam: North Holland (1972).

Goleczka, J. and Tucker, J., CEC Round Table Conf., Coke Oven Techniques, Brussels (1985).

Goleczka, J., Tucker, J. and Everitt, G., Paper to Coma at Durham (1982(a)).

Goleczka, J., Tucker, J. and Everitt, G., Paper to ECSC Round Table Conf., Luxembourg (1982(b)).

Goleczka, J., Tucker, J. and Everitt, G., Paper to ECSC Round Table Conf., Luxembourg (1983).

Goodman, P., Ed., Fifty Years of Electron Diffraction, Dordrecht: Reidel (1981).

Goodman, P. and Moodie, A.F., Acta. Crystallogr., A30, 280 (1974).

Grainger, L. and Gibson, J., Coal Utilisation: Technology, Economics and Policy, Great Britain: Graham and Trotman Ltd. (1981).

Grassie, N., Trans. Far. Soc., 48, 379 (1952).

Gray, R.J., Introduction to Carbon Science (Marsh, H., Ed.), London: Butterworth, p.285 (1989).

Grivet, P., Electron Optics (2nd Edn.), Oxford: Pergamon Press (1972).

Haering, R.R. and Mrozowski, S., Prog. Semicond., 5, 273 (1960).

Haine, M.E. and Cosslett, V.E., The Electron Microscope, London: Spon (1961).

Haine, M.E. and Einstein, P.A., Br. J. Appl. Phys., 3, 40 (1952).

Haine, M.E. and Mulvey, T., J. Sci. Instrum., 31, 326 (1954).

Hall, C.E., Introduction to Electron Microscopy (2nd Edn.), New York: McGraw-Hill (1966).

Hall, C.E. and Hines, R.L., Philos. Mag., 21, 1175 (1970).

Hanszen. K.J., Advances in Optical and Electron Microscopy (Barer, R. and Cosslett, V.E., Eds.), London: Academic, Vol. 4, p.1 (1971).

Hanszen, K.J. and Trepte, L., Optik, 32, 519 (1971).

Harada, Y. and Watanabe, E., JEOL News, 16E, 5 (1978).

Harker, H., Proc. 4th Carbon Conf., New York: Pergamon Press, p.125 (1960).

Hartman, R.S., Hartman, R.E., Alsberg, H. and Nathan, R., Proc. 8th Int. Congr. Electron Microsc. (Sanders, J.V. and Goodchild, D. J., Eds.), Canberra: Aust. Acad. Sci., Vol. 2, p.674 (1974).

Hassel, O. and Mark, H., Z. Physik., 25, 317 (1924).

Hatano, M., Miyazaki, T. and Iwanaga, Y., Trans. ISIJ, 20, 592 and 744 (1980).

Hatano, M, Miyazaki, T. and Iwanaga, Y., Ironmaking Proc., 41, 46 (1982).

Hawkes, P.W., Electron Optics and Electron Microscopy, London: Taylor and Francis (1972).

Hawkes, P.W., Advances in Electronics and Electron Physics, Suppl. 13A: Applied Charged Particle Optics (Septier, A., Ed.), New York: Academic, p.45 (1980).

Hawkes, P.W., Ed., The Beginnings of Electron Microscopy, New York: Academic (1985).

Hawkins, R.J., Monte, L. and Waters, J.J., Ironmaking and Steelmaking, (Quarterly) 1, No.3, 151 (1974).

Hedden, K., Kopper, H.H. and Schluze, V., Z. Physik Chem. (Frankfurt), 22, 23 (1959).

Heerschap, M. and Delavignette, P., Carbon, 5, 383 (1967).

Heerschap, M., Delavignette, P. and Amelinckx, S., Carbon, 1, 235 (1964).

Heidenreich, R.D., Fundamentals of Transmission Electron Microscopy, New York: Wiley-Interscience (1964).

Heinrich, K.F.J. Advances in Optical and Electron Microscopy (Barer, R. and Cosslett, V.E., Eds.), London: Academic, Vol. 6, p.275 (1975).

Hennig, G.R., J. Chem. Phys., 20, 1438 (1952).

Hennig, G.R., Proc. 1st and 2nd Carbon Conf., Baltimore: The Waverly Press Inc., p.103 (1956).

Hennig, G.R., Proc. 4th Carbon Conf., New York: Pergamon Press, p.221 (1960).

Hennig, G.R., Science, 147, 733 (1965).

Hennig, G.R., Chemistry and Physics of Carbon (Walker, P.L. Jr., Ed.), New York: Marcel Dekker, Vol. 2, p.1 (1966).

Hennig, G.R. and McClelland, J.D., J. Chem. Phys., 23, 1431 (1955).

Herold, A., Mater. Sci Eng., 31, 1 (1977).

Herold, A., Physics and Chemistry of Materials with Layered Structures, Intercalated Layered Materials (Levy, F.A., Ed.), Dordrecht: Reidel Publ., Vol. 6, (1979).

Hillier, J., J. Appl. Phys., 17, 411 (1946).

Hillier, J., J. Appl. Phys., 19, 226 (1948).

Hillier, J. and Ramberg, E.G., J. Appl. Phys., 18, 48 (1947).

Hillier, J. and Vance, A.W., Proc. Inst. Radio Eng., 29, 167 (1941).

Hines, R.L. Advances in Optical and Electron Microscopy (Barer, R. and Cosslett, V.E., Eds.), London: Academic, Vol. 9, p.180 (1984).

Hirsch, P.B., Howie, A., Nicholson, R.B., Pashley, D.W. and Whelan , M.J., Electron Microscopy of Thin Crystals, London: Butterworth (1965).

Hobbs, L.W., Introduction to Analytical Electron Microscopy (Hren, J.J., Goldstein, J.I. and Joy, D.C., Eds.), New York: Plenum, p.437 (1979).

Hobbs, L.W., Quantitative Electron Microscopy (Chapman, J.N. and Craven, A.J., Eds.), Edinburgh: Scott. Univ. Summer School Phys., p.399 (1984).

Hobbs, L.W., Ultramicroscopy, 23, 339 (1987).

Holland, F., Ph.D. Thesis, University of Glasgow (1984).

Holland, F., Fryer, J.R. and Baird, T., Electron Microsc. Anal. (Doig, P., Ed.), London: Inst. Phys. Conf. Ser. No. 68, p.19 (1983).

Honda, H., Kimura, H., Sanada, Y., Sugawara, S. and Furuta, T., Carbon 8, 181 (1970).

Horne, R.W. and Markham, R., Practical Methods in Electron Microscopy: Electron Diffraction and Optical Diffraction Techniques (Glauert, A.M., Ed.), Amsterdam: North Holland, Vol. 1, p.325 (1973).

Houska, C.R. and Warren, B.E., J. Appl. Phys., 25, 1503 (1954).

Hull, A.W., Physical Rev., 10(2), 661 (1917).

Humphreys, C.J., Rep. Prog. Phys., London: Inst. Phys., Vol. 42, p.1825 (1979).

Hutchison, J.L., Chem. Sci., 14, 181 (1978).

Hutchison, J.L., Ultramicroscopy, 9, 191 (1982).

Hutchison, J.L. and Briscoe, N.A., Ultramicroscopy, 18, 435 (1985).

Huttinger, K., Chem. Ing. Techn., 43, 1045 (1971).

Iijima, S., Optik, 48, 193 (1977).

Iijima, S., Electron Microsc., Proc. 11th Int. Congr. (Imura, T., Maruse, S. and Suzuki, T., Eds.), Tokyo: Jpn. Soc. Electron Microsc., Vol. 2, p.1437 (1986).

Jones, W., Surf. Defect. Prop. Solids, Spec. Period. Rep. (Roberts, M.W. and Thomas, J.M., Eds.), London: The Chemical Society, Vol. 5, p.65 (1975).

Kammlott, G.W., Surf. Sci., 25, 120 (1971).

Kang, Z.C., Eyring, L. and Smith, D.J., Ultramicroscopy, 22, 71 (1987).

Kay, D.H., (Ed.), Techniques for Electron Microscopy (2nd Edn.), Oxford: Blackwell (1965).

Keown, S.R., Modern Physical Techniques in Materials Technology (Mulvey, T. and Webster, R.K., Eds.), London: Oxford Univ. Press, p.94 (1974).

King, J.G. and Jones, J.H., J. Inst. Fuel., 5, 39 (1931).

Kinney, C.R., Nunn, R.C. and Walker, P.L. Jr., Ind. Eng. Chem., 49(5), 880 (1957).

Kipling, J.J., Sherwood, J.N., Shooter, P.V. and Thompson N.R., Carbon, 1, 315 (1964).

Kipling, J.J. and Shooter, P.V., 2nd Industrial Carbon and Graphite Conference, London: Society of Chemical Industry (1965).

Knoll, M. and Ruska, E., Ann. Physik, 12, 607 and 641 (1932).

Kojima, K., Nishi, T, Yamaguchi, T., Nakama, H. and Ida, S., Trans. ISIJ., 17, 401 (1977).

Kondoh, M., Konishi, Y. and Okabe, K., Iron and Steel Society of AIME, Ironmaking Proc., 40, 454 (1981).

Krevelan, D.W., van, Coal, Amsterdam: Elsevier (1961).

Kroger, C. and Angew Z., Z. Angew Chem., 52, 129 (1939).

Kuzuya, M., Hibino, M. and Maruse, S., Ultramicroscopy, 15, 233 (1984).

Lafferty, J.M., J. Appl. Phys., 22, 299 (1951).

Leung, P.S. and Safford, G.J., Carbon, 8, 527 (1970).

Lewis, I.C., Nuovo Cimento, 10, 89 (1973).

Lewis, I.C., Carbon, 18, 191 (1980).

Lewis, I.C., Carbon, 20, 519 (1982).

Lewis, I.C. and Edstrom, T., Proc. 5th Carbon Conf., New York: Pergamon Press, Vol. 2, p.413 (1961).

Lewis, I.C. and Petro, B.A., J. Polym. Sci., Polymer Chem. Edn., 14 (2), 1975 (1976).

Lewis, I.C. and Singer, L.S., Carbon, 5, 373 (1967).

Lewis, I.C. and Singer, L.S., American Chem. Soc., 13(4), 86 (1969).

Lewis, I.C. and Singer, L.S., Chemistry and Physics of Carbon (Walker, P.L. Jr., and Thrower, P.A., Eds.) New York: Marcel Dekker, Vol. 17, p.1 (1981).

Lewis, J.B., Modern Aspects of Graphite Technology (Blackman, L.C.F., Ed.), New York: Academic Press, p.129 (1970).

Lipson, H. and Stokes, A.R., Nature, 149, 328 (1942(a)).

Lipson, H. and Stokes, A.R., Proc. Roy. Soc. (London), A181, 101 (1942(b)).

Long, F.J. and Sykes, K.W., Proc. Roy. Soc., A193, 377 (1948).

Long, F.J. and Sykes, K.W., J. Chim. Phys., 47, 361 (1950).

Lu, W.K., McMaster Symposium, No.8, 7b-1, Hamilton, Ontario Canada (1980).

Lu, W.K. and Holditch, J.E., Ironmaking Proc., 41, 194 (1982).

Lukesh, J.S., Physical Rev., 80(2), 226 (1950).

Lukesh, J.S., J. Chem. Phys., 19, 384 and 1203 (1951).

Lynch, D.F. and O'Keefe, M.A., Acta. Crystallogr., A28, 536 (1972).

McClure, J.W., Proc. 3rd Carbon Conf., London: Pergamon Press, p.179 (1959).

McDonnell, F.R.M., Pink, R.C. and Ubbelohde, A.R., J. Chem. Soc., 191 (1951).

McKee, D.W., Chemistry and Physics of Carbon (Walker, P.L. Jr., and Thrower, P.A., Eds.) New York: Marcel Dekker, Vol. 16, p.1 (1981).

McKee, D.W. and Chatterji, D., Carbon, 13, 381 (1975).

McMullan, D., Proc. Inst. Elect. Engnrs., 100 (2), 245 (1953).

Maciel, G.E., Bartuska, V.J. and Miknis, F.P., Fuel, 58, 391 (1979).

Maire, J., Colas, H. and Maillard, P., Carbon, 6, 555 (1968).

Maire, J. and Mering, J., Proc. 3rd Carbon Conf., London: Pergamon Press, p.337 (1959).

Maire, J. and Mering, J., Chemistry and Physics of Carbon (Walker, P.L. Jr., Ed.), New York: Marcel Dekker, Vol. 6, p.125 (1970).

Makin, M.J., Electron Microsc., Proc. 9th Int. Congr. (Sturgess, J.M., Ed.), Toronto: Microsc. Soc. Can., Vol. 3, p.330 (1978).

Marks, L.D. and Smith, D.J., J. Microsc., 130, 249 (1983).

Marsh, H., Murdie, N. and Edwards, I.A.S., Chemistry and Physics of Carbon (Thrower, P.A., Ed.), New York: Marcel Dekker, Vol. 20, p.213 (1987).

Marsh, H. and Rand, B., Carbon, 9, 63 (1971).

Marsh, H. and Wynne-Jones, W.F.K., Carbon 1, 269 (1964).

Maughin, C., Bull. Soc. Fr. Min., 49, 32 (1926).

Menter, J.W., Proc. Roy. Soc. (London), A236, 119 (1956).

Mering, J. and Maire, J., J. Chim. Phys., 57, 803 (1960).

Millward, G.R. and Jefferson, D.A., Chemistry and Physics of Carbon (Walker, P.L. Jr., and Thrower, P.A., Eds.), New York: Marcel Dekker, Vol. 14, p.1 (1978).

Misell, D.L., J. Phys., A4, 798 (1971).

Misell, D.L., Advances in Electronics and Electron Physics (Marton, L., Ed.), New York: Academic, Vol. 32, p.63 (1973).

Moodie, A.F. and Warble, C.E., Proc. 8th Int. Congr. Electron Microsc. (Sanders, J.V. and Goodchild, D.J., Eds.), Canberra: Aust. Acad. Sci., Vol. 1, p.230 (1974).

Mulvey, T. Proc. Roy. Microsc. Soc., 2, 201 (1967).

Murata, Y., Fryer, J.R. and Baird, T., J. Microsc., 108, 261 (1976).

Narita, k., Onoye, T., Satoh, Y., Miyamoto, M., Taniguchi, K., Kamatani, S., Sato, T. and Fukihara, S., Trans. ISIJ, 21, 839 (1981).

Neumann, B., Kroger, C. and Fingas, E., Z. Anorg. Chem., 197, 321 (1931).

Nixon, W.C., Ahmed, H., Catto, C.J.D., Cleaver, J.R.A., Smith, K.C.A., Timbs, A.E., Turner, P.W. and Ross, P.M., Electron Microsc. Anal. (1977).

Oatley, C.W., The Scanning Electron Microscope, Cambridge: Cambridge Univ. Press (1972).

Oatley, C.W., Nixon, W.C. and Pease, R.F.W., Advances in Electronics and Electron Physics (Marton, L., Ed.), New York: Academic, Vol. 21, p.181 (1965).

Oberlin, A., Carbon, 22, No.6, 521 (1984).

Oberlin, A., Terriere, G. and Boulmier, J.L., Tanso, No.83, 153 (1975(a)).

Oberlin, A., Terriere, G. and Boulmier, J.L., Tanso, No.80, 29 (1975(b)).

Pacault, A., Chemistry and Physics of Carbon (Walker, P.L. Jr., Ed.), New York: Marcel Dekker, Vol. 7, p.107 (1971).

Patrick, J.W. and Shaw, F.H., Fuel, 51, 69 (1972).

Pauling, L., The Nature of the Chemical Bond, New York: Cornell University Press (1945).

Pauling, L., Proc. Natl. Acad. Sci., 56, 1646 (1966).

Pease, R.F.W., Proc. 4th Annu. Scanning Electron Microsc. Symp. (Johari, O. and Corvin, I., Eds.), Chicago: I.I.T. Res. Inst., Vol.1, p.11 (1971).

Pease, R.F.W. and Nixon, W.C., J. Sci. Inst., 42, 81 (1965).

Perret, R. and Ruland, W., J. Appl. Crystallogr., 1, 308 (1968).

Perret, R. and Ruland, W., J. Chim. Phys. (Special Issue, Apr.), p.98 (1969).

Phillips, R., Br. J. Appl. Phys., 11, 504 (1960).

Pincus, H.J., Advances in Optical and Electron Microscopy (Cosslett, V.E. and Barer, r., Eds.), London: Academic, Vol. 7, p.17 (1978).

Platzer, N., Ann. Chim. (Paris), 51, 805 (1960).

Poole, J.B. le., Philips Tech. Rev., 9, 33 (1947).

Porter, A.B., Proc. Philos. Mag., 11, 154 (1906).

Power, P.C. Jr. and Pincus, H.J. Science (Washington D.C.), 186, 234 (1974).

Read, W.T., Dislocations in Crystals, New York: McGraw-Hill (1953).

Reid, N., Practical Methods in Electron Microscopy (Glauert, A.M., Ed.), Amsterdam: North Holland, Vol. 3, p.211 (1974).

Reimer, L., Proc. 9th Annu. Scanning Electron Microsc. Symp. (Johari, O. and Corvin, I., Eds), Chicago: I.I.T. Res. Inst., Vol.1, p.1 (1976).

Robert, M.C., Oberlin, M. and Mering, J., Chemistry and Physics of Carbon (Walker, P.L. Jr., Ed.), New York: Marcel Dekker, Vol. 10, p.141 (1973).

Rontgen, W.C., Science, 3(59), 227 (1896).

Rudberg, E., Physical Rev., 50(2), 138 and 150 (1936).

Rudorff, W. and Hoffman, U., Z. Anorg. Allgem. Chem., 238, 1 (1938).

Ruland, W., Paper# III-12, Symp. on Carbon, Tokyo (1964).

Ruland, W., Acta. Crystallogr., 18, 992 (1965(a)).

Ruland, W., Carbon, 2, 365 (1965(b)).

Ruland, W., Acta. Crystallogr., 22, 615 (1967(a)).

Ruland, W., Paper# S159, 8th Carbon Conf., New York: Pergamon Press (1967(b)).

Ruland, W., Chemistry and Physics of Carbon (Walker, P.L. Jr., Ed.), New York: Marcel Dekker, Vol. 4, p.1 (1968).

Ruska, E., Z. Physik, 87, 580 (1934).

Ruska, E., Microsc. Acta., Suppl. 5: The Early Development of Electron Lenses and Electron Microscopy (Mulvey, T., Transl.), Stuttgart: Hirzel (1980).

Schafhaeutl, P., J. Prakt. Chem., 21, 155 (1841).

Scherzer, O., J. Appl. Phys., 20, 20 (1949).

Schiller, C. and Mering, J., Paper# S161, 8th Carbon Conf., New York: Pergamon Press (1967).

Schiller, C., Mering, J., Cornualt, P. and Chaffaut, F. du., Carbon, 5, 385 and 507 (1967).

Schiller, C., Mering, J. and Oberlin, M., J. Appl. Cryst., 1, 282 (1968).

Schrodinger, E., Ann. Physik, 81 (4), 109 (1926).

Schultz, R.V., Jorgenson, J.W., Maskarinec, M.P., Novotny, M. and Todd, L.J., 58, 783 (1979).

Selig, H. and Ebert, L.B., Adv. Inorg. Chem. Radio Chem., 23, 281 (1980).

Sharkey, A.G., Schultz, J.L. and Friedel, R.A., Carbon 4, 365 (1966).

Sharma, R., Barry, J. and Eyring, L., Ultramicroscopy, 23, 453 (1987).

Shevlin, M.J.F., Ph.D. Thesis, University of Glasgow, Vol 1 (1987).

Shevlin, M.J.F., Fryer, J.R. and Baird, T., Proc. 8th European Congr. on Electron Microsc., (Eurem 84), Programme Committee of the 8th European Congr. on Electron Microsc.: Hungary, Vol 1, p.239 (1984).

Shevlin, M.J.F., Fryer, J.R. and Baird, T., Electron Microsc. Anal. (Tatlock, G.J., Ed.), London: Inst. Phys. Conf. Ser., 78, 553 (1985).

Shevlin, M.J.F., Fryer, J.R. and Baird, T., Carbon, 24, No. 5, 527 (1986).

Short, M.A. and Walker, P.L., Jr., Carbon, 1, 3 (1963).

Simon, C., Estrande, H., Tchoubar, D. and Conard, J., Carbon, 15, 211 (1977).

Simon, R., J. Appl. Phys., 41 (4), 4632 (1970).

Singer, L.S. and Lewis, I.C., Carbon, 2, 115 (1964).

Singer, L.S. and Lewis, I.C., Carbon, 16, 417 (1978).

Slonczewski, J.C. and Weiss, P.R., Physical Rev., 109(2), 272 (1958).

Smith, D.J., Electron Microsc. Anal. (Tatlock, G.J., Ed.), London: Inst. Phys., Conf. Ser. No. 78, p.311 (1985).

Smith, D.J., Electron Microsc., Proc. 11th Int. Congr. (Imura, T., Maruse, S. and Suzuki, T., Eds.), Tokyo: Jpn. Soc. Electron Microsc., Vol. 2, p.929 (1986).

Smith, D.J., Camps, R.A., Freeman, L.A., Hill, R., Nixon, W.C. and Smith , K.C.A., J. Microsc., 130, 127 (1983(a)).

Smith, D.J., Camps, R.A., O'keefe, M.A., Saxton, W.O. and Wood, G.J., Ultramicroscopy, 18, 63 (1985).

Smith, D.J., McCartney, M.R. and Bursill, L.A., Ultramicroscopy, 23, 299 (1987).

Smith, D.J., White, D., Baird, T. and Fryer, J.R., J. Catal., 81, 107 (1983(b)).

Spence, J.C.H., Experimental High Resolution Electron Microscopy, Oxford: Clarendon (1981).

Strong, S.L., Paper# SS-12, 9th Carbon Conf., Boston, New York: Pergamon Press (1969).

Tate, M., Suzuki, K., Chang, T.S., Kuwano, Y., Go, H., Honda, K., Matsuzaki, M., Tsuji, E. and Nakamura, S., Trans ISIJ, 19, 332 (1979).

Taylor, A. and Laidler, D., Nature, 146, 130 (1940).

Thomas, J.M and Evans, E.L., Nature, 214, 167 (1967).

Thomson, G.P. and Reid, A., Nature (London), 119, 890 (1927).

Thon, F. and Siegel, B.M., Ber. Bunsenges. Phys. Chem., 74, 1116 (1970).

Trzebistowski, W., Roczniki Chem., 17, 73 (1937).

Tsuzuku, T., Proc. 3rd Carbon Conf., London: Pergamon Press, p.433 (1959).

Ubbelohde, A.R., Nature, 180, 380 (1957).

Ubbelohde, A.R., J. Chem. Phys., 58, 107 (1961).

Ubbelohde, A.R. and Lewis, F.A., Graphite and its Crystal Compounds, London: Oxford University Press (1960).

Urban, K., Phys. Status Solidi, A56, 157 (1979).

Vanderhart, D.L. and Retcofsky, H.L., Fuel, 55, 202 (1976).

Walker, P.L. Jr., Rusinko, F. Jr. and Austin, L.G., Advances in Catalysis (Eley, D.D., Selwood, P.W. and Weisz, P.B., Eds.), New York: Academic Press, Vol.11, p.133 (1959).

Walker, P.L. Jr., Shelef, M. and Anderson, R.A., Chemistry and Physics of Carbon (Walker, P.L. Jr., Ed.), New York: Marcel Dekker, Vol.4, p.287 (1968).

Wallace, P.R., Physical Rev., 71(2), 622 (1947).

Wallace, P.R., Solid State Commun., 4, 521 (1966).

Warren, B.E., Physical Rev., 59(2), 693 (1941).

Warren, B.E., Proc. 1st and 2nd Carbon Conf., Baltimore: The Waverly Press Inc., p.49 (1956).

Warren, B.E. and Bodenstein, P., Acta Crystallogr., 18, 282 (1965).

Warren, B.E. and Bodenstein, P., Acta Crystallogr., 20, 602 (1966).

Watt, I.M., The Principles and Practice of Electron Microscopy, Cambridge: Cambridge Univ. Press (1985).

Wells, O.C., Scanning Electron Microscopy, New York: McGraw-Hill (1974).

Wen, W.Y., Catal. Rev. Sci. Eng., 22(1), 1 (1980).

Whelan, M.J., J. Inst. Metals, 87, 392 (1959).

Whelan, M.J., Diffraction and Imaging Techniques in Material Science (Amelinckx, S., Gevers, R. and Landuyt, J. van., Eds.), Amsterdam: North Holland, Vol. 1, p.43 (1978).

White, D., Hutchison, J.L. and Ramdas, S., Electron Microsc. Anal. (Brown, L.M., Ed.), London: Inst. Phys., Conf. Ser. No. 90, p.249 (1987).

Williams, R.C. and Fisher, H.W., J. Mol. Biol., 52, 121 (1970).

Williamson, G.K. and Baker, C., Proc. Eur. Conf. Electron Microsc., Delft, 1, 326 (1960).

Williamson, G.K. and Baker, C., Proc. 5th Carbon Conf., New York: Pergamon Press, Vol 2, p.521 (1962).

Wischnitzer, S., Introduction to Electron Microscopy, 3rd Edn., New York: Pergamon Press (1981).

Wolf, R.J. and Joy, D.C., Electron Microsc. Anal. (Nixon, W.C., Ed.), London: Inst. Phys., Conf Ser. No. 10, p.34 (1971).

Woodruff, E.M., J. Chim. Phys. (Special issue, Apr.) p.96 (1969).

Yonezawa, A., Nakagawa, S. and Suzuki, M., Proc. 35th Annu. Meet. Electron Microsc. Soc. Am. (Bailey, G.W., Ed.), Baton Rouge: Claitor, p.62 (1977).

Zworykin, V.K., Morton, G.A., Ramberg, E.G., Hillier, J. and Vance, A.W., Electron Optics and the Electron Microscope, New York: Wiley (1945).

LIST OF FIGURES

AND TABLES